Universitat Politècnica de Catalunya
Escola Tècnica Superior d'Enginyers
de Camins, Canals i Ports

Departament de Resistència de Materials i Estructures a
l'Enginyeria

Phd Thesis

Numerical calculation model for the global analysis of concrete structures with masonry walls

By

Cuauhtémoc Escudero Torres

Advisors:

Sergio Oller

Alex H. Barbat

Xavier Martínez

Barcelona, December 2014

UNIVERSITAT POLITÈCNICA DE CATALUNYA
BARCELONATECH
Escola de Doctorat

Acta de qualificació de tesi doctoral

Curs acadèmic:

Nom i cognoms
Cuauhtémoc Escudero Torres.

Programa de doctorat
Análisis Estructural.

Unitat estructural responsable del programa
Departament de Resistència de Materials i Estructures a l'Enginyeria

Resolució del Tribunal

Reunit el Tribunal designat a l'efecte, el doctorand / la doctoranda exposa el tema de la seva tesi doctoral titulada

_____

_____.

Acabada la lectura i després de donar resposta a les qüestions formulades pels membres titulars del tribunal, aquest atorga la qualificació:

☐ NO APTE ☐ APROVAT ☐ NOTABLE ☐ EXCEL·LENT

(Nom, cognoms i signatura)	(Nom, cognoms i signatura)	
President/a	Secretari/ària	
(Nom, cognoms i signatura)	(Nom, cognoms i signatura)	(Nom, cognoms i signatura)
Vocal	Vocal	Vocal

_____, _____ d'/de _____ de _____

El resultat de l'escrutini dels vots emesos pels membres titulars del tribunal, efectuat per l'Escola de Doctorat, a instància de la Comissió de Doctorat de la UPC, atorga la MENCIÓ CUM LAUDE:

☐ SÍ ☐ NO

(Nom, cognoms i signatura)	(Nom, cognoms i signatura)
President de la Comissió Permanent de l'Escola de Doctorat	Secretari de la Comissió Permanent de l'Escola de Doctorat

Barcelona, _____ d'/de _____ de _____

This page is intentionally left blank.

Abstract

The numerical simulation in the field of civil engineering, while widely used in structural design, has not benefited from the full potential offered by new technologies for the analysis and design of composite materials within the framework of the finite element, technologies that are already present in industries such as automotive, aerospace and shipbuilding.

This thesis is based on the numerical simulation, and emerges as the need to combine and improve existing technologies in the field of finite element analysis for composite materials, to assess the overall structural behavior of reinforced concrete buildings with masonry in-fills, and consequently, to support the derivation of rational rules for analysis and design purposes.

Prior to the beginning of this thesis, a huge concern was the large amount of computational resources needed for both solving systems of linear equations resulting from the use of the finite elements method, and for storing internal variables needed in the integration of constitutive models. Therefore, in this work, computational strategies used to enable the analysis of *real life* structures are also provided.

The simplicity required to handle meshes with high amount of finite elements pushed us to develop a new layered finite element, that can reproduce the non-linear behavior of its constituent materials when there are out-of-plane stresses, this, without having to introduce additional degrees of freedom. The finite element proposed has been compared to finite element with different kinematics obtaining excellent results.

The robustness and efficiency of the developed methodology for analysis of masonry and concrete buildings, is conditioned by the ability of using different patterns of steel reinforcement, which are typically presented in *real life* structures. That is why it has also been necessary to develop a computing program capable of reading both finite element meshes, and patterns of fibers represented with convex polygons, and as a result of areas intersections between polygons returns volumetric participation of fiber and matrix of constituents materials for each layer, in addition had to return the fiber orientation with respect to the local axis of the finite element.

The numerical results obtained have been compared in some cases with experimental results available in the literature, in other cases, with numerical results obtained using Building Codes, in both cases, there have been good agreement between them. Finally, it has been possible to characterize a representative medium-rise building of Mexico City using the capacity spectrum method. This method is widely used nowadays for the assessment of building behavior, since using fragility curves can represent the ability of a building to resist an earthquake.

Resumen

La simulación numérica en el campo de la ingeniera civil, aunque es ampliamente utilizada en el diseño estructural, no se ha beneficiado de todo el potencial que ofrecen las nuevas tecnologías para el análisis y diseño de materiales compuestos dentro del marco de los elementos finitos, tecnologías que ya están presenten en industrias como la automotriz, aeroespacial o la naval.

Este trabajo de tesis esta basado en la simulación numérica, y surge como la necesidad de combinar y mejorar tecnologías existentes en el campo de los elementos finitos y de análisis de materiales compuestos, para conocer el comportamiento estructural global de los edificios de hormigón armado con rellenos de mampostería, y para apoyar en la derivación de reglas racionales con fines de diseño.

Una preocupación previa al inicio de esta tesis doctoral, era la gran cantidad de recursos computacionales necesarios, tanto para la resolución de los sistemas de ecuaciones lineales resultantes con el uso del método de los elementos finitos, como para el almacenamiento de variables internas necesarias en la integración de modelos constitutivos. Por ello, dentro de este trabajo, también se proporcionan las estrategias computacionales usadas que permiten el análisis de estructuras de la *vida real*.

La simplicidad requerida para el manejo de mallas con gran cantidad de elementos finitos lleva a desarrollar un elemento de lámina con diferentes capas, que pueda reproducir el comportamiento no lineal de sus materiales componentes cuando existen tensiones fuera del plano, sin que haya que introducir grados de libertad adicionales. El elemento finito propuesto ha sido comparado con elementos finitos de diferente cinemática obteniendo excelentes resultados.

La robustez y eficiencia de la metodología desarrollada para el análisis de edificios de hormigón y mampostería, esta condicionada a la capacidad de utilizar los diferentes patrones de acero de refuerzo que típicamente se presentan en estructuras de la *vida real*. Es por ello que también ha sido necesario desarrollar un programa de computo capaz de leer tanto una malla de elementos finitos, como un patrón de fibras representado con polígonos convexos, y que mediante operaciones de intersecciones de áreas entre polígonos, de como resultado la participación volumétrica de matriz y fibra de los materiales componentes por cada capa, además de la orientación de la fibra con respecto a los ejes locales del elemento finito.

Los resultados numéricos obtenidos se han comparado con resultados experimentales presentes en la literatura, y con resultados numéricos obtenidos utilizando normas de construcción, en ambos casos, se han observado buenos ajustes entre ellos. Finalmente,

ha sido posible caracterizar un edificio representativo ubicado en la Ciudad de México usando el método del espectro de capacidad. Dicho método es ampliamente utilizado hoy en día para el diseño y evaluación sismo-resistente de estructuras, ya que mediante el uso de curvas de fragilidad permite representar la susceptibilidad de una estructura a ser dañada debido a un terremoto.

Contents

This page is intentionally left blank.

List of figures

Chapter 1

Introduction

Masonry construction is a combination of individual units (bricks) bound together by a mortar, is an ancient construction technique of prehistoric and civilized peoples, from simply stone, later, shaped stone, to finally bricks: the oldest manufactured building materials. Enormous constructions such as the Great Wall of China, Mayan pyramids in Mexico and Central America, the Taj Mahal at India, point importance of masonry constructions along mankind evolution, becoming the oldest building technique that still finds wide use in today's building industries. Bricks have evolved from shaped stones to sun-baked clay bricks 6,000 years ago, enhanced to reach their final form about 4,000 B.C moving from sun-baked to fire-baked.

Perhaps the most important innovations in the evolution of architecture were the development of masonry arches and domes, overcoming the span limitations at the time.

Masonry building construction has had ups and downs, with the onslaught of Industrial Revolution, factors such as: invention of Portland cement in 1824, refinement on iron production in the early nineteenth century, and the development of the Bessemer furnace in 1854, besides the demand of high-rise constructions, architectural creativity were set away from masonry. By the twenty century, The Chicago School had pioneered the use of iron and steel skeleton frames, so masonry was completely relegated to the usage of facings, in-fill, and fireproofing. The Monadnock Building in Chicago fig.1.1 is generally cited as the last great building in the *ancient tradition* of masonry structures. Its 16-story unreinforced load bearing walls were required by code to be several feet thick at the base, making it seem unsuited to the demands of a modern industrialized society.

Revival of construction on masonry came from profitable reasons, according to Beal C. [19], in the early 1920s, economic difficulties in India convinced officials that alternative to concrete and steel structural system had to be found. Extensive research began into the structural performance of reinforced masonry, which led not only to new systems of low-cost construction, but also to the first basic understanding of the structural behavior of masonry, however, it was not until the late 1940s, that European engineers and architects began serious studies of masonry bearing wall designs.

Significant improvements over old ancient tradition of masonry construction were achieved, contemporary masonry buildings had now thinner, lighter-weight, more efficient structural systems and veneers than in the past.

Over the last 40 years, masonry building construction has been widely practiced in countries and regions of extremely high seismic activity, used for construction of one-

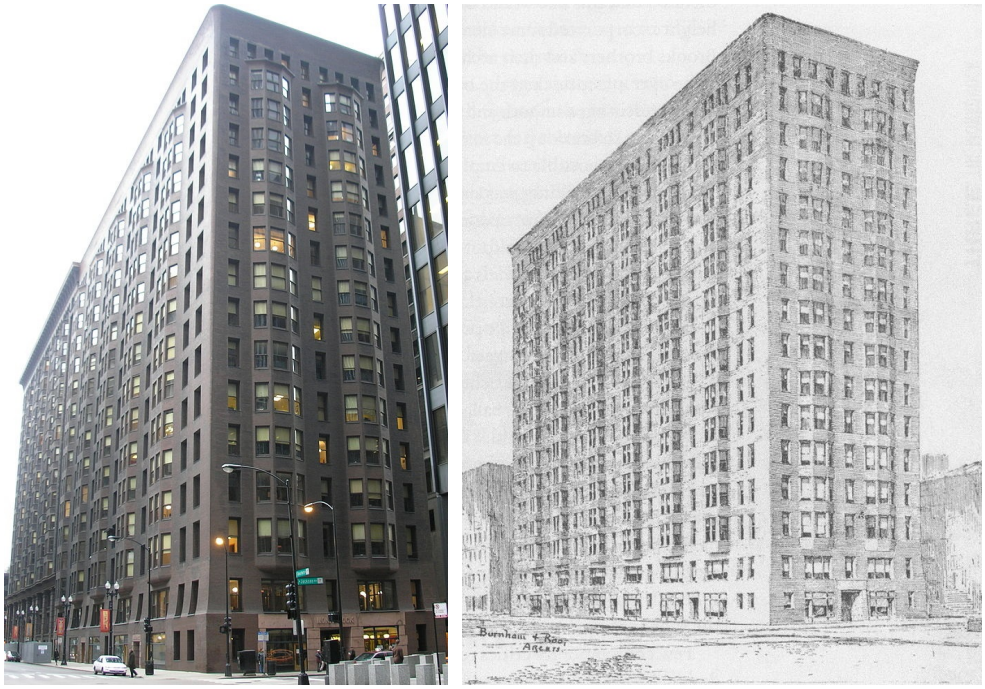

Figure 1.1 *The Monadnock Building in Chicago (1891).*

storey single-family housing to medium-rise apartment buildings (up to six-storey high). Despite such wide range of application few resources have been put in structural masonry research while compared with steel construction or concrete reinforced construction.

Let us use the example of Mexico City, to put in context some aspects such as: economics, demographics and its structural performance, to have a better understanding of the reliability in such construction system, and why it has been adopted as a strategy to overcome housing shortage.

Economic: low-cost construction is the most significant aspect that makes masonry structures reliable, hence, construction of housing buildings made out of reinforced bearing walls (fig.1.2) is highly promoted by INVI. *Instituto Nacional de la Vivienda*, or simply INVI, is a governmental association that assures people with the lowest incomes in Mexico City have affordable and decent homes.

According to its website, in 2012, from January to December, INVI has invested 2,692,452,943.64 Mexican pesos (158,379,584.92 euros) in 198 properties for a total of 1970 houses, not yet been sufficient for the huge demand for housing in Mexico City.

Demographics: as a result of an intense inner in-migration activity toward Mexico City, or the so called Greater Mexico City officially called *Mexico City and Metropolitan Area*, (fig.1.3), in the past 50 years, combined with the lack of space, a essential strategy to solve the housing necessities, is via medium rise constructions, both risk proof and cheap.

Structural performance: Masonry structures designed in compliance with current code requirements perform well, even in cases of significant seismic activity [92].

Mexico City's vulnerability to earthquake damage comes from its location, lays on

Figure 1.2 *Typical apartment building in Mexico City.*

Figure 1.3 *Population distribution of the Greater Mexico City.*

the silt and volcanic clay sediments of the bed of the Lake Texcoco, which are between seven and thirty-seven meters deep and have a high water content. The expansion of Mexico City, and the gradual draining of the lake left one of the world's largest population center located largely on unconsolidated lake-bed sediments. Thus, these soft sedimentary clay deposits amplify the seismic waves, resulting on different ground motion responses within the same city, such effect is known as *seismic microzoning*.

Figure 1.4 depicts a superposition of evolution on the seismic microzoning of Mexico City over the Texcoco Lake.

On the other hand, on the west coast of southern Mexico and Central America, the Cocos Plate dips beneath the North American Plate producing a seismically active zone.

1.1 Background and Motivation

Over the last decades reinforced concrete (RC) frames with masonry in-fills become the preferred construction technique for low-rise buildings worldwide. Yet, due to their need for precise detailing and execution on one hand, and the frequently inadequate level of craftsman-ship on the other, such construction technique proved to be excessively vulnerable to earthquakes. So a less sophisticated construction technique: *Confined Masonry technique* evolved as an informal process based on its satisfactory performance.

Since the work done by Rathbun in 1938 [137], where the influence on the structural performance of in-filled frames subjected to lateral loads was first noticed, structural behavior of masonry wall has been the subject of many experimental and analytical studies around the world, considering different lateral and vertical load conditions and taking into account particular characteristics of masonry components. The first reported use of confined masonry construction was in the reconstruction of buildings destroyed by the 1908 Messina, Italy earthquake (magnitude 7.2) which killed over 70,000 people [24].

In countries with high seismic activity, like Chile, this construction practice started in 1930's after the 1928 Talca earthquake (magnitude 8.0) that affected a significant number of unreinforced masonry buildings [24]. Subsequently, the 1939 earthquake (magnitude 7.8) that struck the mid-southern region of the country, revealed a very good performance of confined masonry buildings [104].

Confined masonry construction was introduced in Mexico City, Mexico in the 1940's to control the wall cracking caused by large differential settlements under the soft soil conditions. Several years later, this system became popular in other areas of highest seismic hazard due to its excellent earthquake performance [93], but was until early 60s when the proper study of confined masonry started in the country, when Esteva [49, 50, 48] tested masonry walls confined with reinforced concrete. Later on, several studies were made at the time, like the ones made by Meli *et al.* [98], Meli and Salgado [97], Madinaveitia and Rodríguez [83], Turkstra [164], Meli and Reyes [96], Madenaveitia [82], Meli and Hernández [94, 95], being the bases upon Hernández in 1975 [60] provided design and construction recommendations for structures made out of masonry bearing walls. Thus, in 1977 the first Mexican code for design and construction of masonry structures was established, where, for design purposes, a simplified use of mechanical of materials theories is used. Appendix D depicts the analysis and design considerations to take into account while designing a confined masonry bearing wall structure.

Over the last 40 years, confined masonry construction has been practiced in Mediterranean Europe (Italy, Slovenia, Serbia), Latin America (Mexico, Chile, Peru, Argentina

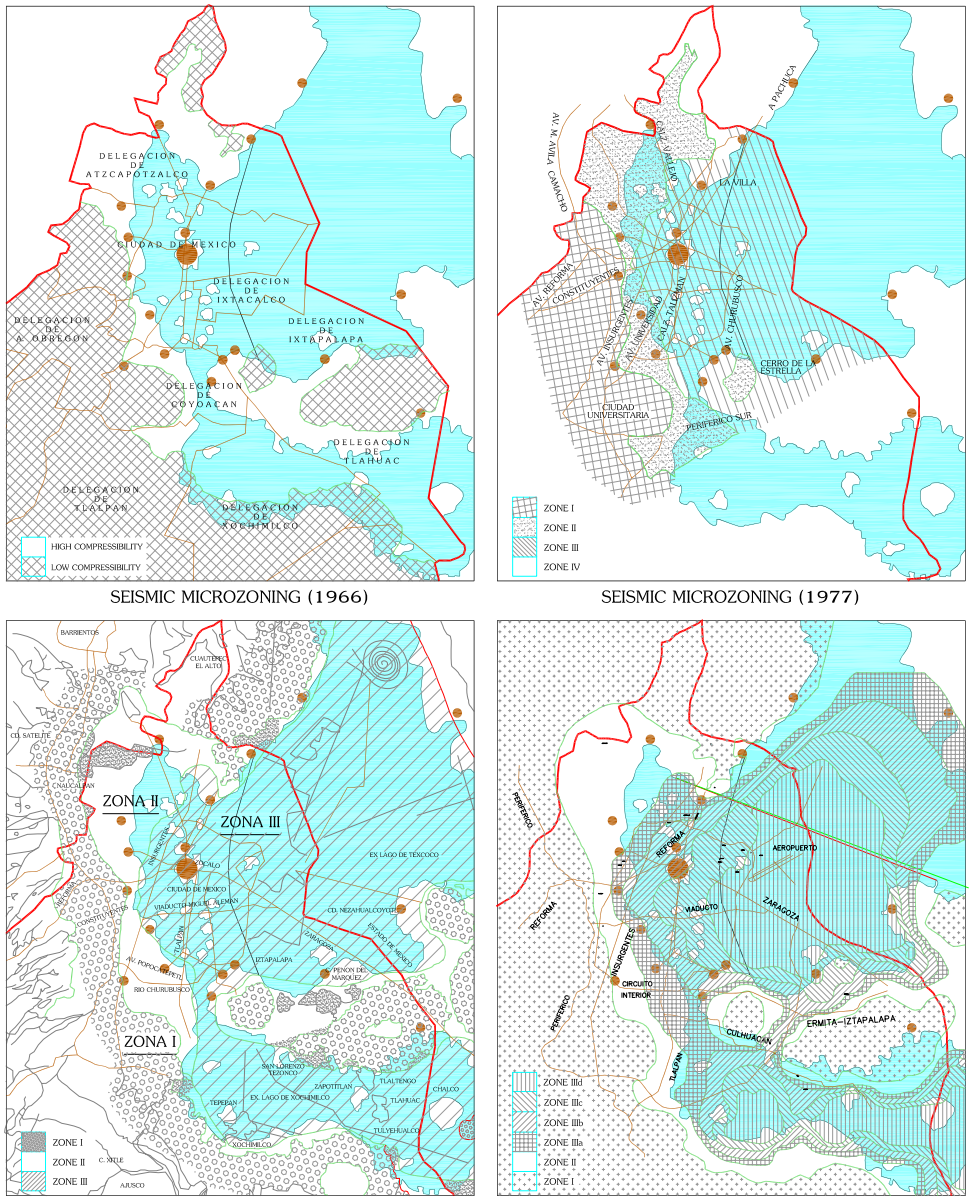

Figure 1.4 *Evolution on Seismic Microzoning of Mexico City.*

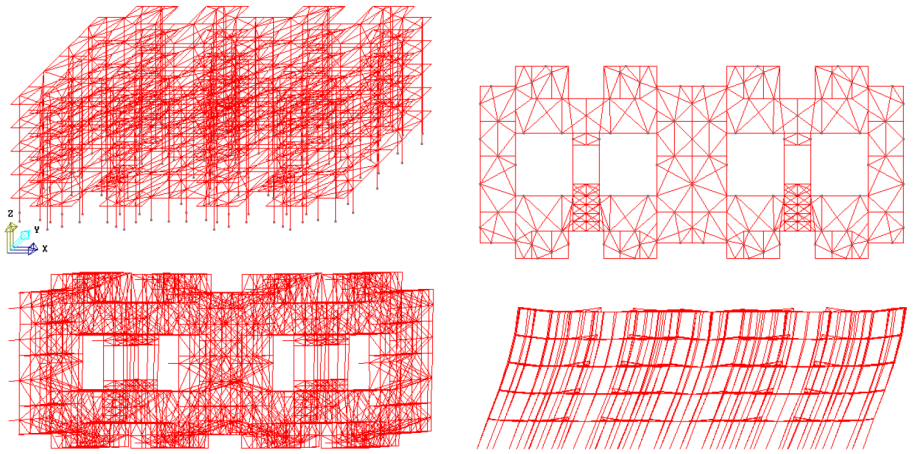

Figure 1.5 *Confined masonry building where walls are modeled as an equivalent column and slabs are modeled with diagonals [55].*

and other countries) The Middle East (Iran), South Asia (Indonesia) and the Far East (China) [24]. Despite the use of masonry in different types of constructions, this material has not been investigated as intensely as other construction materials, like reinforced concrete or steel. Per Se, construction is one of the most traditional and less technified industries when compared to other building industries, like aerospace or automotive more benefited from the development of composite materials. This is an abnormal situation that generates important negative social and economic consequences. Construction industry needs support in research and development in order to be more competitive and integrated within the present world standards. Although literature shows experimental and analytical research on this field has progressively increased in past 50 years, numerous uncertainties still remain.

The current technologies have led to model confined masonry building subjected to ground shaking mainly as:

a. As a **truss** [24], as shown in figure 1.6, where masonry wall act as diagonal struts subjected to compression, whereas the reinforced concrete confining members act in tension/compression, depending on the lateral earthquake forces.

b. As a **frame** [55], where confined masonry walls are modelled using an equivalent column (fig. 1.5), it is assumed the beams have infinite stiffness, and diagonal struts are used to model the slabs.

In both cases, the analogy made are highly simplistic and lack in accuracy. Researching work has also been extended to the numerical field applying the finite element method. Isotropic elastic behavior was first considered by Rosenhaupt [142], and Saw [148] ignoring the influence of mortar acting as planes of weakness, so first approximation was settle, since such assumption was useful in predicting deformation at low stress level, but not at higher stresses level where redistribution stress caused by non-linear material behavior and local failure would occur. Later on, material models, based on average properties and with the influence of mortar joints ignored but including the possibility of local failure, were developed by Ganju [56] and Samarasinghe [145]. On 1978

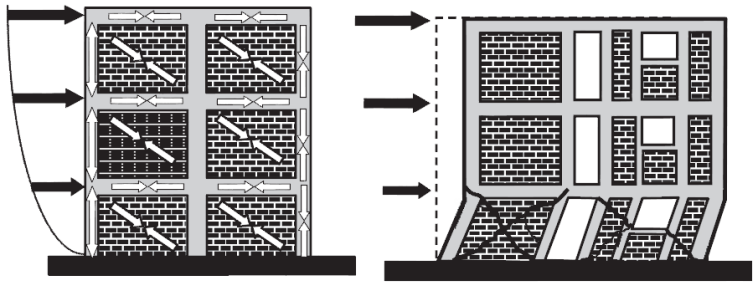

Figure 1.6 *Confined masonry building modeled as a vertical truss [24].*

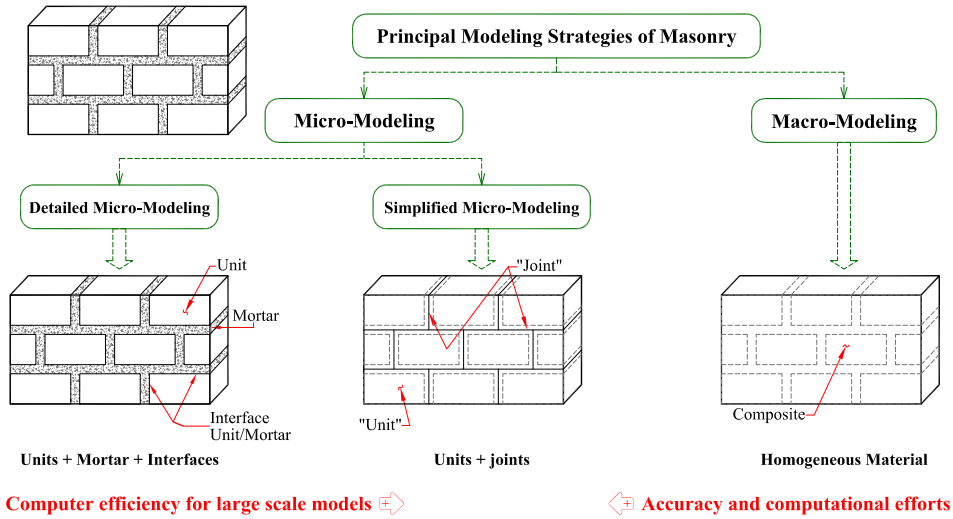

Figure 1.7 *Modeling strategies for masonry structures.*

Page [124] presented a finite element model procedure to reproduce non-linear behavior, where masonry is considered as an assemblage of elastic brick continuum elements acting in conjunction with linkage elements simulating the mortar joints. The joint elements are assumed to have high compressive strength, low tensile strength, and limited shear strength depending upon the bond strength and the acting degree of compression. Lourenço [79] in 1996 focuses on the non-linear analysis of unreinforced masonry structures using a plane stress approximation for shear walls and panels. If the reader may want to go further on the subject, a comprehensive review on the finite element modeling of unreinforced masonry structures, both in the static and dynamic regime, has been conducted by Tzamtzis and Asteris [166].

The majority of the proposed modeling strategies, in order to study the mechanical behavior of masonry has been identified by Lourenço [79] and Rots [143], and can be classified in two categories:

- **Micro-modeling, or two-phase material models**: where the components are considered separately to account the different inelastic behavior in the interaction

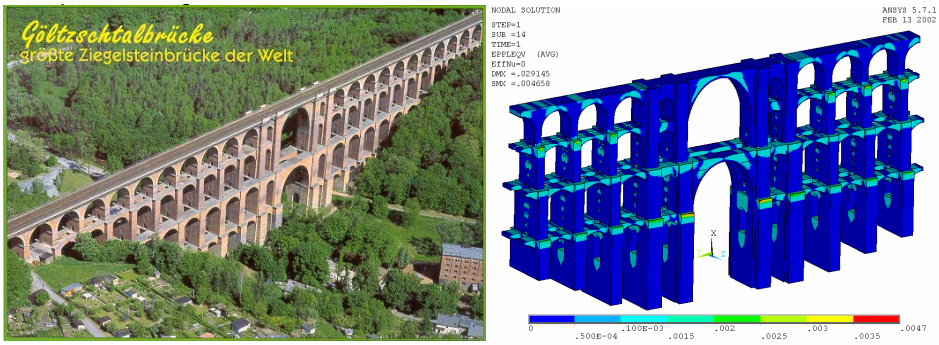

Figure 1.8 *Macro-modeling for Göltzschtal Bridge [150].*

between them. Analysis within this category are relatively costly to use due to the great number of degrees of freedom, require more input data, and their failure criterion has a complicated form due to the brick-mortar interaction. The constitutive equations of the components have normally a simple form, on the other hand, and they are suitable for the study of local behavior of masonry. This modeling strategy is categorized into (see figure 1.7):

a. *Detailed micro-modeling* where units and mortars are represented as continuum, with the unit/mortar interfaces modeled using discontinuous interfaces elements as potential cracks, slip and crushing planes.

b. *Simplified micro-modeling* through the adoption of *geometrically expanded* masonry units with a single average interface representing the mortar and the two mortar/unit interfaces. This models requires the material model of the expanded unit and masonry joints.

- **Macro-modeling or one-phase material models**: treating masonry as an ideal homogeneous single material with constitutive equations that differ from those of the components (mortar and bricks). The constitutive models on this category are relatively simple to use, requires a less input data, and the failure criterion has normally a simple form. On the other hand, their constitutive equations are relatively complicated and are suitable at best for the global behavior of masonry. Figure 1.8 correspond to the work done by Schlegel *et al* [150] using a macro-modeling technique in the structural analysis of the Göltzschtal bridge.

The structural capabilities of confined masonry bearing wall structures, or reinforced concrete structures with masonry in-fills are still being explored. The objective of this work is to continue researching on the matter using a *One-phase material model* [79, 143], so, be able to reproduce the overall behavior of masonry structures, using both classical mixing theories and enhanced mixing theories [135, 88] on laminated composite materials within the finite element method framework.

1.2 Objectives

The main objective of this work, is to develop an efficient methodology, and be able of numerically reproduce the behavior of an entire masonry structure, to subsequently, find reliable estimates of the non-linear response which leads to fully understand the failure mechanisms and assess the safety of the structure.

In order to achieve this objective, the state of the art for shell elements has been reviewed, leading to the proposal of a new integration scheme over the thickness for layered shell elements, enhancing the bending-membrane coupled effect and allowing degradation in different layers of the composite material.

Also, state of the art of rules of mixtures for composite materials has been reviewed, leading to the development of a computational tool. This tool arises as a need of mechanizing and generates the composite material information given a large mesh of triangular finite elements and a *real life* steel reinforcement pattern of every layer within the composite.

A priori, one of the main drawbacks with this proposal, could be that the computational process in terms of time-consuming and RAM memory needed would be rather expensive. Hence, as an attempt to overcome such presumable disadvantage, some alternatives have to be explored, and are listed below.

- To speed it up, the computational code has to be built in parallel programming using OMP directives, and therefore, be able to obtain a response in terms of time as a function of the used number of threads.

- Propose some computational strategies to store only the strictly necessary amount of information, like internal variables, stresses or strain. This, to reduce the consumed memory resources.

- Although *pardiso* [149], the direct solver used for the solution of the linear system equations has a great performance in terms of time, lacks in terms of memory RAM required, due to the size of the matrices required to solve the linear system. An explored solution is the use of a preconditioned iterative solver, although the optimal solution strategy depends on the computational resources.

On the other hand, code regulations regarding the analysis and design of masonry buildings have to be reviewed, to compare the obtained results with the proposed analysis scheme.

Finally, the theoretical principles used will be expressed and applied to assemble a robust numerical tool capable of predicting the behavior of *real life* structures from linear elastic stage, through cracking and degradation until complete loss of strength.

1.3 Outline

Since this work deals with two different topics, the state-of-the-art is provided at the beginning of chapter 2 and chapter 3. The work presented is organized as follows:

In chapter 2 the finite element strategy used along this work is described, first, through a brief review of both plane stress and plate-bending elements. Later, pitfalls of such elements are illustrated, leading to the description of the theoretical contribution

of this work. This is the proposed integration scheme along the thickness for shell elements that allows degradation in different layers and enhances the bending-membrane coupled effect. Finally, some tests are performed, and the results are presented.

In Chapter 3 the state of the art of the modeling techniques for composite materials applied to concrete and masonry structures is reviewed. Also, mesh objectivity within the classical FE formulation following a smeared crack approach is performed for both, membrane and bending response. Due the amount of information along the thickness that a finite element may have, a handy tool that mechanizes and solves the issue of the composites material generation used along this work is also presented. Finally, some numerical tests are performed and compared with experimental results in order to validate the proposed scheme.

In chapter 4 various examples of large structures are presented. In order to evaluate and explore the capabilities of the computational approach presented in this research, several aspects have been studied, such as computational cost and real-life applications. In all cases, results have been compared with the existing structural design regulation valid for Mexico City.

In Chapter 5 conclusions and contributions of the work are shown. Future lines of researching and future developments are given in this chapter as well.

Also, Appendix A has been included as an overview of damage constitutive models with one and two scalars commonly used along the present work.

Appendix B is intended as an overview for the governing equations of the classical rate-independent plasticity models.

Appendix C describes the architectural drawings of the *real-life* building analyzed in chapter 4, and used to illustrate the methodology proposed in this work.

Appendix D has been included in this work, as an overview of the methodology a structural engineer follows to design a structure composed by confined masonry bearing walls in accordance with a Mexican design regulation.

Appendix E reports the obtained results, corresponding to the structural analysis and design of the model presented in appendix D, and also in section 4.2.

Appendix F describes the structural drawings, and the composite material used for the generation of the volumetric participation for each FE of model described in section 4.2.

Finally, appendix G describes the process used in section 4.2 to assess the seismic demand and the probabilistic damage.

Chapter 2

Finite Element Formulation for Membrane and Bending

This chapter discusses the technologies used for finite element analysis, reviewing the existing kinematic, and focusing on two-dimensional F.E. subjected to membrane and bending forces, later, as a combination of such technologies, it is proposed a finite element appropriate for modeling of multi-storey structures with masonry in-fills.

First, a brief overview of one, two and three-dimensional element used to model multi-storey structures is carried out, later, introduction to concepts and equations, to both coupled and separately membrane and plate-bending for two-dimensional elements are reviewed. Pitfalls for such elements are illustrated. The physics of shell elements for thin plates using an enhanced element is described. Is proposed an integration scheme along the thickness for shell elements, that allows degradation in different layers and enhances the bending-membrane coupled effect. Finally, numerical tests are presented.

2.1 Finite Elements applied in the Analysis of Multi-Storey Structures

For the analysis of masonry historical construction, frame structures with masonry in-fills, or confined masonry structures, several approaches have been used. Such approaches are basically a combination of the discretization of the geometry using F.E. with constitutive models to represent the behavior of the component materials. This section focuses on the used F.E. based on their dimensions, and only pretends to be a quick overview. For an extensive reference, reader may consult the work carried out by Roca *et al* [140].

2.1.1 One-dimensional F.E.

Depending on the accuracy required, a multi-storey structure with masonry in-fills, or a multi-storey structure with confined masonry bearing walls could be modeled using only one-dimensional F.E.

There is no doubt that frame structures, in *real-life* structural design, are mainly modeled using one dimensional elements, this is due to the width-to-span or the height-to-span ratio of the elements to be modeled. However, when it comes to frame structures

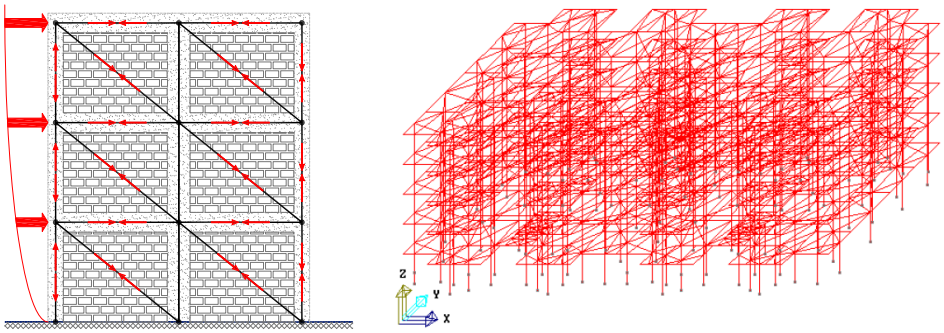

Figure 2.1 *Analysis of masonry structures using one-dimensional F.E. [24, 55].*

with masonry in-fills, a common practice is to model the in-fills is as truss elements without aid of two-dimensional F.E.

This practice has also been extended to the modeling of multi-storey structures with confined masonry bearing walls, that can be modeled only with the use of truss elements [24], hence, it is made the assumption that masonry walls act as diagonal struts subjected to compression, while reinforced confining elements like tie-columns or tie-beams act in tension and/or compression, depending on the direction of the lateral earthquake forces. Figure 2.1 (left) depicts such modeling strategy, as can be seen tie-columns and tie-beams are modeled as truss elements which is the usual, and also the masonry wall is modeled with a truss element.

Another analysis strategy to model multi-storey structures with confined masonry bearing walls, is to model a three-dimensional structure using one-dimensional elements, such structure is depicted in figure 2.1 (right), there, the masonry walls has been modeled as an analogy to a *wide* column, and the slabs have been modeled as diagonal trusses elements [55].

The analysis strategies described in this section, are not commonly used and are mostly associated to the lack of computational resources while modeling multi-storey structures.

2.1.2 Two-dimensional F.E.

Along this work, a common practice will be to refer to these elements as two-dimensional or bi-dimensional indistinctly. This F.E. has been widely used in the analytical study on the behavior of masonry walls when subjected to in-plan static or dynamic loads.

The use of two-dimensional element applied to the study of in-plane stresses for masonry walls are extensive in the literature, but it has hardly been applied to the modeling of three-dimensional structures, however, one case of such strategy is depicted in figure 2.2 (left) carried out by Milani *et al* [99].

Two-dimensional elements are most commonly used to test the proposed constitutive models, as is the case of figure 2.2 on the right that correspond to a constitutive model combined with an algorithm to track crack patterns proposed by Pelà [130].

This work pretends to model a three-dimensional structure using two-dimensional F.E. since the thickness-to-span ratio of such elements make them an ideal solution for the modeling of structures pretended in this work. In this section has been briefly

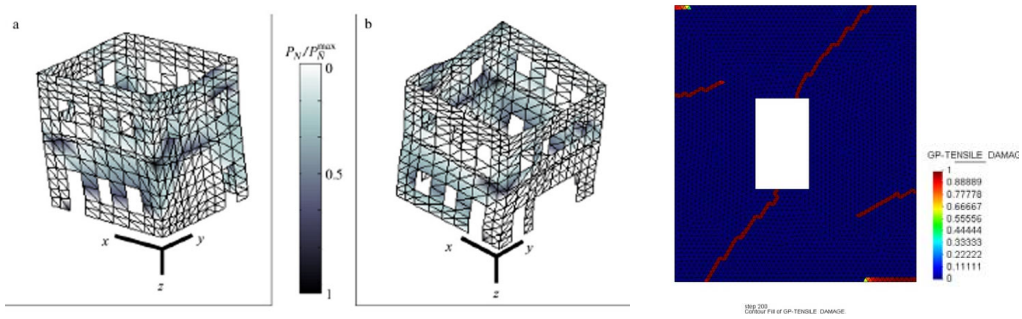

Figure 2.2 *Analysis of masonry structures using two-dimensional F.E. [99, 130]*

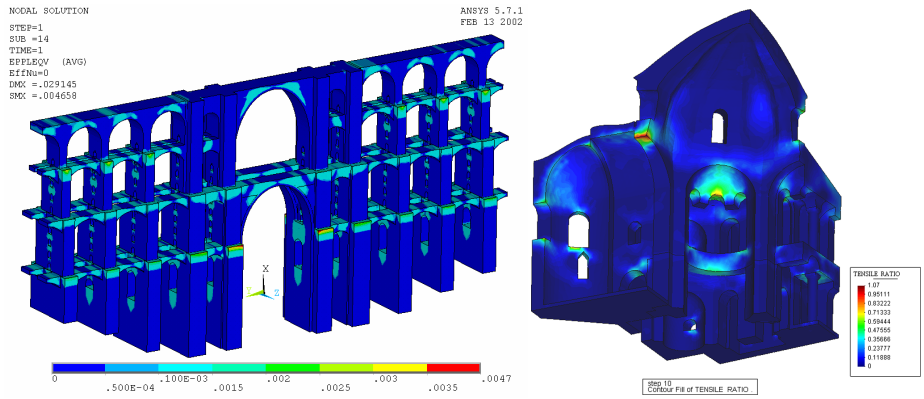

Figure 2.3 *Analysis of complex masonry structures using three-dimensional F.E. [141, 150].*

described, however, it will be more carefully studied in this chapter and in chapter 3.

2.1.3 Three-dimensional F.E.

In order to correctly predict the kinematics of complex structures, three-dimensional F.E. analysis can be the best alternative. However, the simulation of large multi-layered structures with many plies can be unaffordable due to the excessive computational cost, especially when non-linear studies are required. In addition, the discretization of very thin layers can lead to highly distorted elements carrying numerical issues.

Literature shows that [38, 79, 130, 140, 150] three-dimensional F.E. are most commonly used on the analysis of historical unreinforced masonry structures, and hardly used for other purposes. Apply such elements for the analysis of multi-storey construction with reinforced concrete and masonry elements seems cumbersome.

Some examples of the use of three-dimensional F.E. applied in the study of historical masonry structures are presented in figure 2.3, figure on the left corresponds to the work done by Schlegel *et al* [150] for the analysis of the Göltzschtal Bridge. On the other hand, figure 2.3 on the right, corresponds to the analysis of the küçük Ayasofya Mosque

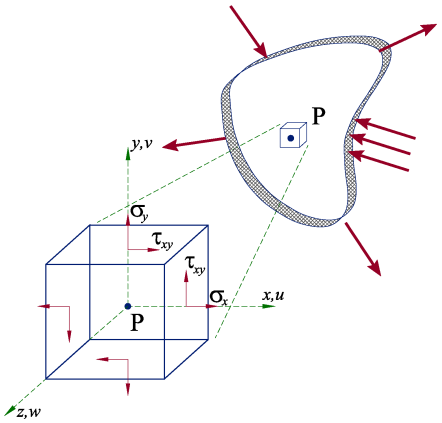

Figure 2.4 *Plane stress state in a continuum*

in Istanbul [141] carried out by Roca *et al.*

2.2 Fundamentals of the F.E. Formulation for Plane Stress State

It is said an element is subjected to a plane stress state when one of the three principal stresses $(\sigma_x, \sigma_y, \sigma_z)$ is zero, usually when a prismatic structural element has a very small dimension compared with the other two, hence, the stresses are negligible to the smaller dimension. So, it is well assumed that if a flat plate is subjected only to parallel loading forces, and has just two in-plane degrees of freedom (u,v), such element will be under plane stress.

Let us consider a two-dimensional generic section whose axis will be named (x,y) fig. [2.4]. Displacement field will be perfectly defined once displacements in x and y directions of any given point within the generic section are known. Thus, the displacement vector of a given point [eq.2.1], strain [eq.2.2] and stress [eq.2.3] field will be stated.

$$\mathbf{u}(x,y) = \begin{Bmatrix} u(x,y) \\ v(x,y) \end{Bmatrix} \tag{2.1}$$

$$\boldsymbol{\varepsilon} = \begin{Bmatrix} \varepsilon_x \\ \varepsilon_y \\ \varepsilon_{xy} \end{Bmatrix} = \begin{Bmatrix} \dfrac{\partial u}{\partial x} \\ \dfrac{\partial v}{\partial y} \\ \dfrac{\partial u}{\partial y} + \dfrac{\partial v}{\partial x} \end{Bmatrix} \tag{2.2}$$

$$\boldsymbol{\sigma} = \begin{Bmatrix} \sigma_x \\ \sigma_y \\ \tau_{xy} \end{Bmatrix} \tag{2.3}$$

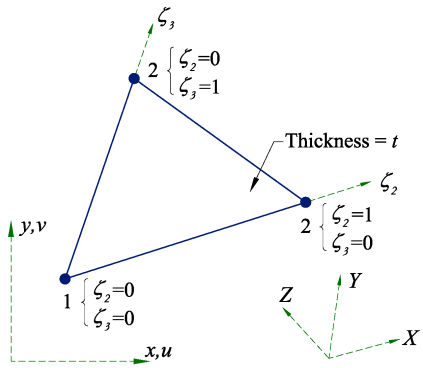

Figure 2.5 *Geometry of a two-dimensional triangle.*

Stress-Strain relationship $\boldsymbol{\sigma} = \mathbf{D}\boldsymbol{\varepsilon}$ can be established using a constitutive matrix $\mathbf{D}$ in such a way [159].

$$\mathbf{D} = \begin{bmatrix} d_{11} & d_{12} & 0 \\ d_{21} & d_{22} & 0 \\ 0 & 0 & d_{33} \end{bmatrix} \tag{2.4}$$

Finally, the generalized stress vector is the result of performing the integration of the stress vector over the thickness, as shown in [eq.2.5].

$$\hat{\boldsymbol{\sigma}} = \begin{Bmatrix} N_x \\ N_y \\ N_{xy} \end{Bmatrix} = \int_{-\frac{t}{2}}^{+\frac{t}{2}} z \begin{Bmatrix} \sigma_x \\ \sigma_y \\ \tau_{xy} \end{Bmatrix} dz = \int_{-\frac{t}{2}}^{+\frac{t}{2}} z\boldsymbol{\sigma} dz \tag{2.5}$$

2.2.1 Constant Stress Triangle Element

Also called *linear triangle*, *Turner triangle*, or simply *CST*, was developed as a plane stress element by Jon Turner, Ray Clough and Harold Martin [165]. Its geometry is shown in fig.2.5, where local and global coordinate systems are xy and XY respectively, ζ_2 and ζ_3 are coordinates and $\zeta_1 = 1 - \zeta_2 - \zeta_3$.

Degrees of freedom of *CST* membrane element are collectable in the nodal displacement vector as

$$\boldsymbol{d}_m = \{u_1 \;\; v_1 \;\; u_2 \;\; v_2 \;\; u_3 \;\; v_3\}^{\mathrm{T}} \tag{2.6}$$

Formulation of the stiffness matrix is based on the following decomposition

$$\mathbf{K}_{\mathrm{CST}} = \iint_{\Omega} \begin{Bmatrix} \mathbf{B}_1^{\mathrm{T}} \\ \mathbf{B}_2^{\mathrm{T}} \\ \mathbf{B}_3^{\mathrm{T}} \end{Bmatrix} \mathbf{D}[\mathbf{B}_1, \;\; \mathbf{B}_2, \;\; \mathbf{B}_3] \, tdA \tag{2.7}$$

Being $\mathbf{B}$ the Cartesian derivatives of shape functions and $\mathbf{D}$ the constitutive matrix shown in eq.2.4.

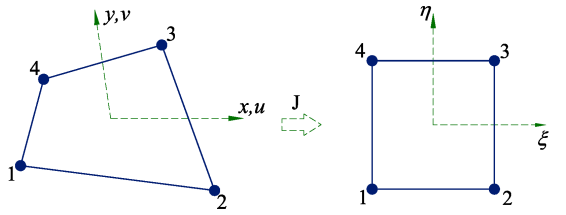

$$N_i = \frac{1}{4}(1+\xi\xi_i)(1+\eta\eta_i)$$

Node	ξ_i	η_i
1	−1	−1
2	1	−1
3	1	1
4	−1	1

Figure 2.6 *Geometry of a 4-Noded Lagrangian Element.*

2.2.2 Four-Noded Lagrangian Element

This is the simplest Lagrangian element based upon two-dimensional polynomial Lagrange interpolation, which allows evaluating a nodal shape function as the product of two unidimensional Lagrange polynomial in isoparametric coordinates ξ and η.

Stiffness matrix of such elements can be evaluated as

$$\mathbf{K}_{ij}^{(e)} = \iint_{A^{(e)}} \mathbf{B}_i^{\mathrm{T}}(x,y)\mathbf{D}\mathbf{B}_j(x,y)\,t\,dx\,dy = \int_{-1}^{+1}\int_{-1}^{+1} \mathbf{B}_i^{\mathrm{T}}(\xi,\eta)\mathbf{D}\mathbf{B}_j(\xi,\eta)\,|\mathbf{J}|\,t\,d\xi\,d\eta \quad (2.8)$$

Where $\mathbf{J}^{(e)}$ is a two dimensional Jacobian matrix and $\mathbf{D}$ the constitutive matrix shown in eq.2.4.

$$\mathbf{J}^{(\mathrm{e})} = \begin{bmatrix} \dfrac{\partial x}{\partial \xi} & \dfrac{\partial y}{\partial \xi} \\ \dfrac{\partial x}{\partial \eta} & \dfrac{\partial y}{\partial \xi} \end{bmatrix} = \sum_{i=1}^{n=4} \begin{bmatrix} \dfrac{\partial N_i}{\partial \xi} x_i & \dfrac{\partial N_i}{\partial \xi} y_i \\ \dfrac{\partial N_i}{\partial \eta} x_i & \dfrac{\partial N_i}{\partial \eta} y_i \end{bmatrix} \quad (2.9)$$

2.2.3 OPT Element

A membrane element without including a in-plane rotation degree (*drilling rotation*) leads to in-plane rotation singularity [64]. Successful attempts at developing membrane elements with drilling degree of freedom are due to the work by Allman [7] and Felippa [21].

OPT element is a high-performance element which include a rotational degree of freedom and based upon the ANDES formulation [100] (*Assumed Natural DEviatoric Strain*). Key concept of ANDES formulation states that only the deviatoric part of the strain is assumed over the element whereas the mean strain part is discarded in favour of a constant stress assumption.

An extensive study of high-performance elements using an ANDES template has been presented [52], where term *OPTimal* is used in the sense of exact in-plane pure-bending response of rectangular mesh units of arbitrary aspects ratio. Later in this section, comparison among such high-performance elements presented in [52] will be reproduced.

The geometry of OPT triangle is presented in fig.2.7. Thickness is t, node numbering is counterclockwise, and there are 6 degrees of freedom [eq.2.12]. Local and global coordinate systems are xyz and XYZ respectively. ζ_2 and ζ_3 are the co-ordinates and $\zeta_1 = 1 - \zeta_3 - \zeta_3$.

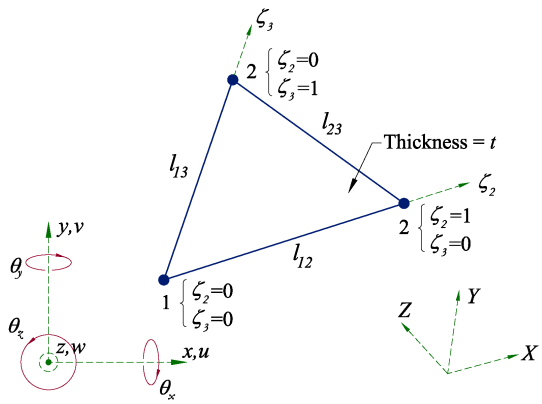

Figure 2.7 *Geometry of a triangular element.*

Coordinate differences are abbreviated as

$$x_{ij} = x_i - x_j, \quad y_{ij} = y_i - y_j \tag{2.10}$$

Area and volume of the element and the length of the side ij are represented by A, V and l_{ij} respectively

$$A = \frac{1}{2}(y_{21}x_{13} - x_{21}y_{13}); \;\; V = At; \;\; l_{ij} = \sqrt{x_{ij}^2 + y_{ij}^2} \tag{2.11}$$

The degrees of freedom of OPT membrane element are collectable in the nodal displacement vector as

$$\boldsymbol{d}_m = \{u_1 \; v_1 \; \theta_{z1} \; u_2 \; v_2 \; \theta_{z2} \; u_3 \; v_3 \; \theta_{z3} \}^{\mathrm{T}} \tag{2.12}$$

The fundamental element stiffness decomposition of the two-stage direct fabrication method is

$$\mathbf{K}_m = \mathbf{K}_{mb} + \mathbf{K}_{mh} \tag{2.13}$$

where $\mathbf{K}_{mb}$ is the basic stiffness, which take care of the consistency, and $\mathbf{K}_{mh}$ is the high order stiffness, which takes care of stability (rank sufficiency) and accuracy. The final form of $\mathbf{K}_m$ is a template with 11 free parameters

$$\mathbf{K}_{(\alpha_b,\beta_0,\ldots,\beta_9)} = \frac{1}{\mathrm{V}}\mathbf{L}\mathbf{D}\mathbf{L}^{\mathrm{T}} + \int_{\Omega} \mathbf{B}^{\mathrm{T}}\mathbf{D}\mathbf{B} \, dv \tag{2.14}$$

where $\mathbf{D}$ is the same described in [eq.2.4], V is the volume of the element, $\mathbf{B}$ matrix is defined as

$$\mathbf{B} = \mathbf{T}_e(\mathbf{Q}_1\zeta_1 + \mathbf{Q}_2\zeta_2 + \mathbf{Q}_3\zeta_3)\tilde{\mathbf{T}}_{\theta u} \tag{2.15}$$

L, T_e, $\tilde{T}_{\theta u}$ and Q_{1-3} are constant matrices over the element and are defined as [52]

$$\mathbf{L} = \frac{h}{2}\begin{bmatrix} y_{23} & 0 & x_{32} \\ 0 & x_{32} & y_{23} \\ \frac{1}{6}\,\alpha_b y_{23}(y_{13}-y_{21}) & \frac{1}{6}\,\alpha_b x_{32}(x_{31}-x_{12}) & \frac{1}{6}\,\alpha_b(x_{31}y_{31}-x_{12}y_{21}) \\ y_{31} & 0 & x_{13} \\ 0 & x_{31} & y_{31} \\ \frac{1}{6}\,\alpha_b y_{31}(y_{21}-y_{32}) & \frac{1}{6}\,\alpha_b x_{13}(x_{12}-x_{23}) & \frac{1}{6}\,\alpha_b(x_{12}y_{21}-x_{23}y_{32}) \\ y_{12} & 0 & x_{21} \\ 0 & x_{21} & y_{12} \\ \frac{1}{6}\,\alpha_b y_{12}(y_{32}-y_{13}) & \frac{1}{6}\,\alpha_b x_{21}(x_{23}-x_{31}) & \frac{1}{6}\,\alpha_b(x_{23}y_{32}-x_{31}y_{13}) \end{bmatrix} \tag{2.16}$$

$$\mathbf{T}_e = \frac{1}{4A^2}\begin{bmatrix} y_{23}y_{13}l_{21}^2 & y_{31}y_{21}l_{32}^2 & y_{12}y_{32}l_{13}^2 \\ x_{23}x_{13}l_{21}^2 & x_{31}x_{21}l_{32}^2 & x_{12}x_{32}l_{13}^2 \\ (y_{23}x_{31}+x_{32}y_{13})l_{21}^2 & (y_{31}x_{12}+x_{13}y_{21})l_{32}^2 & (y_{12}x_{23}+x_{21}y_{32})l_{13}^2 \end{bmatrix} \tag{2.17}$$

$$\mathbf{Q}_1 = \frac{2A}{3}\begin{bmatrix} \frac{\beta_1}{l_{21}^2} & \frac{\beta_2}{l_{21}^2} & \frac{\beta_3}{l_{21}^2} \\ \frac{\beta_4}{l_{32}^2} & \frac{\beta_5}{l_{32}^2} & \frac{\beta_6}{l_{32}^2} \\ \frac{\beta_7}{l_{13}^2} & \frac{\beta_8}{l_{13}^2} & \frac{\beta_9}{l_{13}^2} \end{bmatrix} \quad \mathbf{Q}_2 = \frac{2A}{3}\begin{bmatrix} \frac{\beta_9}{l_{21}^2} & \frac{\beta_7}{l_{21}^2} & \frac{\beta_8}{l_{21}^2} \\ \frac{\beta_3}{l_{32}^2} & \frac{\beta_1}{l_{32}^2} & \frac{\beta_2}{l_{32}^2} \\ \frac{\beta_6}{l_{13}^2} & \frac{\beta_4}{l_{13}^2} & \frac{\beta_5}{l_{13}^2} \end{bmatrix} \quad \mathbf{Q}_3 = \frac{2A}{3}\begin{bmatrix} \frac{\beta_5}{l_{21}^2} & \frac{\beta_6}{l_{21}^2} & \frac{\beta_4}{l_{21}^2} \\ \frac{\beta_8}{l_{32}^2} & \frac{\beta_9}{l_{32}^2} & \frac{\beta_7}{l_{32}^2} \\ \frac{\beta_2}{l_{13}^2} & \frac{\beta_3}{l_{13}^2} & \frac{\beta_1}{l_{13}^2} \end{bmatrix} \tag{2.18}$$

$$\tilde{\mathbf{T}}_{\theta u} = \frac{1}{4A}\begin{bmatrix} x_{32} & y_{32} & 4A & x_{13} & y_{13} & 0 & x_{21} & y_{21} & 0 \\ x_{32} & y_{32} & 0 & x_{13} & y_{13} & 4A & x_{21} & y_{21} & 0 \\ x_{32} & y_{32} & 0 & x_{13} & y_{13} & 0 & x_{21} & y_{21} & 4A \end{bmatrix} \tag{2.19}$$

The exact integration of $\mathbf{K}_m$ is obtained using three numerical integration Gauss points (mid point rule). Final form of $\mathbf{K}_m$ may be written as [52]

$$\mathbf{K}_{(\alpha_b,\beta_0,\ldots,\beta_9)} = \frac{1}{\mathrm{V}}\mathbf{L}\mathbf{D}\mathbf{L}^{\mathrm{T}} + \frac{3}{4}\beta_0\tilde{\mathbf{T}}_{\theta u}^{\mathrm{T}}\mathbf{K}_\theta\tilde{\mathbf{T}}_{\theta u} \tag{2.20}$$

where

$$\mathbf{K}_\theta = Ah(\mathbf{Q}_4^{\mathbf{T}}\mathbf{E}_{nat}\mathbf{Q}_4 + \mathbf{Q}_5^{\mathbf{T}}\mathbf{E}_{nat}\mathbf{Q}_5 + \mathbf{Q}_6^{\mathbf{T}}\mathbf{E}_{nat}\mathbf{Q}_6) \tag{2.21}$$

and

$$\mathbf{E}_{nat} = \mathbf{T}_e^{\mathrm{T}}\mathbf{E}\mathbf{T}_e;\ \ \mathbf{Q}_4 = \frac{1}{2}(\mathbf{Q}_1+\mathbf{Q}_2);\ \ \mathbf{Q}_5 = \frac{1}{2}(\mathbf{Q}_2+\mathbf{Q}_3);\ \ \mathbf{Q}_6 = \frac{1}{2}(\mathbf{Q}_3+\mathbf{Q}_1) \tag{2.22}$$

α_b and β_1 through β_9 are free dimensional parameters, and β_0 is an overall scaling coefficient. Felippa [52] has shown that for an isotropic material with Poisson's ratio v, the followings values for free parameters lead to the *OPTimal* membrane element:

$$\begin{aligned} &\alpha_b = \tfrac{3}{2};\ \ \beta_0 = \tfrac{1}{2}(1-4v^2);\ \ \beta_{1,3,5} = 1 \\ &\beta_2 = 2;\ \ \beta_4 = 0;\ \ \beta_{6,7,8} = -1;\ \ \beta_9 = -2 \end{aligned} \tag{2.23}$$

For non-isotropic materials β_1 through β_9 remain the same, but the following average value for β_0 has been proposed

$$\beta_0 = \max\left(\frac{256|\mathbf{D}|}{W} - 1.5,\ \ 0.01\right) \tag{2.24}$$

where W is evaluated as

$$\begin{aligned} W = &-6D_{12}^3 + 5D_{11}^2D_{22} - 5D_{12}^2D_{22} - D_{22}(75D_{13}^2 + 14D_{13}D_{23} + 3D_{23}^2) \\ &+ 2D_{12}(7D_{13}^2 + 46D_{13}D_{23} + 7D_{23}^2) - D_{11}(5D_{12}^2 + 3D_{13}^2 - 6D_{12}D_{22} \\ &- 5D_{22}^2 + 14D_{13}D_{23} + 75D_{23}^2) + (3D_{11}^2 + 82D_{11}D_{22} + 3D_{22}^2 - 4(6D_{12}^2 \\ &+ 5D_{13}^2 - 6D_{13}D_{23} + 5D_{23}^2))D_{33} + 4(5D_{11} - 6D_{12} + 5D_{22})D_{33}^2 \end{aligned} \tag{2.25}$$

2.3 Fundamentals of the F. E Formulation for Plate Bending State

It is said an element is subjected to bending stress when one of the three principal stresses is zero, as in plane stress, the stress in the smaller direction is neglected. The main difference among them is the way load is applied, whereas in plane stress force's direction is parallel to a middle *x,y* plane, a bending state does not accept such forces[fig.2.8], which means, $\sigma_x = \sigma_y = \tau_{xy} = 0$ at the middle plane. Hence a plate acted upon only by normal forces to its middle *x,y* plane and bending moments whose axis are contained within such *x,y* plane is under a bending state.

Main hypothesis plate theory is based upon are shown below.

1. Points along middle plane only can have vertical displacement ($u = v = 0$).
2. Points along a normal to middle plane have the same vertical displacement.
3. Stress in z direction is zero ($\sigma_z = 0$)

Another hypothesis shall be introduced according to the thickness of the plate. Although there is no a proper way to define whether is a thin or thick plate, as a general rule of thumb [107] we can stablish: a thin plate is such that $^t/_L \leq 0.050$, where t is the thickness and L the smallest length in x, y direction. Hence, hypothesis regarding thickness of a thin plate [fig.2.9], or Kirchhoff plate [160] is shown below.

4. Points along a normal line to the middle surface before a deformation process draw an orthogonal line to middle plane's deformed shape once deformation process has occur.

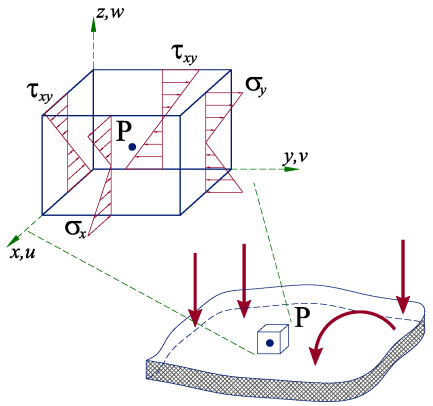

Figure 2.8 *Plate bending state in a continuum.*

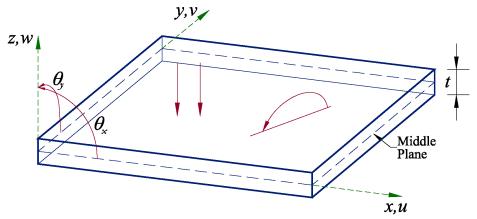

Figure 2.9 *Plate bending geometry.*

A thick plate will be treated as such when $^{t}/_{L} \geq 0.100$ (using the same rule of thumb described in [107]). For thick plates the greater the deformation the greater the distortion within the cross section, which leads to orthogonality among normal line and middle plane is no longer comply. Hence, hypothesis regarding thickness of a thick plate [fig.2.12], or Reissner-Mindlin plate [101] is:

> **4.** Points along a normal line to the middle surface before a deformation process still draw a line, although not necessary orthogonal to middle plane's deformed shape once deformation process has occur.

Along next lines a brief description of both Kirchhoff and Reissner-Mindlin bending plate theories are presented.

2.3.1 Kirchhoff Theory

Since integrals and variables are a function of x,y coordinates of the middle plane of a plate (Fig.2.10), then displacement field can be expressed as:

$$\begin{aligned} u(x,y,z) &= -z\theta_x(x,y) \\ v(x,y,z) &= -z\theta_y(x,y) \\ w(x,y,z) &= w(x,y) \end{aligned} \tag{2.26}$$

Once displacements along w direction and rotations along θ_x, θ_y are known displacement field would be perfectly defined,

$$\mathbf{u}(x,y) = \begin{Bmatrix} w(x,y) \\ \theta_x(x,y) \\ \theta_y(x,y) \end{Bmatrix} \tag{2.27}$$

Both strain and stress vectors are defined by equations 2.2 and 2.3] respectively having into account

$$\begin{gathered} \varepsilon_x = \frac{\partial u}{\partial x} = -z\frac{\partial^2 w}{\partial x^2} \quad ; \quad \varepsilon_y = \frac{\partial v}{\partial y} = -z\frac{\partial^2 w}{\partial y^2} \quad ; \quad \varepsilon_z \approx 0 \\ \gamma_{xy} = \frac{\partial u}{\partial y} + \frac{\partial v}{\partial x} = -2z\frac{\partial^2 w}{\partial x \partial y} \quad ; \quad \gamma_{xz} = \frac{\partial w}{\partial x} + \frac{\partial u}{\partial z} = 0 \\ \gamma_{yz} = \frac{\partial w}{\partial y} + \frac{\partial v}{\partial z} = 0 \end{gathered} \tag{2.28}$$

Since $\sigma_z = 0$ for both plane stress and bending plates, the same stress-strain relationship comply, along with constitutive matrix $\mathbf{D}$ presented in equation 2.4. Generalized stresses are the resultant of performing an integration of stresses $\boldsymbol{\sigma}$ along thickness (eq.2.29).

$$\hat{\boldsymbol{\sigma}} = \begin{Bmatrix} M_x \\ M_y \\ M_{xy} \end{Bmatrix} = \int_{-\frac{t}{2}}^{+\frac{t}{2}} z \begin{Bmatrix} \sigma_x \\ \sigma_y \\ \tau_{xy} \end{Bmatrix} dz = \int_{-\frac{t}{2}}^{+\frac{t}{2}} z\boldsymbol{\sigma} dz \tag{2.29}$$

Shear stresses shall be evaluated *a posteriori*, the way presented in equation 2.30, as can be seen Q_x and Q_y only can be evaluated once bending moments $\hat{\boldsymbol{\sigma}}$ are known [eq.2.29].

$$\begin{aligned} Q_x &= \frac{\partial M_x}{\partial x} + \frac{\partial M_{xy}}{\partial y} \\ Q_y &= \frac{\partial M_y}{\partial y} + \frac{\partial M_{xy}}{\partial x} \end{aligned} \tag{2.30}$$

Due to the existence of a second derivative in 2.28, C_1 continuity of function w is required. Since C_1 continuity is not a easy condition to achieve it rises to *non conform* elements whose study is presented in [107], and shall not be discussed within this work.

2.3.2 DKT Element

Triangular flat elements having displacements and rotations at the corner nodes as degree of freedom (*the engineering DOF*) are particularly appealing for many practical reasons, i.e. they allow to model arbitrary shell geometries, general supports and cut outs, and beam stiffeners. Discrete Kirchhoff Triangle is the most reliable triangular element for the analysis of thin plates, has been developed by Batoz *et al* [15].

Batoz's DKT element is based upon the following assumptions.

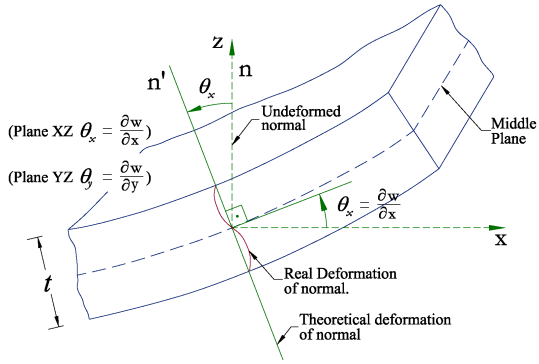

Figure 2.10 *Middle plane deformation for a thin plate.*

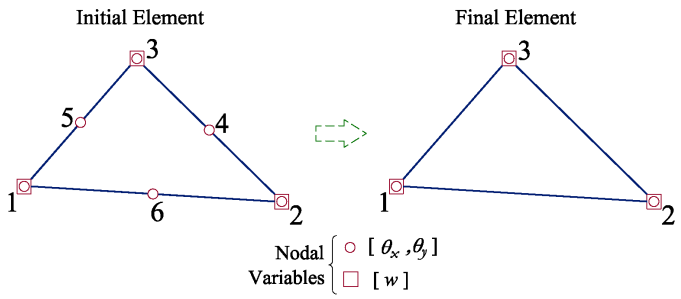

Figure 2.11 *The DKT element.*

1. Rotations vary quadratically over the element

$$\theta_x = \sum_{i=1}^{6} N_i \theta_{xi} \quad ; \quad \theta_y = \sum_{i=1}^{6} N_i \theta_{yi}$$

where θ_x and θ_y are the nodal values at the corners and at the mid-nodes (fig.2.11), and $N_i(\xi, \eta)$ are shape functions.

$$N_1 = 2(1-\xi-\eta)(\frac{1}{2}-\xi-\eta) \qquad N_2 = \xi(2\xi-1)$$

$$N_3 = \eta(2\eta-1) \qquad N_4 = 4\xi\eta$$

$$N_5 = 4\eta(1-\xi-\eta) \qquad N_6 = 4\xi(1-\xi-\eta)$$

2. The Kirchhoff hypothesis is imposed at corners (nodes 1,2,3)

$$\theta_x + \frac{\partial w}{\partial x} = 0 \quad ; \quad \theta_y + \frac{\partial w}{\partial y} = 0$$

and at the mid-nodes ($k = 4, 5, 6$)

$$\theta_{sk} + \left(\frac{\partial w}{\partial s}\right)_k = 0$$

3. The variation of w along the sides is cubic

$$\left(\frac{\partial w}{\partial s}\right)_k = -\frac{3}{2l_{ij}} w_i - \frac{1}{4}\left(\frac{\partial w}{\partial s}\right)_i + \frac{3}{2l_{ij}} w_j - \frac{1}{4}\left(\frac{\partial w}{\partial s}\right)_j$$

with K denoting the mid-node of side ij and l_{ij} equal to the length of the side ij.

4. A linear variation of θ_n is imposed along sides

$$\theta_{nk} = \frac{1}{2}(\theta_{ni} + \theta_{nj})$$

where $k = 4, 5, 6$ denotes the mid-node of the sides 23, 31 and 12 respectively

Degrees of freedom can be presented in a vector as

$$\boldsymbol{d}_b = \{w_1\ \theta_{x1}\ \theta_{y1}\ w_1\ \theta_{x2}\ \theta_{y2}\ w_1\ \theta_{x3}\ \theta_{y3}\} \tag{2.31}$$

The evaluation of the stiffness matrix follows the standard procedures of the finite elements methods.

$$\mathbf{K}_b = \int_\Omega \mathbf{B}_b^{\mathrm{T}} \mathbf{D}_b \mathbf{B}_b \, dA = 2A \int_0^1 \int_0^{1-\zeta_3} \mathbf{B}_b^{\mathrm{T}} \mathbf{D}_b \mathbf{B}_b \, d\zeta_2 d\zeta_3 \tag{2.32}$$

where $\mathbf{D}_b$ is the flexural rigidity of the plate, defined as a function of $\mathbf{D}$ presented in eq.2.4 and the thickness of the plate as

$$\mathbf{D}_b = \int_{-\frac{t}{2}}^{+\frac{t}{2}} \mathbf{D} dz \tag{2.33}$$

and deformation matrix $\mathbf{B}_b$ is defined as [15]

$$\mathbf{B}_b = \frac{1}{2A} \begin{bmatrix} y_{31}\mathbf{H}_1^{\mathrm{T}} + y_{12}\mathbf{H}_3^{\mathrm{T}} \\ -x_{31}\mathbf{H}_2^{\mathrm{T}} - x_{12}\mathbf{H}_4^{\mathrm{T}} \\ -x_{31}\mathbf{H}_1^{\mathrm{T}} - x_{12}\mathbf{H}_3^{\mathrm{T}} + y_{31}\mathbf{H}_2^{\mathrm{T}} + y_{12}\mathbf{H}_4^{\mathrm{T}} \end{bmatrix} \tag{2.34}$$

vectors $\mathbf{H}_1$ - $\mathbf{H}_4$ are functions of ζ_2 and ζ_3 [15]

$$\mathbf{H}_1 = \begin{Bmatrix} P_6(1-2\zeta_2) + (P_5 - P_6)\zeta_3 \\ q_6(1-2\zeta_2) - (q_5 + q_6)\zeta_3 \\ -4 + 6(\zeta_2 + \zeta_3) + r_6(1-2\zeta_2) - \zeta_3(r_5 + r_6) \\ -P_6(1-2\zeta_2) + \zeta_3(P_4 + P_6) \\ q_6(1-2\zeta_2) - \zeta_3(q_6 - q_4) \\ -2 + 6\zeta_2 + r_6(1-2\zeta_2) + \zeta_3(r_4 - r_6) \\ -\zeta_3(P_5 + P_4) \\ \zeta_3(q_4 - q_5) \\ -\zeta_3(r_5 - r_4) \end{Bmatrix} \tag{2.35}$$

$$\mathbf{H}_2 = \begin{Bmatrix} t_6(1-2\zeta_2) + (t_5 - t_6)\zeta_3 \\ 1 + r_6(1-2\zeta_2) - (r_5 + r_6)\zeta_3 \\ -q_6(1-2\zeta_2) + \zeta_3(q_5 + q_6) \\ -t_6(1-2\zeta_2) + \zeta_3(t_4 + t_6) \\ -1 + r_6(1-2\zeta_2) + \zeta_3(r_4 - r_6) \\ -q_6(1-2\zeta_2) - \zeta_3(q_4 - q_6) \\ -\zeta_3(t_5 + t_4) \\ \zeta_3(r_4 - r_5) \\ -\zeta_3(q_4 - q_5) \end{Bmatrix} \tag{2.36}$$

$$\mathbf{H}_3 = \begin{Bmatrix} -P_5(1-2\zeta_3) - (P_6 - P_5)\zeta_2 \\ q_5(1-2\zeta_3) - (q_5 + q_6)\zeta_2 \\ -4 + 6(\zeta_2 + \zeta_3) + r_5(1-2\zeta_3) - \zeta_2(r_5 + r_6) \\ \zeta_2(P_4 + P_6) \\ \zeta_2(q_4 - q_6) \\ -\zeta_2(r_6 - r_4) \\ P_5(1-2\zeta_3) - \zeta_2(P_5 + P_4) \\ q_5(1-2\zeta_3) + \zeta_2(q_4 - q_5) \\ -2 + 6\zeta_3 + r_5(1-2\zeta_3) + \zeta_2(r_4 - r_5) \end{Bmatrix} \tag{2.37}$$

$$\mathbf{H}_4 = \begin{Bmatrix} -t_5(1-2\zeta_3) - (t_6 - t_5)\zeta_2 \\ 1 + r_5(1-2\zeta_3) - (r_5 + r_6)\zeta_2 \\ -q_5(1-2\zeta_3) + \zeta_2(q_5 + q_6) \\ \zeta_2(t_4 + t_6) \\ \zeta_2(r_4 - r_6) \\ -\zeta_2(q_4 - q_6) \\ t_5(1-2\zeta_3) - \zeta_2(t_5 + t_4) \\ -1 + r_5(1-2\zeta_3) + \zeta_2(r_4 - r_5) \\ -q_5(1-2\zeta_3) - \zeta_2(q_4 - q_5) \end{Bmatrix} \tag{2.38}$$

where

$$\begin{aligned} P_k &= -6x_{ij}/l_{ij}^2 = 6a_k \\ t_k &= -6y_{ij}/l_{ij}^2 = 6d_k \\ q_k &= 3x_{ij}y_{ij}/l_{ij}^2 = 4b_k \\ r_k &= 3y_{ij}^2/l_{ij}^2 \end{aligned}$$

$k = 4, 5, 6$ for $ij = 23, 31, 12$ respectively.

2.3.3 Reissner-Mindlin Theory

As previously pointed, main difference among thin and thick plate theories is the rotation of a normal line to the middle plane once deformation has occur (θ_x, θ_y). Reissner-Mindlin theory for thick plates states such rotations are formed by two terms 9fig.2.12). Firsts $^{\partial w}/_{\partial x}$ and $^{\partial w}/_{\partial y}$ due to the change of slope of middle plane, and ϕ_x, ϕ_y is an additional rotation.

$$\theta_x = \frac{\partial w}{\partial x} + \phi_x \quad ; \quad \theta_y = \frac{\partial w}{\partial y} + \phi_y \tag{2.39}$$

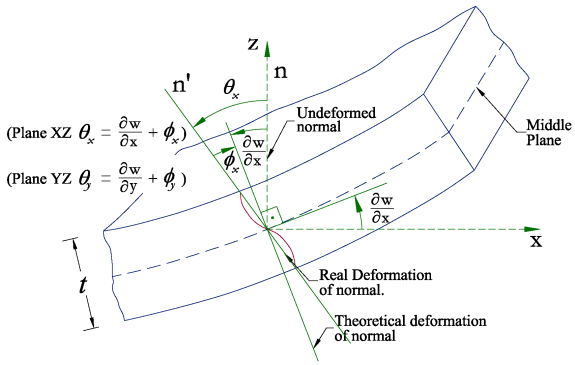

Figure 2.12 *Middle plane deformation for a thick plate.*

In a general manner equations 2.26 and 2.27 apply for thick plates, unless eq.2.28, since γ_{xz} and γ_{yz} will no longer be *zero* (eq.2.40).

$$\begin{aligned} \gamma_{xz} &= \frac{\partial u}{\partial z} + \frac{\partial w}{\partial x} = -\theta_x + \frac{\partial w}{\partial x} = -\phi_x \\ \gamma_{yz} &= \frac{\partial v}{\partial z} + \frac{\partial w}{\partial y} = -\theta_y + \frac{\partial w}{\partial y} = -\phi_y \end{aligned} \tag{2.40}$$

Thus, ϕ_x and ϕ_y arise to the physical meaning of being the deformation due to shear stresses. In such a way strain vector can be defined as:

$$\boldsymbol{\varepsilon} = \begin{Bmatrix} \varepsilon_x \\ \varepsilon_y \\ \gamma_{xy} \\ \cdots\cdots \\ \gamma_{xz} \\ \gamma_{yz} \end{Bmatrix} = \begin{Bmatrix} -z\dfrac{\partial \theta_x}{\partial x} \\ -z\dfrac{\partial \theta_y}{\partial y} \\ -z\left(\dfrac{\partial \theta_x}{\partial y} + \dfrac{\partial \theta_y}{\partial x}\right) \\ \cdots\cdots \\ \dfrac{\partial w}{\partial x} - \theta_x \\ \dfrac{\partial w}{\partial y} - \theta_y \end{Bmatrix} = \begin{Bmatrix} \boldsymbol{\sigma_b} \\ \cdots\cdots \\ \boldsymbol{\sigma_s} \end{Bmatrix} \tag{2.41}$$

Now, starting from a three dimensional elasticity field, and having into account $\sigma_z = 0$, stress-strain relationship is stated as:

$$\boldsymbol{\sigma} = \begin{Bmatrix} \boldsymbol{\sigma_b} \\ \boldsymbol{\sigma_s} \end{Bmatrix} = \begin{bmatrix} \boldsymbol{D_b} & \vdots & \mathbf{0} \\ \cdots & \vdots & \cdots \\ \mathbf{0} & \vdots & \boldsymbol{D_s} \end{bmatrix} \begin{Bmatrix} \boldsymbol{\varepsilon_b} \\ \cdots\cdots \\ \boldsymbol{\varepsilon_s} \end{Bmatrix} \tag{2.42}$$

Where $\boldsymbol{D_b}$ has already been defined in equation 2.4 while

$$\boldsymbol{D_s} = \begin{bmatrix} G_{xz} & 0 \\ 0 & G_{yz} \end{bmatrix} \tag{2.43}$$

Being G_{xz} and G_{yz} shear modulus along xz and yz directions respectively. On the contrary to thin plates, shear stresses are not evaluated *a posteriori*, but they are the result of performing an integration of stresses along thickness (eq.2.44).

$$\hat{\boldsymbol{\sigma}} = \begin{Bmatrix} \hat{\boldsymbol{\sigma}}_{\boldsymbol{b}} \\ ..... \\ \hat{\boldsymbol{\sigma}}_{\boldsymbol{s}} \end{Bmatrix} = \begin{Bmatrix} M_x \\ M_y \\ M_{xy} \\ ..... \\ Q_x \\ Q_y \end{Bmatrix} = \int_{-\frac{t}{2}}^{+\frac{t}{2}} \begin{Bmatrix} z\sigma_x \\ z\sigma_y \\ z\tau_{xy} \\ ..... \\ \tau_{xz} \\ \tau_{yz} \end{Bmatrix} dz = \int_{-\frac{t}{2}}^{+\frac{t}{2}} \begin{Bmatrix} z\boldsymbol{\sigma}_{\boldsymbol{b}} \\ ..... \\ \boldsymbol{\sigma}_{\boldsymbol{s}} \end{Bmatrix} dz \tag{2.44}$$

2.3.4 CLLL Element

CLLL stands for ***C**uadrilatelal element with bi**L**inar displacement, bi**L**inear rotation and **L**inear deformation*, is a four node plate bending element based on Reissner-Mindlin Theory and mixed interpolation, originally developed by Bathe and Dvorkin [14], [46], later Donea and Lamain presented a reformulation on [44].

Its simplicity and accuracy have made this element is widely used in the practice, although two major drawbacks can be pointed out, namely, used interpolation implies both shear and bending stresses to be constant along one direction, which can force to use a dense mesh, and because of its shape (quadrilateral) this element is not optimal to be used in meshes with irregular geometry.

The way stiffness matrix is evaluated is the standard for a four node Lagrangian finite element

$$\mathbf{K}_{ij}^{(e)} = \iint_{A^{(e)}} \hat{\boldsymbol{B}}_c^{\mathrm{T}}(x,y)\mathbf{D}\hat{\boldsymbol{B}}_c(x,y)\, t\, dx\, dy \tag{2.45}$$

where $\hat{\boldsymbol{B}}_c$ is a replacement transversal shear deformation matrix given in [44]

$$\hat{\boldsymbol{B}}_c = \mathbf{J}^{-1}\mathbf{A}\mathbf{P}^{-1}\mathbf{T}\mathbf{C}\overline{\mathbf{B}}_c \tag{2.46}$$

2.4 Shell Plane Elements

Shells can be defined as plates with non-plane middle surface. This non-coplanarity shape confers them a higher resistance due to the ability of supporting both axial and bending stresses at the same time. Also due to such non-coplanarity, obtaining kinematics shells equations in not an easy task to deal with [54], [73], [106] [160], being a way of reducing shells complexity treat them as small plane elements, hence shells can be approached as *membrane* elements coupled with *bending* elements assembled into different coordinate systems [fig 2.13].

Choosing a *membrane* element to couple with a *bending* element is not easy, let us consider the *membrane* element first. Figure 2.14 (which reproduces figure 5.29 from

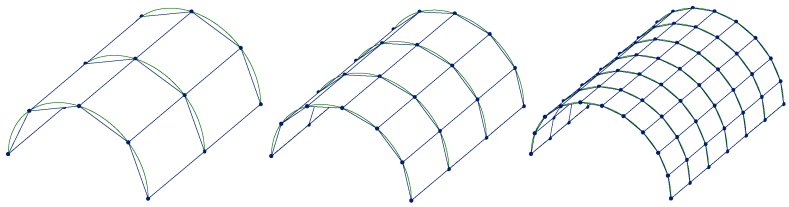

Figure 2.13 *Curved shell discretisation into plane elements.*

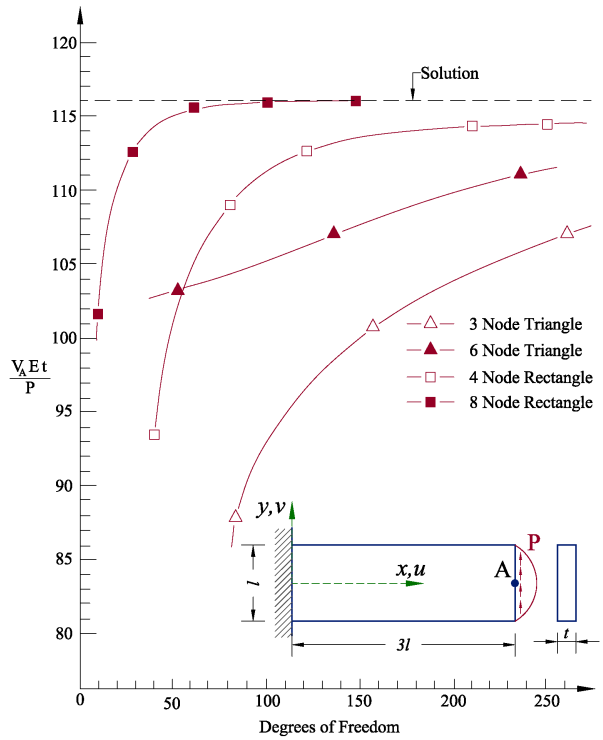

Figure 2.14 *Cantilever beam with parabolic force at the end. Fig. 5.29 of reference [107].*

reference [107]) shows results of the test benchmark proposed in [63], from where can be inferred that both linear and quadratic CST triangles have poor performance, whereas both 4 and 8 nodes Lagrangian elements have a stiff behavior that only reduces with denser meshes. Can also be inferred from fig.2.14 that rectangular Lagrangian elements have a better performance than triangular elements with the same quantity of degrees of freedom, however triangular element fits better to deal with complex geometries.

Now let us have a look on the extensive study done by Felippa [52] on the matter of *high-performance* membrane triangles. Figure 2.15 reproduces table 5 presented in [52], also the poor performance of CST triangles is patent, whereas the OPT triangle bending response is almost perfect no matter the aspect ratio.

Some advantages which lead us to choose the use of OPT membrane elements over both CST and plane stress Lagrangian elements are pointed below.

- **Do exist the θ_z degree of freedom**, so no *trick* will be needed to couple them with a *bending* element. Let us remember two possibles solutions to overcome the singularity that leads the lack of θ_z degree of freedom: *a)* selective assembly in local coordinate system [107], or *b)* the use of a fictitious θ_z stiffness [172]. Not to mention the appearance of *cuasi-coplanarity* where lowered plate theory proposed by Marguerre shall apply [86].

- **High accuracy with less degrees of freedom**, which will be almost mandatory while dealing with non-linear materials due to the amount RAM memory necessary to store information such as internal internal variables, or the always expensive: cotangent tensor.

A drawback of OPT membrane element is that the exact expression for the relationship among strains and nodal displacements is still unknown, although an approximate expression proposed in [70] can be adopted, later in this chapter is described how to deal with such drawback.

On the other hand, there are several triangular plate elements to select and combine with a membrane element. The BCIZ element (named after the author's initials) is one of the simplest plate bending elements, developed by Bazeley *et al* [18], although, we will choose the DKT element due to its reliability, shown by Batoz *et al* in [15] where several triangular Kirchhoff plate bending elements were studied.

2.5 Overall DKT-OPT Element Description

Since the DKT-OPT element is used all the way long this work, a proper description of it shall be mandatory. The *standard* properties of this triangular element, such as, the area integration, enhanced with a proposed scheme for the integration along the thickness has been implemented in PLCd [34], a code whose capabilities (non linear analysis for solids and structures with composites materials) fits with requirements that arise from the study of masonry and reinforced concrete structures.

DKT-OPT flat shell element has 18 degrees of freedom:

$$\boldsymbol{d}_{\mathrm{o}} = \{u_1\ v_1\ w_1\ \theta_{x1}\ \theta_{y1}\ \theta_{z1}\ u_2\ v_2\ w_2\ \theta_{x2}\ \theta_{y2}\ \theta_{z2}\ u_3\ v_3\ w_3\ \theta_{x3}\ \theta_{y3}\ \theta_{z3}\ \}^{\mathrm{T}} \tag{2.47}$$

In order to separate membrane and bending degrees of freedom, displacement shall be written as

Element	Mesh: x-subdivisions × y-subdivisions				
	8 × 2	16 × 4	32 × 8	64 × 16	128 × 32
ALL-3I	96.41	98.59	99.59	99.91	99.99
ALL-3M	82.70	94.78	98.57	99.62	99.91
ALL-EX	89.43	96.88	99.16	99.79	99.96
ALL-LS	89.72	96.94	99.17	99.79	99.96
CST	55.09	82.59	94.90	98.65	99.66
FF84	99.15	99.71	99.87	99.96	99.99
LST-Ret†	70.86	91.10	97.90	99.56	99.90
OPT	101.68	100.30	100.03	100.00	100.00
	4 × 2	8 × 4	16 × 8	32 × 16	64 × 32
ALL-3I	82.27	93.22	97.86	99.38	99.83
ALL-3M	54.23	81.84	94.52	98.50	99.61
ALL-EX	70.71	89.63	96.93	99.15	99.77
ALL-LS	69.97	89.30	96.94	99.17	99.79
CST	37.85	69.86	90.04	97.25	99.28
FF84	94.27	97.85	99.23	99.74	99.92
LST-Ret†	79.58	93.53	98.14	99.49	99.83
OPT	96.68	98.44	99.37	99.78	99.93
	2 × 2	4 × 4	8 × 8	16 × 16	32 × 32
ALL-3I	42.53	72.66	90.72	97.32	99.27
ALL-3M	12.39	31.81	63.68	87.24	96.41
ALL-EX	26.16	56.93	83.54	95.14	98.69
ALL-LS	23.02	52.37	80.84	94.22	98.45
CST	17.83	43.84	75.01	92.13	97.86
FF84	89.26	96.37	98.66	99.50	99.83
LST-Ret†	56.71	83.79	95.14	98.63	99.62
OPT	92.24	96.99	98.70	99.48	99.81

† Requires one drilling freedom to be fixed, else stiffness is singular.

Figure 2.15 *Tip deflections (exact=100) for short cantilever beam under End Shear. Table 5 of reference [52].*

$$\left\{ \begin{matrix} \boldsymbol{d}_m \\ \boldsymbol{d}_b \end{matrix} \right\} = \left\{ \begin{matrix} \{u_1\ v_1\ \theta_{z1}\ u_2\ v_2\ \theta_{z2}\ u_3\ v_3\ \theta_{z3}\ \}^{\mathrm{T}} \\ \{w_1\ \theta_{x1}\ \theta_{y1}\ w_2\ \theta_{x2}\ \theta_{y2}\ w_3\ \theta_{x3}\ \theta_{y3}\ \}^{\mathrm{T}} \end{matrix} \right\} \tag{2.48}$$

and strain-displacement relationship as

$$\left\{ \begin{matrix} \boldsymbol{\varepsilon}_m \\ \boldsymbol{\varepsilon}_b \end{matrix} \right\} = \begin{bmatrix} \mathbf{B}_m & \mathbf{0}_{3x9} \\ \mathbf{0}_{3x9} & \mathbf{B}_b \end{bmatrix} \left\{ \begin{matrix} \boldsymbol{d}_m \\ \boldsymbol{d}_b \end{matrix} \right\} = \mathbf{B}_{\mathrm{o}} \left\{ \begin{matrix} \boldsymbol{d}_m \\ \boldsymbol{d}_b \end{matrix} \right\} \tag{2.49}$$

Thus stiffness matrix of the shell element corresponding to displacement vector of eq.2.48

$$\mathbf{K}_{\mathrm{o}} = \int_A \mathbf{B}_{\mathrm{o}}^{\mathrm{T}} \mathbf{D}_{\mathrm{o}} \mathbf{B}_{\mathrm{o}}\, dA = \begin{bmatrix} \mathbf{K}_m & \mathbf{K}_{m+b} \\ \mathbf{K}_{b+m} & \mathbf{K}_b \end{bmatrix} = \begin{bmatrix} \mathbf{K}_m & \mathbf{0}_{9x9} \\ \mathbf{0}_{9x9} & \mathbf{K}_b \end{bmatrix} \tag{2.50}$$

where $\mathbf{D}_{\mathrm{o}}$ will be defined in section 2.5.2, $\mathbf{B}_{\mathrm{o}}$ is shown in 2.49, and finally, once $\mathbf{K}_{\mathrm{o}}$ of eq.2.50 is evaluated, will be rearranged according to displacement vector shown in eq.2.47. The reason of stiffness matrix $\mathbf{K}_{m+b} = \mathbf{0}$ and $\mathbf{K}_{b+m} = \mathbf{0}$ will be explained in section 2.5.3.

2.5.1 Area Integration Scheme

First, let us recall eq.2.13, where stiffness matrix $\mathbf{K}_m$ of a OPT element is noting but the sum of the a basic stiffness matrix $\mathbf{K}_{mb}$ evaluated using only one Gauss point Gp_0

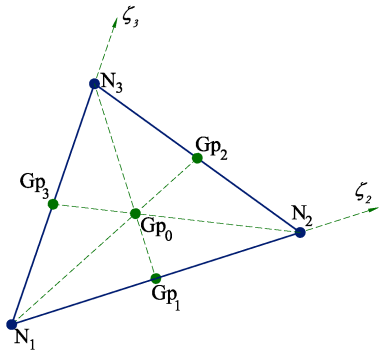

G.p.	ζ_1	ζ_2	ζ_3
0	1/3	1/3	1/3
1	1/2	1/2	0
2	0	1/2	1/2
3	1/2	0	1/2

Figure 2.16 *Coordinates ζ_i for a triangle.*

(fig. 2.16), and a high order stiffness matrix $\mathbf{K}_{mh}$ evaluated using a three Gauss points rule: Gp_1,Gp_2 and Gp_3. This situation lead us to a drawback pointed earlier; there is no a exact relationship among strains and nodal displacements, in [70] expression 2.51 to eval $\mathbf{B}_m$ has been proposed

$$\mathbf{B}_m = \frac{L^{\mathrm{T}}}{V} + \frac{3}{2}\sqrt{\beta_0}T_e(\mathbf{Q}_1(\zeta_1) + \mathbf{Q}_2(\zeta_2) + \mathbf{Q}_3(\zeta_3))\tilde{\mathbf{T}}_{\theta u} \tag{2.51}$$

On the other hand, due to its nature (imposing conditions in corners and mid points of sides, section 2.3.2), exact integration of the stiffness matrix of a DKT element is obtained using a three gauss points integration rule located at the mid-nodes [15], namely, Gp_1,Gp_2 and Gp_3.

In this work the way we will proceed to overcome the previous situation, for both OPT and DKT elements, is shown below:

- Generalized strains $\hat{\boldsymbol{\varepsilon}}$ will be evaluated at Gp_1,Gp_2 and Gp_3 (fig.2.16), in such a way

$$\hat{\boldsymbol{\varepsilon}} = \frac{\hat{\boldsymbol{\varepsilon}}_{Gp1} + \hat{\boldsymbol{\varepsilon}}_{Gp2} + \hat{\boldsymbol{\varepsilon}}_{Gp3}}{3} \tag{2.52}$$

  This is because neither OPT or DKT element are a three G.P. elements, both are 1 G.P. elements using an integration scheme of a 3 G.P., which means stresses and strains are constant all over the element. Hence, no state where one G.P. is *damaged* and the others are not will be acceptable. Also eval $\hat{\boldsymbol{\varepsilon}}$ at $\zeta_2 = 1/3$ and $\zeta_3 = 1/3$ would be possible. Generalized deformation $\hat{\boldsymbol{\varepsilon}}$ from 2.52 is the deformation to be distributed along element's thickness and then to be sent to a constitutive block where stresses $\hat{\boldsymbol{\sigma}}$ will be integrated according to both *Rules of Mixtures* (RoM) of the given composite and constitutive equations of the materials belonging to such composite.

- While assembling the *Left Hand Side* (LHS, for now on), if no *damage* occur in any of the components elastic loads will be evaluated as:

$$\mathbf{E}_{LAOD} = \mathbf{K}_{\mathrm{o}}\,\mathbf{d}_{\mathrm{o}} \tag{2.53}$$

Otherwise, if *damage* has occur within a component of the element, elastic loads will be evaluated as:

$$\mathbf{E}_{LAOD} = \int_A \mathbf{B}_o^{\mathrm{T}} \hat{\boldsymbol{\sigma}} \tag{2.54}$$

2.5.2 Proposed Thickness Integration Scheme

In order to correctly predict the kinematics of complex structures, 3D finite elements analysis seem to be the best alternative. However, simulation of large multi-layered structures with many plies can be unaffordable with 3D analyses because of the excessive computational cost, especially for non-linear materials. In addition, the discretization of very thin layers can lead to highly distorted elements carrying numerical issues, hence, reduced models for modeling multilayer plates arise as an affordable solution.

Thus, simpler and more efficient techniques are required for modeling laminated structures, where 3D descriptions can be reduced to 2D models by introducing hypotheses on the displacements or/and on the stresses field, since laminate thickness is at least one order of magnitude lower than in-plane dimensions.

Reference [28] is an overview of the available theories and finite elements that have been developed for multi-layered, anisotropic, composite plate and shell structures. Multi-scale approaches [147, 117] can also be used to model non-linear multi-layered materials. In such methods a macroscopic model is used to obtain the global response of the structure whereas the material behavior, modeled with a constitutive law, is solved with a microscopic model.

Many reduced approaches have been developed and improved since 19th century, in order to facilitate their classification, they could be distinguished according to [47]:

a) The type of unknown variable chosen, so they could be *Displacement Based Theories* (DB), *Stress-Based Theories* (SB), or if both stress and displacement are considered as unknowns, a *Mixed Approach* (MB) is obtained.

b) How the unknown variables are described. In this classification it may be a *Equivalent Single Layer* (ESL) description, where governing equations are written for the whole plate, or a *Layer-Wise* (LW) description, where each layer is treated independently assuming separate displacement/stress fields within each ply, which leads to write the governing equations for each layer.

The most basic DB-ESL model is the Classical Theory [160], whereas an improvement to the CT theory is the *First Order Shear Deformation Theory* (FSDT) [101] which enhances the CT kinematics by adding shear effects (see section 2.3). Although CT and FSDT are excellent alternatives to accurately model homogeneous thin and thick shell structures, they lead to poor prediction in the cases listed below, the cause is found in the linear thickness distribution of the axial displacement, which does not match the ZZ pattern depicted in figure 2.17 [47].

- Where component materials have a high level of transverse anisotropy.
- When applied to the analysis of composite laminated with embedded debounding.
- When it is necessary to fulfill regions with 3-D stresses fields, i.e. $\sigma_Z \neq 0$.

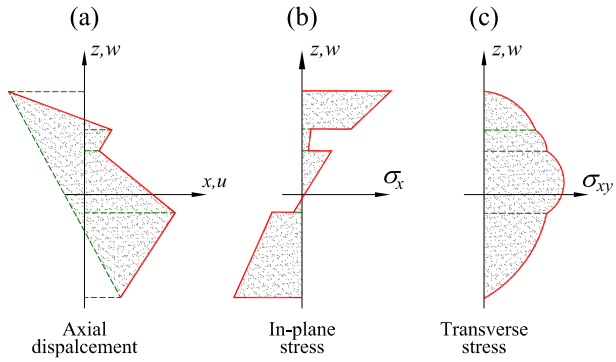

Figure 2.17 *Continuous zigzag in-plane displacement a), discontinuous in-plane stress b), and continuous transverse stress c).*

- When it is required to capture the so called *zig-zag* pattern of in-plane displacements (ZZ condition).
- When it is required to satisfy the condition of continuous transverse shear along the thickness direction (TC condition).

In order to fulfill the previously listed condition while performing the analysis of laminated materials, it must be necessary to use either a theory based on 3-D kinematics, or a LW based theory. Although LW theories accurately fulfill both, the ZZ and the TC condition, the number of unknown variables is proportional to the number of analyzed layers. As a result, these models yield not only to a high level of accuracy but also to a high amount of unknown variables similar to the 3D analysis. For this reason, LW models may result unattractive for simulating large laminated structures with many plies. Therefore, these models should be employed to analyze complex problems where other less expensive approaches fail to give realistic predictions [47].

A special case of LW models where the number of unknowns is independent of the number of analysis layer are the Zigzag theory (ZZT), which are a good compromise between the accuracy of MB-LW theories and the computational efficiency of DB-ESL models. One of the most important advantages of these theories is that the number of kinematics unknowns is independent of the number of analyzed layers.

Have to be remarked that, the study of the cases where it is mandatory to use a LW description are out of the scope of this work, and the only feasible solution from a computational point of view, which allow to achieve good results, is to adopt a ESL scheme. That is why, in this section it has been proposed a scheme capable of reproduce the bending damage of a laminated material without the need of additional degrees of freedom than the ones listed in equation 2.47. This simplification is justified by the fact that stiffness of the simple material used along this work never exceed an order of magnitude, in addition, it has been used a Discrete Kirchhoff Triangle [15] where the shear transverse strain is postulated to be neglected with respect to other strains.

According to the classification of the existing theories, the proposed scheme is a modification of the DB-ESL, where it is taken into account the evolution of the eccentricity of geometric and mechanical planes of a bi-dimensional element during the damage process, also, generalized stresses and strains have been referred to the mechanical plane,

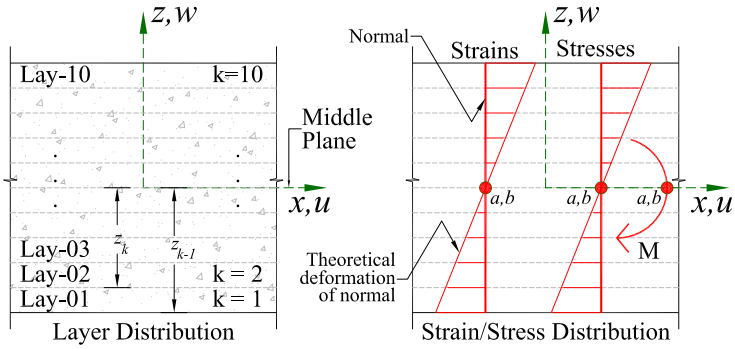

Figure 2.18 *Strain and stress distribution of a homogeneous material.*

not to the geometrical plane as occurs in the classical DB-ESL formulation. First, let us consider $\mathbf{D}_o$ from equation 2.50, which can be written as

$$\mathbf{D}_o = \begin{bmatrix} \mathbf{D}_m & \mathbf{D}_{m+b} \\ \mathbf{D}_{b+m} & \mathbf{D}_b \end{bmatrix} \tag{2.55}$$

and according to [108], can be evaluated as

$$\begin{aligned} \mathbf{D}_m &= \sum_{k=1}^{n} (z_k - z_{k-1}) \mathbf{D}_{ij}^k \\ \mathbf{D}_{m+b} = \mathbf{D}_{b+m} &= \sum_{k=1}^{n} \frac{1}{2} (z_k^2 - z_{k-1}^2) \mathbf{D}_{ij}^k \\ \mathbf{D}_b &= \sum_{k=1}^{n} \frac{1}{3} (z_k^3 - z_{k-1}^3) \mathbf{D}_{ij}^k \end{aligned} \tag{2.56}$$

where $\mathbf{D}_{ij}$ has been defined in eq.2.4, and $k = 1, ..., n$ being n the total numbers of layers within the laminated material. Figure 2.18 shows a typical distributions of the strains and stresses within a laminated material using equation 2.56, figure 2.18 also displays the *position* parameters z_k and z_{k-1} used to state the position of the k_{th} layer, and consequently, to perform the integration of the bending stiffness $\mathbf{D}_b$.

In order to perform the integration scheme over the thickness proposed in this section, equation 2.56 have to be redefined, also, the *position* parameters z_k and z_{k-1} have to be redefined.

First, let us assume the existence of points a and b. Point a is defined as the intersection of the middle plane and the normal of the plate, whereas point b is defined as the intersection of the theoretical deformation of the normal and the normal. The purpose of using points a and b is to refer the displacement field to point a, whereas point b will be the reference for rotations, hence, point b will be used as the reference for in-plane displacements for the layers within the laminate material. If figure 2.18 is used to express this idea, for the particular case of a homogeneous material, then $a = b$.

On the other hand, let us assume laminate from figure 2.19 in its layer 07 has a material stiffener than the rest, this example illustrates a case when $a \neq b$, and the

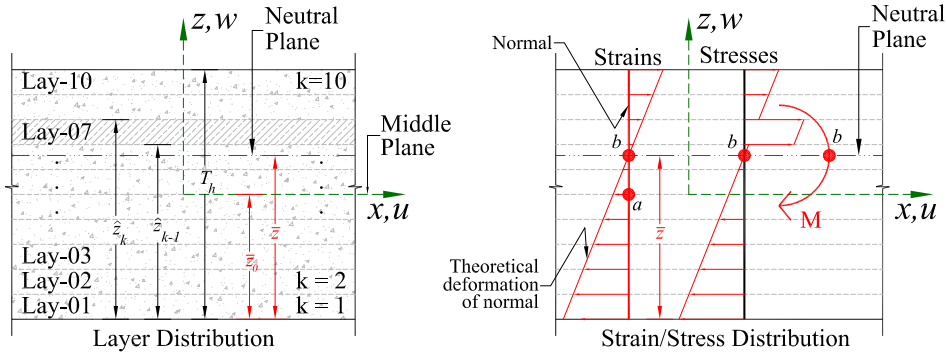

Figure 2.19 *Proposed strain and stress distribution for a laminated material.*

consequences is that the strain distribution although remain linear, no longer remain symmetrical to the middle plane, also there is a variation in the stress distribution and in the generalized stresses $\hat{\boldsymbol{\sigma}}$, which in figure 2.19 are represented using bending moment $\mathbf{M}$. In figure 2.19 also is depicted the new position parameters $\hat{z}_k$ and $\hat{z}_{k-1}$ used for each layer, for convenience they are referred now to the bottom of the plate. As can be seen, for layer 01 $\hat{z}_{k-1} = 0$ and for layer k $\hat{z}_k = T_h$, being T_h the total thickness of the plate. On the other hand, position parameter $\bar{z}_0 = T_h/2$, since is the reference to the middle plane. Finally, the position of $\overline{\mathbf{Z}}$ is the cornerstone of the proposed scheme, to define it let, us start defining the auxiliary matrix $\hat{\mathbf{D}}_b$

$$\hat{\mathbf{D}}_b = \int \bar{y}_k \mathbf{D}_m^k dz = \sum_{k=1}^{n} \bar{y}_k \, t_k \mathbf{D}_{ij}^k \tag{2.57}$$

in equation 2.57, for convenience $\bar{y}_k = (\hat{z}_k + \hat{z}_{k-1})/2$, whereas $t_k = \hat{z}_k - \hat{z}_{k-1}$, this is, the thickness of the layer k, now it is possible to define $\overline{\mathbf{Z}}$ using equation 2.58.

$$\overline{\mathbf{Z}} = \begin{bmatrix} \dfrac{\hat{\mathrm{D}}_{11}^b}{\mathrm{D}_{11}^m} & \dfrac{\hat{\mathrm{D}}_{12}^b}{\mathrm{D}_{12}^m} & \dfrac{\hat{\mathrm{D}}_{13}^b}{\mathrm{D}_{13}^m} \\ \dfrac{\hat{\mathrm{D}}_{21}^b}{\mathrm{D}_{21}^m} & \dfrac{\hat{\mathrm{D}}_{22}^b}{\mathrm{D}_{22}^m} & \dfrac{\hat{\mathrm{D}}_{23}^b}{\mathrm{D}_{23}^m} \\ \dfrac{\hat{\mathrm{D}}_{31}^b}{\mathrm{D}_{31}^m} & \dfrac{\hat{\mathrm{D}}_{32}^b}{\mathrm{D}_{32}^m} & \dfrac{\hat{\mathrm{D}}_{33}^b}{\mathrm{D}_{33}^m} \end{bmatrix} \tag{2.58}$$

Now, using equation 2.58, the bending stiffness tensor $\mathbf{D}_b$ from equation 2.56 is rewritten in equation 2.59.

$$\mathbf{D}_{ij}^b = \sum_{k=1}^{n} \left[\frac{t_k^3}{12} + t_k \, (\hat{\mathbf{Z}}_{ij}^k)^2 \right] \mathbf{D}_{ij} \tag{2.59}$$

finally, $\hat{\mathbf{Z}}_{ij}^k$ from equation 2.59 is defined in equation 2.60.

$$\hat{\mathbf{Z}}_{ij}^k = \bar{y}_k - \overline{\mathbf{Z}}_{ij} \tag{2.60}$$

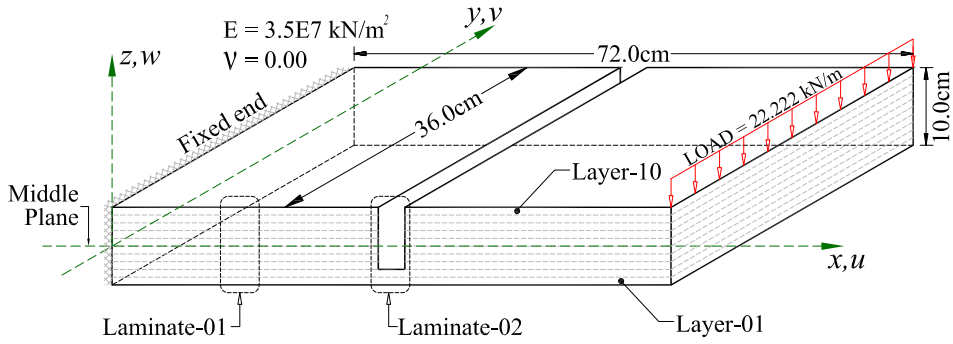

(a) Geometry and boundary conditions.

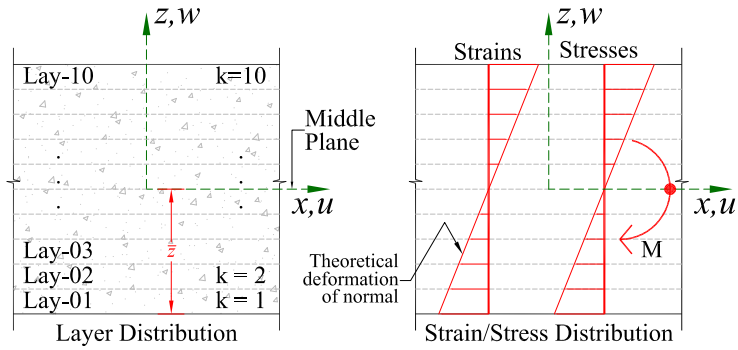

(b) Strain/stress Distribution Laminate-01 (undamaged).

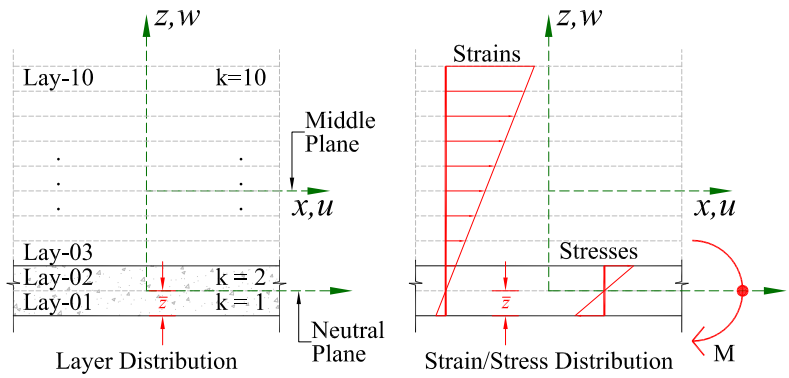

(c) Strain/stress Distribution Laminate-02 (damaged).

Figure 2.20 *Fixed plate at the one end, and vertical load at the other end.*

Basic idea of the proposed integration scheme over the thickness can be inferred using fig.2.20. Let fig.2.20.a be a plate fixed at one end and a free end with a load of $22.22kN/m$, formed by two laminated materials:

- **Laminate 01** with an *undamaged* state shown in fig.2.20.b. Since is a homogeneous material, mechanical plane is laid within the middle plane, and
- **Laminate 02** with a fully *damaged* state of layers 3 to 10 (as shown in fig.2.20.c), layers 1 and 2 stay *undamaged*, hence, there is the gap now between middle and mechanical plane.

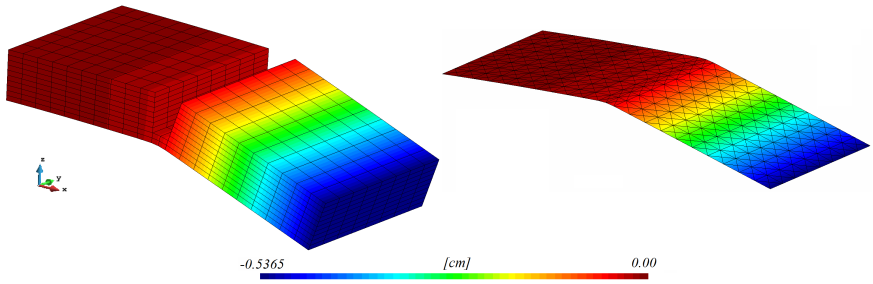

Figure 2.21 *Displacement comparison (fig.2.20) - isometric view.*

From the laminated materials 1 and 2 previously described, obvious distinctions arises, in which the proposed integration scheme along the thickness is based upon, this is: the clear distinction among mechanical plane (also referred as neutral plane) and the middle plane (also referred as geometrical plane along this work). Whereas loading conditions and geometry are referred to middle plane, generalized stresses and generalized strains along thickness will be referred to the mechanical axis, as defined in eq.2.58.

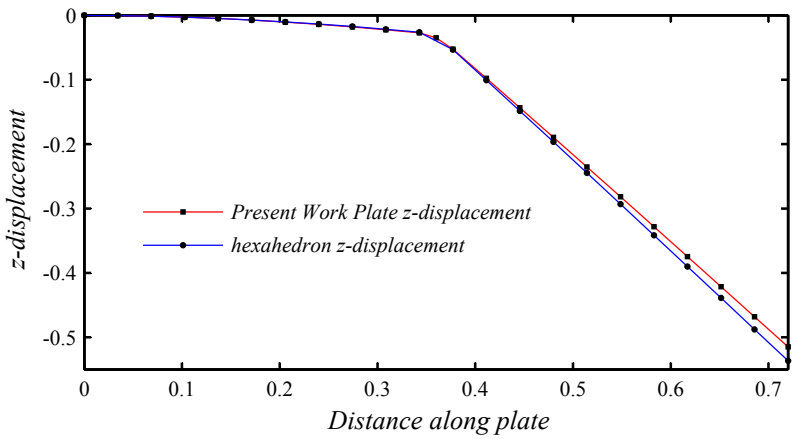

Figure 2.22 *Displacement comparison (fig.2.20) - middle plane.*

Two analysis of the model presented in figure 2.20.a have been performed to test and show the capabilities of the proposed integration scheme. The first test is used as a reference, and has been carried out using a mesh of 1632 8-nodded hexahedron finite elements with a notch of 3.72 centimeters at the center. The second test has been carried out using a mesh of 704 triangular DKT-OPT finite elements with the proposed integration scheme and the two different laminate distributions shown in figure 2.20.a. In both cases the left end of the mesh has been fixed, and only one loading step has been applied on the right end of the mesh.

Obtained results are presented in figure 2.21, where the deformation of both meshes (magnified 25 times) is depicted. Finally fig. 2.22 plots a comparison of middle plane displacement in z direction of both prismatic and plate elements. From such figures clearly can be concluded that the proposed integration scheme over the thickness leads to excellent results and can be used along this work.

Shall be remarked that $\overline{\mathbf{Z}}$ will be evaluated at the beginning of a *quasistatic* loading process, and then in every iteration once damage has occur within the given FE. Also, has to be pointed out that this integration scheme is intended to be used with a secant tensor $\mathbf{D}_{ij}^{sec}$ instead of $\mathbf{D}_{ij}$ from equations 2.57, and 2.59, as an attempt to reproduce the change in the position of the mechanical plane using the information of a non-elastic constitutive equation. A Proper explanation of non-linear evolution, regarding damage or plasticity flow will be carried out next in section 3.6 of this work.

2.5.3 Proposed Bending-Membrane effect

Although in the development of this work it has been tried to keep separated the finite element formulation from the part belonging to the structural analysis, in this section is obligatory to combine them, so, it will be easier to explain the basics in the implementation proposed here.

Let us consider the different types of slabs typically used in the construction of concrete buildings depicted in figure 2.23. Using one, or another, is not only a structural concern to improve the strength-to-weight ratio of a slab, some cases, it could be due to the insulation provided by the polystyrene that leads to a better thermal performance of the structure.

The condensation of a dimension (thickness), mandatory to model structures using two-dimensional finite elements, leads to refer all layers contained within such finite elements to a plane, which is typically named *middle plane* or *geometrical plane*, since its sole function is to serve as a geometrical reference. While modeling structural elements like the ones shown in figure 2.23 it is important to distinguish the geometrical plane of the mechanical plane, which is the application plane of the resultant stiffness of layers contained within a finite element. Figure 2.24 serves to clarify these concepts, in it a distribution of layers is shown for a concrete coffer slab, it is also depicted the position of the geometrical and the mechanical plane. As can be seen, both these planes match in the ribs, on the other hand, they do not match in the region belonging to the polystyrene coffer.

The eccentricity between these two planes: geometrical and mechanical, leads to the appearance of the *bending-membrane* effect, since membrane forces produce bending forces within the element.

Let us first distinguish the two cases to deal with the bending-membrane $(b+m)$ effect. The first one is as presented in [108], and previously shown in eq.2.56 which will be referred as ***C**onstitutive **B**ending **M**embrane **E**ffect* (CBME), will be called that way

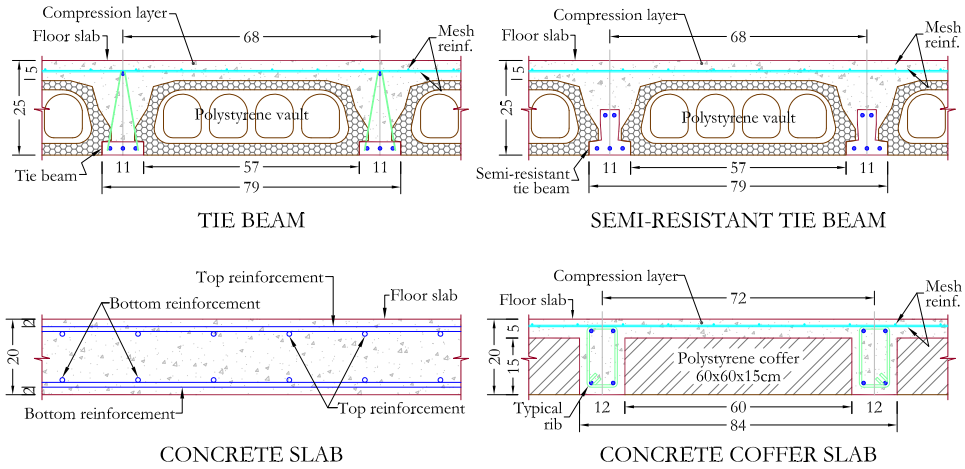

Figure 2.23 *Cross section of different slabs commonly used in construction.*

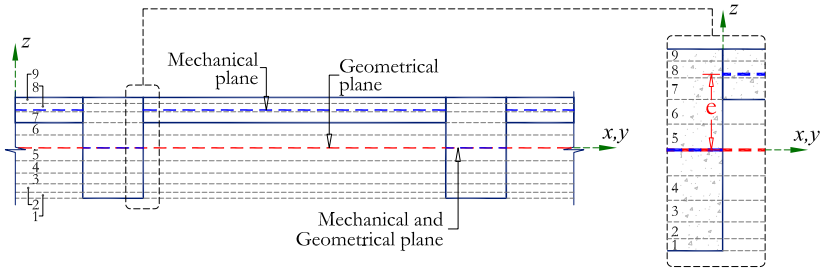

Figure 2.24 *Layered cross section of a concrete coffer slab.*

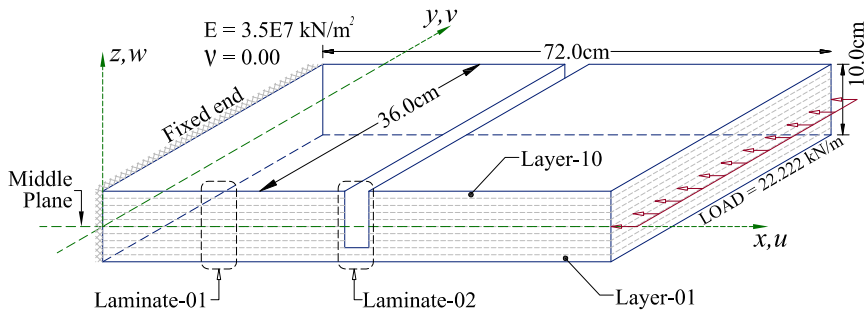

Figure 2.25 *Fixed plate at the one end, and horizontal load at the other end.*

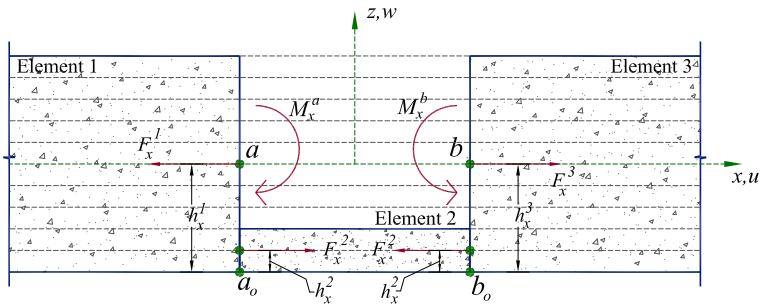

Figure 2.26 *Middle part close up of fig.2.25.*

because; in order to reproduce the $b+m$ effect a constitutive matrix $\mathbf{D}_{m+b}$ is required. The second one (and proposed here) will be named ***F**orce **B**ending **M**embrane **E**ffect* (FBME), because elastic forces will be required to evaluate such $b+m$ effect.

In order to implement the FBME it will be required to follow the next steps.

1) It will be required the list of FE elements belonging to all nodes, and the local numeration of the given node within such elements. A *flag* within the given node can be used to save computational time, in such a way if middle axis equals to neutral axis for all belonging elements $\mathbf{M}^{b+m} = 0$, and consequently, step 3 does not need to be performed for the given node. Also a local coordinate system for the node will be required in the case that $E0^{XZ}$ of the belonging elements were not equal.

2) Let $\mathbf{D}_{m+b} = \mathbf{D}_{b+m} = 0$ in $\mathbf{D}_0$ from 2.55, and perform a linear elastic analysis.

3) It will assume that $\sum \mathrm{M} = 0$ for a given point of reference, a_o and b_o in the case of figure 2.26. Then

$$M_x^i = \sum_{j=1}^{k} F_x^j h_x^j \quad ; \quad M_y^i = \sum_{j=1}^{k} F_y^j h_y^j \tag{2.61}$$

where subindex i is the current node and j is for all the belonging elements of the given node, k is the total number of belonging elements, F_x and F_y stands for the elastic forces in x and y direction respectively, evaluated with local displacements and the local stiffness matrix as in eq.2.54, finally $h_x^j = \overline{\mathbf{Z}}_{1,1}$ and $h_y^j = \overline{\mathbf{Z}}_{2,2}$ of j_{th} element from 2.58.

4) M_x^i and M_y^i will be switch to the i_{th} node's base and assembled into the RHS of the linear equation.

5) Perform again the analysis with the RHS assembled in step 4.

Now, let us consider figure 2.25, which is the same as figure 2.20, but for the direction of the applied load. Such example will be performed in order to test the implemented bending-membrane effect, assuming that a reasonable way to compare the obtained results will be using a hexahedron mesh (as in fig.2.20) and the CBME scheme.

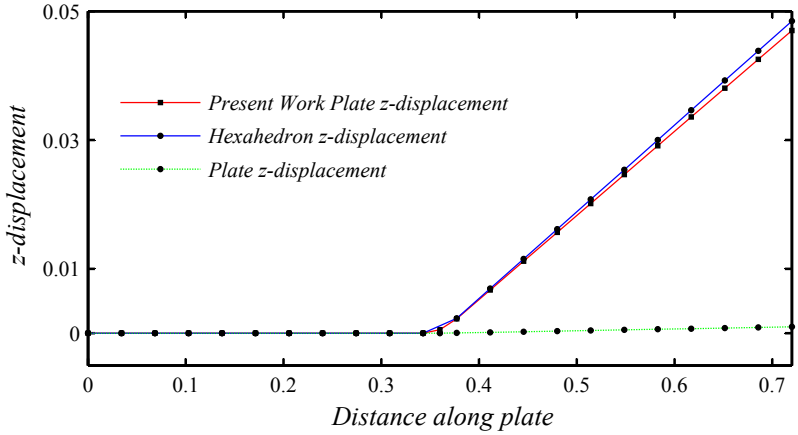

Figure 2.27 *Displacement comparison (fig.2.25) - middle plane.*

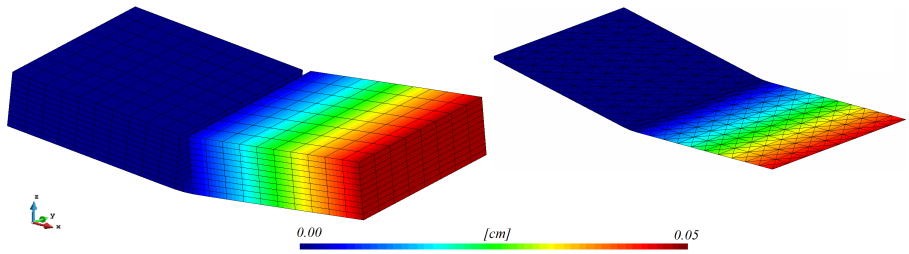

Figure 2.28 *Displacement comparison (fig.2.25) - isometric view.*

A clear drawback arises while going through the steps of the proposed method; both a high amount of memory to store information and more computational time will be require, nevertheless due to the accuracy compared with hexahedron elements it is preferable to apply the proposed method. As can we see from fig.2.27 CBME lacks in accuracy, since obtained results are way far from the FBME method and with the hexahedrons mesh. Finally figure 2.28 depicts an isometric perspective of deformed meshes with a magnification factor of 100.

2.5.4 Large Displacements Approach

Different approaches can be used for non-linear analysis. In the Total Lagrangian (TL) approach, equations are formulated with respect to a fixed reference configuration which is usually the initial configuration, while in updated Lagrangian (UL) approach the reference configuration is the last converged solution. The *corotational* approach (CR) is the most recent formulation developed for geometrically non-linear structural analysis, in this method the finite element equations are referred to two systems: a fixed configuration and a *corotated* configuration. The main advantage of CR formulation is its effectiveness for problems with small strains but large-rotations.

Important work on the development of CR formulation has been done by Wempner

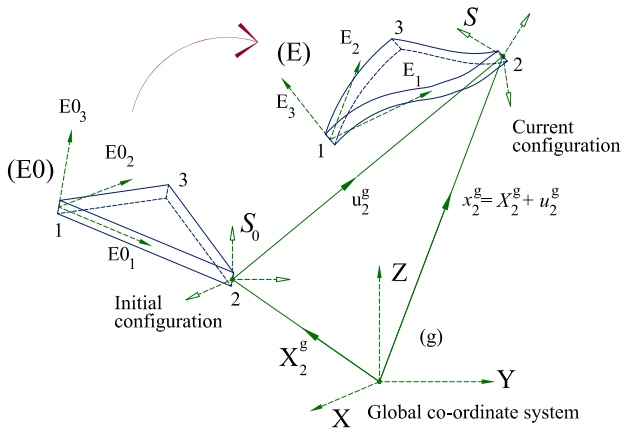

Figure 2.29 *Corotational scheme.*

[171], Belytschko and Hsieh [20], Bergan and Horrigmoe [22], Argyris [10], Rankin and Brogan [133], Szwabowicz [157], Rankin and Nour-Omid [134], Nour-Omid and Rankin [105], Crisfield [39], Peng and Crisfield [131], Pacoste [123], Battini and Pacoste [16], finally, in the work done by Khosravi *et al* [70] a shell laminated element combining a OPT membrane element and a DKT bending element for geometric non-linearity is conducted using the CR approach, although full detail of CR formulation are provided in reference [70] a brief overview is presented in this work.

The general aspects of CR approach are that the total motion of an element is decomposed into a rigid body motion and a pure deformation. Then the contribution of the rigid body motion to the total deformation of the element is removed before performing the element computations. To do so several coordinate systems are required to fully describe the geometry and deformation of a shell structure and a shell finite element, and later within the process remove the rigid body motion.

First let us consider figure 2.29 where is shown a typical FE shell triangle in its initial configuration (undeformed) and at the current configuration (deformed), there can be inferred the coordinates systems required to describe the CR aproach, namely:

- The first one used is the global coordinate system (g).
- The second coordinate system is E and $E0$, one for each element that translates and rotates with it. The origin of the undeformed element frame $E0$ is chosen at node 1, and the axis $E0_1$ (x local direction) is chosen as the line joining nodes 1 and 2, whereas axis $E0_3$ (z local direction) is the normal of the element's middle plane defined by nodes 1, 2 and 3. Axis $E0_2$ (y local direction) then defines the Cartesian right handed coordinate system. Coordinate system E is defined in the same fashion but at the current (deformed) configuration. $E0$ will be updated to E in every Newton-Raphson iteration using the new nodal positions $x^g = X^g + u^g$ (fig.2.29).
- The second coordinate systems are $S0$ and S for undeformed and deformed configurations respectively, one for each node that are rigidly tied to their respective node and rotates with them. Orientation of $S0$ are arbitrary and is chosen to be

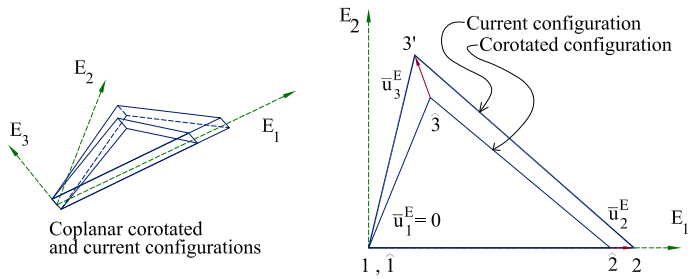

Figure 2.30 *Configurations in corotational scheme.*

parallel to the global co-ordinate system g. Transforming from $S0$ to S is obtained by rotating the $S0$, also such local coordinate system will be updated in every iteration of the Newton-Raphson process. Following expressions shows the way to proceed to rotate old S coordinate system.

$$\mathbf{T}_{S_{\text{NEW}}} = \tilde{\mathbf{T}}\mathbf{T}_{S_{\text{OLD}}} \tag{2.62}$$

where

$$\tilde{\mathbf{T}} = \mathbf{I} + \frac{\tilde{\boldsymbol{\Omega}} + 0.5\tilde{\boldsymbol{\Omega}}^2}{1 + 0.25|\boldsymbol{\omega}|^2} \quad ; \quad |\boldsymbol{\omega}| = \sqrt{\tilde{\theta}_X^2 + \tilde{\theta}_Y^2 + \tilde{\theta}_Z^2}$$

$$\tilde{\boldsymbol{\Omega}} = \begin{bmatrix} 0 & -\tilde{\theta}_Z & \tilde{\theta}_Y \\ \tilde{\theta}_Z & 0 & -\tilde{\theta}_X \\ -\tilde{\theta}_Y & \tilde{\theta}_X & 0 \end{bmatrix} \tag{2.63}$$

Once coordinate system are established and updated after an iteration, the way to proceed according to [133], in order to evaluate both pure nodal displacements and pure nodal rotations are explained below.

a) **Pure nodal displacements** in E are computed by comparing the current configuration with a *corotated* configuration, as seen on figure 2.30. Pure nodal displacements at node i in E may be expressed by the relation:

$$\overline{u}_i^E = \begin{Bmatrix} \overline{u}_i^{E_1} \\ \overline{u}_i^{E_2} \\ \overline{u}_i^{E_3} \end{Bmatrix} = T_E^{\mathrm{T}}(u_i^g + X_i^g - u_1^g - X_1^g) - X_i^{E_0} \ , \qquad i = 1, 2, 3 \tag{2.64}$$

where $X_i^{E_0}$ is the initial coordinate of node i in E_0, and vectors $\overline{u}_i^E$ are shown in figure 2.30.

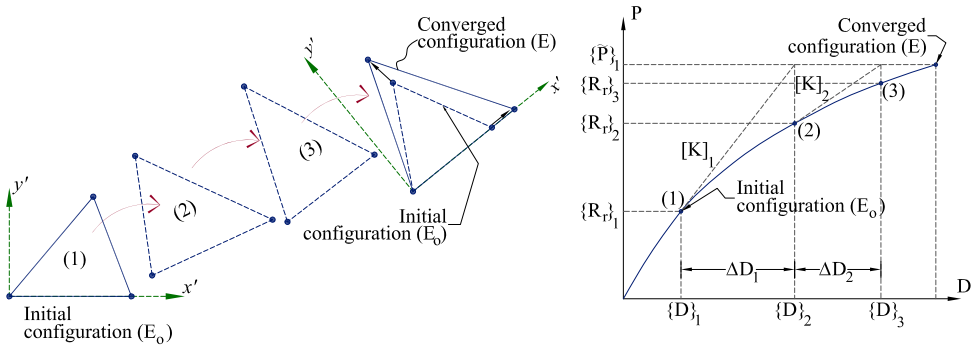

Figure 2.31 *Evolution of configurations in a corotational scheme.*

b) **Pure nodal rotations** in E are equal to the components of an antisymmetric matrix $\mathbf{\Omega}_{3x3}$ called spin tensor as

$$\mathbf{\Omega} = \begin{bmatrix} 0 & -\theta^{E_3} & \theta^{E_2} \\ \theta^{E_3} & 0 & -\theta^{E_1} \\ -\theta^{E_2} & \theta^{E_1} & 0 \end{bmatrix} \tag{2.65}$$

where $\mathbf{\Omega}$ is found by

$$\mathbf{\Omega} = 2(\mathbf{T} - \mathbf{I})(\mathbf{T} + \mathbf{I})^{-1} \tag{2.66}$$

and matrix T describes rotation of nodal triad $S0$ to S in local coordinate system E and can be evaluated as

$$\mathbf{T} = \mathbf{T}_E^{\mathrm{T}} \mathbf{T}_S \mathbf{T}_{E_0} \tag{2.67}$$

Pure deformations at node i computed in E can be expressed as:

$$d_i = \left[\overline{u}_i^{E_1} \quad \overline{u}_i^{E_2} \quad \overline{u}_i^{E_3} \quad \theta_i^{E_1} \quad \theta_i^{E_2} \quad \theta_i^{E_2}\right]^{\mathrm{T}} , \qquad i = 1, 2, 3 \tag{2.68}$$

Pure deformation from eq.2.68 are not really *pure* (without rigid body motion), which can cause problem in case that the element stiffness matrix does not have the correct rigid body motion properties. According to [70], [134] and [105] this problem can be overcome with the help of a projection matrix P whose capabilities of bringing into equilibrium a non-equilibrated force vector are of special interest. Hence pure nodal deflections d, internal forces vector r and element stiffness matrix K shall be modified using P, whose form is fully described in [70].

$$\overline{d} = Pd \quad ; \quad \overline{r} = P^{\mathrm{T}} r \quad ; \quad \overline{K} = P^{\mathrm{T}} K P \tag{2.69}$$

Finally figure 2.31 shows a typical deformation process during the Newton-Raphson iterative process using a loading control approach, whereas a self explanatory flowchart of CR scheme is shown in figure 2.32.

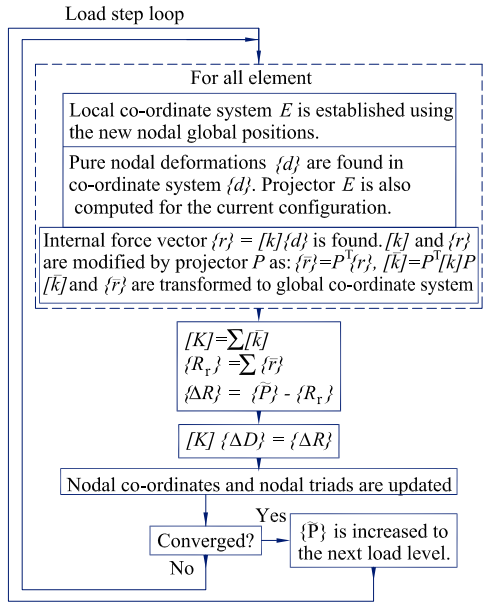

Figure 2.32 *Flowchart of a corotational scheme.*

2.6 Verification Examples

2.6.1 Cantilever Plate Subjected to Uniform end Moments

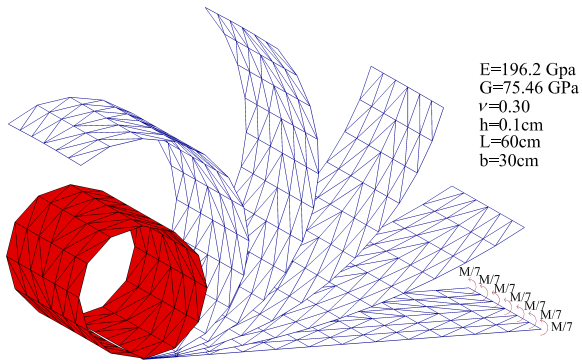

Figure 2.33 *Cantilever plate deformation.*

This case is used to evaluate the geometrically non-linear static capabilities of the DKT-OPT element. Corresponds to a cantilevered isotropic plate with uniform moment along the tip edge, whose geometry and mechanical properties, along with a snapshot of deformed configuration are shown in figure 2.33. Exact deformation W is given by the following analytical formula [70]:

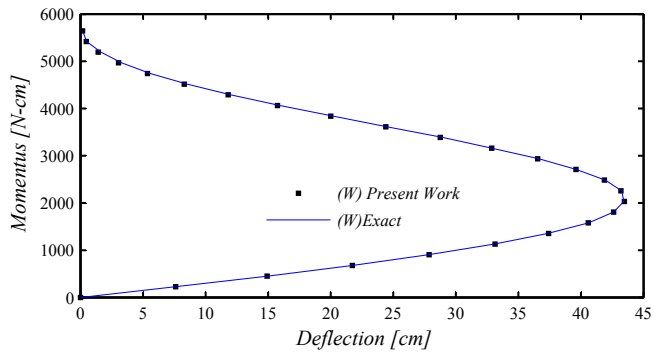

Figure 2.34 *Deflection of a cantilever plate subjected to end moment.*

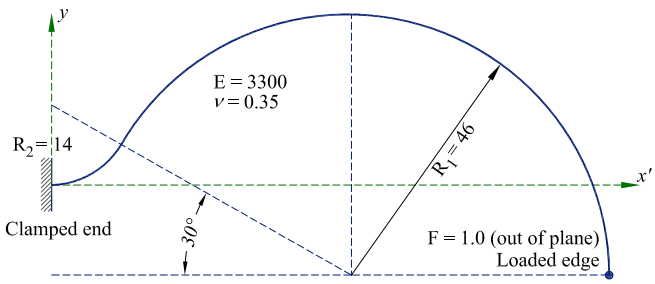

Figure 2.35 *Raasch's hook problem - Geometry, material, loading and boundary conditions.*

$$W = R(1 - cos\theta) = \frac{EI}{M(1-v^2)}\left(1 - cos\frac{ML(1-v^2)}{EI}\right) \tag{2.70}$$

The plate is modeled using 144 FE and applying a bending moment $M = 5644.5Ncm$ is applied at the end in 25 steps. As can be seen on fig. 2.34 there is an excellent match between the two results.

2.6.2 The Raasch Challenge for Shell Elements

The Raasch challenge [71] is a curved strip hook problem with a tip in plane shear load, proposed in 1990 by Ingo Raasch of BMW in Germany. The problem poses a significant challenge to shell elements because of the inherent coupling between three modes of deformation: bending, extension, and twist. So, the Raasch challenge benchmark will be carried out to assure the shell element performance on linear static analysis.

Figure 2.35 shows the top view of the hook, modeled by two circular segments connected at the tangent point. Geometry data, material properties, boundary and loading conditions, and reference value (displacement z =4.9352 at the loaded end) are given according to the work of Ingo Raasch [71].

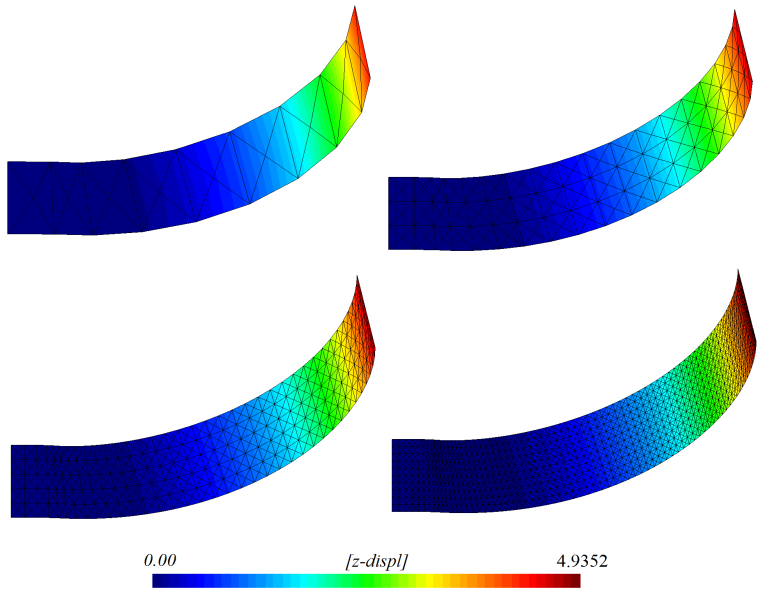

Figure 2.36 *Raasch's hook problem - Deformed mesh magnified 10 times.*

The convergence rate for 5 successively refined meshes is good (fig.2.37), taking into account that for a coarse mesh of 216 triangular elements the accurate achieved is 94.13 percent, staying steady for meshes with 720, 2880 and 11250 triangular elements.

2.6.3 Pinched Hemisphere with 18^{o} Hole

This popular benchmark for both linear and non-linear analysis will be consider. The geometry consist of a hemispherical shell with radius $R = 10$, and a 18^{o} hole at the top, mechanical properties of such shell are an elasticity modulus $E = 6.825x10^{7}$, Poisson's ratio $v = 0.30$ and the thickness $t = 0.04$ (fig.2.38). Symmetry conditions are used on this problem and therefore only one quadrant needs to be modeled.

Let us first consider a linear response whose analytical answer of 0.0924 [81] at loaded points is used to eval the performance of the DKT-OPT element. This benchmark is designed to study the effect of the warped element geometry in the overall performance of the elements. Loading conditions are $\lambda = 1$, graph depicted in figure 2.39 shows the result of a convergence study for successively refined meshes, from there it can concluded that the implemented element has a good ability to handle rigid body rotations about their normal.

On the other hand, non-linear response of the implemented element using the corotational scheme for large deformations proposed in [70] and reproduced in section 2.5.4 will be tested and compared with the results obtained by Simo *et al* [151]. Simo *et al* in [151] solved such non-linear problem using a structured mesh of 16x16 quadrilateral elements, hence, for comparative purposes it will be used a structured and symmetric triangular mesh of 1024 elements (16 elements per side) to have the same amount of Gauss points in the whole structure, also it will be considered a loading step $\Delta\lambda = 5$.

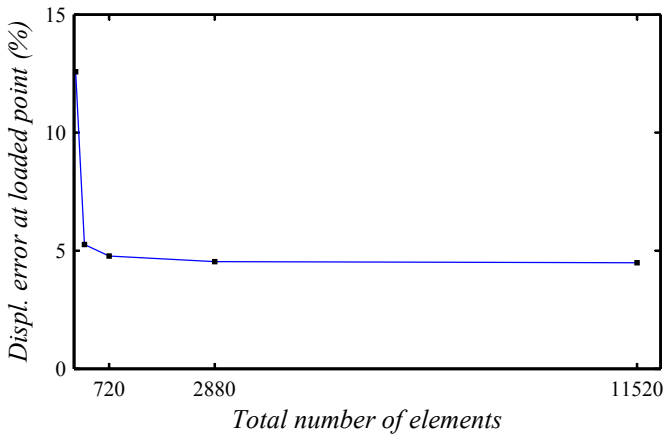

Figure 2.37 *Raasch's hook problem - Results using 5 different meshes.*

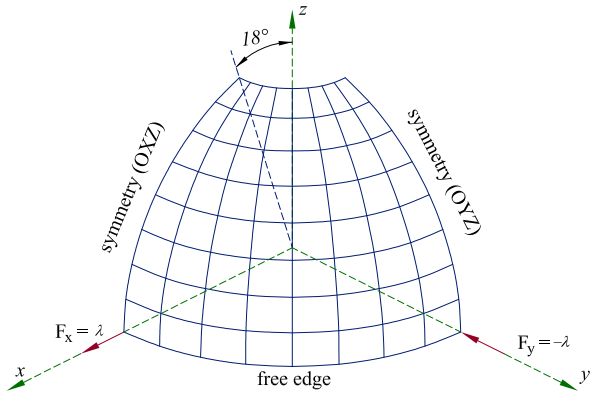

Figure 2.38 *Pinched Hemisphere with a 18°hole - Mesh, loading and, boundary conditions of one quadrant.*

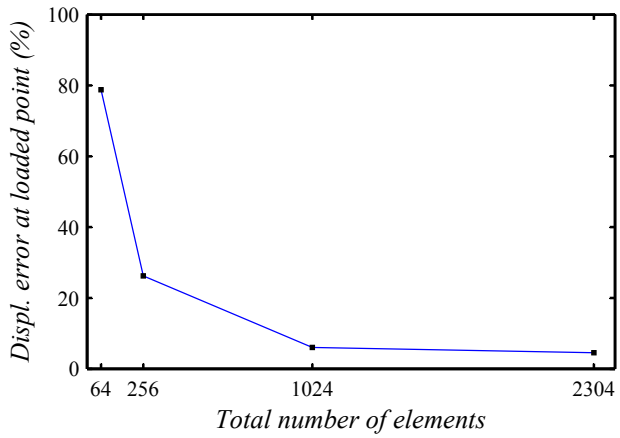

Figure 2.39 *Pinched Hemisphere with an 18°hole - Results using 4 different meshes and loading factor* $\lambda = 1$.

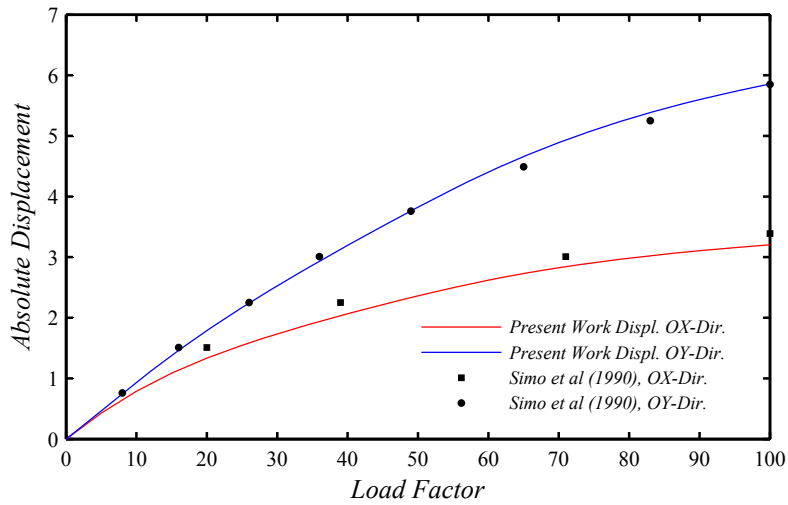

Figure 2.40 *Pinched Hemisphere with an 18°hole - Results using, corotational method and 20 loading steps* $\Delta\lambda = 5$.

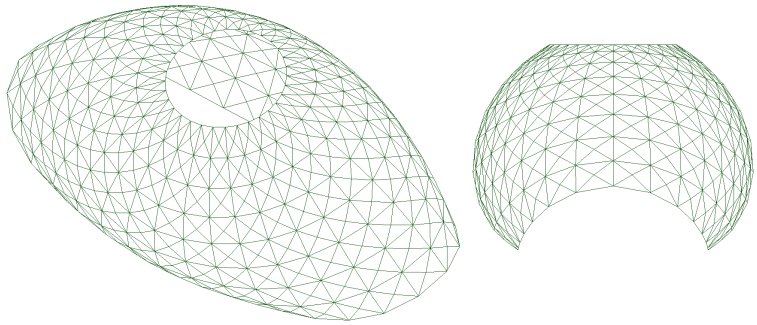

Figure 2.41 *Pinched Hemisphere with an 18°hole - Deformed configuration at* $\lambda = 100$.

Figure 2.40 shows displacement evolution at loaded points of the studied mesh, whereas figure 2.41 depicts the configuration of the deformed mesh (with 4 quadrants) without magnification factors, so it can concluded: also corotational scheme for large deformations has a great performance while dealing with rigid body rotations over element's normal.

Chapter 3

Computational Constitutive Model for In-filled Frames

An introduction to mechanical behavior of simple materials involved in this work is illustrated. Mixing theory's state-of-the-art is briefly reviewed. Pitfalls and drawback of using three nodded triangular elements are summarized. A methodology to generate composite materials for a large amount of finite elements, and capable of handling *real life* steel reinforcement patterns is proposed. A mesh-objectivity test for both, membrane and bending response using the proposed integration scheme along the thickness is performed. Finally, numerical test are presented.

3.1 Behavior and Characterization of Simple Materials

Constitutive models are a set of mathematical equations based upon continuum mechanics to relate two physical quantities specific to a material, whose main aim is to approximates the response of the given simple material to an external *stimuli* (forces in this case). They are combined with other equations governing physical laws to solve physical problems, i.e., constitutive models help us as a connection among applied stresses to strains. Since it has been necessary to use three different simple materials along this work, their mechanical behavior will be briefly described below, although their constitutive models from a mathematical point of view is described in appendices A and B.

3.1.1 Steel

Steel is an alloy of iron and other elements, including carbon, whose mechanical properties exhibit the capacity for plastic deformation. The development and applications of theories of plasticity to engineering problems started with the pioneering work of Tresca [162], St. Venant [155], Levy [77], followed by seminal contributions of von Mises [102], Prandtl [161] and Reuss [139]. Today, the use of plasticity in the engineering disciplines can be divided into two categories:

- **Micromechanical theories**: Analyze the plastic deformation on the microscopic

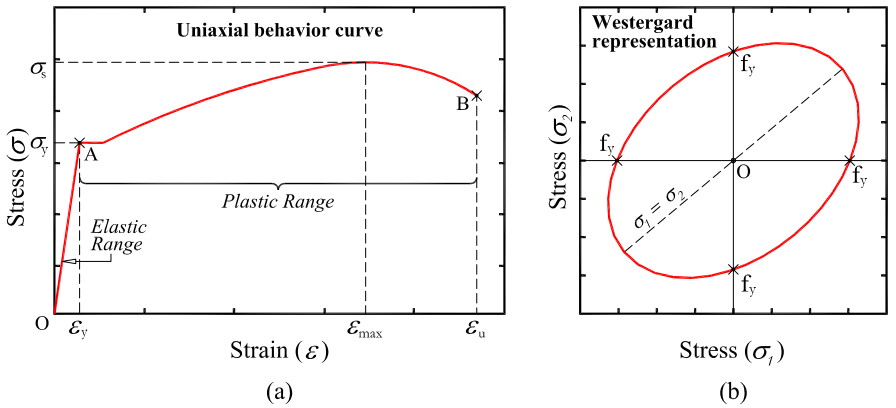

Figure 3.1 *Typical stress-strain relationship of steel.*

level and seek to explain the conditions in crystals and grains of metals leading to a plastic flow.

- **Macromechanical theories**: Also called the mathematical theories, describe plastic deformations phenomenologically, on the macroscopic level, and establish relations among the macroscopic mechanical quantities (such as stresses, strains, etc.). These relations are based on general principles of mechanics and on experimental observations.

A complete reference of the fundamentals of both theories is given in [72], where the reader shall be referred to, since in this work we will not abound on the subject.

The classical macro-mechanical theories of plasticity are based on the notions of a yield surface giving the yield condition, a hardening rule and on the stress-plastic strain relations of the given material. Such notions are used to formulate a material model for the calculation of the material response during plastic deformation.

Let us consider figure 3.1.a , where the idealized uniaxial *Strain-Stress* relationship of steel is depicted. Both Elastic ($\overline{OA}$) and Plastic ($\overline{AB}$) ranges can be clearly distinguished. Elastic range can be mathematically modeled by Hooke's Law for restoring forces, where the stress is linearly proportional to the strain, however, stresses larger than the elastic limit, or yield strength σ_y (point A) cause a permanent deformation known as plastic deformation or plasticity. Figure 3.1.b, on the other hand, is a typical representation in the Westergard stress space of the von Mises yield criterion [102], which applies best to ductile materials such as metals.

Within this work, mechanical behavior of steel will be reproduced using a plasticity model, combined with a von Mises yield function (fig. 3.1.b). Appendix B presents the equations of classical rate-independent plasticity used, within the classical framework of response function formulated as a projection onto plane-stress subspace, according to the work shown in [152].

3.1.2 Concrete

Concrete is a composite materials, since it is produced of a granular material (*aggregate*) embedded in a hard matrix of material (*cement*), however, it is a common practice

to model it as a simple *quasi-brittle geo-material*, even though its high non-linear performance is achieved due formation of micro-cracks and slipping among its aggregate particles [113].

Large interest given to mechanical properties of concrete comes from its wide application range to the construction field, which has led to several authors to develop constitutive models to represent its mechanical behavior. First developments of a *non-linear* fracture model within the FEM framework applied to concrete was carried by Hillerborg *et al* [62], Rots *et al* [144], Bazant *et al* [17] among others.

From there, in 1958, Kachanov [68] established the basis for classical damage theory, used at the time to represent debonding phenomena and softening behavior of mechanical parts. Also, work done by Lemaitre [75], Simo and Ju [154, 153], whose proposed *Continuum Damage Model*, and, Oliver *et al* [111], Chaboche [30, 31] o Ju [67], among others, have guaranteed the establishment of *Continuum Damage Mechanics* (*CDM* from now on), as a scheme to model *quasi-brittle* materials.

However, it was not until early eighty when *CDM* began being used to model concrete materials. Models proposed by Oller [113], Mazars and Pijaudier-Cabot [89], Lubliner *et al* [80], Jason *et al* [66], Tao [158], among others, were based upon *CDM* and classical plasticity theory.

Continuum damage models are defined by a degradation internal variable of both resistance and elasticity modulus. Such variable can be either a scalar or a tensor. In the case of an isotropic damage model, such internal variable is represented by a scalar [154, 111], hence, micro-cracking orientation is neglected, which leads to skip the effect of anisotropic damage, or the effect of material's anisotropy in the direction of the micro-crack.

Some models take into account anisotropy of both non-damaged and damaged material, in such cases, damage variable is then defined as a second of fourth ranked tensor [33, 27]. Using a higher ranked order tensor not only allows to consider damage orientation, but also allows to distinguish among damage mechanisms [85].

Since damage variable does not decrease during a loading process, a challenge for *CDM* was to be able to properly represent the opening and closing of cracks. Opening and closing of fractures, or the stiffness recovering upon loading reversal (visible when passing from tension into compression, or backwards) are typically presented during a cycling loading process, hence, in such cases it becomes necessary use a two-scalar damage model. Mazars *et al* [89] and Faria *et al* [51] presented damage models where damage variables due traction and compression are activated by yield function independent from each other.

An idealization of the concrete's expected behavior during a cycling loading process is depicted in figure 3.2.a. Loading process goes from traction into compression, and it starts in an elastic range $\overline{OA}$, once it reaches the maximum traction resistance A, a degradation of stiffness is activated in $\overline{AB}$, finally stress state B is reached and it starts an unloading process $\overline{BO}$. Now let us consider the unloading process has reached point O again, which is where real advantages of damage models with two scalar damage variables can be seen, whereas $d^+ \neq 0$, $d^- = 0$ (since they are independent from each other), and loading process along $\overline{OC}$ has an elastic behavior again, and until it reaches the maximum compression stress C compression degradation will not be activated. As expected, once loading process reaches stress C degradation of stiffness in compression is activated $\overline{CD}$ until it reaches D and it starts an unloading process again.

Now let us consider figure 3.2.b, where two yield surfaces *superimposed* are shown. In red, only traction state is depicted whereas in blue only compression state is shown. Any

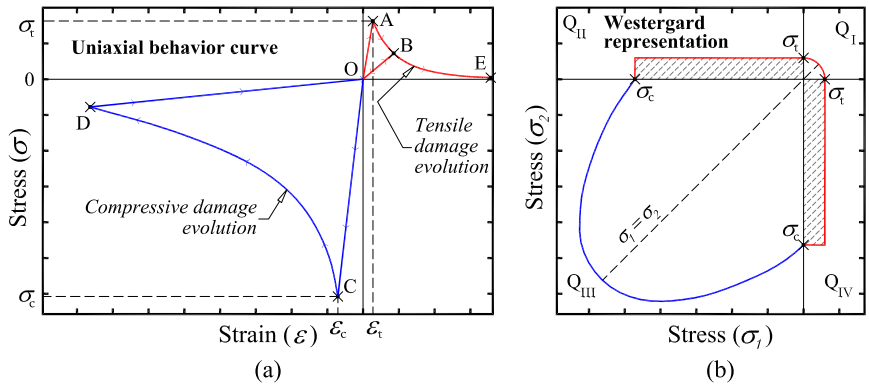

Figure 3.2 *Typical stress-strain relationship for concrete.*

yield function appropriated for concrete can be used, let us take for instance the work in [51], where Faria *et al* used a yield surface based on energy, whereas a modification of Drucker-Prager yield function is used in the compression case, finally results obtained were compared with experimental results got by Kupfer *et al* [74] showing good accuracy among the results.

At only tension states (in red figure 3.2.b) or in only compression state (in blue), results from models proposed by Mazars *et al* [89] and Faria *et al* [51] have shown good results [127], on the other hand, when loading process produces shear stresses and are both compression and traction stresses (hatched zone figure fig.3.2.b), such models exhibit some deficiencies due to its nature, which is to perform and additive decomposition of stress tensor $\boldsymbol{\sigma}$ to split it into its traction part $\boldsymbol{\sigma}^+$ and compression part $\boldsymbol{\sigma}^-$ and handle them separately.

Paredes in [127] proposes a modification of the damage model presented in [51] by Faria *et al*, where a variable for traction d^+ and another for compression d^- is being used. Such modification raises for *quadrants* II and IV of a given yield surface (traction and compression combined, see fig.3.2.b), and it consists on:

- Additive decomposition of the stress tensor $\boldsymbol{\sigma}$ pretends: *a*) check the position within the yield function (in principal stresses) of the current tensional state. In the case tensional state is either in *quadrant* II of IV, *b*) weight traction $\boldsymbol{\sigma}^+$ and compression stresses $\boldsymbol{\sigma}^-$ to obtain a *dominant* stress.
- Stresses $\boldsymbol{\sigma}^+$ and $\boldsymbol{\sigma}^-$ will not be treated separately, but the constitutive equation will be integrated usgin $\boldsymbol{\sigma}$ taking into account the *dominant* stress.
- *Constituive Damage* conditions detailed in [127] are applied.

In this work the damage model presented by Paredes with two scalar damage variables is used, reader may review [127] to abound on the subject, furthermore, appendix A reproduces such damage model from a mathematical point of view.

3.1.3 Masonry

In this subsection, masonry will be treated more carefully than previous simple materials, its failure mechanisms and more common characteristics will be pointed out. Also

proposal to estimate mechanical and constitutive characteristics from other authors will be reviewed.

Same as concrete, masonry is a composite material resulting of individual units laid (brick or rock) bound together by mortar. From now on, it will be implied that whenever it is referred to *masonry* it means *brick masonry*. Although in this work, a brief description of materials involved in composition of masonry walls is given, it is not pursued a complete description of them, a comprehensive description from a manufacturing and mechanical point of view is given in [38], also reader may consult [45, 59].

Masonry has been used as structural material, mainly as structural elements subjected to compressive forces, since ancient civilizations. For a long period they were built in accordance with empirical rules and designed only to support gravity actions using their massive dead load to stabilize structures against lateral forces from winds and earthquakes.

Masonry is usually made of rectangular masonry units bond together with mortar. The construction industry offers masonry units with a very large variety of shapes, materials and sizes. Constructive systems also change from one country to another. This aspect is what makes difficult to extrapolate results from type to type of masonry walls [65, 130].

However, if it is pretended to settle a damage criteria to predict non-linear behavior of masonry, its basic failure mechanisms under the most elemental loading conditions has to be studied, also, test to determine its mechanical properties has to be conducted. Models to represent such mechanical behavior to real scale for more common combination of materials have been driven by several authors, also large amount of test over masonry's simple materials (mortar and units) have been done in order to study the relationship once they are bond together as a masonry prism.

From this combination results an anisotropic material. Depending on the accuracy and the simplicity desired, masonry can be modeled using the following strategies [79].

- **Detailed Micro-Modeling**: Units and mortar in the joints are represented by continuum elements whereas the unit-mortar interface is represented by discontinuous elements.

- **Simplified Micro-Modeling**: Expanded units are represented by continuum elements whereas the behavior of the mortar joints and unit-mortar interface is lumped in discontinuous elements.

- **Macro-Modeling**: Units, mortar, and unit-mortar interface are bonded in the continuum.

- **Homogenized Modeling**: This strategy is placed midway between micro-modeling and macro-modeling, since it consists in obtaining macro-constitutive laws starting from the micro-constitutive law of the constituents and the texture of the masonry.

Advantages and disadvantages of each approach are discussed in [78, 79, 130], in this work we just must point out that it will be uses a *Macro-Modeling* approach, since it is more practice oriented due to the reduced time and memory requirements as well as for the implied user-friendly mesh generation. This modeling scheme is the most valuable when a compromise between accuracy and efficiency is needed.

The Unit or Brick

Some authors use the word *brick* referring to a kind of unit smaller than *block*, although *block* is usually used also referring to units made of concrete. In the present work the work *brick* will be used as a synonym of *masonry unit* regardless its size or material.

Bricks are made of clay, shale, fire clay or a mixture of them, and shaped by molding, pressing or extrusion, most common type of units are: clay brick, concrete masonry units and clay silicate masonry unit. From a structural point of view, the compressive strength of the unit is the most important controlling factor [59, 65], whose value shows a wide variation, depending on the material type of masonry unit, with typical ranging from 5 to 100MPa [129], commonly, the strength of concrete masonry units varies from 10 to 40MPa, and sand-lime and clay masonry units from 8 to 50 MPa.

Compressive strength of masonry units is evaluated from a direct compression test, usually referred to the average gross area perpendicular to the direction of the load [41]. The distinct testing methods will not be discussed in the present work, only must be pointed out that they do not only influence the compressive strength, but also alter the mode of failure of the masonry unit [38, 65]. The specifications `ASTM C-67` and `ASTM C-140` [41], the New Zealand standard `NZS 3102:1983` [156], the Mexican `NMX-C-036-ONNCCE-2004` [121], or the Spanish code `NBE FL-90` [36], among others, present a detailed procedure for testing clay and concrete masonry units, also Crisafulli in [38] presents a modification to such testing procedures.

Another important mechanical property of masonry units is its tensile strength. Such property can be measured using three different tests: flexural test, splitting test (or indirect tension) and direct tension test. Advantages and disadvantages of such tests are listed in [38]. Test conducted by Hamid and Drysdale [58] showed that the uniaxial tensile strength f'_{bt} may be related to the uniaxial compressive strength f'_{bc} according to the following expression:

$$f'_{bt} = c\sqrt{f'_{bc}} \qquad \begin{cases} c = 0.28 & \text{for uniform tensile test} \\ c = 0.34 & \text{for splitting test} \\ c = 0.69 & \text{for flexural test} \end{cases} \tag{3.1}$$

According to Crisafulli [38] the splitting test seems to be the most reliable measure of the tensile strength when masonry is subjected to in-plane forces. This is the case of masonry panels surrounded by steel or reinforced concrete frames subjected to gravity or lateral in-plane loads.

Strains-Stress relationship of unit mortars depends significantly on their constitutive materials. The elasticity modulus of masonry units present a wide variation and basically depends on the type of material and the compressive strength f'_{bc}. There is no standardized method to evaluate the modulus of elasticity and usually it is adopted as the secant modulus of elasticity from zero stress to one third of the material strength. About Poisson's ratio of masonry units there is an insufficient amount of information, since parameter ν_b is not usually investigated by researches. Atkinoson *et al* [11] and McNary and Abrams [90] reported ranging from 0.13 to 0.22 for three different types of masonry units and Ameny *et al* [9] found values ranging from 0.07 to 0.14 testing dry-pressed masonry.

The Mortar

Mortar is a mixture of cementitious materials, aggregates and water used to bind masonry units into a structural mass. Fresh mortars must be workable, and when hardened, the mortar must provide bond between the masonry units and strength to bear loads. Mortar mixes are usually indicated in parts of volume, namely, for masonry with loadbearing proposes [59] mortar should be a cement:lime:sand mix whose proportions may vary according to a given construction code. There are many cementitious material for making mortars: Portland cement and lime mixed in adequate proportions are frequently used.

Opposite to masonry units, most relevant property of mortars is not its compressive strength, although mortar's standard of quality is based upon such property. Deformability and adherence, on the other hand, have a significant role to play in masonry's overall performance. Mortar deformability has direct relationship with total deformation of a masonry wall and the compressive strength under vertical loads, while adherence frequently defines shear strength [65].

The compressive strength of the mortar f'_{jc} usually ranges from 5 to 20 MPa and it depends on many factors, such as, lime content, characteristics of aggregates, cement-water ratio and curing process. The determination of compressive strength is conducted using a 50mm cube (`ASTM C 109`) or cylinders of different dimensions (usually length-diameter ratio equal to 2.0) [41] although authors like Crisafulli [38] recommends the use of cylinders of 75x150mm because of the handling of specimens is easier and the variation of the results is less significant. The standard test method `CRD-C 260-01` [41] covers the determination of tensile strength of hydraulic cement mortar employing the briquette specimen.

Stress-Strain relationship obtained from mortar compressive test is, in a general sense, similar for those for unconfined concrete [9, 11, 90]. Also it may be observed that lime has an important effect on the mortar behavior, modifying the compressive strength as well as the elasticity modulus decreases when content of lime increases [38].

Compression Strength in Masonry

Masonry structures present good behavior when they are stressed in compression, additionally, when the loading direction is perpendicular to bed joints they presents linear behavior at a low force level. As the compressive load increases material behaves non-linearly and vertical cracks appear at a force level smaller than the compressive capacity (see figure 3.3).

Compressive strength is one of the most important parameters to quantify the characteristics of masonry, and has been extensively studied for researches and engineers. This parameter is also commonly used to establish the allowable flexural and shear stresses. The numerous possible combinations of mortars, masonry units and mortar joint thickness, lead to an ample variation of the compressive strength.

Behavior and failure mechanisms of masonry under axial load are highly dependent on interaction between its units and mortar. Interpretation of this dependence is due the difference stress-strain response on component materials, i.e., while being under the same stress level, the less deformable material (generally the masonry unit) restricts transversal deformation on the most deformable material inducing transversal compressive stresses in it. On the other hand, in the less deformable material, transversal stresses are introduced reducing its compressive strength [65]. Figure 3.4.a-d shows a typical stress-strain distribution of a masonry pile using the FEM.

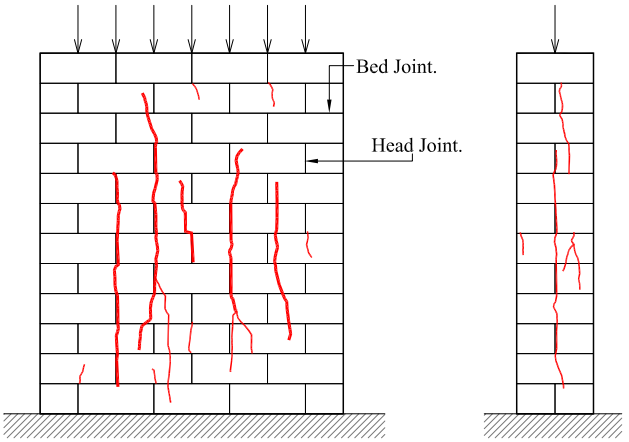

Figure 3.3 *Typical failure mode of masonry under compression loading.*

Compressive failure mechanism is manifested through vertical cracks along the units, when this vertical cracking becomes excessive a brittle failure on the masonry appears. For units with low compressive strength failure is produced by crushing on them. Mortar crushing does not produce failure when only axial stresses are presented, since when mortar crushes, it is still bonded by friction to masonry units. Although in thin masonry elements, mortar crushing may cause instability conditions [65].

The failure mechanisms previously described is valid for masonry panels subjected to compressive loading in the perpendicular direction to the bed joints. When the compressive load is applied in the direction parallel to the bed joints, failure occurs by debounding along the bed joints due the lateral spreading of the panel [125].

Figure 3.4.e shows a typical stress-stress response under uniaxil compression for mortar, masonry units and the composite material. It can be observed that the strength of masonry in compression is smaller than the nominal compression strength of the units as given by a standard compressive test. On the other hand, the masonry strength may greatly exceed the cube crushing strength of the mortar used in it [59].

Masonry prisms are primarily used to evaluate the strength, they are small masonry walls built one or two bricks in length and three or more bricks in height, tested under a compressive load perpendicularly applied to the bed joint. Many consideration have been proposed by several authors regarding the proportion length l_p, height h_p and thickness t_p such walls should have, in [38] a study has been carried out on the matter.

Shear Stress in Masonry

The adequate evaluation of shear strength is required for the design of masonry panels subjected to lateral loads introduced by action of the wind or earthquake. Shear stress is usually combined with compressive stress produced by gravity loads or other actions. Consequently, the case of pure shear has no practical application and the shear strength of masonry is usually investigated considering the effect of compressive stress acting in normal direction to the bed joints.

Failure mechanism of masonry under shear stress usually happens as sloped cracks along the joints, which depends on the resistance of the masonry unit and its bonding

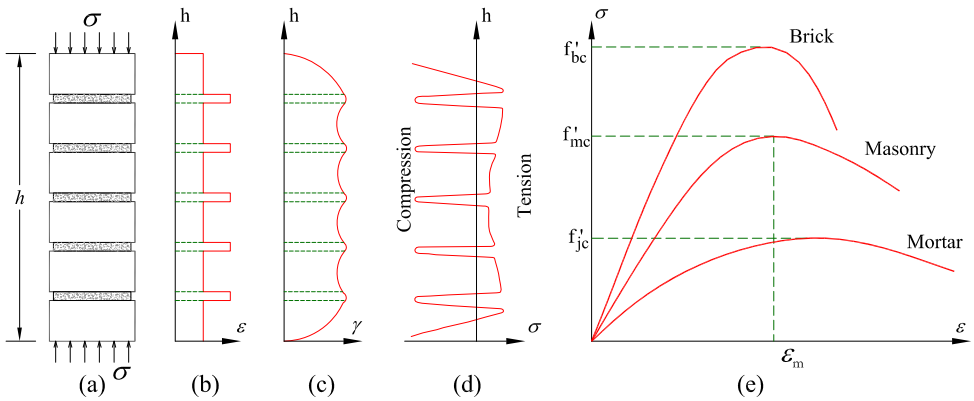

Figure 3.4 *Stresses and strain distribution of a pile of bricks under compression stress.*

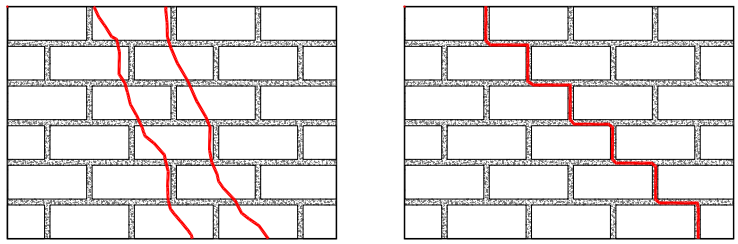

Figure 3.5 *Modes of failure of masonry panels subjected to shear.*

with mortar. Typically happens that for low resistance masonry units, cracks will cross indistinctly throughout masonry unit or mortar (fig. 3.5.a), however, for walls made of masonry units with high resistance and good bonding with mortar, cracks appears throughout joints [65] (fig. 3.5.b). Hence, the resistance and bonding skills of the mortar play a very important role while determining the shear strength of a masonry wall.

The shear behavior has been investigated by many researches. In 1873 Bauschinger (as reported by Dialer [43]) apparently conducted the first test to investigate the strength of masonry subjected to shear loading. Nowadays, different testing methodologies are used that go from simple prisms made with two bricks to full-scale masonry walls subjected to biaxial load.

The simplest test procedure (direct shear test) consists of testing prism built with two, three or four masonry units (fig. 3.6.a). The compressive load P is applied first and then the specimen is subjected to a second load V, which induces increasing shear stress up to the failure [38]. Tests of masonry panels (fig. 3.6.b) are a more realistic procedure to investigate the shear strength, and different methods are employed for the application of the loads. Studies to determine shear strength also have been conducted by Meli and Reyes [96] and Hernández and Meli [61] introducing stresses in different directions using walls with different aspect ratio (fig. 3.6.c). Another method often used

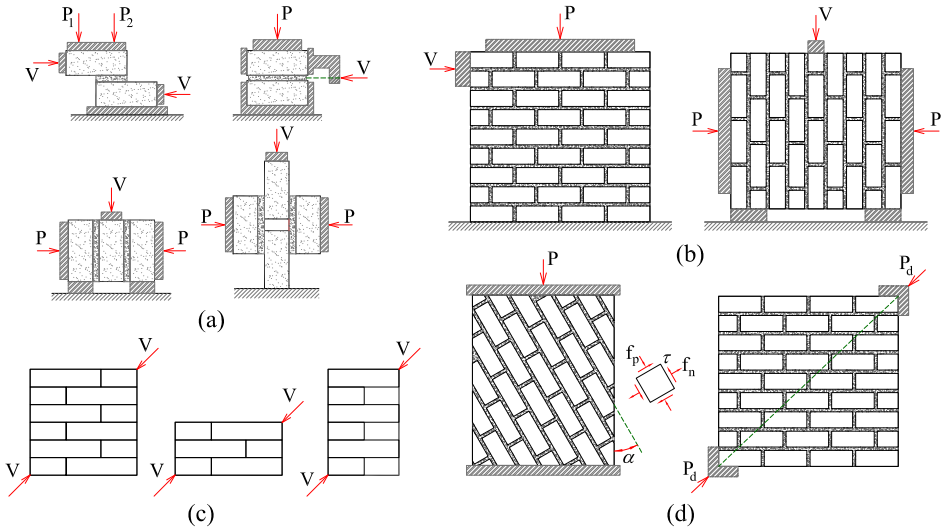

Figure 3.6 *Typical tests of masonry panels to determine shear strength.*

in experimental work is represented in figure 3.6.d. In this case small masonry panels are tested under compressive loading, but the angle α between the bed joint direction and the applied load is different from 90°. Consequently, shear and axial stresses are introduced in the mortar joints.

Tensile Stress in Masonry

Direct tensile strength can arise in masonry as a result of in-plane loading effects. There may be caused by wind, by eccentric gravity loads, by thermal or moisture movements of by foundation movements. Tensile strength of masonry particularly along bed joint direction, is low and variable and therefore is not generally relied upon in structural design [59]. Nevertheless it is essential that there should be adhesion between units and mortar, and it is necessary to be aware of those conditions, since tensile strength of masonry is primarily controlled by the bond strength developed at the mortar brick interface. Nature of tensile strength is similar to the shear bond: it relies on bond strength of masonry's components.

Different type of failures may occur according to the direction of the tensile load, the relative magnitude of the bond resistance or the tensile strength of the brick. Figure 3.7a,b show two typical crack patterns for masonry subjected to tensile stresses parallel to the bed joints. In the first case (a), cracks occur through brick in alternate courses and the tensile strength is controlled by the tensile strength of the masonry units. On case (b), cracks do not affect bricks and only occurs along the mortar joints. The mode of failure, for tensile load acting perpendicularly to the bed joints, usually occurs by debonding of the mortar-brick interface (fig. 3.7.c), however, the tension failure of the brick could also occur as shown in figure 3.7.d.

Different test techniques have been used to determine the tensile strength of masonry. The test of masonry panels under direct tensile strength present some difficulties, its variability have to be kept in mind, and it should only be used with great caution.

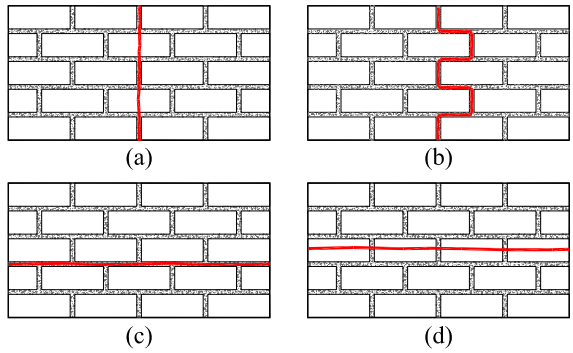

Figure 3.7 *Mechanism of failure of masonry subjected to direct tension.*

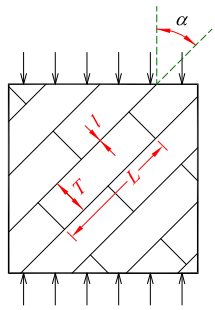

$$\frac{E_m}{E_b} = \frac{[\,\gamma\cos\alpha + \sin\alpha + \beta\,(\sin\alpha + \cos\alpha)]}{\eta\cos\alpha + \sin\alpha + (\beta/\eta)\,(\cos\alpha + \sin\alpha)}$$

$$\text{if } \alpha = 0° \;;\; \frac{E}{E_b} = \frac{\gamma + \beta}{\gamma + (\beta/\eta)} \;;\; \beta = \frac{t}{T}, \quad \gamma = \frac{L}{T}$$

$$\text{if } \alpha = 90° \;;\; \frac{E}{E_b} = \frac{1 + \beta}{1 + (\beta/\eta)} \;;\; \eta = \frac{E_j}{E_b}$$

Figure 3.8 *Elasticity modulus of masonry along different directions.*

Direct tensile strength is typically about 0.4 N/mm^2 [59].

The splitting test is another typical test used to define the modulus of rupture, or flexural tensile strength (out-of-plane stress). Has great practical importance, since the same factors that influence the direct tensile bond apply to the development of flexural tensile strength. If a wall is supported only at its base and top, its lateral resistance will depend on the flexural tensile strength developed across the bed joints If it is supported also on its vertical edges, lateral resistance will depend also on the flexural strength of the masonry in the direction across the header joints. Tensile strength across header joint is typically about three times as across the bed joint [59], and for clay units ranges from 0.8 up to 2.0 N/mm^2 in the stronger direction (header direction), hence, strength across bed joint's direction is about one-third of this value [59]. The tensile strength obtained from the splitting test, f'_{mt} is evaluated in eq. 3.2 based on the linear elastic theory.

$$f'_{mt} = \frac{2P}{\pi A_t} \tag{3.2}$$

3.2 Macro-Modeling of Masonry

3.2.1 Mechanical Properties

Masonry is generally treated as a linear elastic material, although tests indicate that the stress-strain relationship is approximately parabolic. Various formulae have been suggested for the determination of Young's modulus. This parameter is rather variable even for nominally identical specimens, and as an approximation several researches have derived expressions assuming linear elastic behavior for both materials and equating the compressive deformation of masonry to the sum of the deformation of the brick and mortar joints. Although the most common approach is to relate the modulus of elasticity E_m of masonry with its compressive strength f'_{mc}. Most of the results ranges from $400f'_{mc} < E_m < 1000f'_{mc}$. To name few authors, Hendry [59] proposes eq. 3.3, San Bartolome [146] at the Colorado Building Code proposed eq.3.4, and Meli and Reyes [96] proposed eq. 3.5.

$$E_m = 700 f'_{mc} \tag{3.3}$$

$$E_m = 500 f'_{mc} \tag{3.4}$$

$$E_m = \begin{cases} 450 f'_{mc} & \text{for clay units} \\ 650 f'_{mc} & \text{for concrete units} \end{cases} \tag{3.5}$$

Previous values of masonry's elasticity modulus E_m, are obtained from axial compression acting normal to the bed joints f'_{mcy}, in the normal direction of the header joint, however, it would be necessary to consider the different amount of material's joint density causing the masonry orthotropy.

Meli in [91] proposes an expression to determine the elasticity modulus of masonry in a given orientation, determined using mechanical properties of the components of a two-phase composite material (fig. 3.8). Mechanical properties of components shall be evaluated according to eq. 3.6.

$$\begin{aligned} E_j &= 250 f'_{jc} && \text{for mortar.} \\ E_b &= 200 f'_{bc} && \text{for clay units.} \\ E_b &= 570 f'_{bc} && \text{for block units.} \end{aligned} \tag{3.6}$$

The shear modulus of masonry G_m can be calculated from deflection measurement made on masonry panels. It has been observed that the shear modulus depends on the type of brick, mortar class and the moisture content when laying. For approximate calculations, it can be assumed that masonry behaves as an isotropic material (in terms of deformational properties), thus:

$$G_m = \frac{E_m}{2(1+\nu_m)} \tag{3.7}$$

This expression indicates that the ratio G_m/E_m varies from 0.40 to 0.45 for usual values of Poisson's ratio, ranging from 0.10 to 0.25. Although different authors reported contradictory conclusions [38].

3.2.2 Failure Envelope

From a computational-cost point of view, the only viable strategy to perform the analysis of masonry structures built from a large number of units and joints is using macro-models. In such models average stress-strain relationships in the composite material are established.

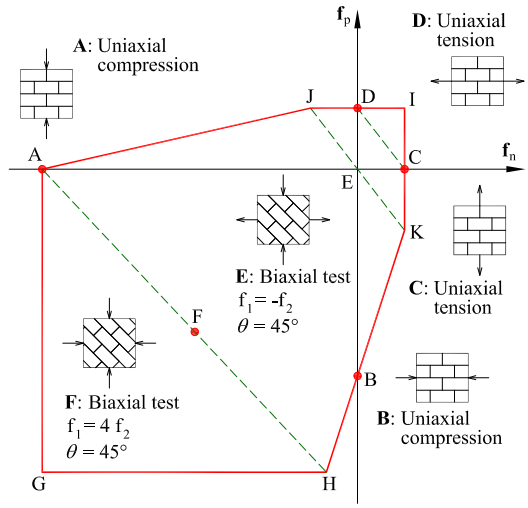

Figure 3.9 *Masonry yield function proposed by Dhanasekar et al [42].*

As an attempt to develop specific macro-models for the analysis of masonry structures, let us first consider the work carried out by Dhanasekar *et al* in [42], to approximate a failure surface (fig 3.9) using a representation in the space $f_p - f_n$, where f_p represents the stress parallel to the bed joint, f_n is the stress normal to the bed joint, using f_1 and f_2 as the principal stresses and their orientation referred to the bed joints θ. Dhanasekar *et al* proposed six different tests, and also proposed a complete description of the biaxial stress-strain relationship for brick masonry, considering anisotropic behavior, although the criterion developed by Dhanasekar *et al* is essentially phenomenological and it is not directly based on physical considerations [38].

Now let us consider work done by Lourenço [79] and Pelà [130], where composite yield criterion suitable for modeling anisotropic materials under plane stress conditions are presented, in such cases individual yield criterion for both tension and compression have been considered, according to different failure mechanisms (figure 3.10 and 3.11). Then, proposed yield criterion are compared with the most complete set of strength data for biaxially loaded masonry walls carried out by Page [125, 126].

Although both cases miss to reproduce the uniaxial compressive strength parallel to the bed joints, globally, good accuracy can be notice from such yield criterion.

Lourenço in his work [79] even proposed the required information to define the anisotropic composite yield criterion. Necessary data to plot such anisotropic damage yield function and to evaluate damage evolution is shown below. Typical position of the natural tests and non-standard tests proposed by Lourenço are shown in figure 3.16.

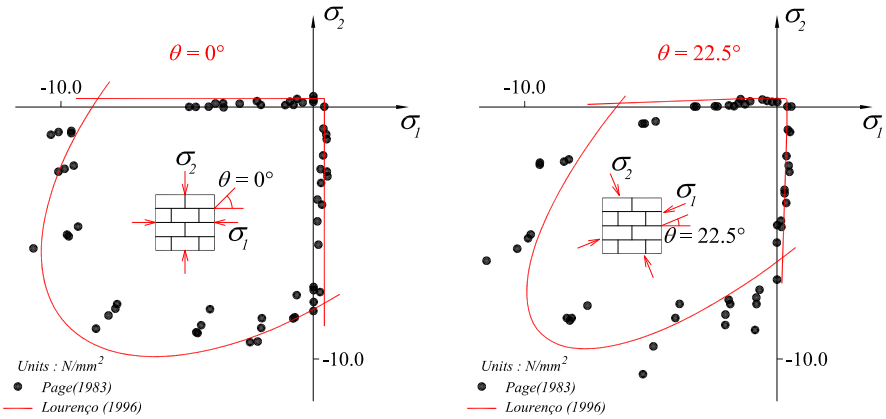

Figure 3.10 *Comparison among plasticity model of Lourenço [79] and Page [125, 126].*

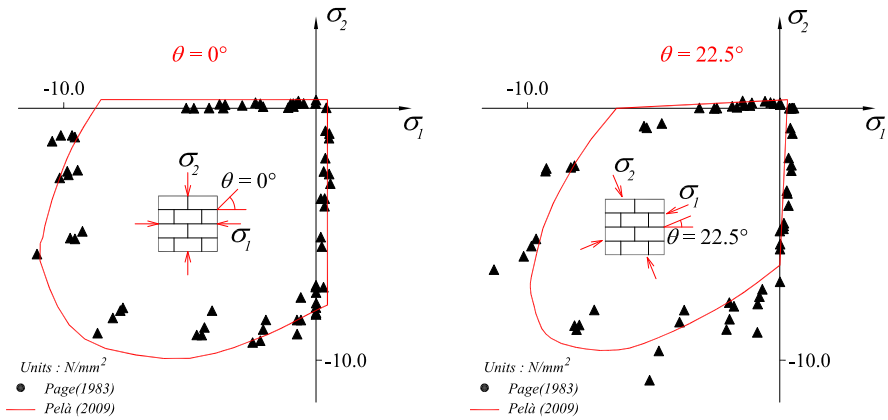

Figure 3.11 *Comparison among plasticity model of Pelà [130] and Page [125, 126].*

1. Four natural tests to calibrate the composite model. *a*) uniaxial tension parallel to the bed joints f'_{mtx}, *b*) uniaxial tension normal to the bed joints f'_{mty}, *c*) uniaxial compression parallel to the bed joints f'_{mcx} and finally, *d*) uniaxial compression normal to the bed joints f'_{mcx}

2. Three additional tests are required to fully calibrate the yield criterion. Parameter α, which weights the shear stress contribution to tensile failure. Parameter β, which controls the coupling between normal stress values in the case of compressive failure, and parameter γ, which weight the shear stress contribution to compressive failure. Such parameters are evaluated as follow:

$$\alpha = \frac{1}{9}\left(1 + 4\frac{f_{mtx}}{f_\alpha}\right)\left(1 + 4\frac{f'_{mty}}{f_\alpha}\right)$$

$$\beta = \left[\frac{1}{f_\beta^2} - \frac{1}{(f'_{mcx})^2} - \frac{1}{(f'_{mcy})^2}\right] f'_{mcx} f'_{mcy} \tag{3.8}$$

$$\gamma = \left[\frac{16}{f_\gamma^2} - 9\left(\frac{1}{(f'_{mcx})^2} + \frac{\beta}{f'_{mcx} f'_{mcy}} + \frac{1}{(f'_{mcy})^2}\right)\right] f'_{mcx} f'_{mcy}$$

3. The four independent fracture energies, two under tensile load (G_{ftx}, G_{fty}), and two under compressive load (G_{fcx}, G_{fcy}), also the peak strain compression would be required κ_p.

3.2.3 Properties of the Unit-Mortar Interface

A salient feature of masonry is its softening behavior, which is a typical non-linear response of quasi-brittle materials. Softening is a gradual decrease of mechanical resistance under continuous increase of deformation and it is due to a process of progressive internal crack growth.

Masonry's softening behavior is typically attributed to the heterogeneity of its components or defects on them. Although the non-linear response of the unit-mortar interface has a relevant influence on masonry's mechanical behavior. For continuum macromodels, the effect of the interface playing an important role on masonry's post-peak behavior will not be directly included, because the unit and mortar geometries are not discretized. However, such effect can be taken into account through the fracture energy in the material.

Fracture energy, in its general form, is defined as the integral of the $\sigma - \delta$ response diagram (mode I), or the $\tau - \delta$ diagram for shear failure mode (mode II), although Van der Pluijm in [167] defined it as a function of the crack length along the unit-mortar interface of the masonry, i. e. is the amount of energy to create a unitary area of a crack along the unit-mortar interface.

Mode I Failure

Van der Pluijm [167] carried out deformation-controlled tests in small specimens of solid clay and calcium-silicate units (fig. 3.12.a). Such tests resulted in an exponential tension softening curve with a mode I fracture energy G_f^I ranging from 0.005 to 0.02 $[Nmm/mm^2]$ for a tensile bond strength ranging from 0.30 to 0.90 $[N/mm^2]$, according to the unit-mortar combination.

A closer observation of the cracked specimens revealed that the bond area was smaller than the cross sectional area of the specimen (fig. 3.13.a). The subsequently so-called net bonding surface seems to concentrate in the inner part of the specimen. For a wall the net bonding surface must be corrected according to a smaller number of edges. Values given in figure 3.13.b refer to the real cross section of a wall and result from an extrapolation of the measured net bonding surface of the specimen to the assumed net bonding surface of the wall, neglecting any influence of the vertical joints.

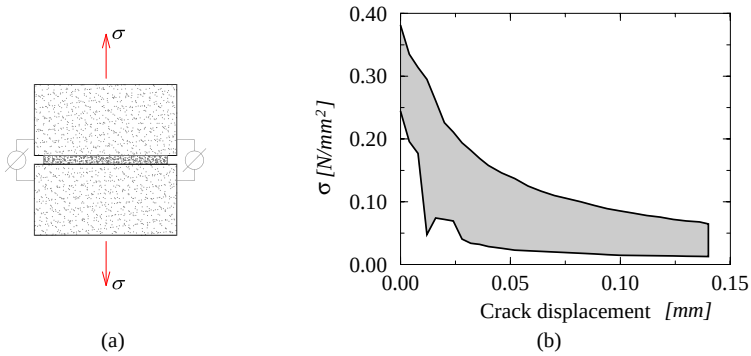

Figure 3.12 *Tensile bond behavior, Van der Pluijm [167].*

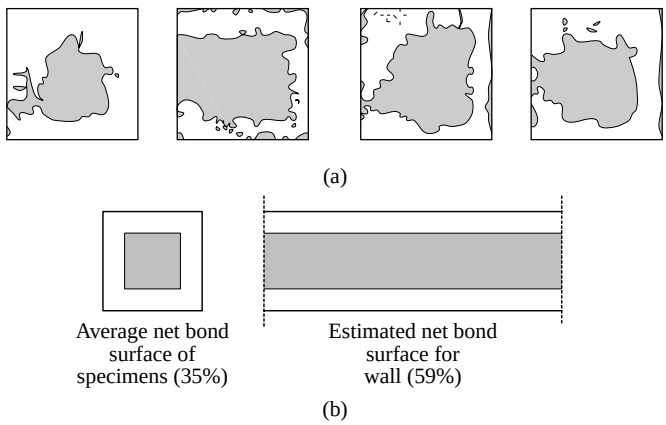

Figure 3.13 *Tensile bond surface, Van der Pluijm [167].*

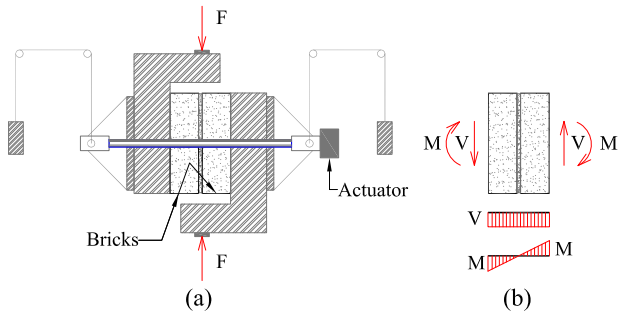

Figure 3.14 *Test set-up to obtain shear bond behavior, Van der Pluijm [167].*

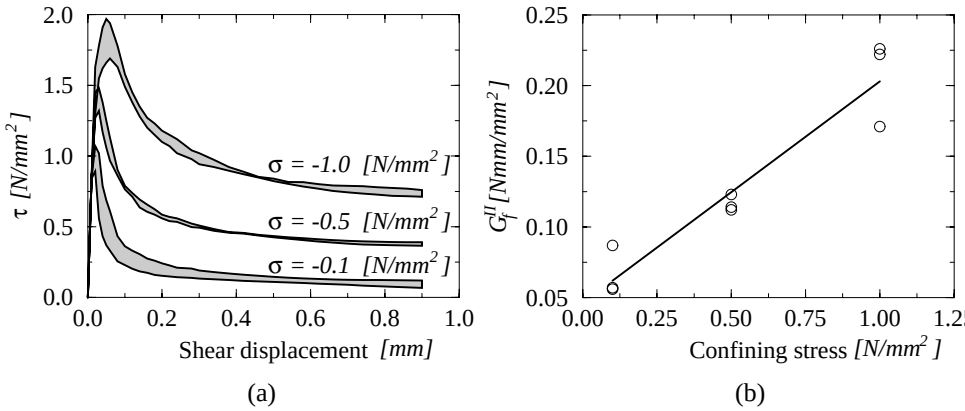

Figure 3.15 *Typical shear bond behavior of the joints for solid clay units, Van der Pluijm [167].*

Mode II Failure

An important aspect in the determination of the shear response of masonry joints is the ability of the test set-up to generate a uniform state of stress in the joints. This objective is difficult because the equilibrium constrains introduce non-uniform normal stresses in the joint.

Van der Pluijm in [168] presented the most complete characterization of the masonry shear behavior, for solid clay and calcium-silicate units. Test set-up shown in figure 3.14.a permits to keep a constant normal confining pressure upon shearing. Confining stresses were applied with three different levels: 0.1, 0.5 and 1.0 $[N/mm^2]$.

The experimental result yield an exponential shear softening diagram (fig. 3.15). The area defined by the stress-displacement diagram is named mode II fracture energy G_f^{II}, with values ranging from 0.01 to 0.25 $[Nmm/mm^2]$ for initial cohesion values ranging from 0.10 to 1.80 $[N/mm^2]$. The value of the fracture energy depends also on the level of the confining stress (fig. 3.15.b).

The initial internal friction angle ϕ_0, associated with the Mohr-Coulomb friction model, ranges from 30° to 50° for different unit-mortar combination. The residual inter-

nal friction angle ϕ_r seems to be approximately equal to 37°. The dilatancy angle ψ for low confining pressure falls in the range from 11° to 35 ° depending on the roughness of the unit surface. For high confining pressures ψ decreases to zero due to the smoothing of the shared surfaces.

3.2.4 Remarks Regarding Mechanical and Non-Linear Response

In this section, the use of existing experimental and analytical data, plus the use of a masonry designing code (`Normas Técnicas Complementarias para Diseño y Construcciones de Estructuras de Mampostería, 2004 [6]`) will be required as an attempt to reproduce mechanical and non-linear behavior of generic masonry. Points 1 to 5 down below, show a guidance to plot a orthotropic yield function, point 6 is a brief description to determine mechanical properties of masonry, and finally, point 7 treats post-peak response of masonry in a diffused form.

Scheme proposed by Lourenço [79] to plot an anisotropic damage yield function seems ideal, however, scarcity of experimental information makes it useless for practical applications.

1) Typically there are two forms of determining the value f'_{mcy}. The first one: is trough a standard compressive analysis of a pile of masonry, containing the given unit and mortar, or the second: once the uniaxial compressive strength of unit f'_{bc} is known, and also the proportion of cement:lime:sand which will compose the mortar, `Table 2.6` from reference [6] can be used.

2) Reference [6] does not allude a ratio among f'_{mcx} and f'_{mcy}. It is so, in this work we propose to use equation 3.9 based on results of Lourenço [79] and Pelà [130].

$$\begin{aligned} \frac{f'_{mcx}}{f'_{mcy}} &= 1.08 \text{ for solid brick masonry} \\ \frac{f'_{mcx}}{f'_{mcy}} &= 4.00 \text{ for hollow brick masonry} \end{aligned} \tag{3.9}$$

3) Both f'_{mtx} and f'_{mty} tensile strength are considered null according to `section 2.8.4` of [6]. However, we shall use a conservative value got from direct tensile tests. As proposed by Hendry [59] it could be $f'_{mty} = 0.13N/mm^2$ and $f'_{mtx} = 0.40N/mm^2$ used regardless the type of unit or mortar.

4) Lacking experimental information, or guidance from reference [6] to obtain necessary parameters α, β and γ to settle Lourenço's [79] anisotropic yield criterion model, it is decided to use only-compression model proposed by Faria *et al* [51]. Where $K = 0.118$ for solid brick masonry, whereas $K = 0.072$ for hollow brick masonry based on results from Pelà [130]. To model only-tension case a modified Mohr-Coulomb model will be used [113] (such model also will be used for both tension-compression and compression-tension cases, see appendix A). Shear strength under compression case f_{12}^- will be defined equal to V_m^* (see `Seccion 2.8.2` [6]). Also, resistance f_{12}^+ will be considered equal to f'_{mty}.

5) To model masonry as a homogeneous material, a diagonal fourth order tensor is assumed for each transformation tensor, according to Batten [23], Oller *et al*

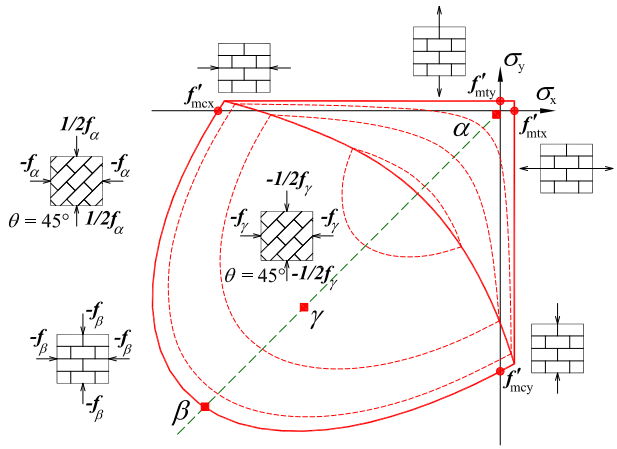

Figure 3.16 *Typical position of the natural tests and non-standard tests proposed by Lourenço [79].*

[115, 118], and Car *et al* [25, 26], and used by Pelà [130] to model masonry as an orthotropic material.

6) Masonry's elasticity modulus E_{mx} will be determined according to `Section 2.8.5` of reference [6]. Elasticity modulus in y direction (E_{my}) will be determined according to Meli [91] (fig. 3.8), namely:

$$E_m = E_b \frac{\gamma\, cos\,\alpha + sin\,\alpha + \beta(sin\,\alpha + cos\,\alpha)}{\eta\, cos\,\alpha + sin\,\alpha + \dfrac{\beta}{\eta}(cos\,\alpha + sin\,\alpha)} \tag{3.10}$$

where E_b is the elasticity modulus of the masonry unit, E_j is the elasticity modulus of the mortar joint (see fig. 3.8) defined according to equation 3.6. $\alpha = 0°$, β, γ and η are defined as seen in figure 3.8. Finally, Poisson's ratio ν_{12} and ν_{21} values ranges from 0.10 to 0.25.

7) In reference [6], or in any other designing code for that matter, does not exist any allusion to fracture energy, and due to the uncertainty surrounding such value, it is only recommended to have in mind section 3.2.3 of this work, and choose a value for G_f or G_c from an initial calibration using experimental results.

3.3 Orthotropic Yield Criterion

In this section will be reproduced the adopted scheme to model the masonry as an orthotropic material, which is an *implicit* definition of the orthotropic yield function based on the transformed-tensor method proposed by Oller *et al.* [116]. The reader may abound in the subject consulting reference [130] where an extensive review of the state of the art has been carried out, also, the underlying principles, numerical implementation

and numerical examples of concepts reproduced in this section have been presented in reference [130].

The objective of the approach proposed by Oller *et al.* [116] is to adjust an arbitrary isotropic yield criterion to the behavior of an anisotropic material. The transformed-tensor method is based on assuming the existence of a *real anisotropic space* of stresses $\boldsymbol{\sigma}_{ij}$ and a conjugate space of strains $\boldsymbol{\varepsilon}_{ij}$, such that each of these spaces has its respective image in a *fictitious isotropic space* of stresses $\overline{\boldsymbol{\sigma}}_{ij}$ and strains $\overline{\boldsymbol{\varepsilon}}_{ij}$ respectively (figure 3.17). The corresponding relationships among them are;

$$\overline{\boldsymbol{\sigma}}_{ij} \overset{\text{def}}{=} A^{\sigma}_{ijkl}\boldsymbol{\sigma}_{kl} \qquad ; \qquad \overline{\boldsymbol{\varepsilon}} \overset{\text{def}}{=} A^{\varepsilon}_{ijkl}\boldsymbol{\varepsilon}_{kl} \tag{3.11}$$

where A^{σ}_{ijkl} and A^{ε}_{ijkl} are the transformation tensors, for stress and strain, respectively, relating the fictitious and real spaces. These four-rank tensors embody the natural anisotropic properties of the material.

The stress transformation tensor A^{σ}_{ijkl} is a result of the properties of the materials and the shape of the yield surface, namely,

$$A^{\sigma}_{ijkl} = \left(B^{\sigma}_{ijkl}\right)^{-1} = \left(W_{ijrs}\alpha_{rskl}\right)^{-1} \tag{3.12}$$

where, W_{ijrs} contains information on the yield stress along every axis of orthotropy, and α_{rskl} is the shape adjustment tensor (section 6 ref. [116]).

The relationship between the stress and strain transformation tensors can therefore be expressed as

$$A^{\varepsilon}_{rsmn} = \left[\overline{C}^{\sigma}_{rsij}\right]^{-1} A^{\sigma}_{ijkl}C^{\sigma}_{klmn} \tag{3.13}$$

where $\overline{C}^{\sigma}_{rsij}$ and C^{σ}_{klmn} represent the constitutive tensor in the fictitious and real space, respectively.

The present formulation allows the solution for the behavior of a point in the real anisotropic solid by transporting it into a fictitious isotropic space, in which the classical isotropic formulation is used. It is thus possible to use the classical isotropic formulation of small-deformation plasticity for the solution of an anisotropic plasticity model. In this context, the anisotropic yield function F^{σ} and the anisotropic plastic potential G^{σ} are defined respectively in equation3.14.

$$\begin{aligned} F^{\sigma}(\sigma_{ij}, q^m_s) &\equiv \overline{F}^{\sigma}(\overline{\sigma}_{ij}, \overline{q}^m_s) = 0 \\ G^{\sigma}(\sigma_{ij}, q^m_s) &\equiv \overline{G}^{\sigma}(\overline{\sigma}_{ij}, \overline{q}^m_s) = K \end{aligned} \tag{3.14}$$

where q^m_s represents a set of m internal variables, and K is a constant. The plastic flow rule is defined by the chain rule as [115]

$$\dot{\bar{\varepsilon}}^p_{rs} = A^{\varepsilon}_{rsij}\dot{\varepsilon}^p_{ij} = A^{\varepsilon}_{rsij}\frac{\partial G^{\sigma}}{\partial \sigma_{kl}} = A^{\varepsilon}_{rsij}\frac{\partial \overline{G}^{\sigma}}{\partial \overline{\sigma}_{kl}}\frac{\partial \overline{\sigma}_{kl}}{\partial \sigma_{kl}} = \dot{\lambda}A^{\varepsilon}_{rsij}\overbrace{\frac{\partial \overline{G}^{\sigma}}{\partial \overline{\sigma}_{kl}}}^{\overline{R}_{kl}}A^{\sigma}_{klij} = \dot{\lambda}\tilde{\mathbf{R}}_{rs} \tag{3.15}$$

The direction tensor of the classical flow rule in an isotropic space $\overline{R}_{ij}$ is modified by A^{σ}_{ijkl} in order to obtain its analogue in the anisotropic space, $R_{ij} = \overline{R}_{ij}A^{\sigma}_{klij}$. The transformation $\tilde{\mathbf{R}}_{rs} = A^{\varepsilon}_{rsij}R_{ij}$ introduces the influence of anisotropic elasticity on anisotropic yielding.

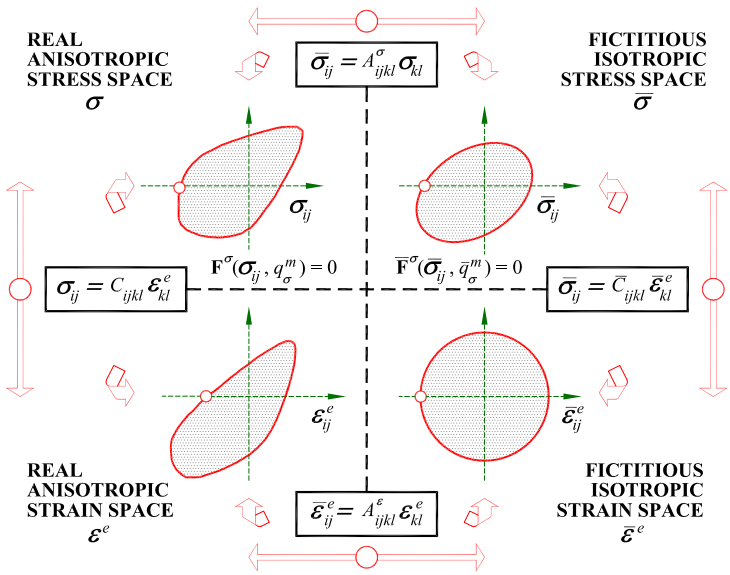

Figure 3.17 *Relation between the fictitious isotropic and the real anisotropic space.*

Finally, the secant and tangent constitutive tensors in real space are expressed in equation 3.16.

$$
\begin{aligned}
\sigma_{ij} &= m\frac{\partial \Psi^{\sigma}(\varepsilon^{e}_{kl}, q^{m}_{s})}{\partial \varepsilon^{e}_{ij}} = \left(A^{\sigma}_{ijkl}\right)^{-1}\bar{\sigma}_{kl} \\
\dot{\sigma}_{ij} &= \left(A^{\sigma}_{ijkl}\right)^{-1}\dot{\bar{\sigma}}_{kl} \equiv \left(A^{\sigma}_{ijkl}\right)^{-1}\left(\overline{C}^{\sigma}_{klrs}\right)^{ep}\dot{\bar{\varepsilon}}_{rs}\left(\overline{C}^{\sigma}_{ijkl}\right)^{ep} \\
\dot{\sigma}_{ij} &= \overline{C}^{\sigma}_{ijkl} - \frac{(\overline{C}^{\sigma}_{ijkl}\,\tilde{\mathbf{R}})\left(\dfrac{\partial \overline{F}^{\sigma}}{\partial \bar{\sigma}_{rs}}\overline{C}^{\sigma}_{rskl}\right)}{H + \dfrac{\partial \overline{F}^{\sigma}}{\partial \bar{\sigma}_{pq}}\overline{C}^{\sigma}_{pqtn}\tilde{\mathbf{R}}_{tn}}
\end{aligned}
\tag{3.16}
$$

where Ψ^{ε} is the free-energy density, m is the mass density and H is the hardening parameter.

3.4 Mixing Theory

In a general sense, a mixing theory is a weighted mean proposed for modeling non-linear mechanical behavior of composite materials made up of continuum or unidirectional fibers.

Classical mixing theory (CMT) was firstly studied by Truesdell and Toupin [163] establishing the basis for subsequent developments, like the ones made by Ortiz and Popov [122], Oller *et al* [119] and Oñate *et al* [120].

CMT takes into account the volume fraction of components but not its morphological distribution, since it assumes all component of the composite experiment the same

strain state in all directions (pure parallel behavior). This feature is a strong limitation for the use of CMT to predict the behavior of most composites, and consequently modifications to this theory were developed by Rastellini [136] making the composite behavior dependent on the constitutive laws of component materials according to their volume fractions and to their morphological distribution inside the composite.

Serial-parallel (SP) mixing theory proposed by Rastellini [136] assumes that components behave as parallels materials in the fibers alignment and as serial materials in orthogonal directions. Later SP theory was implemented by Martinez [87], in next lines numerical model of both CMT and SP mixhing theory are briefly reproduced.

3.4.1 Classical Mixing Theory

Due to the pure parallel behavior within the components it is also referred as parallel mixing theory, and their basic hypothesis are:

1. Every infinitesimal volume of the mixing is composed by a finite number of component materials.
2. The ratio of component's participation in the overall behavior of the composite is the same ratio of its volume.
3. All components substances have the same deformations as the component (strain compatibility).
4. Volume of each component substance is less than the total volume of the component.

Other hypothesis implies an homogeneous distribution of all substances for a given region of the composite. Interaction between such substances, each with its own constitutive model, results in the behavior of the component which depends on the volume ratio of each of the components.

Also CMT theory assumes that in absence of atomic diffusion (moderate temperatures) between substances within the components of the solid, next compatibility equation is fulfilled:

$$(\varepsilon_{ij})_1 = (\varepsilon_{ij})_2 = \ldots = (\varepsilon_{ij})_n = \varepsilon_{ij} \tag{3.17}$$

Furthermore, for composite materials, free energy can be written as shown in equation 3.18 [163].

$$m\boldsymbol{\Psi}\left(\varepsilon^e_{ij}, \alpha, \beta\right) = m\boldsymbol{\Psi}\left(\varepsilon_{ij}, \overbrace{\varepsilon^p_{ij}, \alpha, \beta}^{Pr}\right) = m\sum_{c=1}^{n} k_c \boldsymbol{\Psi}_c \left((\varepsilon_{ij})_c, (P_r)_c\right) \tag{3.18}$$

where $\boldsymbol{\Psi}_c$ is the free energy of the c-th component of all the n involved in the mixture, $(pr)_c$ is a set of internal variables for the c-th component, and $k_c = \frac{dV_c}{dV}$ is the volume ratio of the c-th component. It is convenient to acknowledge regarding to volume ratio, that have to be fulfilled condition shown below.

$$\sum_{c=1}^{n} k_c = 1.0 \tag{3.19}$$

Stress of the composite is now a function of the free energy, same as for simple materials. For thermally steady cases:

$$\sigma_{ij} = m\frac{\partial \boldsymbol{\Psi}\left(\varepsilon_{kl}, Pr\right)}{\partial \varepsilon_{ij}} = m\sum_{c=1}^{n} k_c \frac{\partial \boldsymbol{\Psi}_c\left(\varepsilon_{kl}, (Pr)_c\right)}{\partial \varepsilon_{ij}} = \sum_{c=1}^{n} k_c \left(\sigma_{ij}\right)_c \tag{3.20}$$

where $(\sigma_{ij})_c$ is the stress of the c-th component material.

Via the Clausius Planck inequality, a thermodynamic expression for mechanical dissipation can be obtained.

$$\Xi_{mec} = \frac{\partial \boldsymbol{\Psi}\left(\varepsilon_{mm}, Pr\right)}{\partial P_i}\dot{P}_i = m\sum_{c=1}^{n} k_c \frac{\partial \boldsymbol{\Psi}_c\left((\varepsilon_{mm})_c, (Pr)_c\right)}{\partial \varepsilon_{ij}\partial \varepsilon_{ij}} = \sum_{c=1}^{n} k_c \left(C_{ijkl}\right)_c \tag{3.21}$$

Finally, considering strain compatibility, strains in the composite can be written as:

$$\varepsilon_{ij} = \left(\varepsilon_{ij}\right)_c = \left(\varepsilon^e_{ij}\right)_c + \left(\varepsilon^p_{ij}\right)_c = \left(C^s_{ijkl}\right)^{-1}_c \left(\sigma_{kl}\right)_c + \left(\varepsilon^p_{ij}\right)_c \tag{3.22}$$

3.4.2 Serial-Parallel Mixing Theory

Numerical model developed to obtain stress-strain relationship of composite material from their components under a serial-parallel behavior is based upon the next hypothesis.

1. Component materials have the same strains in the parallel direction of the fiber (iso-strain condition).
2. Component materials have the same stress in the serial direction (iso-stress condition)
3. The ratio of component's participation in the overall behavior of the composite is the same ratio of its volume.
4. It is considered a homogeneous distribution of components within the composite.
5. Only two components are considered: matrix and fiber, and it is assumed they are perfectly bonded to each other.

Mechanical behaviors of components within the composite are related by their own constitutive equation. In this work, SP theory will be mainly considered to reproduce the mechanical behavior of reinforced concrete, although can also be used to reproduce the behavior of reinforced masonry, in any case, matrix material will follow a damage constitutive equation (eq. 3.23), whereas fiber material (steel) will be modeled with a classical plasticity constitutive equation (eq. 3.24).

$${}^k\boldsymbol{\sigma} = (1-d)\,{}^k\mathbf{C}_o : ({}^k\boldsymbol{\varepsilon}) \tag{3.23}$$

$${}^k\boldsymbol{\sigma} = {}^k\mathbf{C}_o : {}^k\boldsymbol{\varepsilon}^e = {}^k\mathbf{C}_o : ({}^k\boldsymbol{\varepsilon} - {}^k\boldsymbol{\varepsilon}^p) \tag{3.24}$$

following same notation presented in [136], ${}^k\boldsymbol{\sigma}$ is the stress tensor of the material k-th; ${}^kC_o$ is the constitutive tensor of the k-th material, whereas ${}^k\boldsymbol{\varepsilon}$ and ${}^k\boldsymbol{\varepsilon}^p$ are the total

and plastic deformation tensors respectively, finally, d is a internal variable of isotropic damage (see appendix A).

Stress-strain relationship shown in equations 3.23 and 3.24, can be rewritten considering decomposition of constitutive tensors in their serial and parallel components.

$$\begin{bmatrix} {}^{k}\boldsymbol{\sigma}_P \\ {}^{k}\boldsymbol{\sigma}_S \end{bmatrix} = \begin{bmatrix} {}^{k}\mathbf{C}_{PP} & {}^{k}\mathbf{C}_{PS} \\ {}^{k}\mathbf{C}_{SP} & {}^{k}\mathbf{C}_{SS} \end{bmatrix} : \begin{bmatrix} {}^{k}\boldsymbol{\varepsilon}_P \\ {}^{k}\boldsymbol{\varepsilon}_S \end{bmatrix} \tag{3.25}$$

Decomposition of constitutive tensor for each simple material is defined by the double contraction of fourth order projection tensors, and the constitutive tensor itself, hence

$$\begin{aligned} {}^{k}\mathbf{C}_{PP} &= \mathbf{P}_P : {}^{k}\mathbf{C} : \mathbf{P}_P \\ {}^{k}\mathbf{C}_{PS} &= \mathbf{P}_P : {}^{k}\mathbf{C} : \mathbf{P}_S \\ {}^{k}\mathbf{C}_{SP} &= \mathbf{P}_S : {}^{k}\mathbf{C} : \mathbf{P}_P \\ {}^{k}\mathbf{C}_{SS} &= \mathbf{P}_S : {}^{k}\mathbf{C} : \mathbf{P}_S \end{aligned} \tag{3.26}$$

Considering that both matrix and fiber material have a common four order constitutive tensor, and as a function of volumetric fraction, material constitutive tensor is defined as:

$$\begin{aligned} {}^{c}\mathbf{C}_{PP} &= \left({}^{f}k^{f}\mathbf{C}_{PP} + {}^{m}k^{m}\mathbf{C}_{PP} \right) + {}^{m}k^{f}k \left({}^{f}\mathbf{C}_{PS} - {}^{m}\mathbf{C}_{PS} \right) : \mathbf{A} : \left({}^{m}\mathbf{C}_{SP} - {}^{f}\mathbf{C}_{SP} \right) \\ {}^{c}\mathbf{C}_{PS} &= \left({}^{f}k^{f}\mathbf{C}_{PS} : \mathbf{A} : {}^{m}\mathbf{C}_{SS} + {}^{m}k^{m}\mathbf{C}_{PS} : \mathbf{A} : {}^{f}\mathbf{C}_{SS} \right) \\ {}^{c}\mathbf{C}_{SP} &= \left({}^{m}k^{f}\mathbf{C}_{SS} : \mathbf{A} : {}^{m}\mathbf{C}_{SP} + {}^{f}k^{m}\mathbf{C}_{SS} : \mathbf{A} : {}^{f}\mathbf{C}_{SP} \right) \\ {}^{c}\mathbf{C}_{SS} &= \frac{1}{2} \left({}^{m}\mathbf{C}_{SS} : \mathbf{A} : {}^{f}\mathbf{C}_{SS} + {}^{f}\mathbf{C}_{SS} : \mathbf{A} : {}^{m}\mathbf{C}_{SS} \right) \end{aligned} \tag{3.27}$$

being

$$\mathbf{A} = \left({}^{m}k^{f}\mathbf{C}_{SS} + {}^{f}k^{m}\mathbf{C}_{SS} \right)^{-1} \tag{3.28}$$

again, using the same notation as in [136], superindex c, m and f are referred to the: composite, matrix and fiber material respectively. Parameters ${}^{f}k$ and ${}^{m}k$ represent volumetric fraction of matrix and fiber materials, respectively.

Finally, equilibrium and compatibility equations to be fulfilled in the composite are shown below.

$$Parallel \begin{cases} {}^{c}\boldsymbol{\varepsilon}_P = {}^{m}\boldsymbol{\varepsilon}_P = {}^{f}\boldsymbol{\varepsilon}_P \\ {}^{c}\boldsymbol{\sigma}_P = {}^{m}k^{m}\boldsymbol{\sigma}_P + {}^{f}k^{f}\boldsymbol{\sigma}_P \end{cases} \tag{3.29}$$

$$Serial \begin{cases} {}^{c}\boldsymbol{\varepsilon}_S = {}^{m}k^{m}\boldsymbol{\varepsilon}_S + {}^{f}k^{f}\boldsymbol{\varepsilon}_S \\ {}^{c}\boldsymbol{\sigma}_S = {}^{m}\boldsymbol{\sigma}_S + {}^{f}\boldsymbol{\sigma}_S \end{cases} \tag{3.30}$$

3.5 Mesh Objectivity of FE Formulation Response with Strain-Softening

Masonry, as some other materials subjected to the action of imposed displacements exhibit, after a certain limit, a phenomenon called softening. During a process of uniaxial quasi-static loading, softening appears as a reduction of the magnitude of the stress and an increment of strains.

In continuum mechanics, it is known that the inclusion of strain-softening leads to the increment of strains in narrow strips. This phenomenon is known as strain localization. Two major approaches may be distinguished for analyzing crack propagation, namely:

- **Discontinuous (or Discrete) crack approach**, where displacement that jumps across the crack are explicitly considered, and the non-linear behavior is established through a softening traction-displacement law. A mayor disadvantage that adheres this approach is the fact that the topology of the finite element mesh is changed continuously, although this concept has been refined in recent years in models where cracks are no longer forced to align with the original inter element boundaries.

- **Smeared crack approach**, that is, standard finite elements with continuous displacement fields and standard local constitutive model with strain-softening. Softening modulus is adjusted according to the material fracture energy and the element size. The crack is assumed to be distributed over the entire area belonging to an integration point.

Objective of this section is only to point out in a briefly manner the strain-softening phenomena, reader may abound in the subject by consulting reference [29]. Also some remarks on the selected approach in this work (SC approach) are listed below.

- **The simplicity of this approach**. Smeared crack models can be readily implemented in any non-linear FE code, by simply writing a routine for a new material constitutive model.

- **Re-meshing is unnecessary**. Since the cracking material is assumed to remain continuum and material properties (stiffness and strength) are modified to account for the effect of cracking.

- **Mesh dependency**. A drawback is that the total energy dissipated in the cracking process is proportional to the size of the element.

The requirement that the result from the numerical modeling should be independent of the mesh choice is named mesh objectivity. This requirement can be bring into the numerical modeling by modifying the softening law as proposed in [109]. Bazant and Oh in [109] remark that in a FEM framework, the concept of strain softening should not be considered as a characteristic of the material only, since this aspect is related to the fracture energy G_f and to the size of the FE where the energy dissipation process occurs, hence, in each FE, the width of the fracture zone is computed depending on the geometric dimensions of the elements, in other words, fracture energy is now adopted as a bonding parameter between fracture mechanics and the constitutive model based on classical mechanics. Following a simple formulation based on a uniaxial behavior, the fracture energy D_f per unit area can be expressed as:

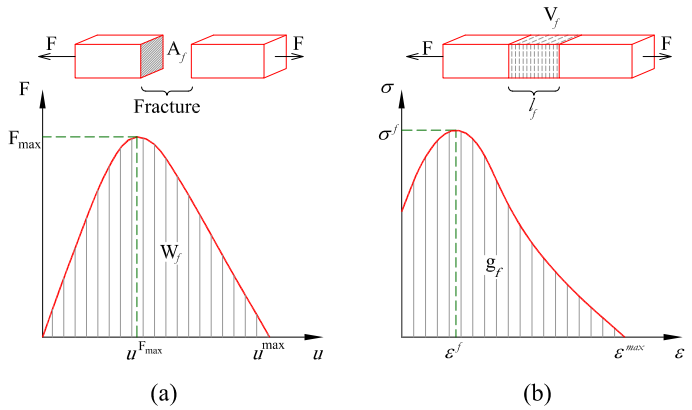

Figure 3.18 *Schematic representation of crack approaches.*

$$G_f = \frac{W_f}{A_f} \tag{3.31}$$

where W_f is the total energy dissipated by the fracture at the end of quasi-static process, and A_f is the total area of the crack. Finally, the coupling of classical mechanics framework and a given constitutive model via G_f is given in equation 3.32.

$$W_f = G_f A_f = \int_V g_f \, dV \tag{3.32}$$

where g_f is the maximum energy dissipated by a continuum model in pure traction. Figure 3.18.a depicts a schematic representation of a discontinuous crack approach, whereas figure 3.18.b represents a smeared crack approach.

From equation 3.32, relationship among fracture energy per unit area G_f and the total energy per unit of volume g_f is expressed as:

$$G_f = \frac{W_f}{A_f} = \int_V \frac{g_f}{A_f} \, dV \tag{3.33}$$

Since the process where fracture occurs is defined as $V = l_p A_f$ then equation 3.33 becomes

$$G_f = \frac{W_f}{A_f} = l_f \, g_f \quad \Rightarrow \quad g_f = \frac{G_f}{l_f} = \frac{W_f}{l_f A_f} \tag{3.34}$$

where l_f is the length of the area where the non-linear behavior will occur. Since G_f is a property of the material, mesh objectivity comes while defining the fracture length l_f of a given finite element. Several studies have been done to provide objectivity on the results independently of the size of the finite element mesh (Oliver [110], Oller [114], Oliver *et al* [112], Cervera and Chiumenti [29], among others). Finally, it is important to point out the work done by Cervera and Chiumenti, since is the scheme to evaluate l_{ch} adopted in this work. In [29] characteristic length is defined as the representative size of the element l_{ch} for linear simplex elements and for 2D triangular elements using equation 3.35.

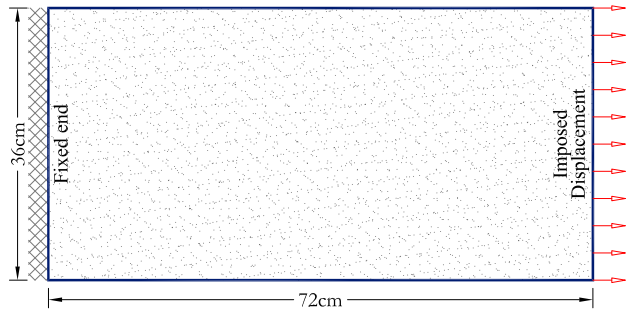

Figure 3.19 *Schematic representation of axially loaded plate.*

$$l_{ch} = \sqrt{\frac{4}{\sqrt{3}} A_e} \tag{3.35}$$

being A_e the area of the element assuming that the triangular elements are equilateral.

3.5.1 Objectivity Analysis - Membrane Test.

A numerical example of a damage constitutive model with strain-softening using standard triangular FE (CST triangle) has been carried out in this subsection. To carry an objectivity analysis, the example used by Badillo in [12] has been chosen. The model consists on a plate fixed on its left part whereas on its right part a displacement has been imposed (fig. 3.19), this has been done in order to simulate an ideal uniaxial tensile test.

Studied plate is 1 centimeter thick, and is composed by a matrix-like material whose non-linear behavior is expressed by the continuum damage model with exponential softening. The formulation of the constitutive model used is fully described in appendix A.

Material properties of the plate are: Young's modulus $E = 3.5E4MPa$, Poisson's ratio $\nu = 0.2$, internal friction angle $\phi = 30^{\circ}$, compression strength $\sigma_{yc} = 20MPa$, tensile strength $\sigma_{yt} = 2.0MPa$, fracture energy $G_f = 0.25kN/m$ and compression energy $G_c = 26.0kN/m$.

Mesh arrangements for specimens are presented in figure 3.20 consisting in: *a*) nearly equilateral triangles elements (P-2x24 and P-6x12), *b*) triangular elements with their longest side perpendicular to the loading direction (P-2x8 and P-4x16), and *c*) triangular elements with their longest direction parallel to the loading direction (P-4x4 and P-2x8).

For each mesh presented in figure 3.20, three different values of the characteristic length have been assigned for comparative purposes:

1. Equal to the root area of the finite element $l_{ch} = \sqrt{A_e}$.
2. Equal to the scheme proposed in [29] $l_{ch} = \sqrt{\frac{4}{\sqrt{3}} A_e}$.
3. Equal to the full length of the element in the load direction $l_{ch} = h_e$.

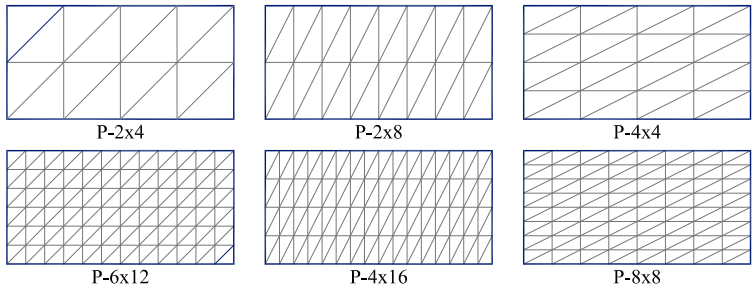

Figure 3.20 *Mesh arrangements for softening objectivity analysis.*

Finally, solution has been compared with the response of a plate obtained by modeling it with one single finite element, which is considered as the reference solution, as presented in [12]. Figures 3.21.a, 3.21.b and 3.21.c depict results of the performed analysis in terms of the capacity curves for the different mesh models and for the given value of the characteristic length assigned.

Figure 3.21.a rendering results of specimens using $l_{ch} = \sqrt{A_e}$ seems confusing, since finite elements with high aspect ratio (P-2x8 and P-4x16) fits exactly as the reference solution. On the other hand, both, meshes with FE with the longest side parallel to the loading direction (P-4x4 and P-8x8) and meshes with FE sensibility equilateral overestimate the response.

Results obtained from figure 3.21.b confirm scheme presented in [29] by Cervera and Chiumenti. The characteristic length used in equation 3.35 tends to be the ideal, since finite elements in specimens P-2x4 and P-6x12 are closer to be equilateral triangles are the ones with the best approximation to the theoretical response. On the other hand, responses of specimens with higher finite element's aspect ratio both under or overestimate the response compared with the reference solution.

Finally, results from figure 3.21.c are straightforward, and according to a smeared crack approach, demonstrate that the characteristic length that gives objectivity in the response and that match reference solution is when l_{ch} equals the theoretical fracture length for the case of pure uniaxial test.

It also must be noticed that the use of fracture length depending on the size of a finite element brings different evolution of stresses in the non-linear range [12], since total energy depends in the volume of a given finite element. Namely, for large elements (and large fracture energy too) the fracture energy per unit of volume is lower, resulting in a lower stress state compared with smaller elements.

3.6 Bending performance of the proposed shell element

In this section is presented a numerical example of a laminated plate subjected only to bending stresses. The aim of this section is to point out that with the proposed integration scheme along the thickness, a layered plate is perfectly capable of reproducing the expected bending degradation that arises when some layers are beyond the elastic threshold and others are not.

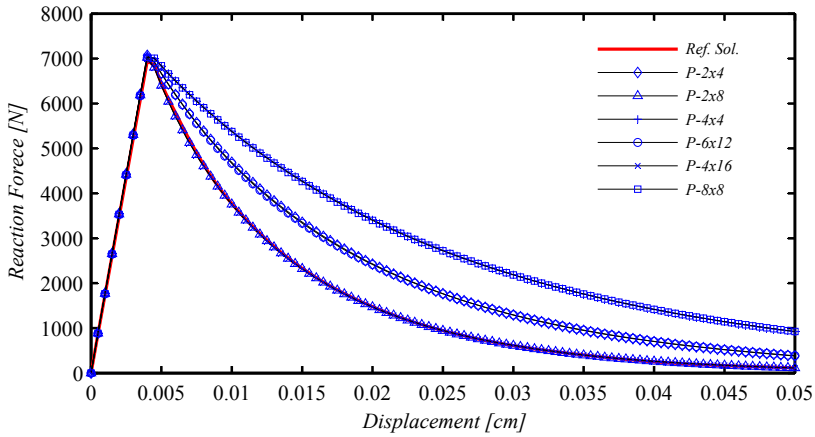

(a) Characteristic length $l_{ch} = \sqrt{A_e}$

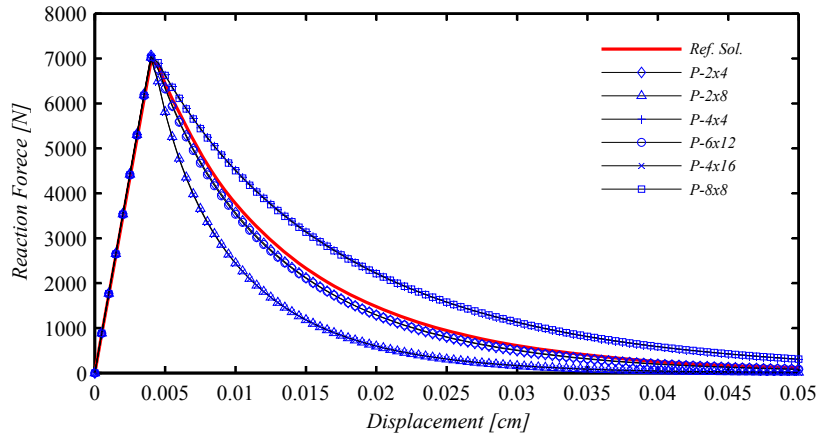

(b) Characteristic length $l_{ch} = \sqrt{\frac{4}{\sqrt{3}} A_e}$

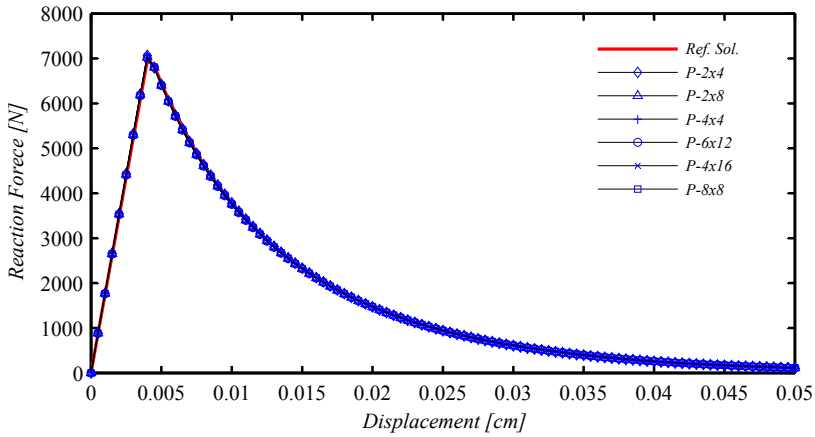

(c) Characteristic length $l_{ch} = h_e$

Figure 3.21 *Non-linear FEM response using different characteristic length* l_{ch}

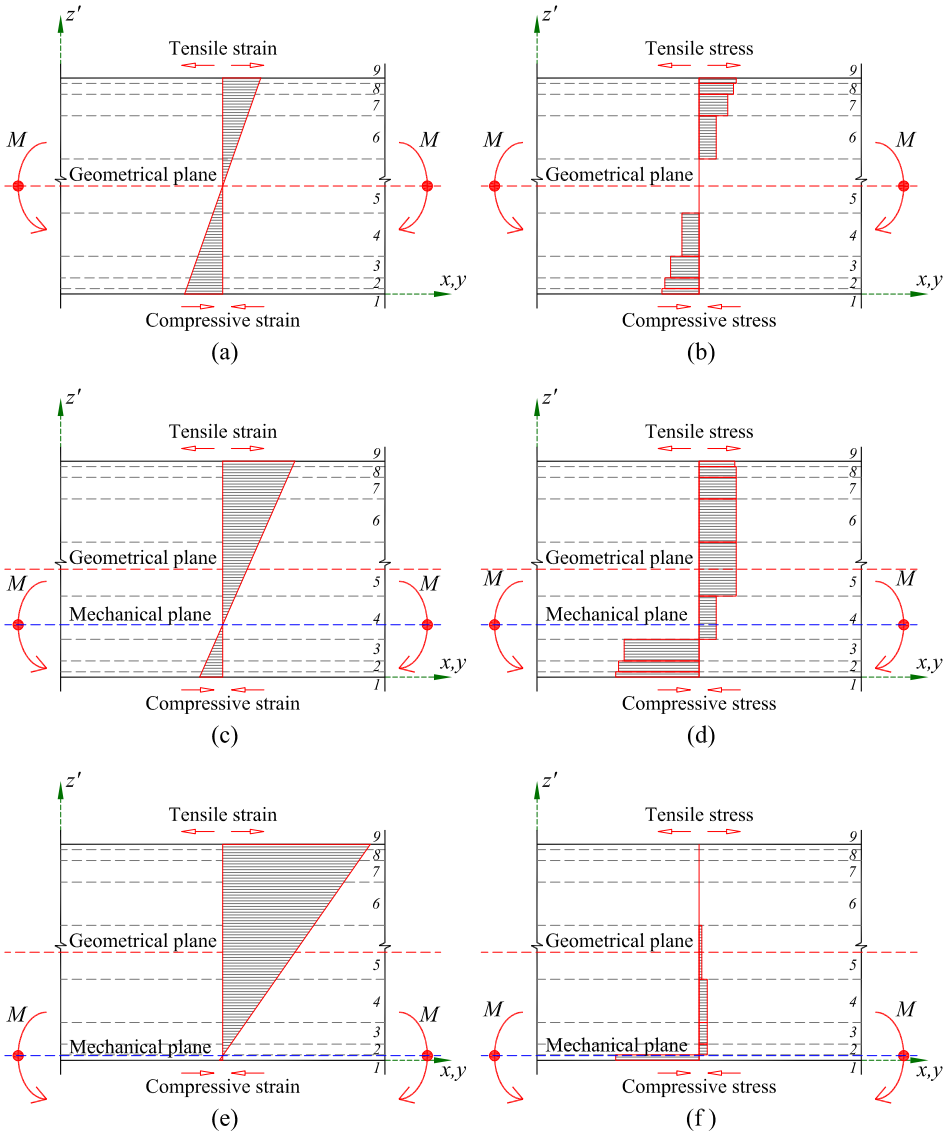

Figure 3.22 *Schematic representation of bending damage.*

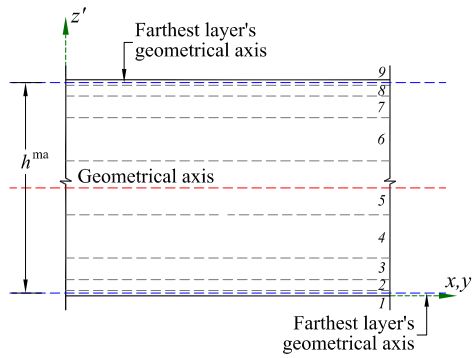

Figure 3.23 *Schematic representation of range in which moves the mechanical axis.*

First, the expected behavior due the damage evolution is briefly described; then, numerical results obtained with the proposed integration scheme over the thickness are compared with obtained results from a model formed with hexahedron elements.

Let us considered the example shown in figure 3.22 where the layer distribution of a plate under a monotonic bending stress is depicted. Layers of the composite material are formed by a homogeneous and isotropic material, in such a way mechanical plane lie in the geometrical plane. Let us also consider that the simple material forming the laminated plate is a concrete-like material, where there is a pronounced difference among tension and compression damage threshold.

As bending moment monotonic load starts being applied, the expected distribution of strains along the thickness would be the shown in figure 3.22.a, whereas stress distribution would be like the ones shown in figure 3.22.b. Both stresses and strains corresponding to figures 3.22.a and 3.22.b would be in the elastic range.

As bending moment continues to impose, a non-liner response would be reached. The expected response of the composite material is such that only the layers under tension stress (since tension is by far the less resistant stress) reach the non-linear range, and due to this, layers subjected to compression forces undergo a gradual increase of stress. Consequently, strain level of a the laminated material slightly beyond the damage threshold would be as shown in figure 3.22.c, also, from such figure can be notice that mechanical and geometrical planes no longer correspond. On the other hand, expected stress distribution would be the presented in figure 3.22.d.

Finally, if it stills imposing a bending moment up to a fully damaged state in the plate, strain distribution would be very much alike at the one presented in figure 3.22.e and the corresponding stress distribution shall the one shown in figure 3.22.f.

This effect can be summarized as a gradual loss of bending stiffness due to damage that occurs in some layers of the composite material. Mathematically, such effect is evaluated using secant constitutive tensors of the layers, this in order to determine the position of the mechanical plane, and then, integration along the thickness of the composite material is performed (as previously explained in chapter 2). It is easy to notice that, by definition, mechanical plane of the shell only can move within range h^{ma} shown in figure 3.23. With the proposed integration scheme it becomes mandatory to perform a finer layer distribution in the following cases:

- At the farthest zones away from the geometric axis of the shell, since such layers

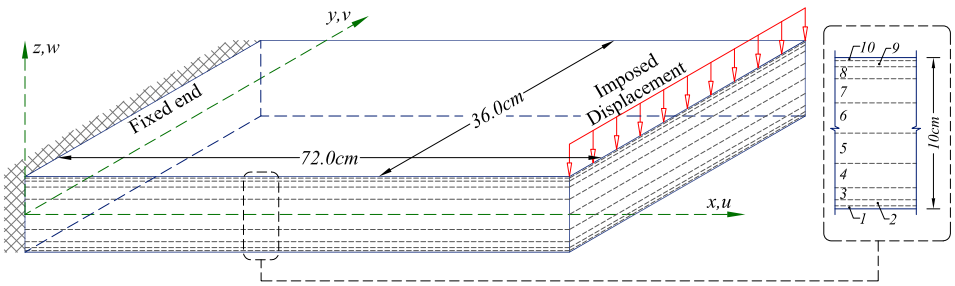

Figure 3.24 *Schematic representation of bending loaded plate.*

will be subjected to the higher stresses while acting a bending stress.

- At zones where exist an abrupt change of stiffness, which correspond to the presence of steel reinforcement within the concrete, no matter the position within the overall thickness.

Main idea of such layer distribution, is to endow the proposed integration scheme, with the capability of capturing the mechanical axis once the shell element has undergone a non-linear effect. Because as the element damages, the mechanical axis moves away from its original position toward one end (according to the bending moment's direction), and the nearest to one end the more damage state is able to represent.

Let us consider the example shown in figure 3.24, where a model subjected to bending moment is depicted. Two cases are considered, a shell element with the proposed integration scheme, and a conventional hexahedron element. In both cases, boundary conditions will be the same, namely, one end fixed, and in the other end, a vertical displacement monotonically increased will be imposed. Dimensions of the model are 72x36x10cm. For the shell model, it has been used a mesh with a total of 144 triangular elements with a single integration point, on the other hand, the model with hexahedron elements has been performed using a mesh with 720 finite elements with 8 integration points each.

Mechanical properties of the material forming the layers of the shell (and hexahedron elements, for that matter) are the ones previously presented in section 3.5.1. In order to stay away from the definition and evaluation of the fracture length, since for both bi-dimensional and three-dimensional elements different theory may apply, fracture length will be fixed in both examples to $l_{ch} = h_{gp} = 3cm$, where h_{gp} is the length of a gauss point in the load direction of a hexahedron element .

Figure 3.25 depicts the evolution on the non-linear force-displacement response of both models. It is easy to notice that a good agreement among two models has been achieved, although the layered shell element slightly underestimated the response. Also it is easy to notice that bending moment at the support is equal to $M_a = PL$. Values corresponding to imposed displacements δ_1, δ_2 and δ_3 are used as a reference to the information output for a random F.E (figures 3.26 and 3.27).

Once both analysis has been performed, the first comparison point is the deformation undergone by both models, such comparison is shown in figure 3.26, as expected, damage takes place in the nearest elements to the fixed end in both models, this seems obvious, since such elements are subjected to the highest levels of tensile stresses at the top

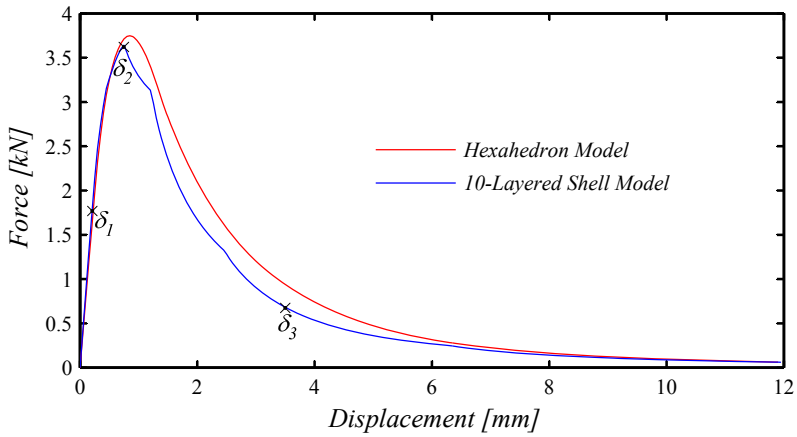

Figure 3.25 *Non-linear FEM response of a vertically loaded plate using* $l_{ch} = 3cm$.

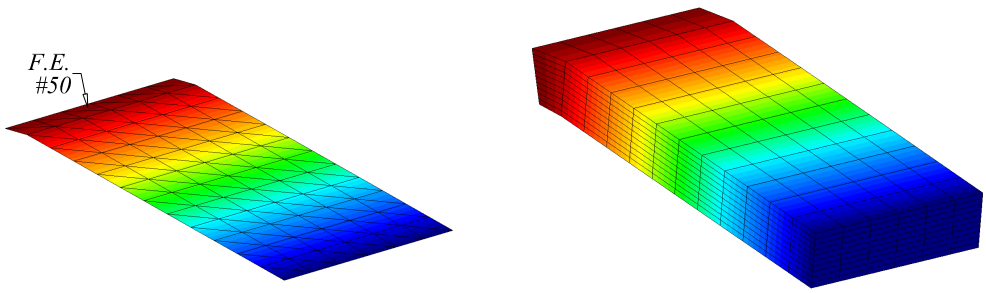

Figure 3.26 *Final deformation of vertically loaded models.*

layers. In both cases, damage starts at the top most layers/elements, then it propagates to the inner layers/elements.

In figures 3.27,(a), (b) and (c) three graphics are shown, from left to right they correspond to: strain distribution along thickness's element, stress distribution along thickness and generalized stress M_{XX}. Such figures show the stresses and strains undergone by a random element near the model's fixed end (F.E. 50, fig. 3.26).

First loading stage (fig. 3.27.a) corresponds to an initial state of stresses within the elastic range. As seen, mechanical plane lays on the geometrical plane. Strains are depicted as a straight vertical line due to the selected scale used to show the results (the same scale has been kept for the three figures), although such distribution shall look very much alike the one shown in figure 3.25.a. On the other hand, stress distribution stills symmetric with respect to the geometrical plane.

Second loading stage chosen, is the one of the figure 3.27.b, it correspond at the loading stage, where is presented the maximum bending stress in the shell ($M_{max} = 7.774\ kN - m/m$), it is also the point where it becomes more visible the damage along the layers of the element, since mechanical and geometrical plane no longer correspond.

Finally, loading stage shown in figure fig. 3.27.c corresponds to a high damaged state (although not fully damaged), it becomes notorious that layers at the top of the element are fully damaged, it is also notorious the huge change in the position of the mechanical plane from its original position.

Additionally, in order to point out the biggest advantage of using the proposed scheme, has been selected a model with the same geometry and boundary conditions as the shown in figure 3.24. Although there is a change in the distribution of the layers, the total thickness remains the same as in the previous example. The change in the layer distribution of the laminate material is because steel reinforcement has been added at the top of the laminate, in such a way the reinforcement enhances bending resistance, its thickness is $Th_i = 3mm$, with a volumetric participation of steel reinforcement equal to 5% embedded in a matrix of concrete. To numerically reproduce the behavior of such layer, it has been used the serial-parallel mixing theory [87, 136] described in section 3.4.2 of this work, and has been split into 6 layers to get a total amount of 15 layers within the laminated material.

The reason of using an non-symmetric arrangement of the layers with respect to the geometric plane, is to show that, even within the linear range there is a difference between the position of the geometric plane and the mechanical plane, such difference increases once the a monotonically increased displacement is applied.

Such effect can be appreciated in the obtained results once the analysis has been performed, a resume of such results is presented in figure 3.28. Figure 3.28.a shows a comparison among the results obtained for non-reinforced plate (previous example) and for a reinforced plate. There is a significant improvement in the bending strength even with a small amount of steel reinforcement, in addition, there is no longer a brittle failure, but degradation is presented in a more gradual manner.

The graph of figure 3.28.a also displays displacements δ_1, δ_2, δ_3 and δ_4 used as a reference for the output results for F.E. 50 shown in figure 3.26, whose stresses and strains undergone are presented from figure 3.28.b to 3.28.e. For display purposes different horizontal scales has been used in such figures.

The stresses and strains of the F.E. studied when an imposed displacement $\delta_1 = 1.25mm$ are depicted in figure 3.28.b, as can be seen, although in such loading step the element is in a linear range, already exist a difference between mechanical and

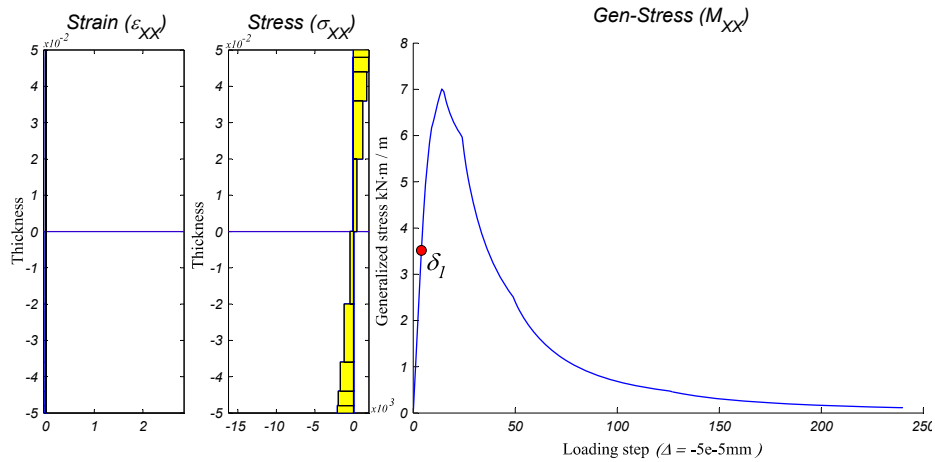

(a) Step 4, δ_1= 0.2mm

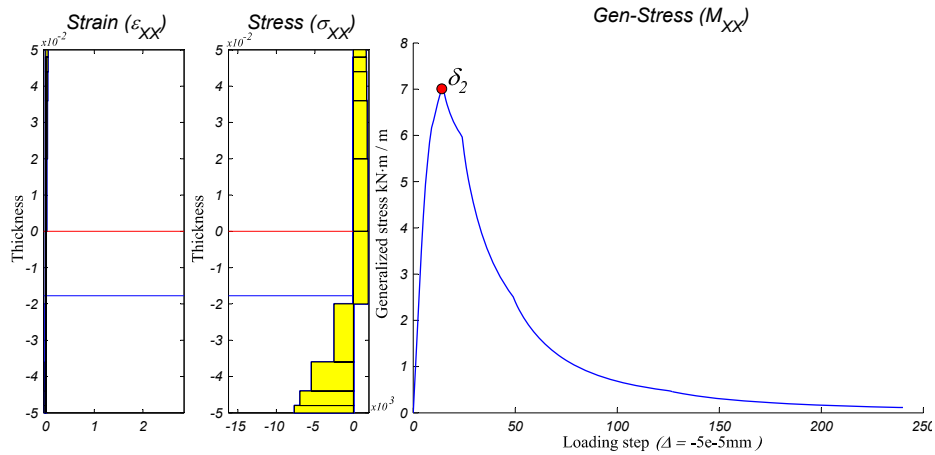

(b) Step 14, δ_2= 0.70mm

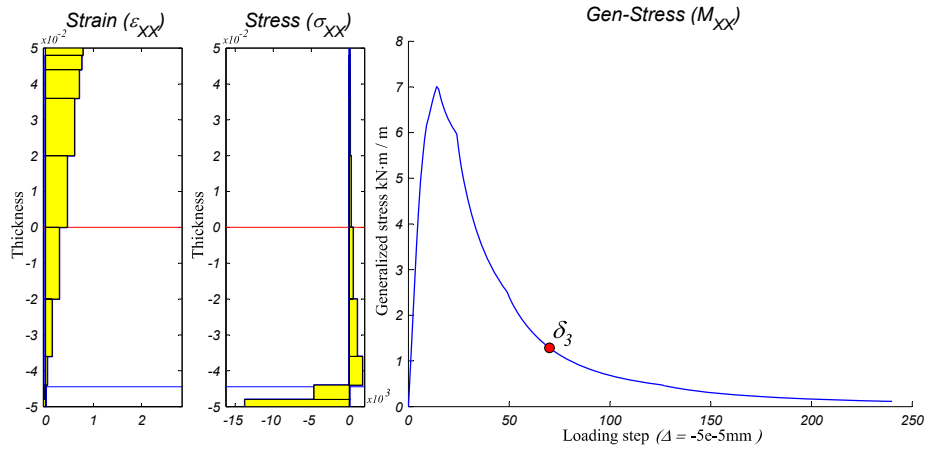

(c) Step 70, δ_3 = 3.5mm

Figure 3.27 *Evolution of strains and stresses of FE 50(units: kN, meters)*

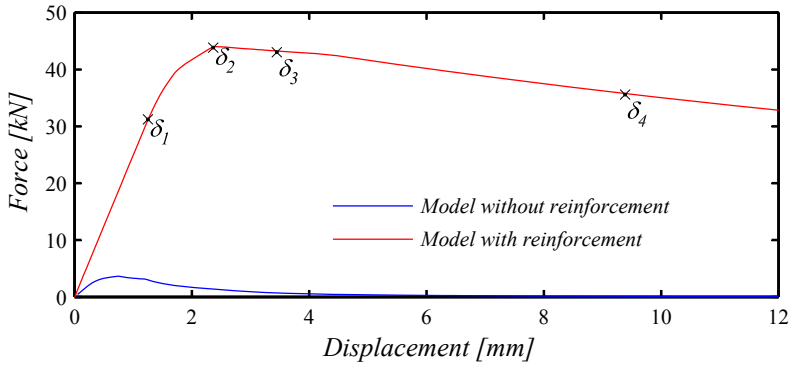

(a) Load-displacement comparison.

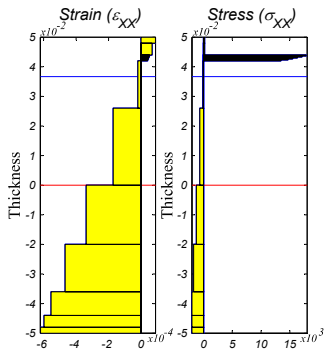

(b) $\delta_1 = 1.25mm$

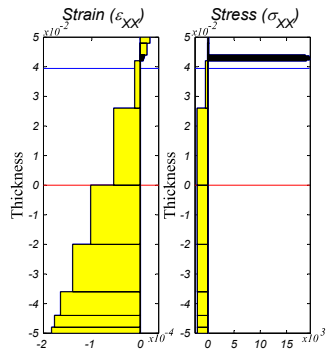

(c) $\delta_2 = 2.30mm$

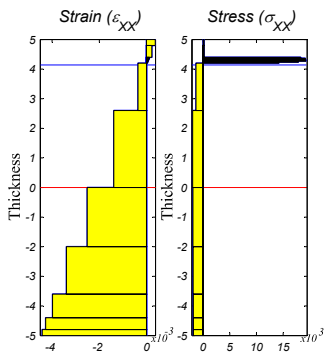

(d) $\delta_3 = 3.45mm$

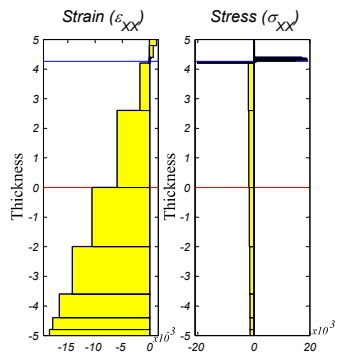

(e) $\delta_4 = 9.40mm$

Figure 3.28 *Evolution of strains and stresses of FE 50, for a plate with steel reinforcement (units: kN, meters).*

geometrical plane. On the other hand, the maximum bending strength of the model is achieved when $\delta_2 = 2.30mm$ (figure 3.28.c). Although there is no a significant difference among the position of the mechanical plane of loading steps δ_1, δ_2 and δ_3, and consequently, neither there is among the undergone stresses and strains, there is when imposed displacement $\delta_4 = 9.4mm$. Figure 3.28.e depicts a significant change in the stresses accompanied with slight change of strains. This is due to the degradation in the lower layers of the laminated material, this has caused a change in the location of the mechanical plane, now it is somewhere inside the reinforced layers, and some of those layers are under compressive forces.

Main advantage of the proposed scheme is to accurately reproduce the behavior of laminated materials, using composites within each layer which are formed by simple materials with different constitutive equations, this, with a low amount of computational resources while compared with three-dimensional finite elements, since it is not *expensive* to add a higher number of layers within the thickness in order to make a more refined analysis.

3.7 Meshing and Composite Materials Generation

In this section, a complete description of the composite material's generation is conducted. Such generation will be performed in terms of volumetric participation of their components and reinforcement's direction.

To cover the meshing needs, is selected the use of a pre and post processor for numerical simulations, in this case GiD [35]. GiD is a universal, adaptive and user-friendly pre and post-processor for numerical simulations in science and engineering. It has been designed to cover all the common needs in the numerical simulations field from pre to post-processing: geometrical modeling, effective definition of analysis data, meshing, data transfer to analysis software, as well as the visualization of numerical results.

On the other hand, in order to reproduce *real life* structures, in term of steel reinforcement patterns, a computational tool was developed having in mind the 3 principal requisites shown below.

1. Reproduce a more realistic reinforcement pattern.

2. Mechanize process where volumetric part of components on composite materials is generated.

3. Capable of handling information of large meshes.

Such tool arises as a need of mechanizing and generating the composite material information given a large mesh of triangular finite elements and the *real life* steel reinforcement pattern of every layer within the laminated material. To achieve this, it is necessary to read pre-defined text files, where the information regarding the steel reinforcement patterns has been stored.

The starting point for the generation of the composite materials presented here, is something we called *structured composite material* (*SCM* from now on), where a pattern is selected to represent both, the reinforcement steel within layers and the *SCM* 's boundary. Main idea behind the use of this method is making as mechanical as possible the generation of the composite material for any finite element.

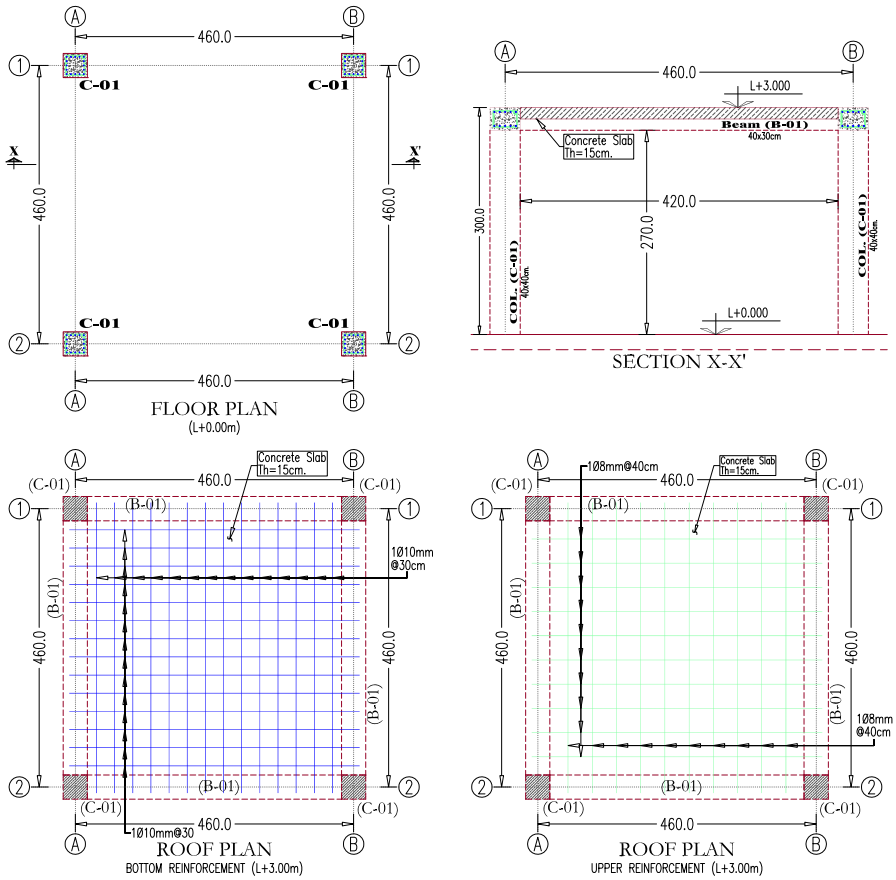

Figure 3.29 *Structural drawings (plans and elevations) of a typical one-storey construction.*

A reader experienced in computer drawing design (using AutoCAD), would find similarities of a *SCM* with a *hatch*. Namely, both are a general pre-generated pattern of bi-dimensional closed polygons (steel reinforcement in the case of a *SCM*) stored in a text file, such pattern is ready to be used as much as needed, and becomes particular, once is given to it, information such as: a contour, a local *x', y'* plane and an insertion point. Then the code on purpose will take care of generate information such as: volumetric participation, fibers direction (when applicable), and thickness for every layer of the *SCM*. The process to generate the composite material's information for any finite element is carried out as follows:

1. Is generated the text file containing information related to all *SCM* within the model, also boundaries and insertion points are included.

2. Finite element mesh is generated for the model.

3. The code on purpose searches for the finite elements intersecting the contour of the *SCM* .

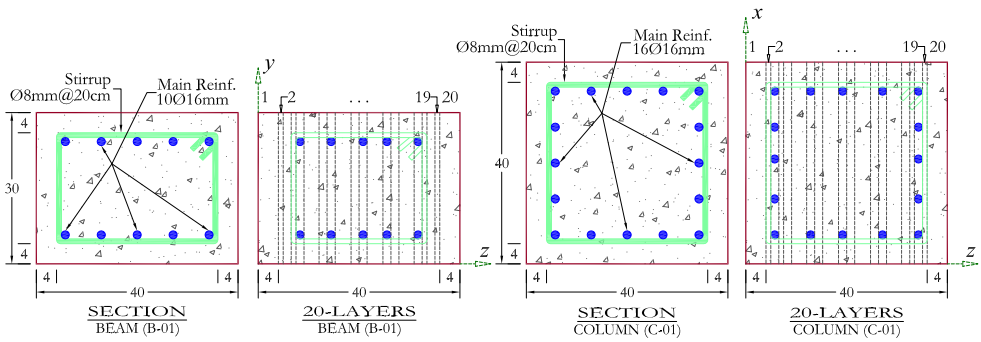

Figure 3.30 *Structural drawings (detailed sections of columns and beam) of a typical one-storey construction.*

4. With the information obtained, volumetric participation of the matrix ${}^{m}k$ and fiber ${}^{f}k$ for each layer are evaluated, in the case, when ${}^{f}k = 0$ the classic mixing theory is selected, whereas ${}^{f}k \neq 0$ serial-parallel mixing theory shall be used.

5. Finally, in order to reduce the number of composite materials, a smoothing procedure is performed.

Let us consider figures 3.29 to 3.32 as an aid for a better explanation of the proposed method. Figure 3.29 shows structural drawings of a building with a square shape in plan, with 5.0 meters along each side direction, and only one storey with 3.0 meter high. Structuring of such construction, is formed by two frames along each orthogonal direction, with columns type `C-01` and beams type `B-01`. Steel reinforcement of beams and columns, are shown in figure 3.30, whereas, in figure 3.31, the distribution of the steel reinforcement for the concrete slab is shown. In both cases, layer distribution for the cross sections is also depicted. A total of three *SCM* will be required in this example, the first one (`SCM-01`), represents the frame of both; axis `1` and `2`, the second one (`SCM-02`) represents only the beams along construction axis `A` and `B`, finally, a third one (`SCM-03`) will be needed to represent the concrete slab.

Section `X-X'` from figure 3.29 can be seen as `SCM-01`, since it can be repeated over axis `1` and axis `2`, hence, the first step of the proposed method, is to search the finite elements that overlap with the boundary of `SCM-01`, later, the intersection area of elements belonging to the `SCM-01` (steel reinforcement) with finite elements are evaluated. An example of `SCM-01` repeated for the axis `2` is depicted in figure 3.32.a, where is highlighted the boundary of `SCM-01`, on the other hand, boundaries for `SCM-02` and `SCM-03` are depicted in light gray. Only finite elements belonging to `SCM-01` repeated for axis `2` are shown, also, elements belonging layers `4` and `17` (stirrups of beam `B-01`) are displayed. Figure 3.32.b, on the other hand, shows information related to layers `03` and `18`, which is the main steel reinforcement along column type `C-01` of `SCM-01`.

Again, figure 3.32.c displays boundaries of all *SCM* considered in the current example, plus, the finite elements and information of layers `2` and `19` (column's stirrups) belonging to `SCM-01` repeated for construction axis `1`. Figure 3.32.d displays main steel reinforcement of beam `B-01` (layers `5, 8, 11, 13` and `16`).

`SCM-02` is the one corresponding to beam `B-01` of construction axis `A` and `B` shown in figure 3.32.e and 3.32.f. In this case, figure 3.32.e displays information of finite elements

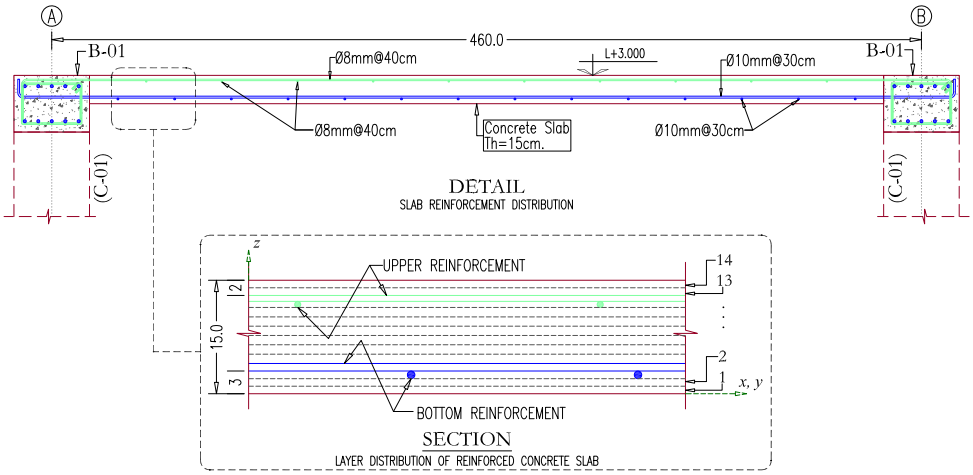

Figure 3.31 *Structural drawings (detailed sections of slab) of a typical one-storey construction.*

within the given boundary (axis `A`), and the reinforcement information concerning to layers `4` and `17`, whereas, figure 3.32.f displays information of layers `5, 8, 11, 13` and `16`, along structural axis `B`.

Finally, the third case of the used *SCM* correspond to the concrete slab, as in previous cases, in figures 3.32.g and 3.32.h are displayed only finite elements belonging to `SCM-03`, and contours of all used *SCM* . In both cases, bottom steel reinforcement is displayed, on one hand, figure 3.32.g displays information along vertical direction (layer `3`), on the other hand, figure 3.32.h displays information along horizontal direction (layer `4`).

Once the volumetric participation for each layer within the laminated material has been generated, it is possible to perform the analysis using PLCd [34]. An example has been conducted in order to show the handling of the obtained information.

Let us first clarify that the structure shown in figures 3.29 to 3.32 has been meshed using GiD [35], then, the following boundary conditions have been applied to it: *a*) displacements and rotations have been restricted at the bottom of the columns to reproduce a fixed support, *b*) a lateral force in global Y direction has been imposed at the top of columns. Forces due to the action of gravity have been neglected, neither surface loads at the top of the slab have been applied. Mechanical properties of the materials are $E = 2.5x10^4 MPa$ and $\upsilon = 0.20$ for concrete, whereas for steel $E = 2.1x10^5 MPa$ and $\upsilon = 0.00$.

Figure 3.33 summarizes some of the obtained results focusing on the stresses undergone by the steel reinforcement. Figure 3.33.a shows the mesh obtained using GiD, and the lateral displacement on the structure. As expected, given the used boundary conditions, the maximum displacement appears at the top of the structure.

The remaining figures (from 3.33.b to 3.33.h) show the stresses on the steel reinforcement of some layers of the different laminated materials, as can be seen, it is depicted only the information of the FE containing steel reinforcement. From figure 3.33 can also be inferred the amount of information stored in each FE.

Main idea behind the use of this method to generate composite materials, is to bring about the needed versatility while dealing with a complex structure where different

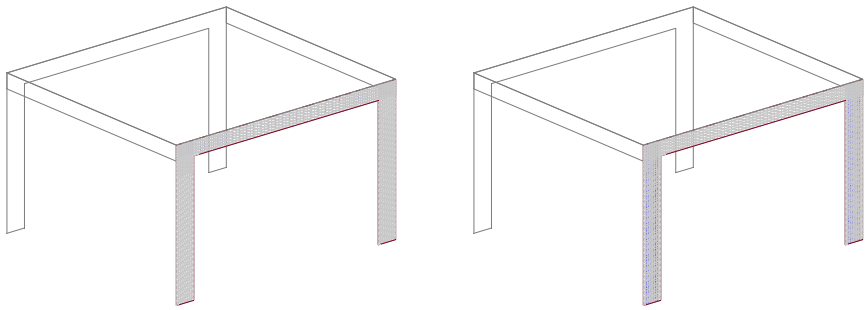

(a) SCM-01, Axis 2, Layer-04

(b) SCM-01, Axis 2, Layer-03

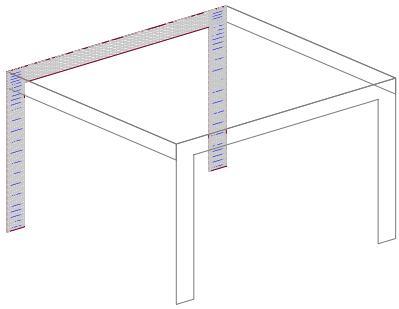

(c) SCM-01, Axis 1, Layer-02

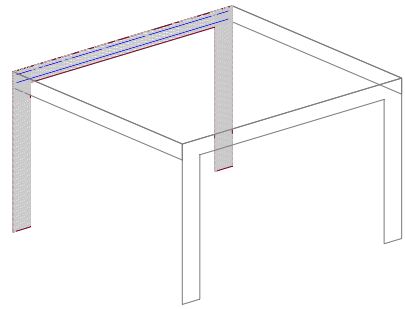

(d) SCM-01, Axis 1, Layer-05

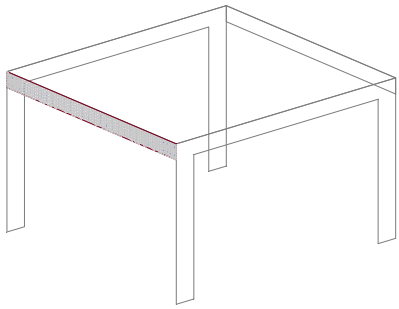

(e) SCM-02 , Axis A, Layer-04

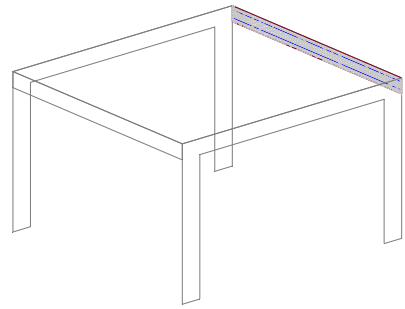

(f) SCM-02, Axis B, Layer-05

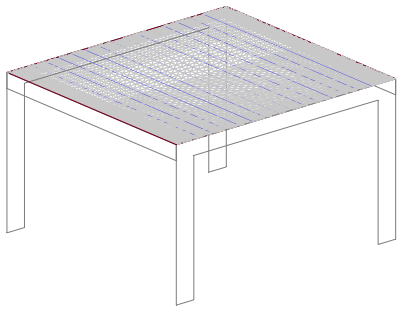

(g) SCM-03, Layer-03

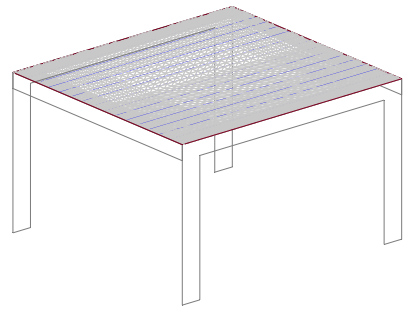

(h) SCM-03, Layer-04

Figure 3.32 *Boundaries of SCM with their FE and some of the steel reinforcement patterns.*

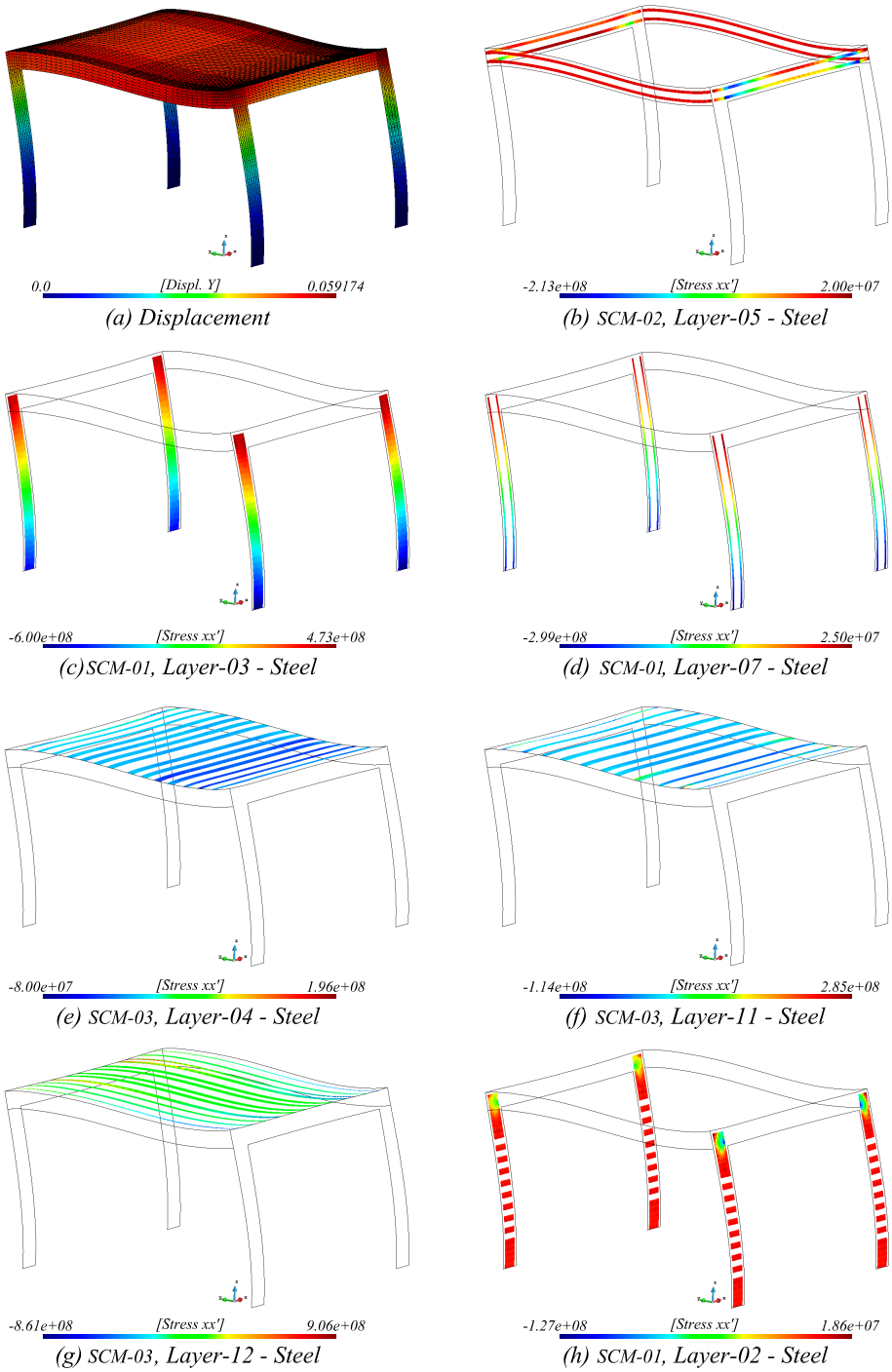

(a) Displacement
(b) SCM-02, Layer-05 - Steel
(c) SCM-01, Layer-03 - Steel
(d) SCM-01, Layer-07 - Steel
(e) SCM-03, Layer-04 - Steel
(f) SCM-03, Layer-11 - Steel
(g) SCM-03, Layer-12 - Steel
(h) SCM-01, Layer-02 - Steel

Figure 3.33 *Representation of some obtained results for a typical one-storey construction.*

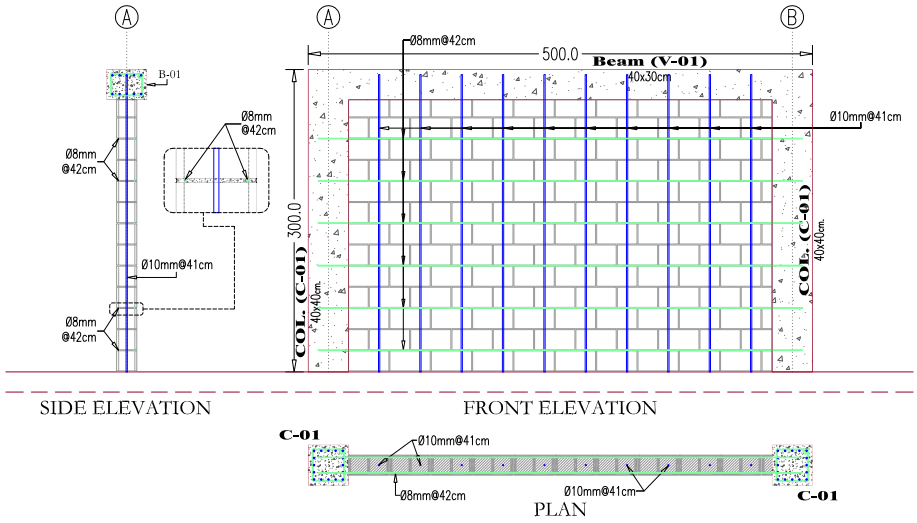

(a) Concrete frame with reinforced masonry wall in-fill.

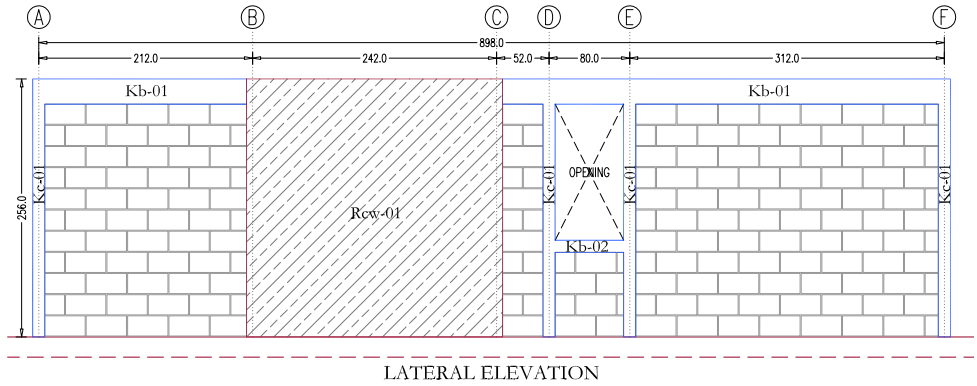

(b) Confined masonry wall with a reinforced concrete shear wall.

Figure 3.34 *Front elevation of typical structures.*

structural sections are normally used. Also, it makes possible the use of more realistic patterns for reinforcement steel, becoming a handy tool in the pre-processing task.

Some application examples using the method described in this section are listed in the section 3.8. In the following, only will be mentioned some casuistry that would apply, and that comes to mind. As in the case of figure 3.34.a, where is depicted a typical case of a reinforced concrete frame with a masonry wall in-fill, also, the masonry wall, has being reinforced with steel dowels in both, bed and head joint direction.

Figure 3.34.b displays a typical case present in confined masonry buildings, which is, the abrupt change in stiffness among structural elements. In zones with high seismic hazard, it becomes almost mandatory the use of concrete stiffeners, to endow the building with a better performance in terms of withstanding lateral forces. Although in this case only one storey is represented, it is implied that upper storeys have the same configuration.

3.8 Application Examples

Some representative examples have been chosen as a comparison, although the full potential of the shell element presented here, only can be noticed along chapter 4. Example shown in sections 3.8.1 and 3.8.2 are based on the work done by Molina *et al* [103], where a set of reinforced concrete frames has been tested numerically. On the other hand, examples shown in sections 3.8.3 and 3.8.4 correspond to experimental tests carried out by Meli [91] and Vermeltfoort and Raijmakers [170] respectively.

3.8.1 Unreinforced Concrete Frame

An unreinforced concrete frame is presented, in which it is intended to reproduce the mechanical response it exhibits a brittle material. Geometry of the frame is shown in figure 3.35.a, where dimensions are presented in centimeters. For both cases, thickness of column `C-01` and beam `B-01` is 40 centimeters, whose discretization has been done using 4 layers of 10 centimeters each. Figure 3.35.b shows the mesh of triangular finite elements used. This example correspond to a case where only unreinforced concrete has been used, thus, cross sections shall not be confused with the sections presented in figure 3.38.a, since they correspond to the model of section 3.8.2.

There is only one simple material used to model the current frame, it corresponds to concrete, whose mechanical properties agree with the used by Molina *et al* in [103], and for convenience have been reproduced in below lines.

- Elasticity modulus: $E = 2.5x10^4 MPa$
- Poisson's ratio: $\upsilon = 0.20$
- Yield criterion: Mohr Coulomb.
- Damage thresholds:

  $\sigma_c = 30MPa$

  $\sigma_t = 3MPa$

- Fracture energy:

  $G_c = 50.0kPa \cdot m$

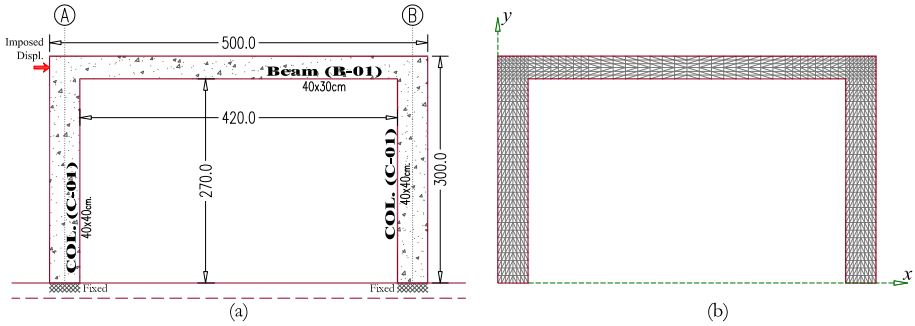

Figure 3.35 *Front elevation of typical concrete frame.*

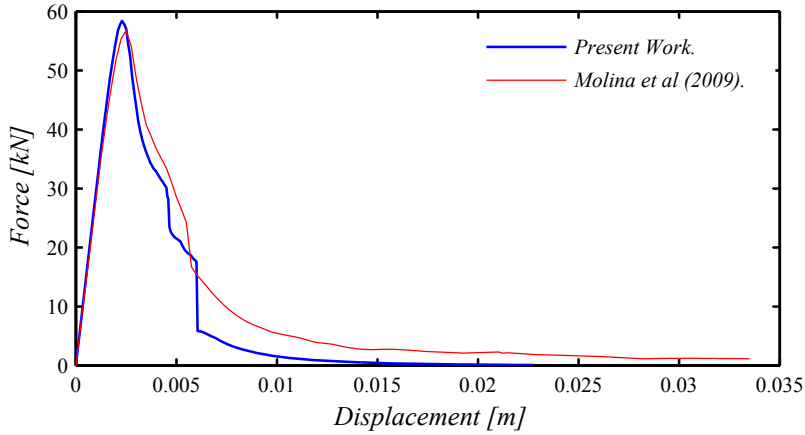

Figure 3.36 *Displacement comparison.*

$$G_t = 5.0kPa \cdot m$$

- self-weight $\gamma = 2500kg/m^3$

The present analysis has been performed using two loading phases, the first one correspond to the self-weight loading condition, and the second one, corresponds to a displacement monotonically increased, imposed at the left top of the frame.

Figure 3.37 displays the final deformation of the unreinforced concrete frame, corresponding to a fully damaged state. It becomes evident the apparition of hinge joint due to the tensile stresses that caused damage on concrete. Firsts appearing hinge joints are at the bottom of the columns, giving way to the formation of hinge joints at the beam-column joint.

A manifest brittle material behavior is noticed in the force-displacement response (fig. 3.36). The low performance of the concrete under tensile stresses, and the absence of reinforcing steel on it, conditioned a poor overall efficiency of the structural system.

Finally, figure 3.36 also depicts a comparison between results obtained in [103], by Molina *et al* (using a 4-node Lagrangian element) and the present work, where an acceptable similarity is achieved for both, initial stiffness and damage evolution.

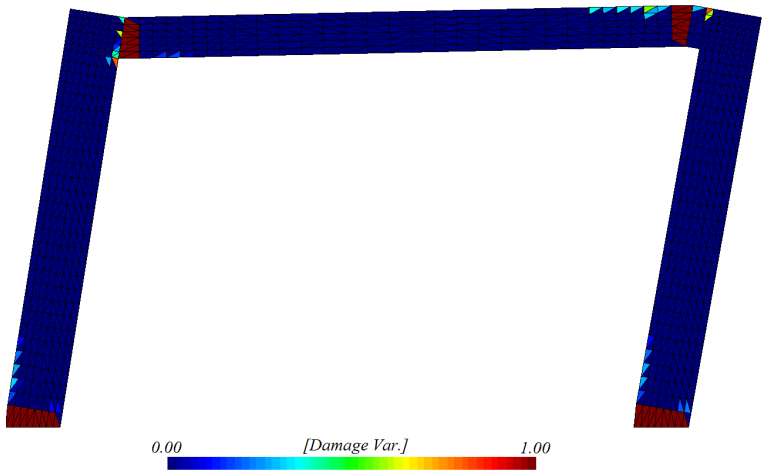

Figure 3.37 *Damage field distribution and deformed geometry (20x).*

3.8.2 Reinforced Concrete Frame

The example of this section, has been originally proposed by Molina *et al* in [103], to be used as the starting point in the comparison with frames reinforced with fibers reinforced polymers (FRP), for comparative purposes has been reproduced here, to show the full potential of the serial/parallel mixing theory for composite materials.

Geometry and mesh of this model are similar to the ones presented in the section 3.8.1, i.e., they correspond to figure 3.35. Also, loading conditions are the same, namely, two lading stages have been applied, first a self-weight loading condition, and then, a monotonically increased displacement.

In this example, the presence of reinforcement steel makes it necessary the use of the serial-parallel rule of mixtures (section 3.4.2), and the method to generate composite materials previously described in section 3.7.

Mechanical properties used for modeling concrete, agree with the used in section 3.8.1, whereas mechanical properties of steel fibers are reproduced below.

- Elasticity modulus: $E = 2.1x10^5 MPa$.
- Poisson's ratio: $\upsilon = 0.00$.
- Yield criterion: Von Mises.
- Damage thresholds:

$$\sigma_c = 270MPa$$
$$\sigma_t = 270MPa.$$

- Fracture energy:

$$G_c = 2.0MPa \cdot m$$
$$G_t = 2.0MPa \cdot m$$

- self-weight $\gamma = 7845kg/m^3$.

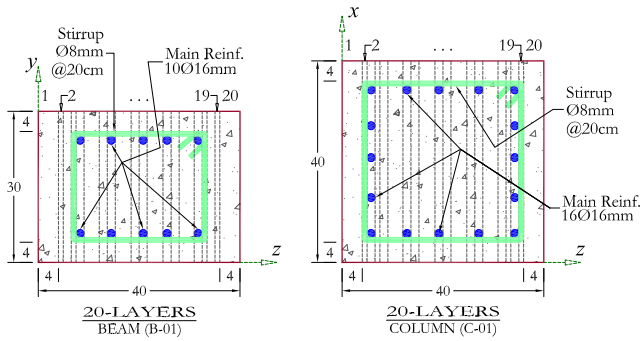

(a) Cross sections of structural elements

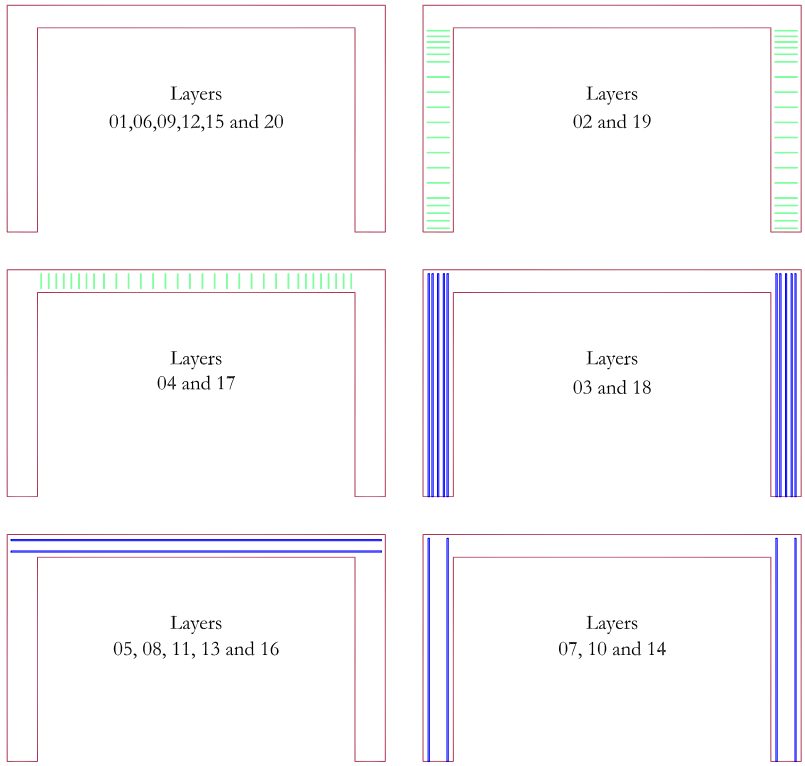

(b) Distribution of steel reinforced fibers within layers

Figure 3.38 *Distribution of reinforced fibers, and cross sections of structural elements for a concrete frame.*

Cross sections of structural elements with steel reinforcement are presented in figure 3.38.a. Both sections have been discretized using 20 layers with different thickness. Layer's thickness has been adjusted to the position of the steel reinforcement.

Also, steel reinforcement's location is being shown in figure 3.38.b. As can be seen, layers `01, 06, 09, 12, 15` and `20` do not contain steel reinforcement, whereas layers `02, 04, 17` and `19` contain stirrup steel reinforcement (ϕ8mm) of both sections `C-01` and `B-01`. On the other hand, layers `03, 07, 10, 14` and `18` contain the main steel reinforcement for columns (ϕ16mm). Finally, layers `05, 08, 11, 13` and `16` contain the longitudinal steel reinforcement (ϕ16mm) of beams `B-01`.

Figure 3.39.a displays the force displacement response for both analysis, the one carried out by Molina *et al* [103] with four-nodded Lagrangian elements, and the one of the present work. From such figure it can be seen a perfect matching between initial stiffness of both models. A slight difference appears for an applied load close to 50kN, when damage in concrete starts (point A). A higher difference takes place when the steel reinforcement at base of the columns, goes into plastic range (point B). The difference in the obtained results at point B may be due to the difficulties the linear triangular elements exhibit during a plastic process, such effect is fully documented in [32]. Point B of figure 3.39.a is where the reinforced concrete frame presents its higher resistance to lateral forces, beyond such point, a slight difference is presented between both results, the tendency depicted infers a plastic process taking place in the steel reinforcement.

Damage on layer `01` (only concrete) is shown in figure 3.39.b, its evolution shows the same initial behavior as the case studied in section 3.8.1, namely, it starts at the bottom of the columns, and then at the beam-column joint, however, due to the presence of steel reinforcement, a most uniform distribution of damaged elements is achieved. On the other hand, figure 3.39.c depicts the final plastic strain along main reinforcement steel for columns (layer `03`), being evident that steel yields due to the tensile stresses taking place at the bottom of the column.

As a conclusion, shall be remarked the fact that, the proper steel within the frame, gives the structural system efficiency, in terms of lateral loading resistance and ductility.

3.8.3 Reinforced Concrete Frame With Masonry In-fill

The example reproduced in this section, corresponds to an experimental test carried out by Meli, and fully described in [91], where it is intended to reproduce, from an experimental stand of view, the mechanical behavior of a masonry wall confined with two columns and a beam made of reinforced concrete.

Geometry of analyzed specimen is depicted in figure 3.40, where it is presented a lateral view (fig. 3.40.a) and a frontal view (fig. 3.40.b), also it is presented the location of the confining structural elements (`C-01` and `B-01`), the distribution of the masonry units, and the boundary conditions such as, an imposed displacement at the top, and a fixed support at the bottom.

Figure 3.40.b also depicts an overlapping (on red) of the crack patterns of the experimental test [91]. In the present study the masonry in-fill exhibits the typical response that happens for low resistance masonry units, i.e. crack will cross indistinctly throughout masonry unit or mortar.

To reproduce numerically the present model, three simple materials are involved. Mechanical properties used for steel reinforcement already have been presented in previous models (section 3.8.2), on the other hand, mechanical properties of concrete have been evaluated considering a compression resistance equal to $f'_{cy} = 250kg/cm^2$

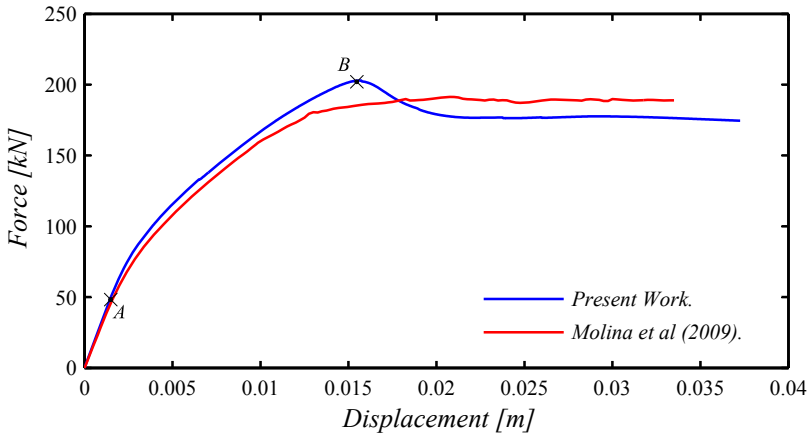

(a) Load-displacement comparison.

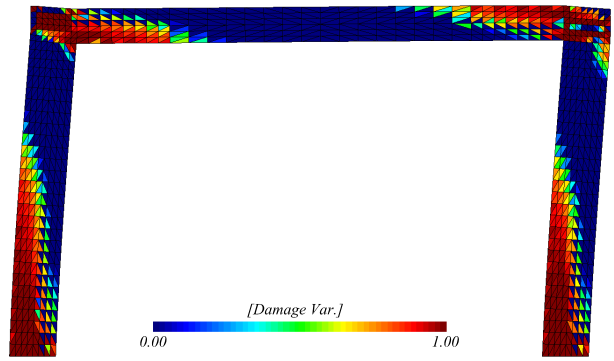

(b) Damage variable on Layer-01

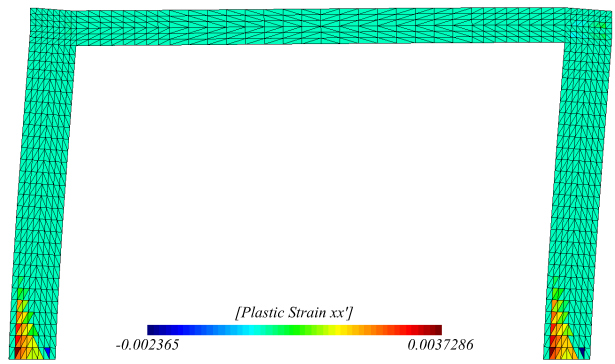

(c) Plastic strain on Layer-03

Figure 3.39 *Numerical results for a reinforced concrete frame.*

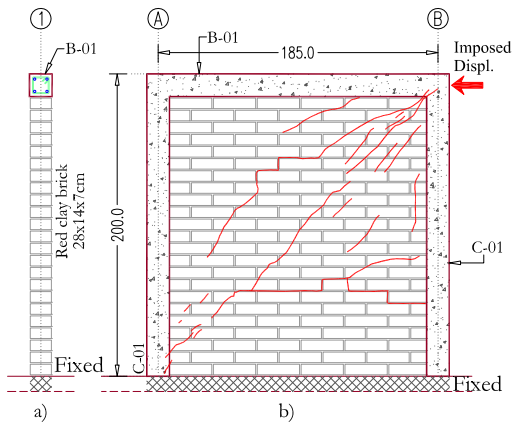

Figure 3.40 *Geometry, loading and boundary conditions for cantilever wall with masonry in-fill [91]*

($24.53x10^6 N/m^2$), to later, evaluate the elasticity modulus according to section `1.5.1.4` of reference [4], namely:

$$E = 4400\sqrt{f'_{cy}} \tag{3.36}$$

where units of equation 3.36 are given in MPa. All other mechanical properties needed are shown below.

- Elasticity modulus: $E = 2.18x10^4 MPa$
- Poisson's ratio: $\upsilon = 0.20$
- Yield criterion: Mohr Coulomb.
- Damage thresholds:

$$\sigma_c = 24.53MPa.$$
$$\sigma_t = 2.45MPa.$$

Fracture energy:

$$G_c = 50.0KPa \cdot m.$$
$$G_t = 5.0KPa \cdot m.$$

- self-weight $\gamma = 2500kg/m^3$

Mechanical properties used to reproduce behavior of the masonry in-fill, have been obtained assuming a compression resistance of $f'_m = 40kg/cm^2$ ($3.92MPa$) and $\upsilon^*_m = 1.1kg/cm^2$ ($0.15MPa$). Hence, elasticity modulus $E_{mx} = 1.37x10^3 MPa$ according to section `2.8.5.2` of reference [6], where

$$E_{mx} = 350f'_{mcy} \tag{3.37}$$

elasticity modulus is evaluated under sustained loads (eq. `2.6`) reference [6].

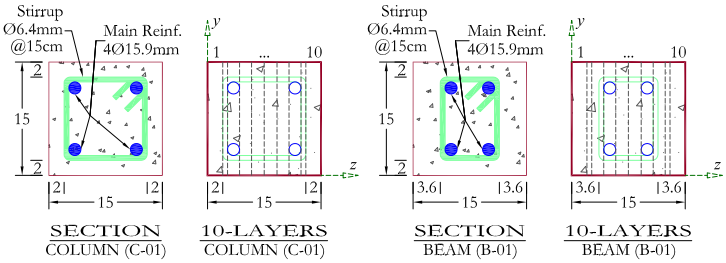

(a) Cross sections of structural elements

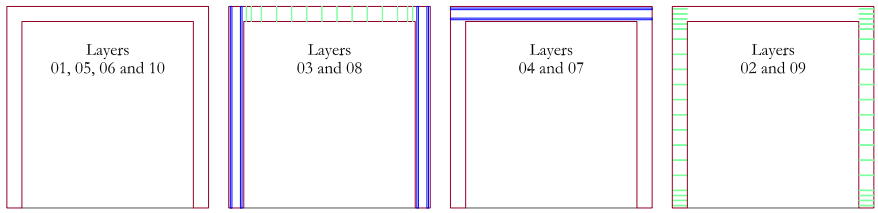

(b) Distribution of steel reinforced fibers within layers

Figure 3.41 *Distribution of reinforced fibers, and cross section of structural elements for a reinforced concrete frame with masonry in-fills.*

- Elasticity modulus:

$$Emx = 1.37x10^3 MPa$$
$$Emy = 0.73x10^3 MPa$$

- Poisson's ratio: $\upsilon_{xy} = 0.10$, $\upsilon_{yx} = 0.15$
- Yield criterion: Mohr Coulomb.
- Damage thresholds:

$$\sigma'_{mcx} = 3.920MPa \qquad \sigma'_{mtx} = 200KPa$$
$$\sigma'_{mcy} = 1.270MPa \qquad \sigma'_{mty} = 65KPa$$

- Fracture energy:

$$G_c = 20.0KPa \cdot m.$$
$$G_t = 0.2KPa \cdot m$$

- self-weight $\gamma = 1300kg/m^3$

Cross section of confining elements are presented in figure 3.41.a. Both section `C-01` and `B-01` have been discretized using 10 layers with different thickness, since they have been adjusted to the location of the steel reinforcement. General location of the steel reinforcement is displayed in figure 3.41.b, there, it can be seen that layers 01, 05, 06 and 10 do not have steel reinforcement, whereas, layer 03 and 08 contain both beam's stirrup steel reinforcement ($\phi 6.4mm$) and column's main steel reinforcement ($\phi 15.9mm$). On

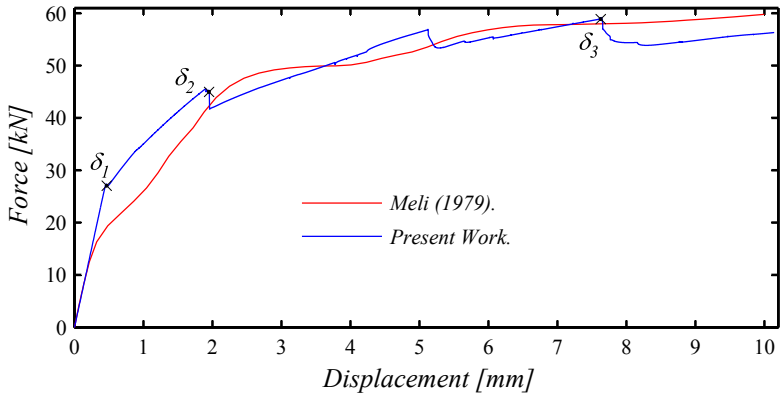

(a) Load-displacement comparison.

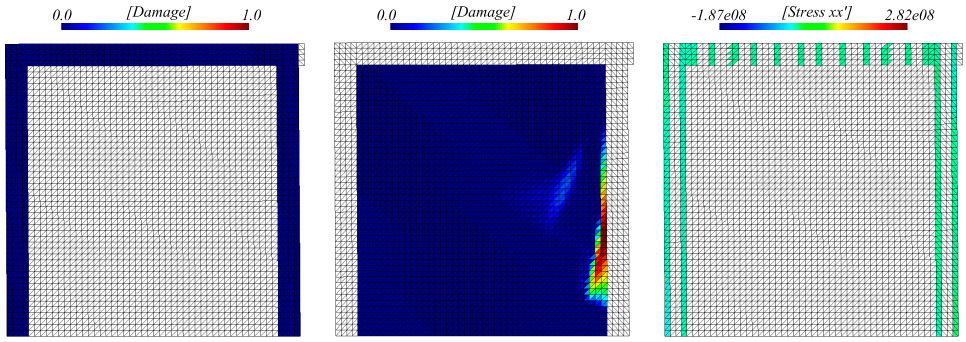

(b) Imposed displacement δ_1= 0.46mm

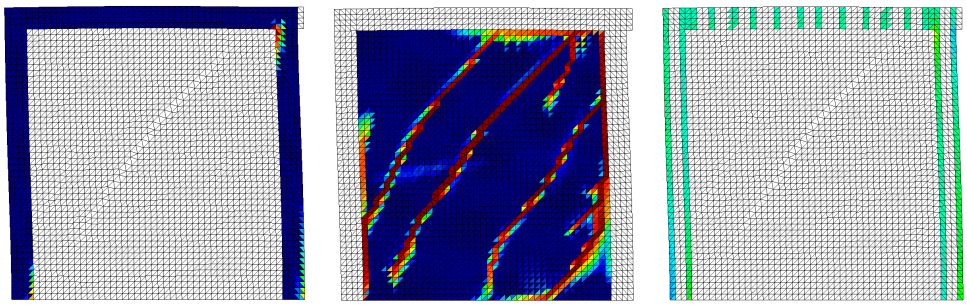

(c) Imposed displacement δ_2= 1.94mm

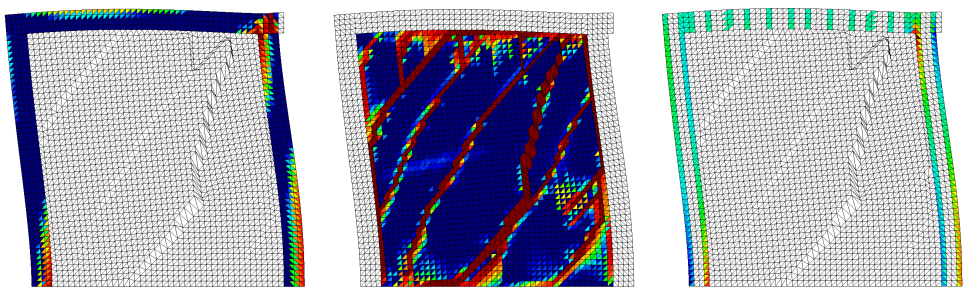

(d) Imposed displacement δ_3= 7.66mm

Figure 3.42 *Numerical results for a reinforced concrete frame with a masonry in-fill.*

the other hand, layers 04 and 07 contain only the main steel reinforcement of beams, and finally, layers 02 and 09 contain only the stirrup steel reinforcement of columns.

The analysis has been performed using two lading stages, the first one corresponds to gravity loads evaluated using the self-weight of the corresponding material, the second loading stage correspond to a pushover analysis intended to predict the force-displacement response of the structure.

Comparison among force-displacement response of both, Meli [91] and the present work is presented in figure 3.42.a. Figure 3.42 from b to d depict the damage state of three different loading steps $\delta_1 = 0.46mm$, $\delta_2 = 1.94mm$ and $\delta_3 = 7.66mm$. Column on the left shows the damage state of layer 01 of the confining elements, column on the center displays the damage state of the masonry in-fill, and finally column on the right shows the stresses in local direction of steel fibers within layer 03.

In both cases depicted in figure 3.42.a, the response is characterized by a high-stiffness zone at the beginning of the loading process. However, such response is followed by a slight decreasing of stiffness due the separation of the masonry corners and the confining elements, as reported by Meli, such behavior was not captured in the present work leading to a significant difference in the force-displacement response, since only one diagonal crack is starting to grow while performing the numerical simulation, as can be seen in figure 3.42.b.

Finally, beyond the point where occurs a slight loss of stiffness (δ_2), characterized by the apparition of several diagonal cracks, a better concordance in the response between both testes is observed.

3.8.4 Raijmakers And Vermeltfoort Test

In this section, we consider the shear wall tests carried out by Raijmakers and Vermeltfoort [170], such specimen consist is a wall with a central opening whose dimensions are 990x1000 millimeters constituted by 18 courses, from which 16 courses are active and 2 courses are clamped in steel beams (fig. 3.43).

Units of the wall have been made wire-cut solid clay bricks with dimension (in millimeters) 210x100x52, whereas mortar joints have 10mm thick prepared with a volumetric cement:lime:sand ratio 1:2:9.

Experimental behavior as reported by Raijmakers and Vermeltfoort [170] is shown in figure 3.44. Where diagonal zigzag cracks arise initially from two corners of the opening at four possible locations. Shortly afterwards, tensile cracks arise from the outside of the wall at the base and the top of the small piers. Under increasing deformation, predominant diagonal cracks occur leading to partial closing of the cracks that were opened before. Finally, a collapse mechanism is formed with failure of the compressed toes, located at the bottom and top of the wall and at the bottom and top of the small piers.

Although micro-modeling, is probably the best tool available to understand and represent the behavior of masonry, due to its nature, it is not always a good choice in terms of computational cost. Such modeling strategy will be used only in this section for comparative purposes, also alternatives presented by Lourenço [79] regarding micro-modeling and Pelà in [130] regarding macro-modeling are briefly described.

Lourenço [79] has proposed a simplified modeling strategy, in which interface elements are used as potential cracks, slip or crushing planes, where all the inelastic phenomena occur. Also, interface elements are considered to model potential cracks within the masonry units. Remarks on the Lourenço modeling strategy are shown below.

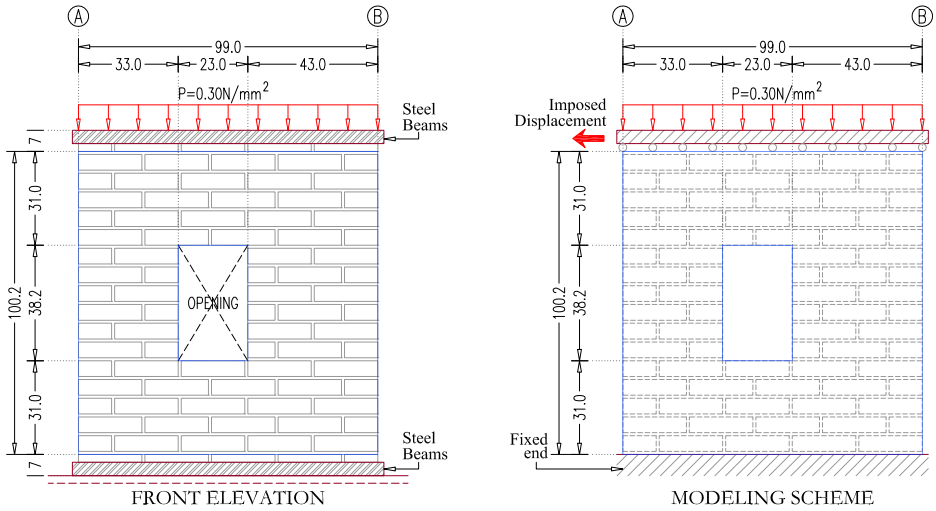

Figure 3.43 *Geometry, loading and boundary conditions for tests conducted by Raijmakers and Vermeltfoort (1992).*

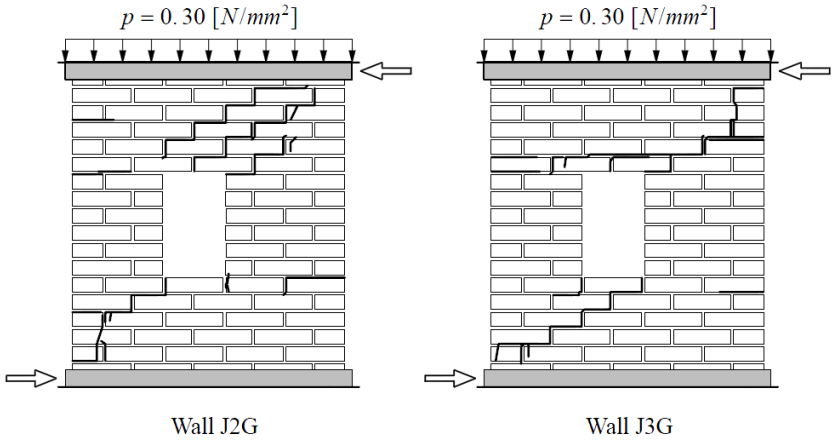

Figure 3.44 *Experimental crack patterns for different tests [79].*

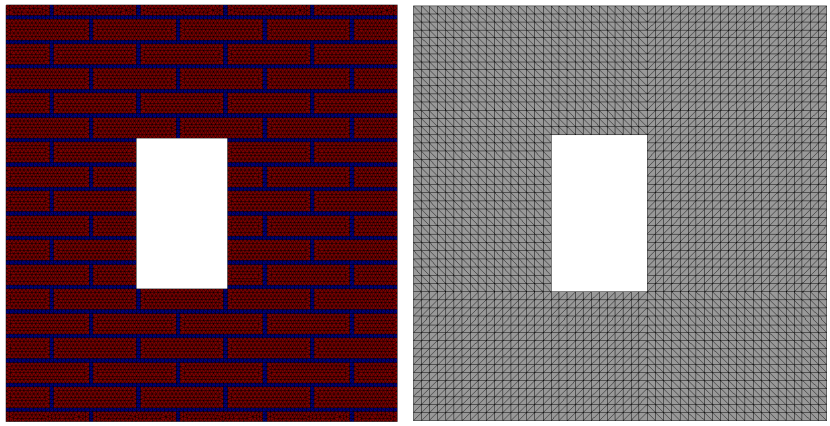

Figure 3.45 *Finite element meshes for micro and macro scale modeling.*

1. Masonry units are modeled with bi-dimensional plane stress continuum elements assuming a linear elastic response.
2. Interface elements are used to represent the mortar joints, allowing discontinuities in the displacement field.
3. Potential and predefined cracks are modeled within the continuum element using zero-thickness interface elements where a non-linear response could occur.
4. In the plasticity framework, a constitutive formulation is presented, including a tension cut-off for mode I failure, a Coulomb friction envelope for mode II failure and a cap mode for compressive failure.

Macro-modeling strategy, on the other hand, brings efficiency in terms of computational performance, although drawbacks are bonded to it. Let us take for instance the work done by Pelà in [130], where a macro-modeling strategy is enhanced with a crack tracking algorithm technique combined with a two-scalar damage model for orthotropic materials, whose results where finally validated via a comparison with shear wall test carried out by Raijmakers and Vermeltfoort [170]. Later on, on this section such results will be reproduced.

Due to computational restrictions, one of the premises along this work is to keep the modeling strategy as simple as possible where good results could be achieved. Hence, no crack tracking technique, nor interface elements will be used. It has been choose to use a slightly different damage model than the one proposed by Pelà, and is the one presented by Paredes [128]. This is a two scalar damage model for orthotropic materials.

In the present study, both a micro and a macro modeling strategies have been conducted, for this purpose two different meshes have been used (fig. 3.45). In both cases, geometry and boundary conditions are the ones presented in figure 3.43, whereas, three loading conditions have been used in the numerical simulation of both models, namely:

a) Self-weight load is applied.

b) Vertical pre-compression uniformly distributed force ($P = 0.30N/mm^2$).

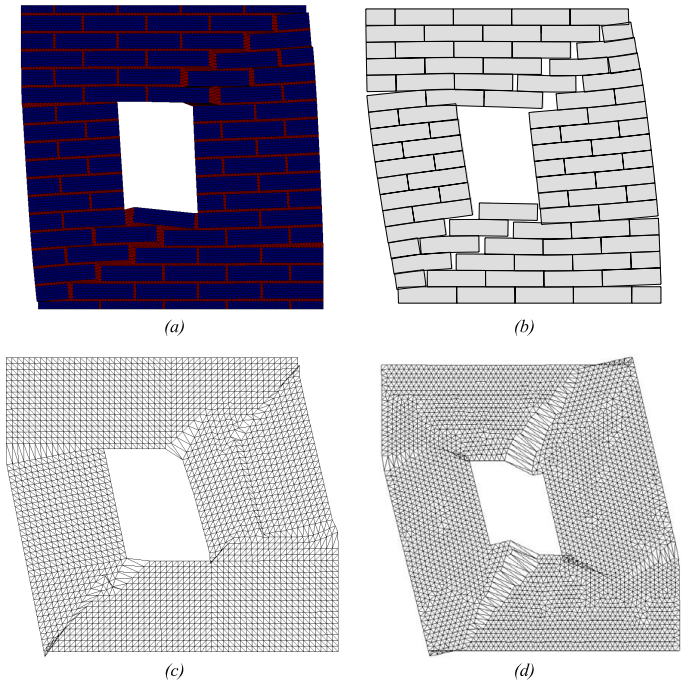

Figure 3.46 *Mesh configurations for deformed models.*

c) Horizontal displacement monotonically increased is imposed, keeping both the bottom and top boundaries horizontal.

Mechanical properties of both mortar joints and masonry units have been taken from [130], although, to induce the phenomena described in [91] (high resistance masonry units bonded with low resistance mortar joints) mechanical behavior of masonry units has been fixed for a linear response.

- Elasticity modulus:

$$E_1 = 7.52x10^3 MPa.$$
$$E_2 = 3.96x10^3 MPa.$$

- Poisson's ratio: $\upsilon_{12} = 0.09$, $\upsilon_{21} = 0.05$.
- Yield criterion: Mohr Coulomb.
- Damage thresholds:

$$f_{11}^+ = 0.35MPa \qquad f_{11}^- = 5.25MPa.$$
$$f_{22}^+ = 0.25MPa \qquad f_{22}^- = 3.75MPa.$$
$$f_{12}^+ = 0.32MPa \qquad f_{12}^- = 4.77MPa\ .$$

- Fracture energy:

$$G_f^+ = 1.00KPa \cdot m$$

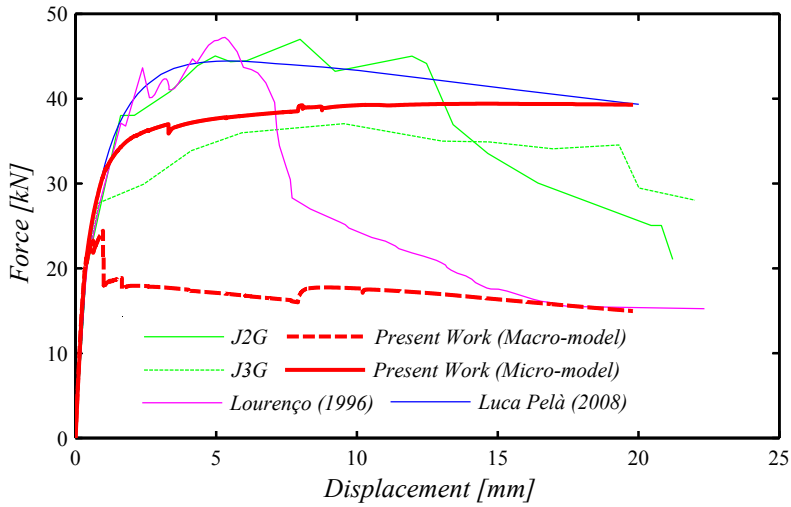

Figure 3.47 *Load displacement comparison of a wall subjected to a imposed displacement.*

$$G_f^- = 100.0KPa \cdot m$$

- self-weight $\gamma = 1300kg/m^3$.

As expected, micro-model notoriously overcome the accuracy of results obtained with a macro-modeling scheme. Results showing the final configuration of the deformed mesh are shown in the figure 3.46, where mesh (a) corresponds to the micro-model reproduced here, (b) corresponds to the deformed configuration presented in [79] by Lourenço, mesh (c) corresponds to the macro-model presented here, and finally, mesh (d) corresponds to the deformed configuration presented in [130] by Pelà.

Using a macro-modeling scheme, a diagonal crack that crosses indistinctly both masonry units and mortar joints is formed along the whole shear wall (fig. 3.46.c), allowing the structural system to dissipate less energy along such crack. On the other hand, using a micro-modeling scheme cracks propagates along mortar joints (fig. 3.46.a) making this result very much alike at the one of figure 3.46.b.

Finally, numerical results obtained have been compared with experimental results of Raijmakers and Vermeltfoort [170], and with the numerical results of Lourenço [79] and Pelà [130] (figure 3.47). As seen, micro-model has reasonably well agreement whereas a poor performance in terms of dissipated energy and overall response is achieved using a macro-modeling scheme.

It is important to distinguish the type of structure addressed in this section, it is a non reinforced nor confined masonry structure, that is why from graph on figure 3.47 it can be concluded that the use of a *plain* macro-modeling strategy is inadequate to reproduce the behavior of such structures. Moreover, from a practical standpoint, the failure mechanism exhibited on the model reproduced by Raijmakers and Vermeltfoort is not desired, since remarks by Meli in [91] pointed out that failure along mortar joints is typical in some masonry walls, such as:

1. Masonry walls with high-resistance masonry units bonded with low resistance mortar joints.
2. Scarce bonding resistance between mortar joint and masonry unit, most commonly presented in both smooth-surface and big-opening masonry units.
3. Walls are not subjected to high vertical stresses.

For today's masonry construction, this failure mechanisms is evidence of a poor technique construction, or a bad choice of the constituent materials, however, case **1** shown in the previous list, is of a great academic importance, since such is the behavior of historical constructions, namely, they are masonry structures with high-resistance shaped-stones bonded with low resistance mortar joints.

As a conclusion we shall remark that the use of a macro-scale as modeling strategy will bring some notorious disadvantage while modeling unreinforced masonry walls formed by high resistance masonry units and low resistance mortar joints. A solution to such drawback tends toward a homogenized scheme, which will not be treated in this work.

Chapter 4

Applications to Large Structures

A set of practical examples are proposed and intended to test the capabilities of the proposed analysis scheme. The proposed models are outlined through structural drawings, sized and structured following the building code regulations for masonry structures in Mexico City. Computational requirements for the analysis of large structures are indicated, in addition to the improvements to the non-linear computing code PLCd [34] for a better performance in terms of memory management and execution times. Finally, a comparison between obtained results and the building code regulation is carried out, highlighting the differences in the obtained results.

4.1 One Storey Construction

The first selected example is relatively simple; it is a one-storey construction with the typical dimensions of a bedroom. It is evident that such construction does not correspond to a *real life* structure, although it will serve to highlight the capabilities of the analysis scheme proposed in this work, for now on, such model will be referred to as `B-OSC`.

Building `B-OSC` is structured with load-bearing walls and a roofing system based on a solid reinforced concrete slab. It has a window in the rear façade, and a window and a door in the front façade. Load-bearing walls have been structured to meet the requirements of the masonry code regulation [6] in force for the Mexico City, namely:

- Masonry units meet the minimum width necessary to prevent buckling problems in slender walls, according to section `5.1.4` of reference [6].
- Reinforced concrete elements whose purpose is confining the load-bearing masonry wall, meet the maximum separation among themselves in plan, in addition, also meet the rates of reinforcing steel necessary due bending and temperature, according to provisions stated in section `5.1.1`, reference [6].
- Openings like doors and windows in masonry load-bearing walls have been reinforced in the whole perimeter using beams and columns, according to provision stated in section `5.1.3`, reference [6].

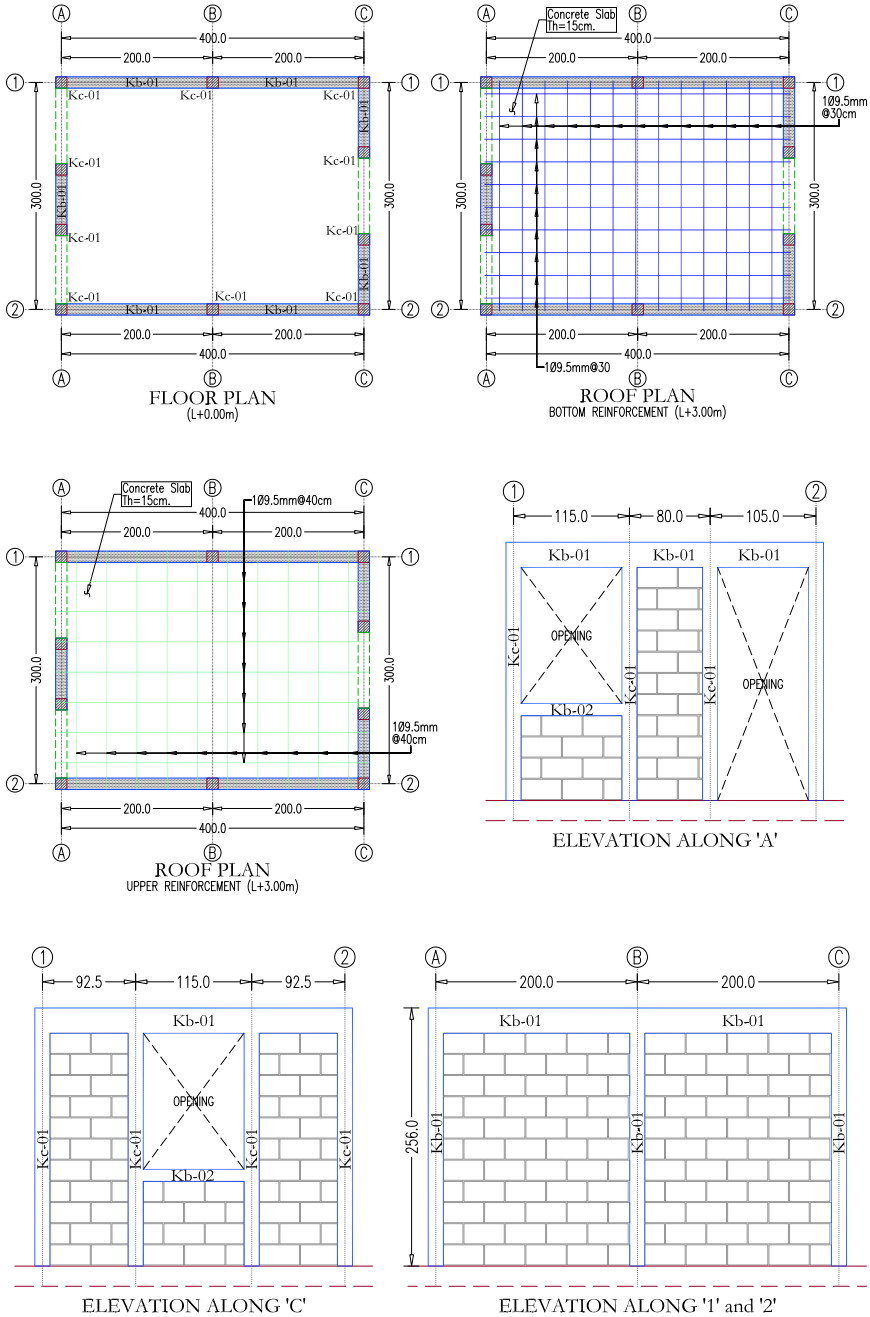

Figure 4.1 *Structural Drawings - One storey construction (units: cm).*

- The thickness of the roof slab meets the requirements necessary to maintain the deflections within the serviceability limits stated in section `3` of reference [4].

4.1.1 Structural Drawings

The structural drawings for the construction `B-OSC`, discussed in this section, are shown in figure 4.1. In such drawings effort has been put to make them as close to *real life* construction as possible, especially regarding the distribution of steel reinforcement, where the simplifications that a structural engineer would make for an easy placement in the field.

Scales used in plan view drawings are 1:100, while the scale for elevation view drawings is 1:75. Typically, in all drawings the diameters of the reinforcing steel rods are shown in millimeters, although they correspond to the British nomenclature, where diameters of 6.4mm, 9.5mm y 1.27mm correspond to 1/4", 3/8" y 1/2" respectively, this will be maintained as a common practice in structural drawings presented along this chapter.

As seen in figure 4.1, the structure has a regular distribution in a plan view, having a substantially symmetrical rigidity in x direction, where stiffness of the whole structure in such direction is given by two walls, both 4.15 meters long, and placed along constructive axis **1** and **2**. In both walls an intermediate column has been placed (axis **B**) in order to meet the maximum separation among confining columns, according to provision stated in section `5.1.1` of the reference [6]. None of such walls have openings.

On the other hand, stiffness along y direction of the structure is asymmetric, since it is provided by three short walls, of which only one, 0.95 meters long, lays over constructive axis **A**, while the remaining two (both 1.075 meters long) lay along constructive axis **C**.

The roof plan drawings show the distribution of reinforcing steel in both directions in which has been endowed the slab. Since it is an isolated slab, more steel reinforcement has been placed in the lower bed, namely, it has been used steel rods of 3/8"(9.5mm) diameter, placed every 30 centimeters. Same diameter has been used in the upper bed, although spacing among them has been changed to 40 centimeters.

In the structural drawings it is also shown the elevation view, the purpose of this, is to achieve a more detailed perspective of the confining elements, such as beams and columns. In the elevation views shown, a modulation is presented using masonry units whose dimensions are 15x20x40 centimeters and the joints are 10 millimeters thick. Once the modulation has been performed, the total height of the walls can be obtained:

- The walls forming the opening of the windows are 101 centimeters height, this is: 4 rows of bricks (or *courses*) plus the height of the beam (15 centimeters).

- The regular masonry walls are 256 centimeters height, this is: 11 courses plus the height of the beam (25 centimeters).

In the elevation view along constructive axis **A** (principal façade) two openings are displayed, one is the window and the other one is a door. Rear façade displays only one opening (a window), whereas no opening is shown in the lateral façades (constructive axis **1** and **2**).

A brief description of the reinforced concrete structural elements involved in the structure of this section is carried out next. In all cases, the scales of the structural drawing presented in figures 4.2, 4.3 and 4.4 is 1:10. Regarding the masonry wall layer

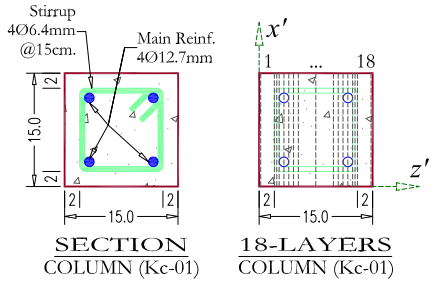

Figure 4.2 *Detailed section of columns (units: cm).*

1	**2**	**3**	**4**	**5**	**6**
2.0	4.0	8.0	12.0	24.0	25.0

7	**8**	**9**	**10**	**11**	**12**
25.0	24.0	12.0	8.0	4.0	2.0

Table 4.1 *Thickness of layers (in millimeters) for masonry walls.*

distribution, it will only be mentioned that has been discretized using an arrangement of 12 layers whose thickness have been detailed in table 4.1.

Columns

The purpose of these structural elements is to endow the brickwork of vertical confinement. In the model of this section, it has only been selected one cross section for columns, which is shown in figure 4.2, and has total dimensions of 15x15 centimeters. Such cross section has been named `Kc-01` and has been endowed with a main steel reinforcement of 4 rods of 1/2 inches of diameter, whereas the secondary steel reinforcement is formed by steel rods of 1/4 inches of diameter with a separation among themselves of 15 centimeters. Cross section `Kc-01` has been discretized using an arrangement of 18 layers whose thickness is presented in table 4.2, and distribution can be seen on figure 4.2.

1	**2**	**3**	**4**	**5**	**6**	**7**	**8**	**9**
2.0	18.0	3.2	3.2	6.35	6.35	6.35	6.35	23.2

10	**11**	**12**	**13**	**14**	**15**	**16**	**17**	**18**
23.2	6.35	6.35	6.35	6.35	3.2	3.2	18.0	2.0

Table 4.2 *Thickness of layers (in millimeters) for columns and beams.*

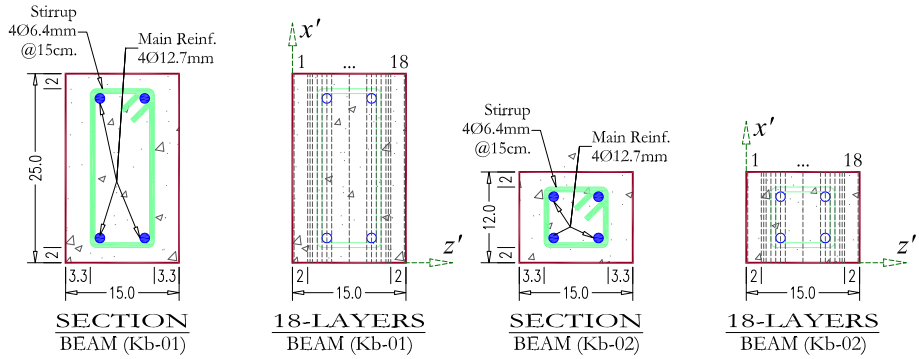

Figure 4.3 *Detailed section of beams (units: cm).*

Beams

Reinforced concrete beams will endow the horizontal confinement to the brickwork. In this case, two different sections of beams have been selected. The first one named `Kb-01` to be used in the *regular* walls (union of the beam with the concrete slab), and the second one named `Kb-02` to be used in the *lower* walls (walls forming the window opening).

Figure 4.3 shows the steel reinforcement pattern and layer distribution of both sections `Kb-01` and section `Kb-02`. The basic difference among them is their height, since in both cases, the main steel reinforcement (4 rods of 1/2" diameter) and the secondary steel reinforcement (rods of 1/4" diameter separated 15 centimeters) are the same. Also, in both cases, the thickness has been discretized using an arrangement of 18 layers (table 4.2).

In both cases, beam sections have a coating for the transverse steel of 33 millimeters (left and right side) and 20 millimeters at the upper and lower part, this is usually done in the field as an adjustment to prevent longitudinal steel overlaps.

Slabs

Although simple materials that make up the concrete slab of the structure were fixed to have a linear behavior, it has discretized along the thickness using a pattern of 20 layers for a total thickness of 15 centimeters (table 4.3). Layer distribution of reinforced concrete slab can be seen in figure 4.4, where also can be noticed the steel reinforcement in both beds and in both orthogonal directions. In all cases, the diameter of the steel reinforcement rods remains the same, this is 3/8 inches, which varies is the separation among themselves. The separation of the steel reinforcement for the lower bed is 30 centimeters, whereas for the upper bed, a separation of 40 centimeters has been used.

4.1.2 Simple Material Properties

As in chapter 3, only three simple materials are needed to perform the analysis of models presented in this chapter, namely: steel, concrete and masonry. Their mechanical and constitutive properties are detailed next.

It should be noted that constitutive equation for both simple materials (concrete and steel) only in the slab are set to be elastic. This has been done to simplify the analysis

1	2	3	4	5	6	7	8	9	10
2.0	8.0	11.2	5.0	5.0	4.75	4.75	9.5	12.4	12.4
11	**12**	**13**	**14**	**15**	**16**	**17**	**18**	**19**	**20**
12.40	12.40	9.5	4.75	4.75	5.0	5.0	11.2	8.0	2.0

Table 4.3 *Thickness of layers (in millimeters) for slabs.*

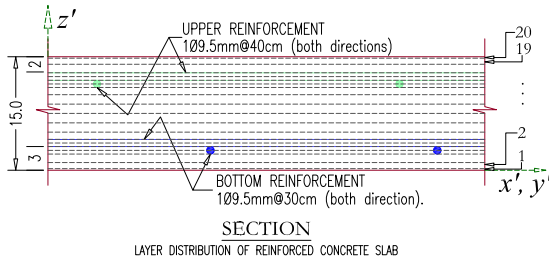

Figure 4.4 *Detailed section of slab (units: cm).*

process, and it has been justified by the fact that in such area no damage is expected.

Mechanical Properties of Steel

The rods used shall be of circular cross section, with corrugations to bring on adhesion with the concrete, in this work, only medium resistance corrugated steel rods ($f_y = 4200kg/cm^2$) will be used. A detailed description of the mechanical properties of the steel considered in this work is presented next.

- Elasticity modulus: $E = 2.1x10^5 MPa$.
- Poisson's ratio: $\upsilon = 0.00$.
- Yield criterion: Von Mises.
- Damage thresholds:

  $$\sigma_c = 420MPa$$
  $$\sigma_t = 420MPa.$$

- Fracture energy:

  $$G_c = 2x10^3 kPa \cdot m$$
  $$G_t = 2x10^3 kPa \cdot m$$

- self-weight $\gamma = 7845kg/m^3$.

Mechanical Properties of Concrete

One of the most important properties of the concrete (from the stand of view of a structural engineer) is its compressive strength. For confined masonry ranges of such

properties varies from 200 to 250 kg/cm^2 (20 to 25 MPa). It is a common practice, due to the cost of high compression resistance concrete, to use a resistance equal $f'_c = 250kg/cm^2$ only for foundation elements, since they are exposed to ground contact and more prone to erosion, on the other hand, a compressive strength of $f'_c = 200kg/cm^2$ is typically used in both confining elements and slabs. In any case, in this work the compressive strength is assumed equal to $f'_c = 250kg/cm^2$.

- Elasticity modulus: $E = 2.5x10^4 MPa$
- Poisson's ratio: $\upsilon = 0.20$
- Yield criterion: Mohr Coulomb.
- Damage thresholds:

$$\sigma_c = 25MPa$$
$$\sigma_t = 3.5MPa$$

- Fracture energy:

$$G_c = 50.0kPa \cdot m$$
$$G_t = 5.0kPa \cdot m$$

- self-weight $\gamma = 2500kg/m^3$

Mechanical Properties of Masonry

The mechanical properties of masonry described in this section, have been obtained assuming that simple compressive strength (f'_{mcy}) of the combination of masonry units and mortar is equal to $f^*_m = 120kg/cm^2$, whereas the maximum shear strength is equal to $\upsilon^*_m = 3.5kg/cm^2$. Once such parameters have been settled, using reference [6] and having into account section 3.2.4 of this work, are defined the mechanical and constitutive properties used to model the masonry elements.

- Elasticity modulus: $E_m = E_1 = E_2 = 600f^*_m = 7.06x10^3 MPa.$
- Elasticity modulus: $G_{xy} = 0.4E_m = 2.825x10^3 MPa$
- Yield criterion: Mohr Coulomb.
- Damage thresholds:

$$f'_{mtx} = 0.35MPa \qquad f'_{mcx} = 5.15MPa.$$
$$f'_{mty} = 0.60MPa \qquad f'_{mcy} = 12.0MPa.$$

- Fracture energy:

$$G_c = 20.0kPa \cdot m$$
$$G_t = 0.5kPa \cdot m$$

- self-weight $\gamma = 1500kg/m^3$.

4.1.3 Structured Composite Materials

In this section, a description of the patterns of steel reinforcement is described. As previously detailed in section 3.7 of this work, in order to generate the composite material for each finite element, the use of a set of SCM is necessary. A description of the layer distribution arrangement and their thickness has been omitted, since they have been previously detailed in tables 4.1, 4.2 and 4.3. Color red has been used to delimit the contour of every SCM, whereas light gray is used to show the FE belonging to the given SCM. For a better reference of the whole structure, light gray is also used to show the rest of the SCM. Color blue has been used to represent the fibers (rods) forming the main steel reinforcement (or *longitudinal* reinforcement). Finally, color green has been used to represent rods of the secondary steel reinforcement.

Images shown in figures 4.5, 4.6, and 4.7 correspond to the SCM-01 repeated for the columns Kc-01 and beams Kb-01 of walls along constructive axis **1** and **2**. As can be noticed in figure 4.5, layers $3, 4, 15$ and 16 correspond to the secondary steel reinforcement (stirrups) of columns Kc-01. On the other hand, figure 4.6 shows fibers information contained in layers $5, 6, 13$ and 14 belonging to the main steel reinforcement of columns, and the secondary steel reinforcement of the beams. Finally, figure 4.7 shows fibers information of layers $7, 8, 11$ and 12 corresponding only to the main steel reinforcement of beams Kb-01.

Fibers or steel reinforcement pattern used for SCM-03 (constructive axis A) and SCM-06 (constructive axis **C**) are closely similar to the used in the SCM-01. Main difference among them is the use of two beam's cross sections, since it is added a new beam in the perimeter of the window, as can be seen from figure 4.8 to 4.13.

From figures 4.14 to 4.17 it is shown the finite element mesh (light gray) and the contour (red) belonging to the SCM-09. Information belonging to the steel reinforcement of lower bed in its both directions is displayed in figures 4.14 and 4.15, while upper bed reinforcement pattern of the slab is shown in figures 4.16 and 4.17. In such figures, it also can be noticed the different separation among steel reinforcement of upper and lower bed.

Finally, figure 4.18 depicts the contours of SCM's 02, 04, 05, 07 and 08. Since it is non-reinforced masonry, there is no fiber information to show and only the finite elements belonging to the SCM's are displayed.

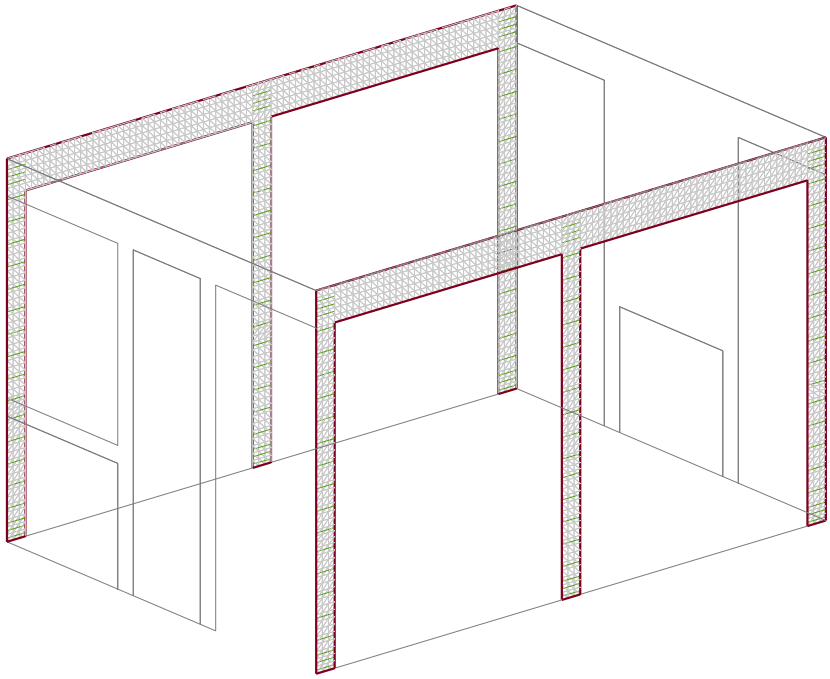

Figure 4.5 *SCM-01 - Layer 3, 4, 15 and 16.*

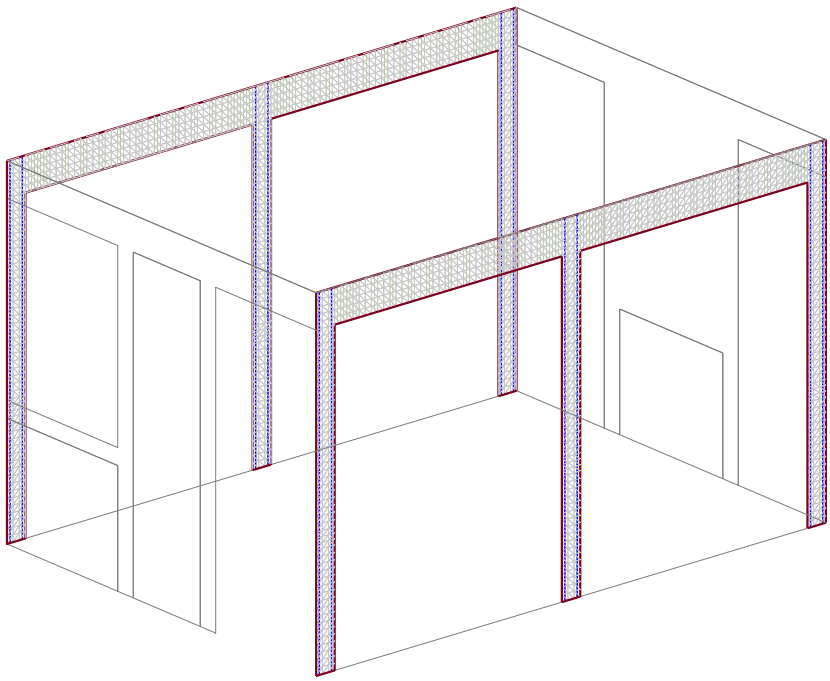

Figure 4.6 *SCM-01 - Layer 5, 6, 13 and 14.*

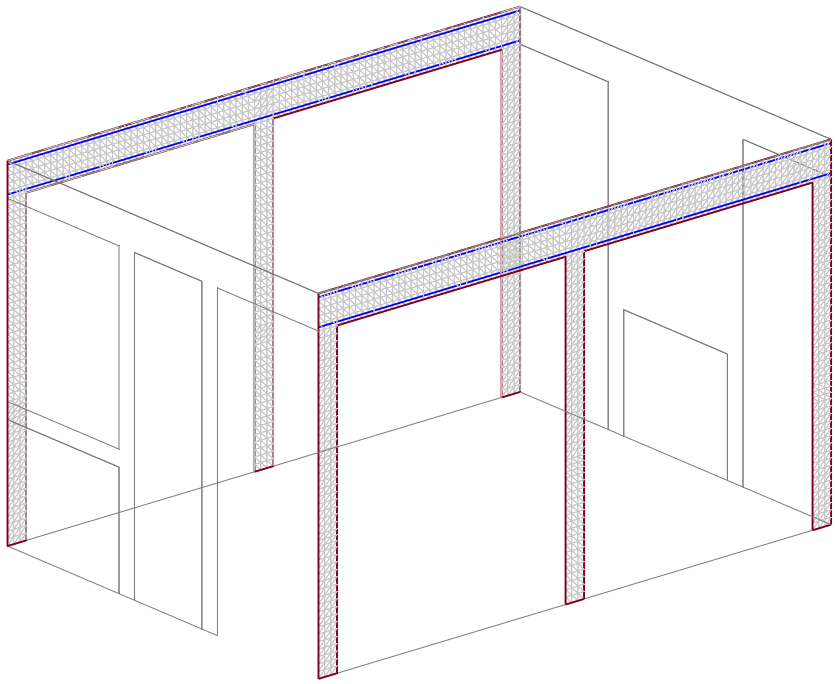

Figure 4.7 *SCM-01 - Layer 7, 8, 11 and 12.*

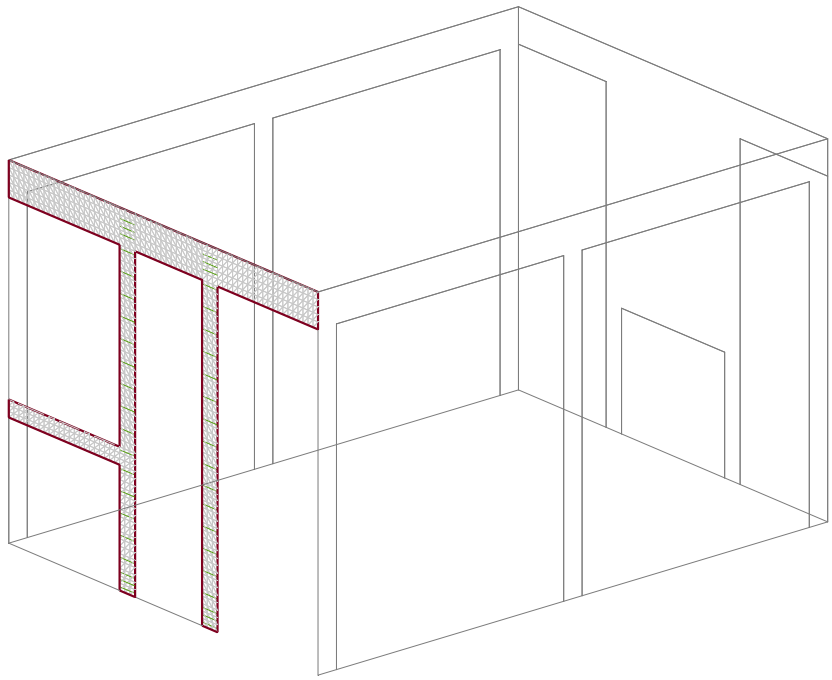

Figure 4.8 *SCM-03 - Layer 3, 4, 15 and 16.*

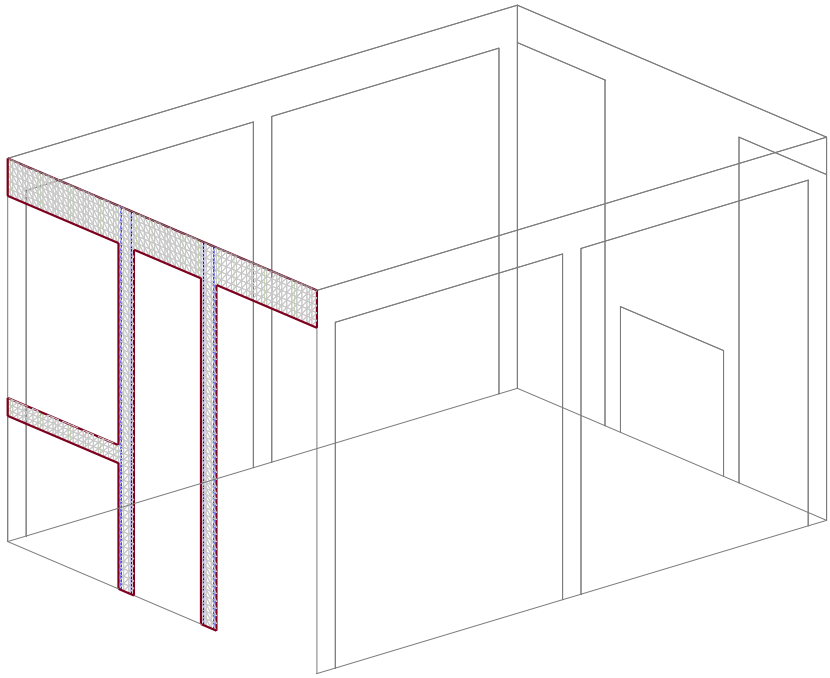

Figure 4.9 *SCM-03 - Layer 5, 6, 13 and 14.*

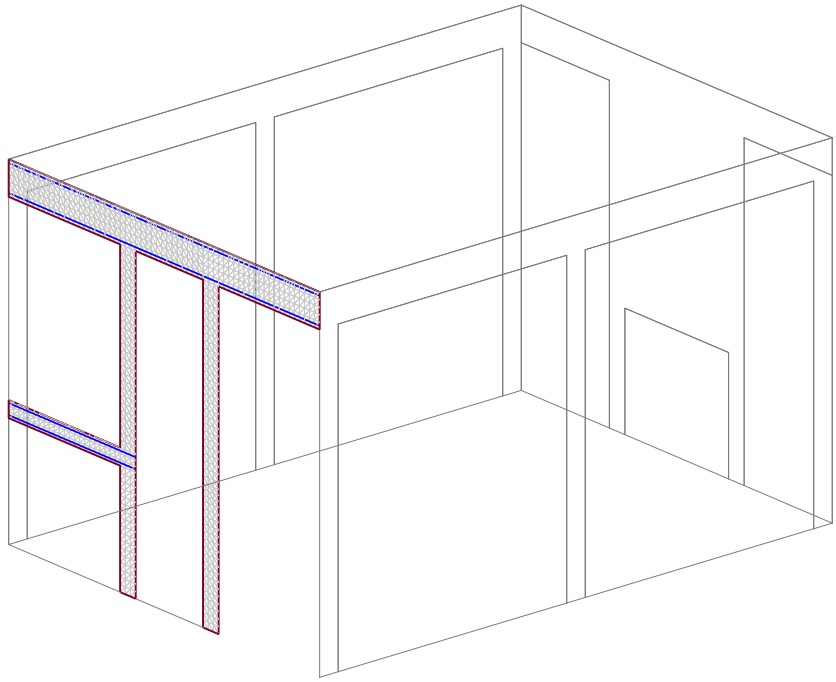

Figure 4.10 *SCM-03 - Layer 7, 8, 11 and 12.*

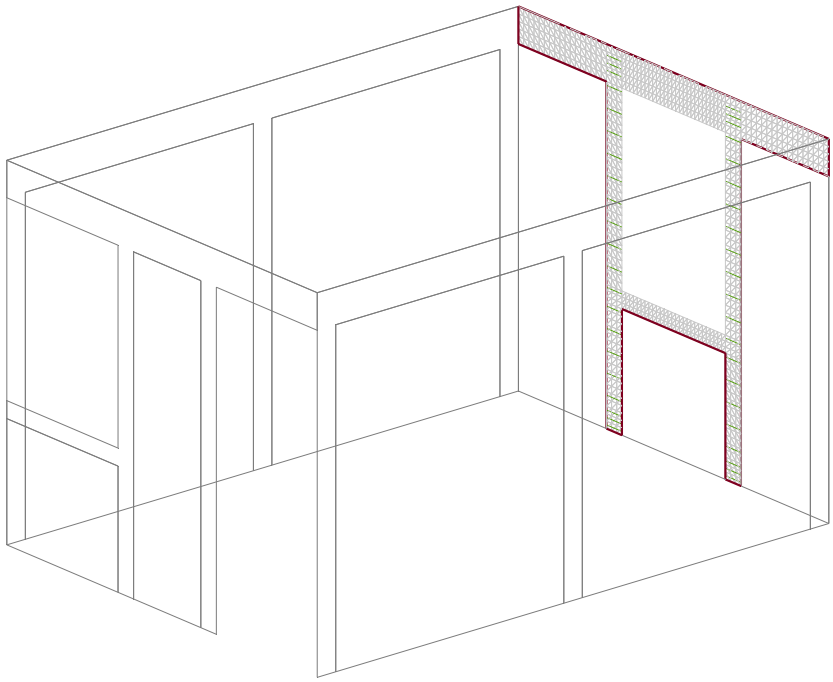

Figure 4.11 *SCM-06 - Layer 3, 4, 15 and 16.*

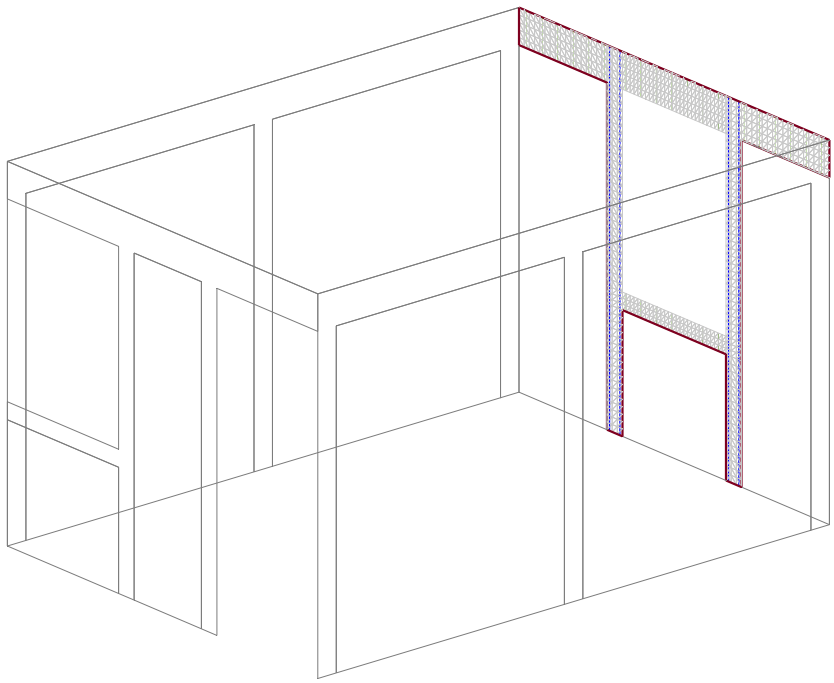

Figure 4.12 *SCM-06 - Layer 5, 6, 13 and 14.*

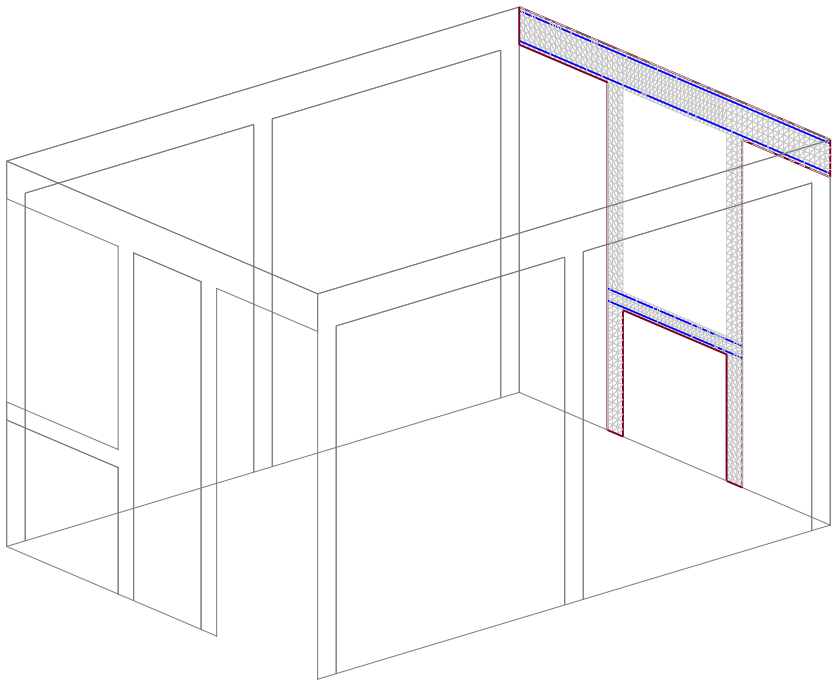

Figure 4.13 *SCM-06 - Layer 7, 8, 11 and 12.*

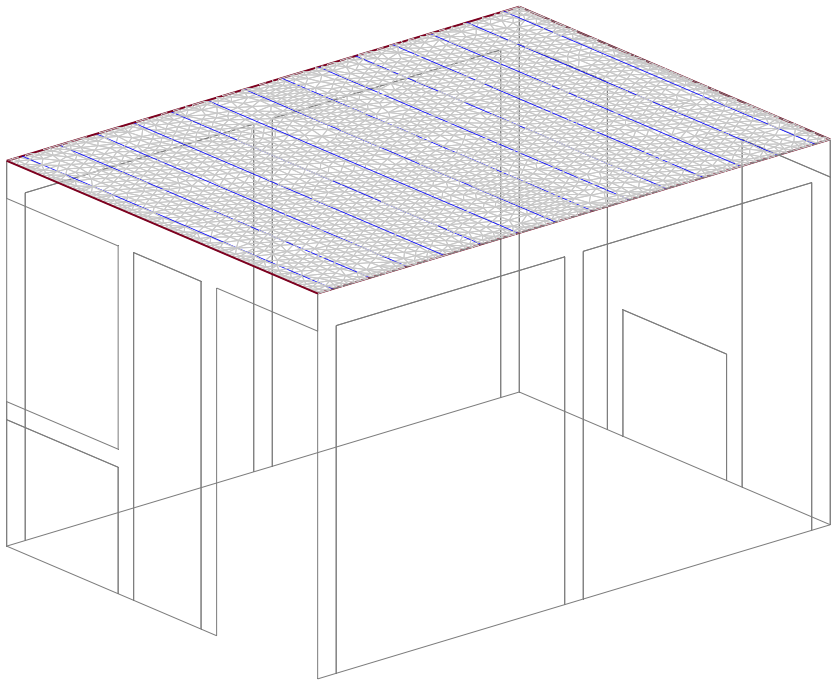

Figure 4.14 *SCM-09 - Layer 4 and 5.*

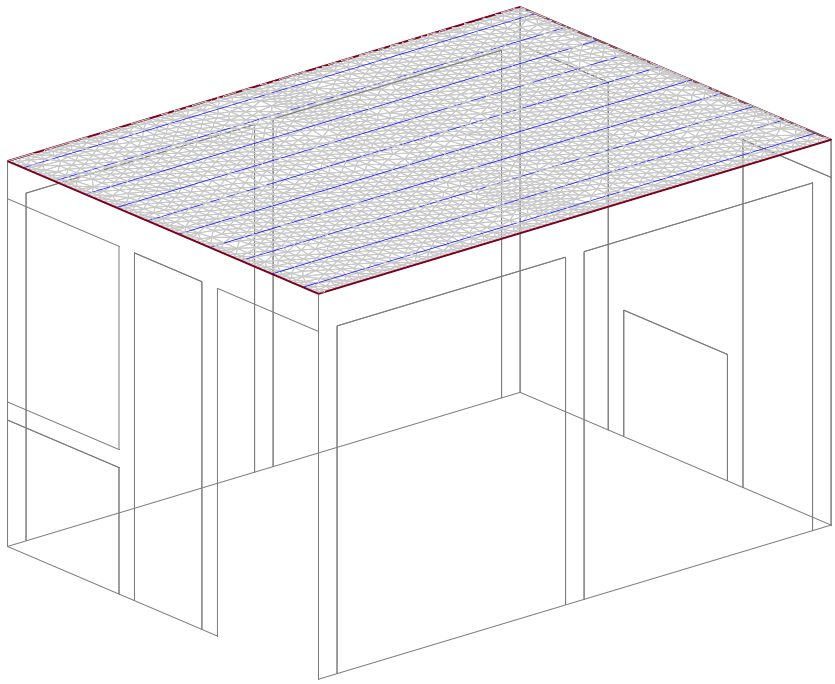

Figure 4.15 *SCM-09 - Layer 6 and 7.*

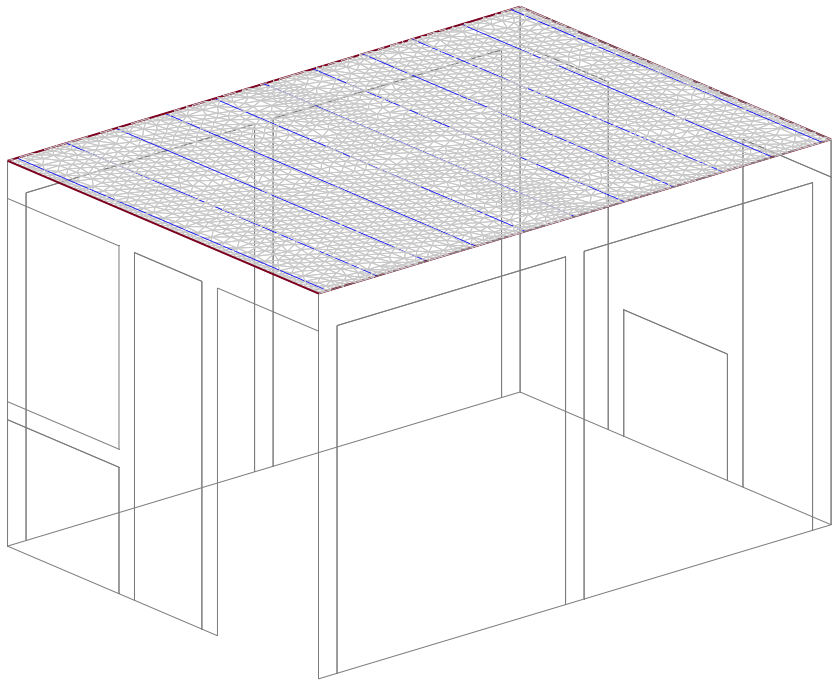

Figure 4.16 *SCM-09 - Layer 14 and 15.*

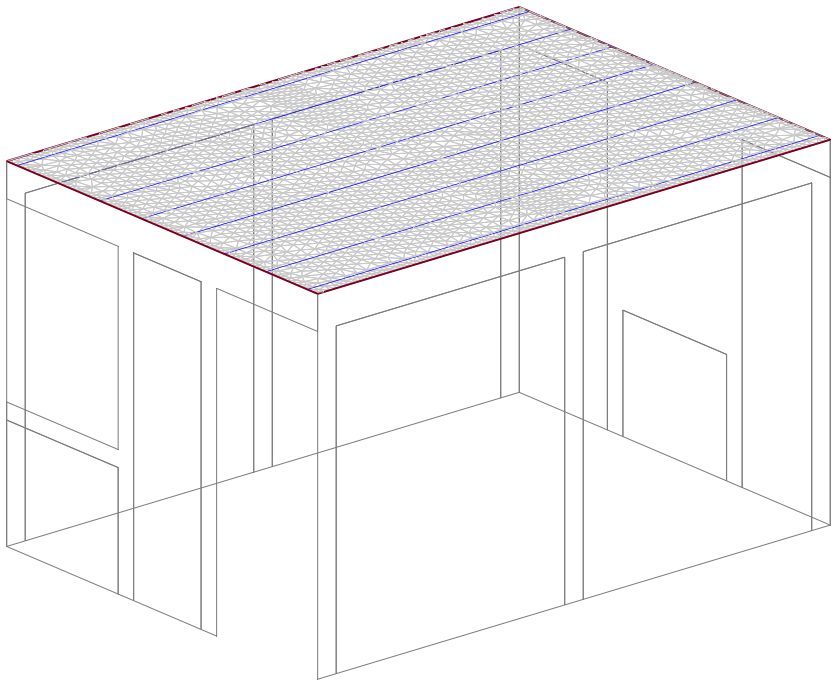

Figure 4.17 *SCM-09 - Layer 16 and 17.*

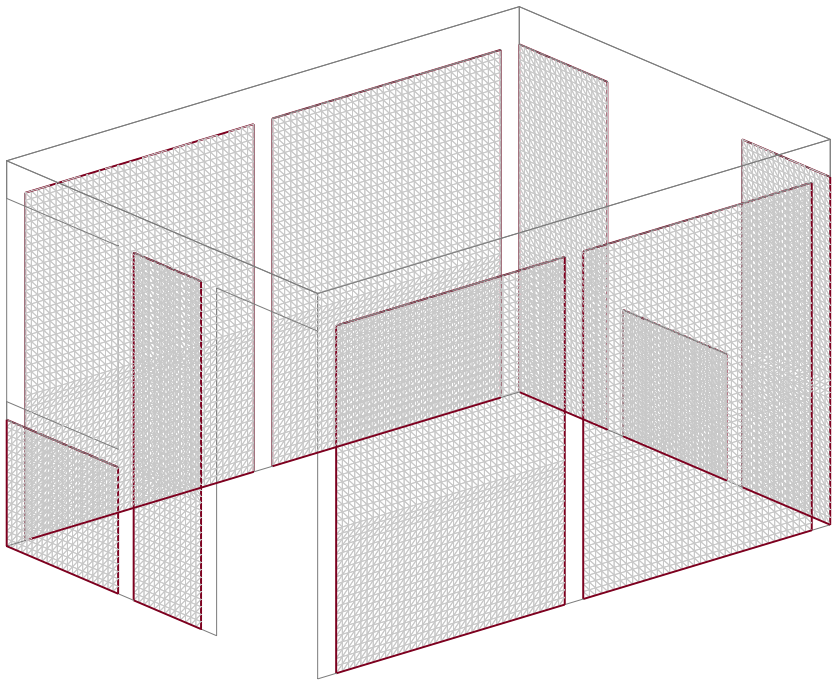

Figure 4.18 *Masonry Material - 12 layers.*

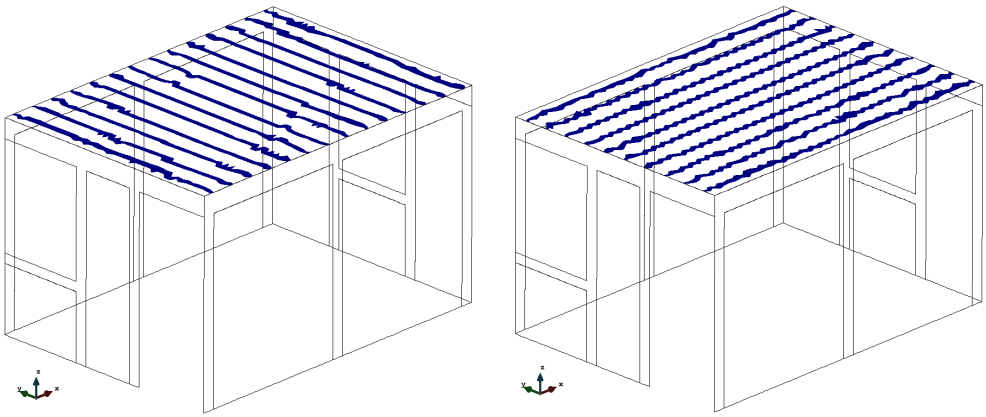

Figure 4.19 *Fibers reinforcement on slab.*

One resulting output of the composite generation is depicted in figure 4.19 for a non-structured mesh, the case in the figure corresponds to the bottom steel reinforcement of the concrete slab, and represents the finite elements that have a volumetric participation of steel, similar drawings are obtained for the remaining layers.

4.1.4 Boundary Conditions

Analysis process has been performed using 3 different loading phases. It is convenient to point out that in none of the 3 loading phases have been used the loading factors that are normally included in building code regulations, neither have been used security factor for designing purposes. Analysis has been performed in this way on purpose, so results obtained using a design code can be properly compared with the results obtained using the scheme proposed in this work.

Fixed Displacements

In all loading phases, the basement of the structure has been set to remain rigidly fixed, hence, neither displacements nor rotations will be allowed.

First Stage Loading Condition: Dead Loading

The first loading step the model is subjected to corresponds to the dead loading condition. This is, the sum of the weight of elements used with structural purpose (bear-loading masonry walls, columns, beams and slabs), plus the weight of the elements belonging to the structure without a structural purpose and only used to fulfill architectural requirements (plaster, paving or infill aggregates).

It is almost mandatory for a structural engineer to start the modeling process by performing a detailed weight analysis of all elements involved in the structure. Let us consider figure 4.20, where a small sketch (on the left) of structural and architectural elements belonging to masonry walls is displayed. It is also shown (on the right) a table displaying thickness and weight of all components involved. Some building code regulations, due to uncertainty in the building process, recommend to add weight to

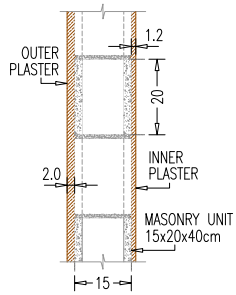

MASONRY BEARING WALL

MATERIAL	THICKNESS (cm)	WEIGHT (kg/m^3)	WEIGHT (kg/m^2)
MASONRY WALL	15.0	1500	225
INNER PLASTER	1.2	1500	18
OUTER PLASTER	2.0	2100	42
DEAD LOAD*	DUE TO CONCRETE		--
	DUE TO MORTAR		20

D_L = 305 kg/m^2

Figure 4.20 *Dead loads - Masonry bearing walls.*

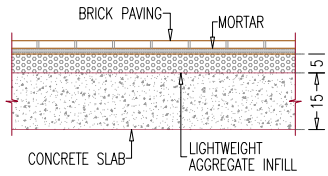

ROOFING SYSTEM

MATERIAL	THICKNESS (cm)	WEIGHT (kg/m^3)	WEIGHT (kg/m^2)
BRICK PAVING	2.0	1500	30
MORTAR	1.50	2100	31.5
AGGREGATE	5.0	1200	60
CONRETE SLAB	15.0	2400	360
DEAD LOAD*	DUE TO CONCRETE		20
	DUE TO MORTAR		20

D_L = 521.5 kg/m^2

Figure 4.21 *Dead loads - Roofing system.*

dead loads, depending on the materials involved. This is the case of code regulation used (reference [2] `art. 197`), that recommends to add 20 kg/m^2 while in the presence of concrete or mortar. In the case shown in figure 4.20 it is only used mortar for the masonry joints, hence, the total weight considered for a masonry wall will be equal to $D_L = 305kg/m^2$.

Figure 4.21 also shows a dead loading analysis; in this case, it is about the roofing system. As in the previous example, on the left is shown a sketch pointing all materials involved, while in the right part a table detailing weights and thicknesses are displayed. Also due the recommendation of article `197` of reference [2], it will be added $40kg/m^2$, yielding to the total weight due to the presence of concrete and mortar $D_L \approx 525.0kg/m^2$.

Second Stage Loading Condition: Live Loading

Live loads, are temporary and of short duration (while compared to permanent loads), such loads are based upon published regulations, in the case of this work, it has been used the *Reglamento de construcciones para el Distrito Federal* [2] to predict them. Such code regulation in its chapter V article `199.V.g`, marks a uniform load of 100 kg/m^2 to be used in the roof for residential homes, being only valid when the slope of the roof is less or equal to 5%.

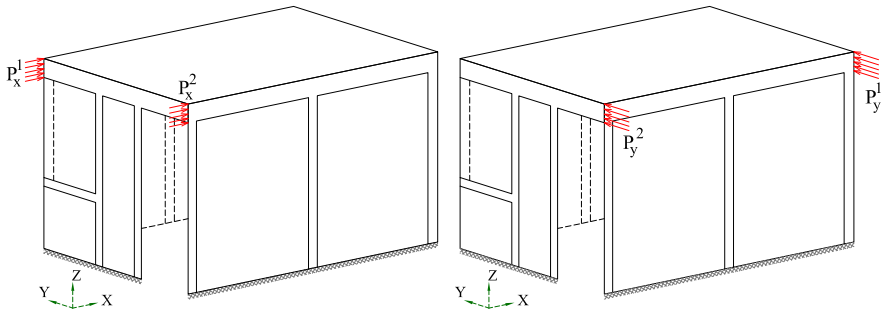

Figure 4.22 *Application loads on pushover analysis.*

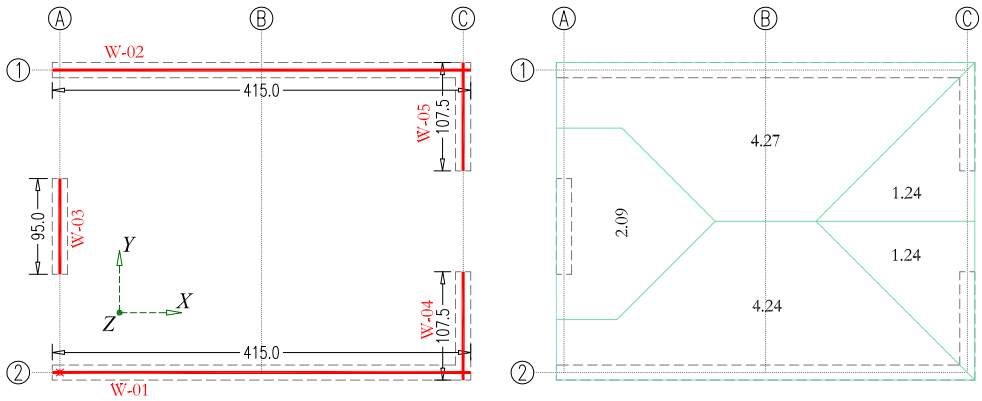

Figure 4.23 *Bearing walls and tributary areas (units: cm).*

Third Stage Loading Condition: Pushover

Finally, the third loading stage corresponds to a pushover applied separately in both orthogonal direction x and y. Hence, for both directions the displacements displayed in figure 4.22 have been imposed and their purpose is to predict the force-displacement response of the structure. Obtained results are detailed in next section.

4.1.5 Results Obtained Using a Design code

As stated in section 4.1.4, both dead and live loads have not been factorized, and no security factors will be used either, this in order to make a proper comparison between obtained result with the proposed analysis scheme and results obtained using the building code regulation [6].

Figure 4.23 (on the left) shows a numeration for masonry walls and their total length, it is important to state a numeration like this, since most of the results presented next will be referred to it. On the right side of the same figure, the tributary load of each masonry wall is presented. The total amount of bear-loading masonry walls is 5.

For the analysis purposes regarding the code regulation [6], the *short* walls that form part of the window have not been considered, nor the stiffness due to reinforced concrete

Wall Number	W-01	W-02	W-03	W-04	W-05
Stiffness(kN/m)	474002.72	474002.72	14787.67	20907.57	20907.57
Shear Strength (kN)	221.53	221.59	52.77	57.65	57.65

Table 4.4 *Stiffness and shear strength of masonry walls.*

confining elements.

It is also necessary to point out that according to the *detailed* analysis shown in reference [6], the walls perpendicular (in plan view) to the analysis direction have to be neglected, hence, in such cases, stiffness and shear strength is equal to 0. Thus, to evaluate the total stiffness and shear strength of the structure in X direction, only have to be considered walls W-01 and W-02 (fig. 4.23), while for direction Y only walls W-03, W-04 and W-05 have been considered.

Stiffness of a Masonry Wall, Using a Design Code (reference [6])

According to reference [6], the stiffness of a masonry wall can be evaluated using equation 4.1

$$K_m^i = \frac{1}{h^i \left[\frac{(h^i)^2}{3E^i I^i} + \frac{1}{A_T^i G^i} \right]} \tag{4.1}$$

where, h^i is the total height, E is the elasticity modulus, I it the inertia momentum, A_T is the gross area, and G is the shear modulus of the wall i, evaluated according to appendix D of this work.

From equation 4.4 it is straight that steel reinforcement and concrete section of the confining elements are neglected.

Shear Strength of Masonry Wall, Using a Design Code (reference [6])

Shear strength of an unreinforced confined masonry wall is detailed in section 5.4.2 of the reference [6], and it can be evaluated using equation 4.2

$$V_R = F_R \left(0.50 v_m^* A_T^i + 0.3 P^i\right) \;\leq\; 1.5 F_R v_m^* A_T^i \tag{4.2}$$

where A_t is the gross area of the wall i, v_m^* is the shear strength of the masonry used, P is the vertical load acting upon wall i. Once resistance factors are removed from equation 4.2, it follows that:

$$V_R = v_m^* A_T^i + 0.3 P^i \tag{4.3}$$

where magnitude of P^i is evaluated using the tributary area of the wall shown in figure 4.23 and the slab weight from figure 4.21, A_T^i has been evaluated using the total length of the walls (figure 4.23) and a thickness $Th = 15cm$, finally $v^* = 0.35MPa$.

Table 4.4 shows the stiffness and shear strength of walls involved in the present model, obtained according to the masonry building code regulation [6]. From table 4.4 it also can be inferred the total stiffness of the structure in both orthogonal directions being presented in 4.4.

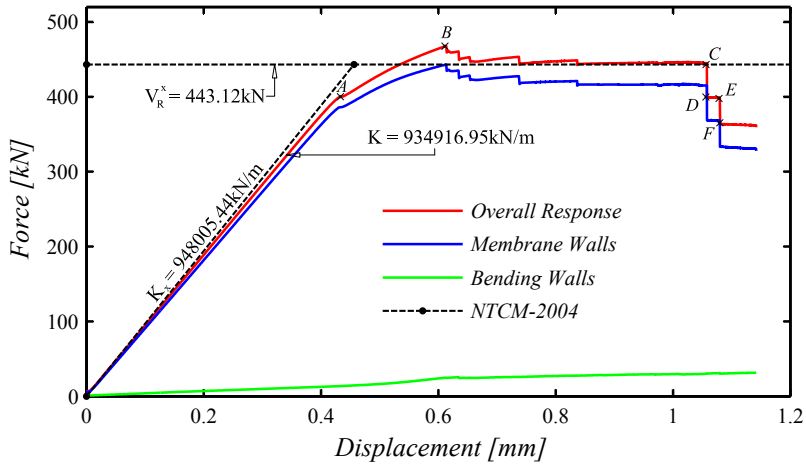

Figure 4.24 *Displacement-force response of model* `B-OSC` *in* X *direction.*

$$\mathbf{K}_x = 948005.44kN/m \quad ; \quad \mathbf{K}_y = 56602.81kN/m \tag{4.4}$$

also from table 4.4 it is possible to obtain the total shear strength of the structure in both orthogonal direction, this is:

$$\mathbf{V}_R^x = 443.12kN \quad ; \quad \mathbf{V}_R^y = 168.07kN \tag{4.5}$$

values shown in 4.4 and 4.5 will be used as a comparison point with results obtained using a non-linear finite element analysis.

4.1.6 Result Comparison

As mentioned above, and according to reference [6], the behavior of the structure in X direction only depends on walls `W-01` and `W-02`. It is easily noticed analysing figure 4.23 that the structure is able to withstand more loading force in X than in Y direction, although this is also confirmed in equation 4.5.

X Direction Analysis

The response of the structure when an imposed displacement has been applied in X direction (figure 4.22 on the left) will be described using the graph of figure 4.24. There, the combined response of walls `W-03, W-04` and `W-05` will be referred as *shell-acting* walls, or simply *shell* walls (green), since their ability to impede displacements in X direction is given by their flexural stiffness, in other words, such walls act like a cantilever beam whose height is equal to the thickness of the masonry wall when a load is applied in X direction. On the other hand, the combined response of walls `W-01` and `W-02` is referred as *membrane-acting* walls or simply *membrane* walls (blue), since their ability to prevent displacements in X direction is given by their membrane stiffness acting as cantilever beams whose height is equal to the corresponding length of the masonry wall. Finally, in red is shown the combined response of both *membrane* and *shell* walls.

In graph from figure 4.24 can be noticed the well agreement among the stiffness evaluated using reference [6] (black hidden line) from equation 4.4, and total stiffness of masonry walls evaluated with the proposed scheme of this work (red), even though neither concrete or steel stiffness are considered by reference [6]. Not only stiffness shows a reasonably good agreement, also total shear strength of the structure, that in the case of reference [6] is defined as the point where non-linear process begins. Total shear strength in figure 4.24 is represented as an black horizontal line whose value equals to $\mathbf{V}_R^x = 443.12kN$ (equation 4.5).

The graph shown in figure 4.24 also confirms reference [6] regarding the low stiffness presented by *bending* walls and that have to be neglected for analysis and design purposes. In order to carry out a proper description of the displacement-force response graph, it has been divided into 6 segments, this is:

- Segment $\overline{\mathbf{OA}}$, where the elastic response occurs.
- Segment $\overline{\mathbf{AB}}$, where the first crack appears, reaching the maximum shear strength of the entire structure in x direction at point **B**.
- Segment $\overline{\mathbf{BC}}$ corresponds to the process of spending the entire capability of masonry walls to support lateral forces, beyond **C** point, high discontinuities are expected, since the resistance due lateral forces are only provided by the confining elements.
- Segment $\overline{\mathbf{CD}}$ is a sudden lost of stiffness due the rupture of confining elements at one of the points where the loads have been applied, which is point P_x^2 from figure 4.22.
- Segment $\overline{\mathbf{DE}}$ can be described as a small amount of lateral force that the structure is able to support until the next rupture of a confining element occurs.
- And finally, segment $\overline{\mathbf{EF}}$ which is the sudden rupture at point P_x^1 (figure 4.22).

Figures 4.25 and 4.26 are a set of images displaying the undergoing deformation process of the entire structure when a lateral displacement in X direction is applied. Figures 4.25 are from a frontal perspective where mostly can be appreciated the principal façade and the masonry wall `W-01`, on the other hand, the isometric view of figure 4.26 correspond to the rear part of the model, where walls `W-02`, `W-04` and `W-05` are shown. In all cases the deformation has been amplified 200 times, although images of cases *a* correspond to the undeformed mesh. The difference among both figures is the perspective from where the structure is being viewed, and there is a correspondence among undergone deformation, hence, for reference purposes, figure 4.25.b or figure 4.26.b could be used indistinctly, or figure 4.25 and figure 4.26 for that matter.

Figure 4.25.b correspond to a damage state when imposed displacement is equal to $0.58mm$, can be noticed a diagonal crack propagating from the joint of the masonry wall and the middle of the column `Kc-01`. Also can be noticed a slight damage due flexural stresses in the lower part of some walls in principal façade. The state of undergone deformation depicted in figures 4.25.b correspond to point between segment $\overline{\mathbf{AB}}$ from figure 4.24.

Figures 4.25.c and 4.25.d correspond to a damage state where imposed displacements are equal to $0.64mm$ and $0.70mm$ respectively, this is, in points within segment $\overline{\mathbf{BC}}$. In such figures, a new crack appears in the masonry wall `W-01` only interrupted by the

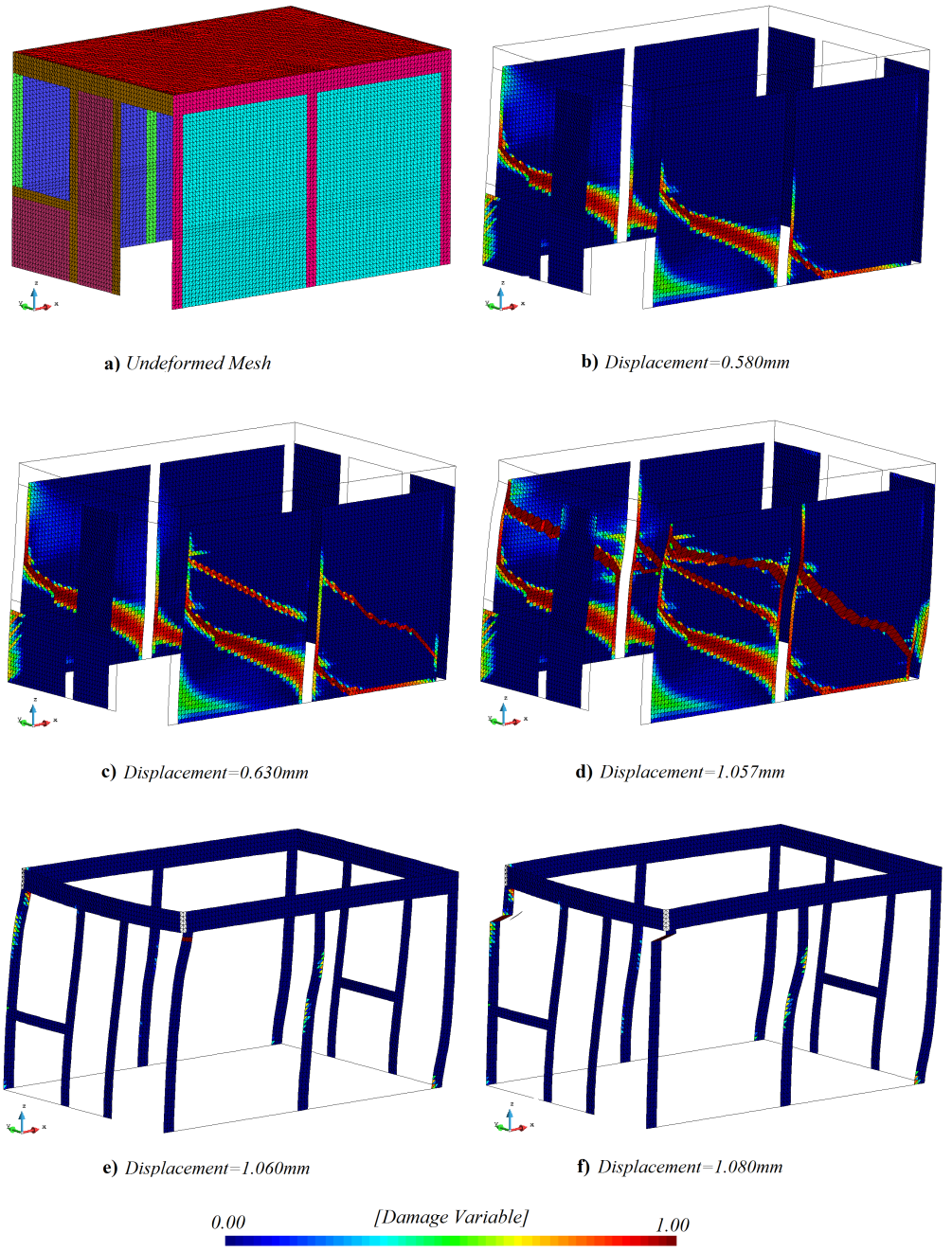

Figure 4.25 *Front isometric view - Damage evolution of masonry walls in X direction.*

presence of column `Kc-01` located at the middle of the masonry wall. Although in the set of figures 4.25 a perspective view from the rear facade is presented, in figure 4.25.c and 4.25.d also can be noticed some cracks in wall `W-02` through the window and door openings.

In figure 4.25.e it is only displayed the damage of confining elements, and such image is intended to represent the instant where point **D** (of displacement-force response in fig. 4.24) has been reached. Same occurs with figure 4.25.f which corresponds to the previously defined point **F**.

As seen from figures 4.25 and 4.26 there is a slight difference between crack patterns of walls `W-01` and `W-02`, this might be due to the asymmetry caused by door and windows openings, or may also be because of a mesh dependency.

In any case, the cracking pattern presented in walls `W-01` and `W-02` is very similar, as a reference let us consider figures 4.25.b and 4.26.b in both cases, the same diagonal crack propagates when a displacement of $0.580mm$ is imposed.

Y Direction Analysis

From the performed analysis in Y direction, the first inference obtained is the low stiffness of the structure while compared with the X direction. Let us consider displacement-force graph of figure 4.27, where the same consideration regarding *bending* and *masonry* walls have been made as in the X direction analysis, but in this case, the *bending-acting* walls are `W-01` and `W-02`, whereas `W-03`, `W-04` and `W-05` are the *membrane-acting* walls. Their combined contribution is represented in blue for *membrane* walls, green for the *bending* walls and finally, the overall response has been represented in red. It is also shown the stiffness (black hidden line) and the total shear strength (horizontal black line) obtained according to reference [6].

The first obvious conclusion from the displacement-force response in Y direction (figure 4.27) is the apparent mismatch among stiffness evaluated using reference [6] and the results obtained using the proposed scheme. Concordance as appears in X directions does not exist, this huge difference (apart from the omission of steel and concrete) is due the contribution of *short* walls (walls forming the windows openings), since they act as stiffeners over the rest of the walls parallels to Y direction, shortening the total height of such walls and completely modifying the equation 4.1. Such stiffening behavior is also described below using figures 4.28 and 4.29.

As in the previous section, where the response of the structure in X direction has been described, in this section, the displacement-force graph (fig. 4.27) also has been divided into segments in order to carry out a proper description, such segments are described in next paragraph.

- Segment $\overline{\mathbf{OA}}$, is where the elastic response occurs, reporting a total stiffness $\mathbf{K} = 291981.95kN/m$ which is 5.15 times the stiffness evaluated using equation 4.1 from reference [6], and as previously described, such difference comes from the stiffening effect of the *short* walls over their adjacent walls. Let us consider table 4.5, where is reported the stiffness evaluated with equation 4.1 of the *shortened* walls, this is, reducing their total heigh in such a way it is not considered from the top of the *short* walls to the basement. If we make such consideration, the reported stiffness using equation 4.1 is $\mathbf{K}_y = 219404.31kN/m$ (table 4.5), which lead to a more precise prediction of the total stiffness.

- Segment $\overline{\mathbf{AB}}$, corresponds to the propagation of the cracks, reaching the maximum

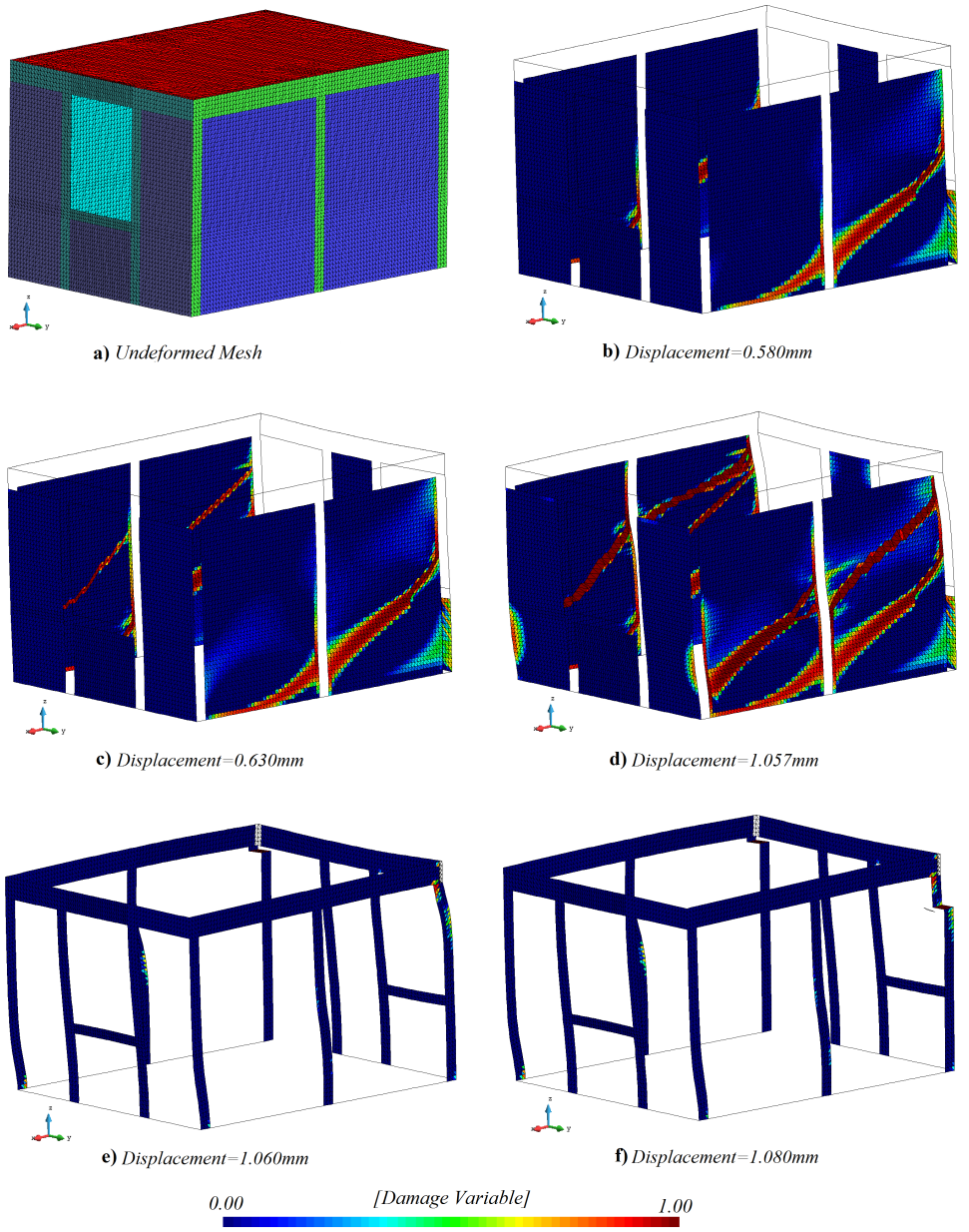

Figure 4.26 *Rear isometric view - Damage evolution of masonry walls in X direction.*

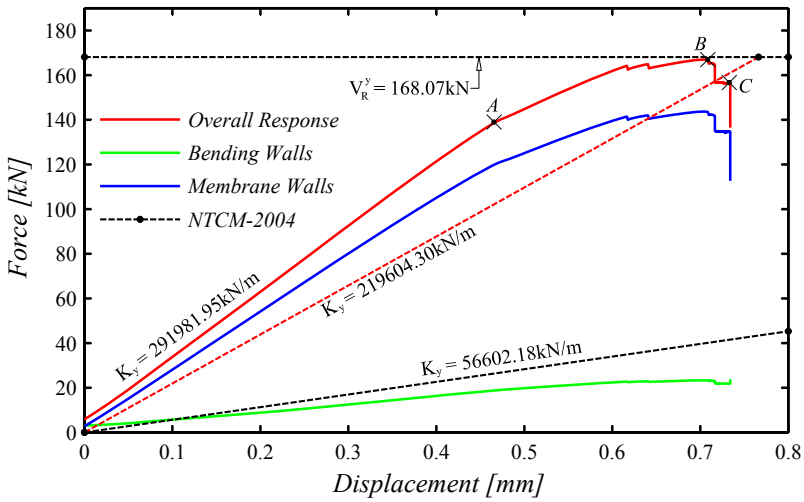

Figure 4.27 *Displacement-force response of model* `B-OSC` *in* Y *direction.*

Wall Number	`W-03`	`W-04`	`W-05`
Stiffness(kN/m)	58733.22	80335.54	80335.54

Table 4.5 *Stiffness and shear strength of shortened masonry walls.*

shear strength of the structure at point **B**. It can be appreciated a well agreement among both shear strengths, the one evaluated using reference [6] and shown in equation 4.5, with the maximum shear strength obtained using the proposed scheme.

- And finally, segment $\overline{\mathbf{BC}}$ where the resistance of the structure start to decrease, until it reaches **C** point, beyond such point, appears a sudden loss of stiffness due to the rupture at the bottom corner of the confining elements in the walls of the rear façade.

As in previous section, a set of images (figures 4.28 and 4.29) is used to describe the damage evolution of walls while a displacement in Y direction is imposed. Deformation in all cases has been amplified 500 times, except for the case a that corresponds to the reference mesh. The first set of images (fig. 4.28) correspond to an isometric view of the front part of the structure, intended to display the damage in walls `W-02` and `W-03`, whereas the second set of images (fig. 4.29) corresponds to a rear isometric view intended to show the damage on masonry walls `W-01`, `W-04` and `W-05`.

Figure 4.28.b displays a point (at a imposed displacement equal to $0.4726mm$) where the non-linear process starts, as can be seen, a timid damage process starts in wall `W-03` in the union of confining column `Kc-01` with the brickwork. Next, the crack propagates vertically along wall `W-03` (figures 4.28.c and 4.28.d) until it reaches the horizontal confining element at the top (beam `Kb-01`), then the diagonal crack propagates diagonally until it reaches the confining element `Kb-02`. Also in figures 4.28.e and 4.28.f can

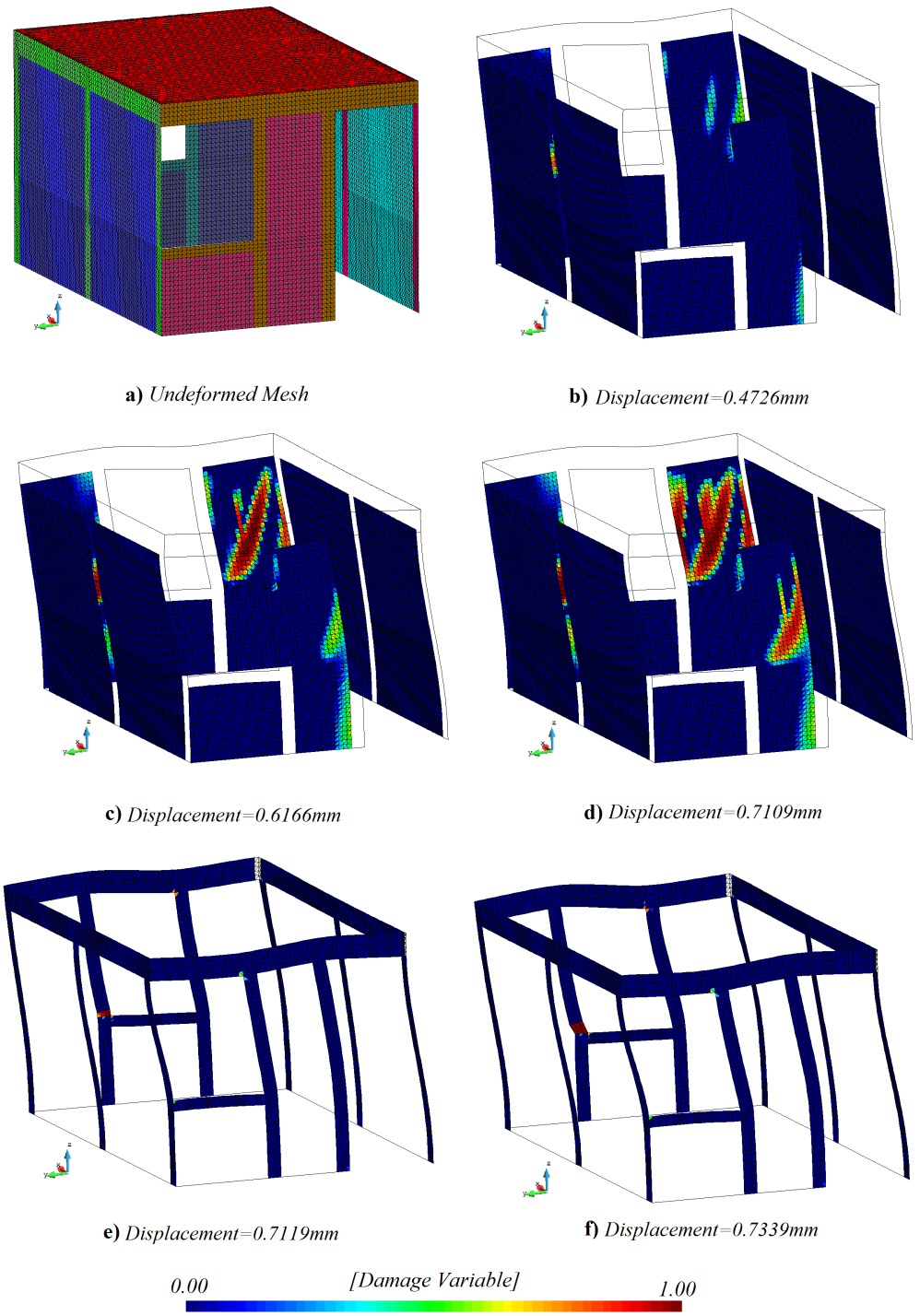

Figure 4.28 *Front isometric view - Damage evolution of masonry walls in Y direction.*

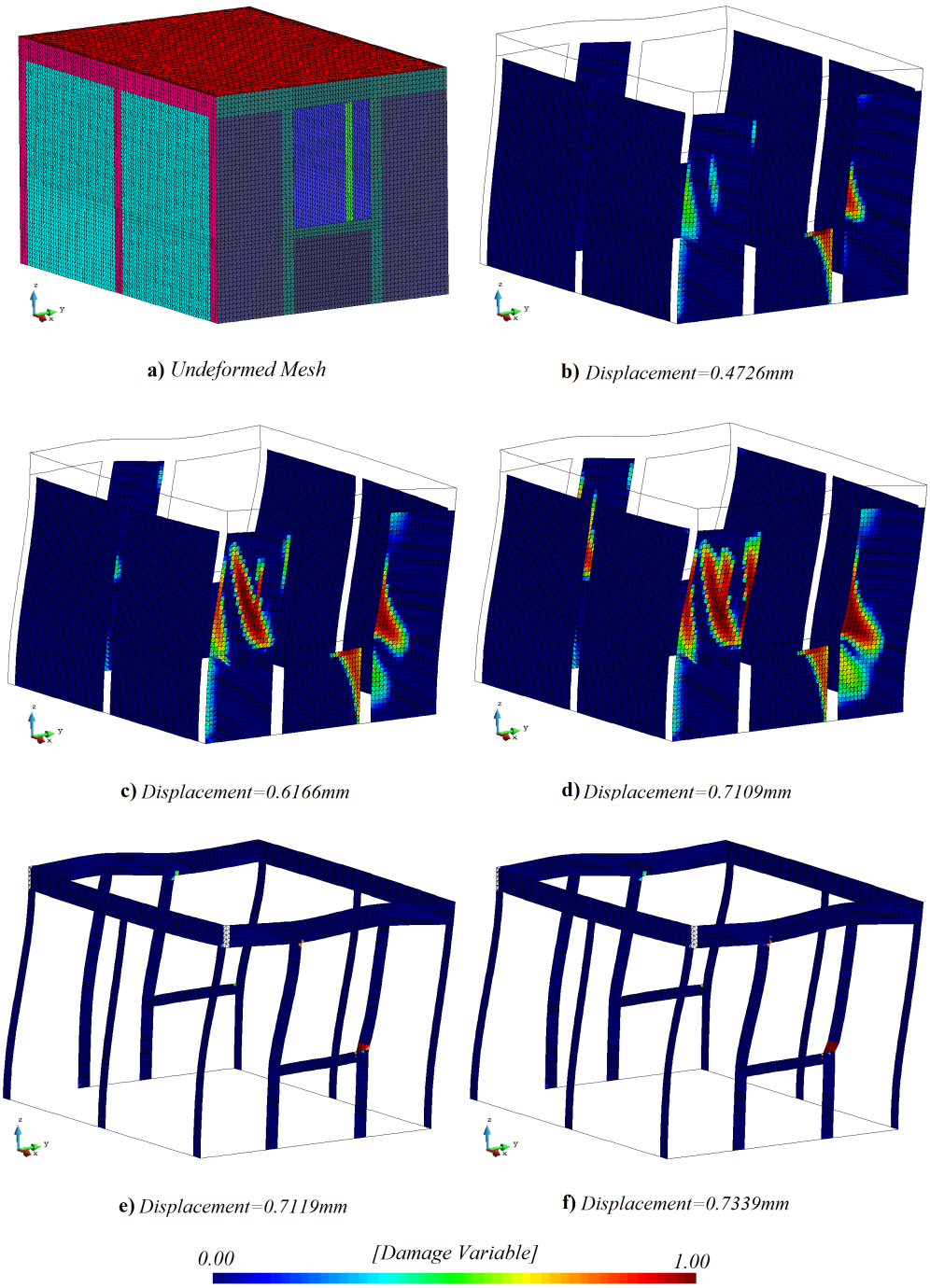

Figure 4.29 *Rear isometric view - Damage evolution of masonry walls in Y direction.*

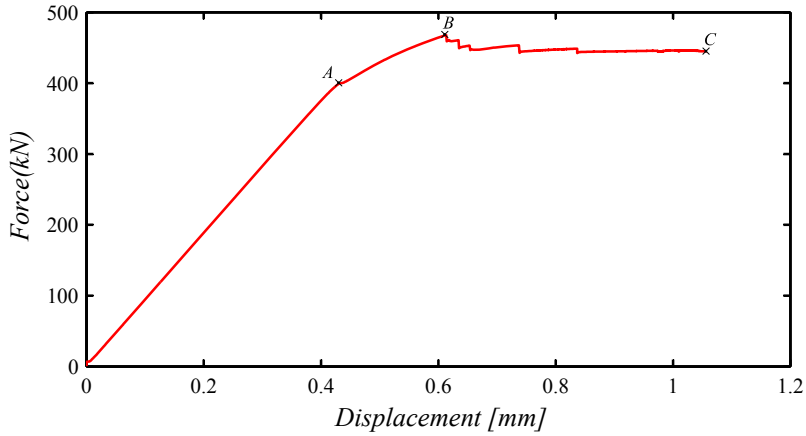

Figure 4.30 *Capacity curve response of model* `B-OSC` *in* X *direction.*

be appreciated a slight damage of the confining element at the corners of the window openings.

It is necessary to point out that the damage process at the bottom (from the bottom of the window opening to the foundation of the wall) of wall `W-03`, is present, although is almost zero due to the small tensional stress which such wall is subjected to in that area. Hence, a *short wall* effect appears in which case, only the upper part of wall `W-03` is subjected to the high tensional stresses that lead to a damage process.

The *short* wall effect is also present in walls `W-04` and `W-05` (figure 4.29), where only the upper part of such walls is subjected to high level of tensional stresses, whereas the bottom part is stiff, leading to small strain states, and consequently to a low level of stresses. Finally, figures 4.29.e and 4.29.f display the damage undergone by confining elements, as can be seen, the damage is more evident in the corners of the window opening.

4.1.7 Damage Assessment for Model B-OSC

Although displacement-force response displayed in figure 4.24 shows an excellent agreement compared with a code regulation, it cannot be clearly appreciated the magnitude of the stiffness and resistance model `B-OSC` has, and in general, masonry structures have. That is why, in the present section it is pretended, with the aid of methodology described in appendix G, to characterize the damages scenarios the `B-OSC` structure could undergo in a high seismic activity zone. The starting point to do so will be the two next assumptions:

1. The capacity curve used to characterize the damage scenarios depicted in figure 4.30, corresponds to the displacement-force response in X direction (figure 4.24), where point **C** corresponds to a complete damage scenario according to classification of RISK-EU [132].

2. It is assumed that model `B-OSC` is located somewhere within the European Union whose soil is **D**, type **1**, with peak ground acceleration equal to 0.20_g according to

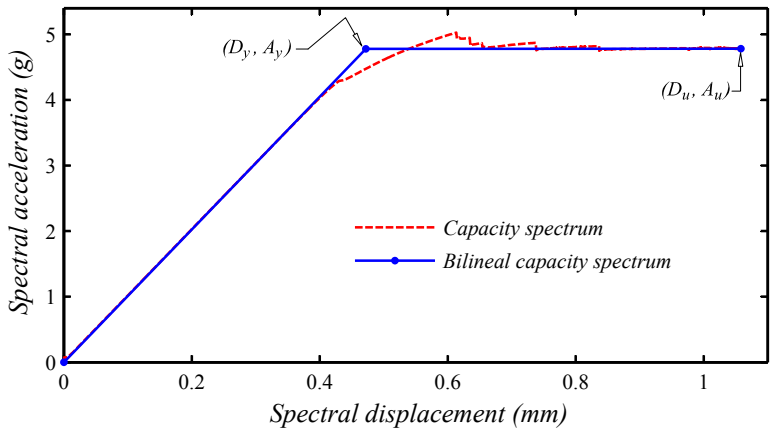

Figure 4.31 *Bilinear capacity curve of building* `B-OSC` *in* X *direction.*

classification of Eurocode 8 [40], the corresponding design spectrum in a $sa - sd$ representation is depicted in figure G.6.

The goal of using the methodology described in appendix G is that the probabilistic damage undergone by a structure during a seismic event can be assess using a *standard* design spectrum and the capacity curve of a given structure. By *standard* design spectrum is meant the ones recommended by Eurocode 8 [40] for countries within the European Union, the ones recommended by reference [3] for Mexico City, or any one for that matter, given in a $T - sa(T)$ representation, where T is vibrational period of a linear system with one-degree-of-freedom and $sa(T)$ is the design acceleration as a function of the vibrational period and the design ground acceleration a_g.

The method described in appendix G is based upon two main simplifications, the aim of the first simplification is to convert a multi-storey model with several degrees of freedom into a model with equivalent stiffness and *one-degree-of-freedom* per storey where the mass of the whole storey is concentrated, such model is usually referred to as a *mass-concentrated* model (figure G.2). The aim of the second simplification is to convert the mass-concentrated model into a *one-degree-of-freedom* model, to do so, it is used the modal decomposition described in appendix G.

Since the model `B-OSC` consists in only one storey, to apply the methodology to assess the probabilistic damage, it is only required to perform the first of the previously described simplifications, hence, $PF_1 = 1$, and $\alpha_1 = 1$ from equation G.4 (appendix G), so spectral displacements sd and spectral accelerations can be obtained using equation 4.6.

$$sd_j = \delta_j \qquad ; \qquad sa_j = \frac{V_j}{W} \tag{4.6}$$

where the total weight of model `B-OSC` is $W = 93.087kN$.

The spectral capacity curve for model `B-OSC` and the bilinear capacity curve obtained using equation 4.6 are depicted in figure 4.32.

Next step, is to obtain the point that represents the seismic demand, or *performance point*, as described in appendix G. One way to obtain such point, is by overlaying the

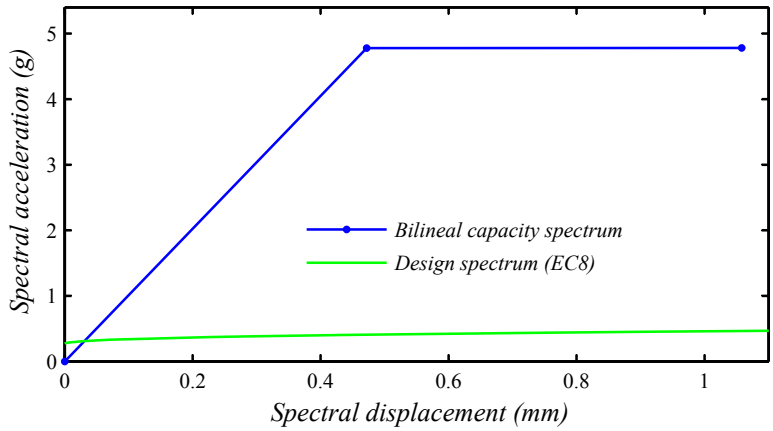

Figure 4.32 *Graphic representation of a linear equivalent approximation for building* `B-OSC` *(X direction).*

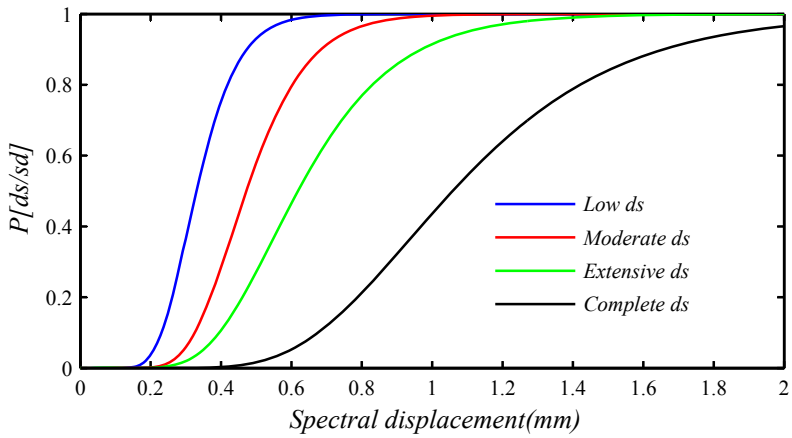

Figure 4.33 *Fragility curves for building* `B-OSC` *(X direction).*

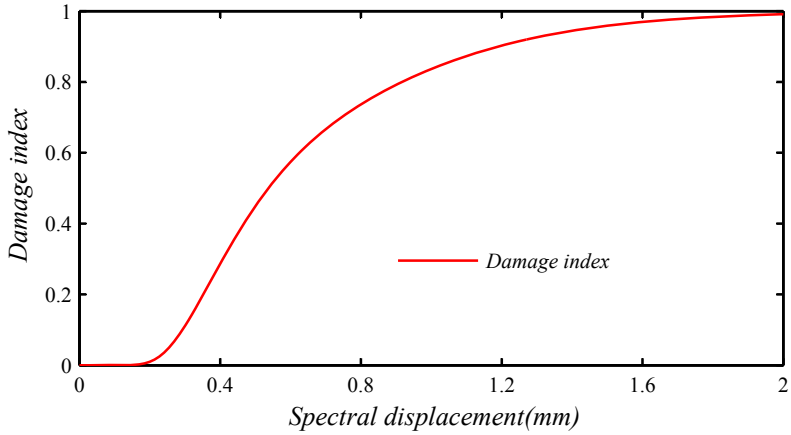

Figure 4.34 *Damage index curve for building* `B-OSC` *(X direction).*

elastic response spectrum in a $sa - sd$ representation and the obtained bilinear capacity spectrum, in figure 4.32 such point represent the crossing point of both spectra, although the shape of the design spectrum may not resemble the one presented in figure G.6, this is due to the magnitude of the obtained displacements.

Using the points (D_y, A_y) and (D_u, A_u) defined in figure 4.31, and equation 4.17, it is now possible to plot the corresponding fragility curves (figure 4.33)and the damage index curve (figure 4.34) for model `B-OSC`.

$$\begin{aligned} ds_1 &= 0.7\, D_y \\ ds_2 &= D_y \\ ds_3 &= D_y + 0.25(D_u - D_y) \\ ds_4 &= D_u \end{aligned} \tag{4.7}$$

The meaning of the obtained performance point $ds_e = 0.03mm$ from figure 4.32, is that structure `B-OSC` can withstand high demanding seismic events with no damage, even in the case of a spectral acceleration equal to 1.0_g, where the corresponding displacement would be $ds_e = 0.0978mm$, which is confirmed by the damage index (fig. 4.34) where the damage starts when the spectral displacement is equal to $ds = 0.16mm$.

4.2 Typical Masonry Building at Mexico City

The geometry, plan distribution and elevation of the studied model in this section, has been adjusted to a masonry building confined with reinforced concrete elements, that typically is designed and built in Mexico City. Such building will be referred from now on as the `B-SSC` model, and fictitiously is being located in the seismic zone `ZIIIa` (placed at the former *lake* area of Mexico City) according the classification depicted in reference [3].

Due to the great necessities for low income housing in Mexico City, a typical practice adopted is the construction of 6 storeys housing buildings. Although the code construc-

tion regulation for Mexico City [2] in the article `101`, subsection `I` states: *buildings that are more than 4 levels high in addition to the ground floor, or height or depth greater than 12 meters from the access to the building, except for single family construction, must have a lift or elevator system for passengers.*

It is evident (from figure 4.36) that, since the proposed building of this section has 6 levels does not meet the previsions stated in [3] `Art. 101.I`. In any case, these issues are beyond the scope of this research work and has been decided to model a building with 6 levels of masonry bearing walls confined with reinforced concrete elements, this in order to exploit the capabilities of the scheme proposed here.

4.2.1 Architectural and Structural Drawings

The proposed housing building is a construction of 6 levels, having two apartments for each storey for a total of 12 apartments with an area of $58m^2$ each. Distribution in plan view is shown in the architectural drawing of figure 4.35.

Figure 4.36 shows an architectural view in elevation of the proposed building. In the present section it has only been reproduced the architectural drawings of figure 4.35 and figure 4.36, although a complete description of both, architectural and structural drawings is presented in appendix C and appendix F respectively.

It is also explained in detail in appendix E the designing process that leads to the structural drawing presented in figure 4.37. In this section only the general aspect of such designing process has been covered, and it is presented in next lines.

1. The geometry of the building (architectural project), is usually defined with the type of simple materials to be used along the construction of the building, also it is necessary to specify the location of the building, in order to define seismic hazard.

2. Bearing masonry walls with structural purpose have to be distinguished, discarding walls with only architectural purpose, like dividing walls or *short* walls forming the windows.

3. Loading conditions such dead loads, additional dead loads, and live loads have to be defined using reference [2]. It is also mandatory to perform an analysis of tributary areas for each bearing wall.

4. The first performed design is through gravity loads, paying special attention to walls in the ground floor, since they are the ones subjected to the highest vertical stresses.

5. An iterative design due lateral loads is performed (for each orthogonal direction). The starting point of such analysis is the assumption that all walls are made of confined masonry. In the case where do exist walls out of the security range stated in [6] reinforced concrete walls will be required as stiffeners, and accordingly, to change the dynamical response of the building. Reinforced concrete wall also lowers the stress the masonry walls are subjected to.

6. The last step of the designing process is the revision due in-plane bending moment of the masonry walls, where the confining columns forming the masonry wall have to be endow with the required amount of steel reinforcement.

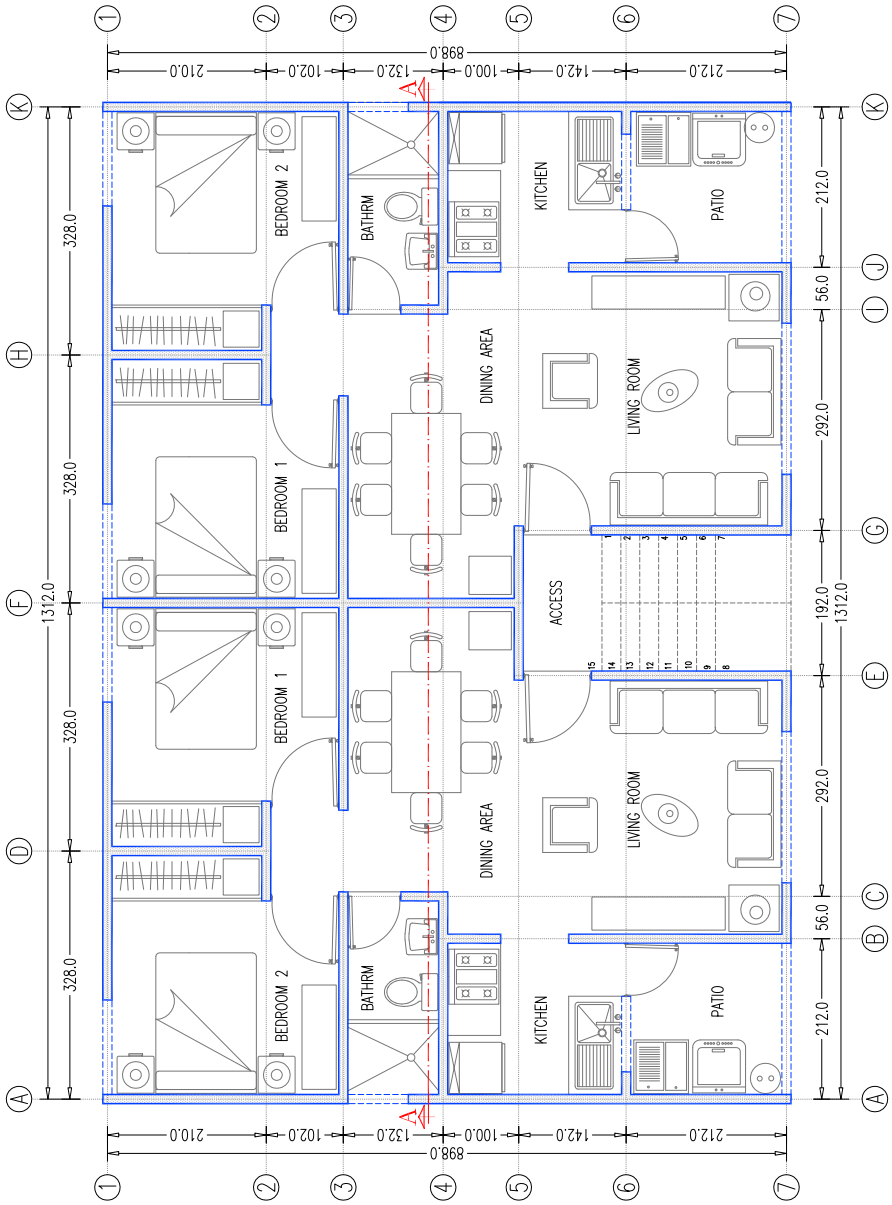

Figure 4.35 *Architectural drawing - floor plan (units: cm).*

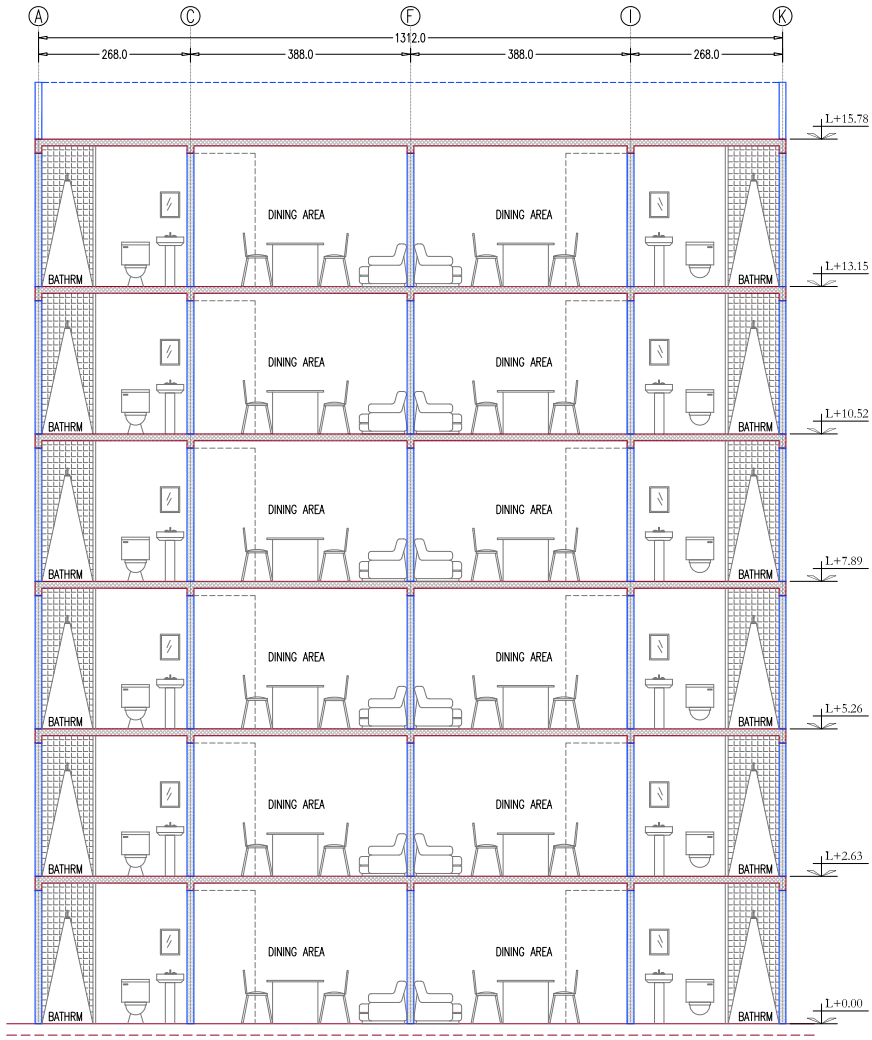

Figure 4.36 *Architectural Drawing - Section A-A' (units: cm).*

1	**2**	**3**	**4**	**5**	**6**
2.0	4.0	8.0	12.0	14.0	20.0

7	**8**	**9**	**10**	**11**	**12**
20.0	14.0	12.0	8.0	4.0	2.0

Table 4.6 *Thickness of layers (in millimetres) for masonry walls.*

7. Finally, structural drawings are generated using the information obtained throughout the designing process.

A tool used in this researching work, in order to make faster the designing process is the *ANEMgcW* program [57] (Analysis of Masonry Buildings). Since the structural analysis program *ANEMgcW* follows the steps depicted in appendix D, it has been used as an aid for analysis and design process, and consequently, to generate the structural drawings shown in figure 4.37. Hence, structural drawings of figure 4.37 become the basis of the upcoming comparisons among the designing process using a code regulation and the analysis scheme proposed in this work.

4.2.2 Structural Elements

The typical structural plan shown in figure 4.37 corresponds to a plan view for the proposed building located in the former *lake* area `ZIIIa` of Mexico City, according to the classification described in [3]. In this section, is carried out a description of the structural elements that conform model `B-SSC`, although not all of the structural elements are shown in figure 4.37, for a full reference appendix F can be consulted.

Masonry Walls

Masonry walls have been structured to fulfill requirements pointed out in reference [6], namely, they meet the minimum thickness required to avoid out-of-plane buckling problems, and they are confined with reinforced concrete elements along the whole perimeter.

Regarding the masonry walls layer's distribution, has to be mentioned that has been discretized using an arrangement of 12 layers with different thickness (table 4.6) for a total thickness of 12 centimeters.

Reinforced Concrete Walls

Drawing 4.37 reports a designation of sections that goes from `CW-01` (`CW` stands for concrete wall) to `CW-10`. Concrete walls from `CW-03` to `CW-10` has been used for constructive purposes, this is, since they are considerably small, it is preferable to make them of reinforced concrete, whereas concrete walls `CW-01` and `CW-02` provide the stiffness the building requires to prove compliance with the requirements for mechanical strength, stability and safety according of reference [3].

In this case, the main purpose of the reinforced concrete walls (or simply concrete walls) is to modify the dynamical properties of the building. Such elements have a very high in-plane stiffness which made them an ideal solution to lower the period of vibrations for a given structure. Not only that, but, due to their stiffness, they lower the

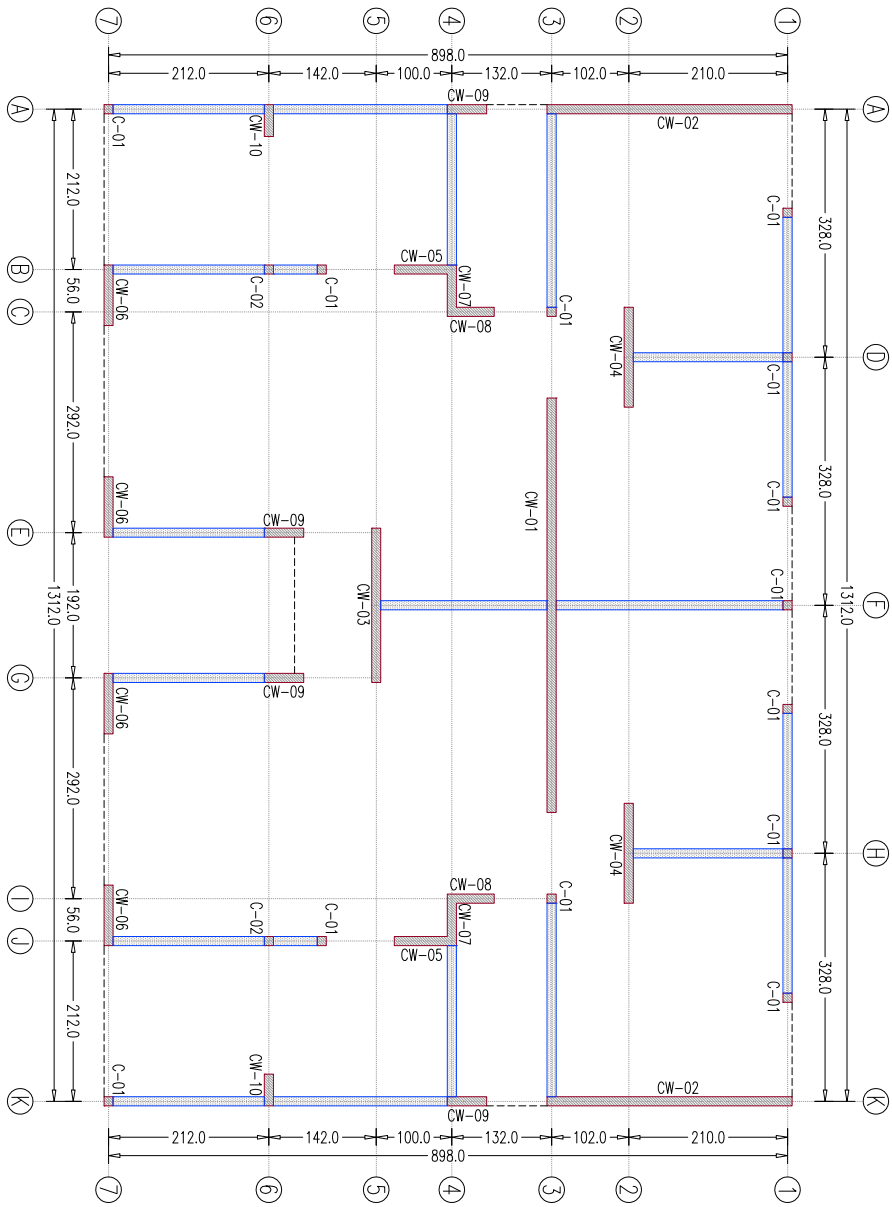

Figure 4.37 *Structural drawing - floor plan view (units: cm).*

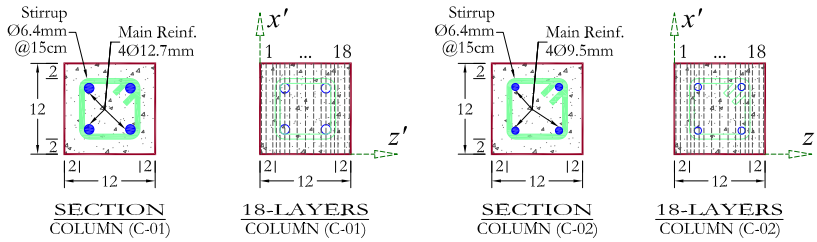

Figure 4.38 *Detailed section of columns (units: cm).*

deformation other walls undergone, and consequently, the stress levels they are subjected to. Such effect can be inferred while attending reference [3], which states that the total lateral force acting on each level of a building has to be distributed over bearing walls depending of their stiffness, in other words, the higher the stiffness the higher the lateral force.

The typical arrangement for the steel reinforcement's pattern used in concrete walls is two grids on each bed of the wall. In this case, is used a vertical reinforcement of steel rods with 3/8 inches ($9.5mm$) of diameter with 20 centimeters of separation among themselves, whereas for horizontal reinforcement have been used steel rods of 1/4 inches ($6.4mm$) of diameter with 15 centimeters among themselves. All concrete walls have been reinforced with columns `C-01` placed at both ends. Steel distribution of all concrete walls (from `CW-01` to `CW-10`) have been detailed in appendix F. Thickness and distributions of layers regarding the concrete wall's cross sections is presented in table 4.7, as can be seen, the same arrangement will be used for columns, beams, and concrete walls.

1	**2**	**3**	**4**	**5**	**6**	**7**	**8**	**9**
2.0	18.0	3.2	3.2	6.35	6.35	6.35	6.35	23.2
10	**11**	**12**	**13**	**14**	**15**	**16**	**17**	**18**
23.2	6.35	6.35	6.35	6.35	3.2	3.2	18.0	2.0

Table 4.7 *Thickness of layers (in millimeters) for columns, beams and concrete walls.*

Columns

Only two different sections of columns have been used while designing the model `B-SSC`, which are shown in figure 4.38. Both sections have dimensions of 12x12 centimeters.

The columns with section type `C-01` have been used for the two first levels of the building (L+0.00 and L+2.63), they have been endowed with a main steel reinforcement of 4 rods with 1/2 ($12.7mm$) inches of diameter, whereas their secondary steel reinforcement consist in rods of 1/4 ($6.4mm$) inches of diameter placed with a separation of 15 centimeters among themselves.

On the other hand sections type `C-02` have been used from third level to sixth level of the building (levels $L + 5.26$, $L + 7.89$, $L + 10.52$ and $L + 13.15$). Basically, they

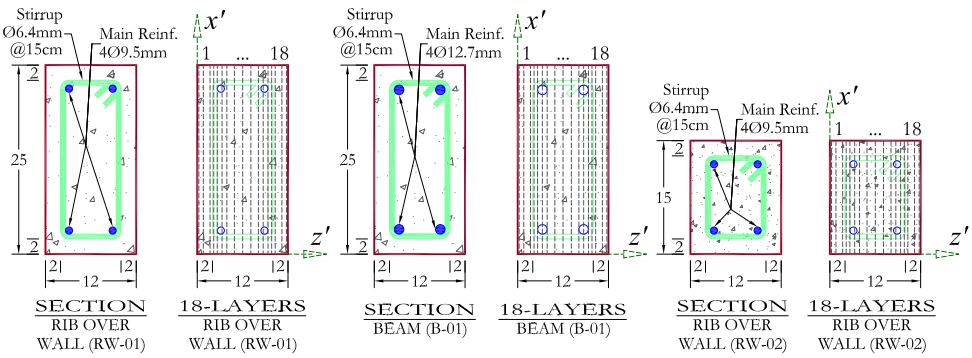

Figure 4.39 *Detailed section of beams (units: cm).*

have the same secondary steel reinforcement as section `C-01` have. What make them different is in their main steel reinforcement, since section's `C-02` is formed by 4 steel rods of 3/8 (9.5mm) inches of diameter.

Beams

Figure 4.39 shows the three different sections used in `B-SSC` model. Two of them have been used to endow horizontal confinement to masonry walls, whereas one of them has been used with the purpose of shorten concrete slabs.

Beams with the section type `RW-01` (`RW` stands for *rib over wall*, technically not a beam) are used to infer confinement on *regular* masonry walls, the dimension of their cross section are 12x25 centimeters, their main steel reinforcement consist in 4 rods with 3/8 (9.5mm) inches of diameter. Beams with section type `RW-02` are used to endow horizontal confinement to *short* masonry walls (under the window openings), and although both sections `RW-01` and `RW-02` have different dimensions, they have the same steel reinforcement arrangement (figure 4.39).

On the other hand, beam section `B-01` (this is a proper beam) has been used to reduce the dimension of the slab in construction axis **2**, from **B-E** and **G-J** (see appendix F). Although has the same dimensions as section `RW-01` the difference is the main steel reinforcement, which consist in 4 rods with 1/2 (12.7mm) inches of diameter.

Finally, it has to be pointed out that the three section types of beams have the same secondary steel reinforcement, which consist in rods of 1/4 (6.4mm) inches of diameter placed with a separation of 15 centimeters among themselves.

Slabs

As in the model presented in the previous section, the simple materials that make up the concrete slab of the structure have been fixed up to have a linear elastic behavior. The thickness of slabs have been designed to meet requirements regarding serviceability loads stated in reference [4] section 3, although in some cases, it has been necessary to shorten concrete slab boards with a concrete beam.

Slabs have been discretized along the thickness using a pattern of 20 layers for a total thickness of 15 centimeters. Their layer distribution can be seen on figure 4.8, where also can be noticed the steel reinforcement pattern in both beds and in both orthogonal

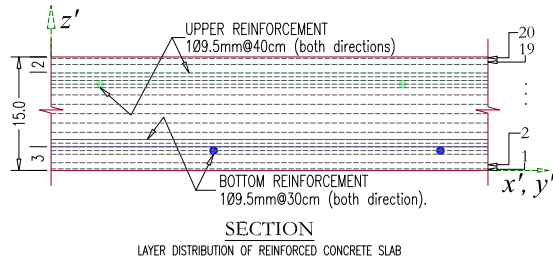

Figure 4.40 *Detailed section of slab (units: cm).*

1	**2**	**3**	**4**	**5**	**6**	**7**	**8**	**9**	**10**
2.0	8.0	11.2	5.0	5.0	4.75	4.75	9.5	12.4	12.4
11	**12**	**13**	**14**	**15**	**16**	**17**	**18**	**19**	**20**
12.40	12.40	9.5	4.75	4.75	5.0	5.0	11.2	8.0	2.0

Table 4.8 *Thickness of layers (in millimeters) for slabs.*

directions. In all cases, the diameter of the steel reinforcement rods remain the same, this is 3/8 inches, which varies is the separation among themselves. The separation of the steel reinforcement for the lower bed is 30 centimeters, whereas for the upper bed, a separation of 40 centimeters has been used.

4.2.3 Simple Material Properties

Since mechanical and constitutive properties of simple materials are the same as the materials presented in section 4.1.2, for convenience they have not been reproduced here.

4.2.4 Structured Composite Materials

In this section is carried out a brief description of `SCM` used to generate volumetric participation of composite materials within each layer of the finite elements. The procedure used has been previously described in section 3.7 of this work. In next figures, color red has been used to delimit the contour of current `SCM`, whereas, as an aid for reference, light gray has been used to represent the contour of the remaining `SCM`. Although in all cases, has only been presented one storey of the building, it is implied that the process has been repeated for the six storeys. A complete description of all `SCM` involved in the models are shown in appendix F of this work.

Figure 4.41 shows the `SCM` of constructive axis **3** for model `B-SSC`. The fibers of longitudinal steel reinforcements (main reinforcement) are shown in blue, whereas color green has been used to represent the transversal steel reinforcement (secondary reinforcement). It is convenient to point out that figure 4.41 shows a superposition of all layers within the `SCM`, and in no case, finite elements belonging to the `SCM` have been displayed.

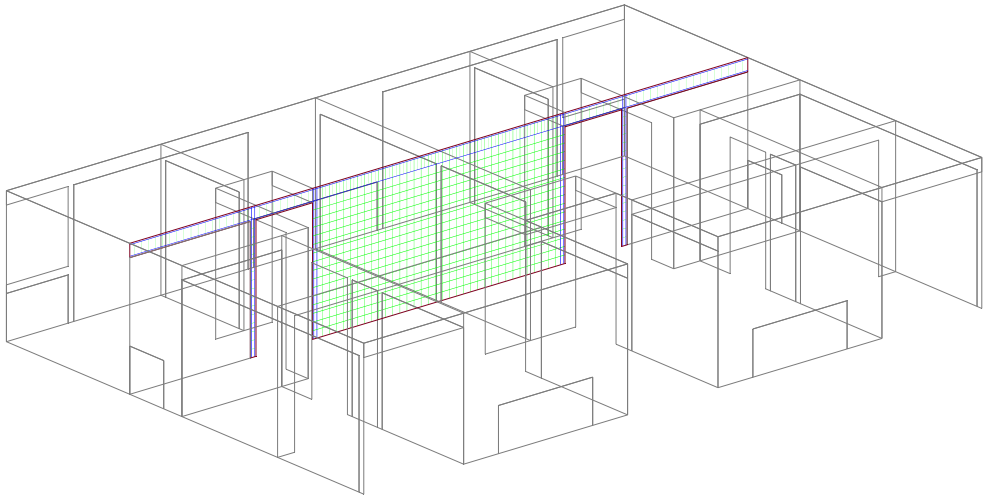

Figure 4.41 *Steel fibers of Axis 3.*

The others SCM shown in this section correspond to the constructive axis **A** and **K** depicted in figure 4.42, as in the previous example, the information of all layers has been superimposed, and finite elements has not been shown, this due to visibility matters. The purpose of displaying SCM from constructive axis **A** and **K** (as in the previous example) is to remark the existence of the reinforced concrete wall and their steel reinforcement pattern.

Finally, figure 4.43 displays the steel reinforcement pattern of structural elements belonging to construction axis **1** (rear façade), **7** (font façade) and **F**.

4.2.5 Boundary Conditions

The analysis process has been performed using 3 different loading phases. It is convenient to point out that; in no one of the loading phases has been used any loading factors, which are commonly included in code regulations due to the uncertainty in the assessment of loading forces.

Fixed Displacements

In all three loading phases, the basement of the structure has been set to remain rigidly fixed, hence, neither displacements nor rotations would be allowed.

First Stage Loading Condition: Dead Load

First loading stage corresponds to the dead load condition, namely, it is the force structural (walls, beams, columns, slabs) and non-structural elements (in-fills, plaster) acting due to gravity.

Let us take, for instance figure 4.44, where a typical loading analysis for the walls used in the construction of the building is displayed. A small sketch (on the left) shows both structural and non-structural components of a masonry wall, whereas in the right, a table depicts in detail thickness and weight of all components involved. Table on the

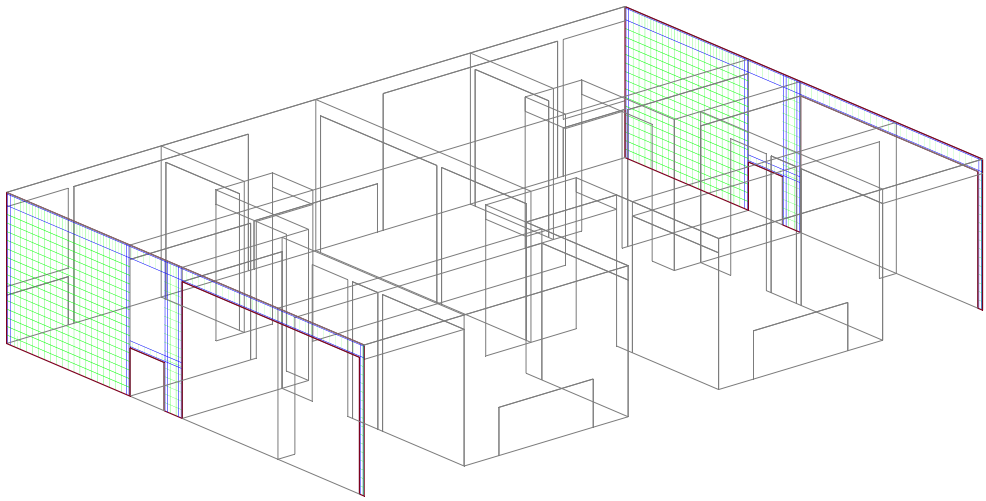

Figure 4.42 *Steel fibers of Axis* ***A*** *and* ***K****.*

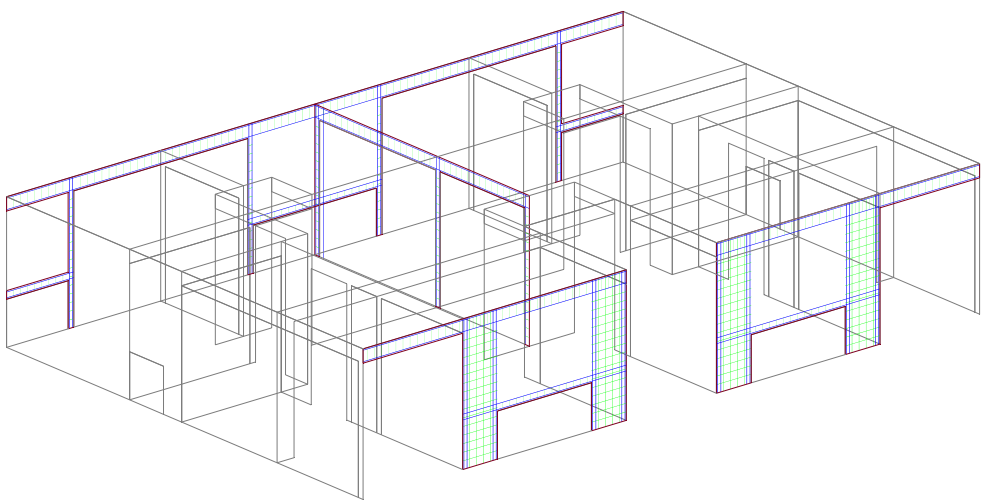

Figure 4.43 *Steel fibers of Axis* ***1****,* ***7*** *and* ***F****.*

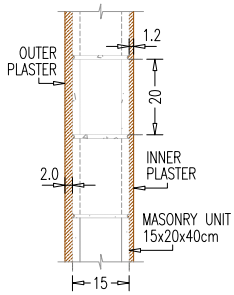

MASONRY BEARING WALL

MATERIAL	THICKNESS (cm)	WEIGHT (kg/m^3)	WEIGHT (kg/m^2)
MASONRY WALL	15.0	1500	225
INNER PLASTER	1.2	1500	18
OUTER PLASTER	2.0	2100	42
DEAD LOAD*	DUE TO CONCRETE		--
	DUE TO MORTAR		20

D_L = 305 kg/m^2

Figure 4.44 *Dead loads - Masonry bearing walls.*

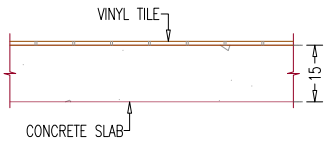

STOREY SYSTEM

MATERIAL	THICKNESS (cm)	WEIGHT (kg/m^3)	WEIGHT (kg/m^2)
VINYL TILE	---	---	5
CONRETE SLAB	15.0	2400	360
DEAD LOAD*	DUE TO CONCRETE		20
	DUE TO MORTAR		---

D_L = 385.0 kg/m^2

Figure 4.45 *Dead loads - Storey system.*

right also shows the additional loads (reference [2] art. 97) due uncertainties regarding *real* thickness of components or in the assessment process of the weights. In the case considered, only will be necessary to add $20kg/m^2$ due the presence of mortar. Finally, figure reports the total weight for the masonry wall to be equal to $W_D = 260kg/m^2$.

Figure 4.45 shows (on the left) the sketch of the storey system used in the building, as can be noticed, it consist in only a vinyl tile to cover the concrete slab. The thickness of the vinyl tile is not detailed in the table on the right, but only its uniform weight equal to $5kg/m^2$ (included the resin to bond it to the concrete slab). Due to the presence of concrete, $20kg/m^2$ has been added to the total weight. Hence, the total weight of the storey systems is equal to $D_L = 385.0kg/m^2$.

Finally, figure 4.46 depicts the loading analysis for the roofing system. The sketch on the left shows an average in-fill of aggregate material considered in the whole area of the roof. Such in-fill is necessary to provide a slope to the roof, so the water does not become stagnant when it rains. The table on the right (figure 4.46) details thicknesses and weights of elements forming the roof, in this case it has been necessary to add 40 kg/m^2 (ref. [2]) due the presence of mortar and concrete. Hence, the total weight of the roofing systems is equal to $D_L \approx 525.0kg/m^2$.

Second Stage Loading Condition: Live Loading

Live loads, are temporary, of short duration, and are based upon published regulations, in this case, it has been used the *Reglamento de construcciones para el Distrito Federal*

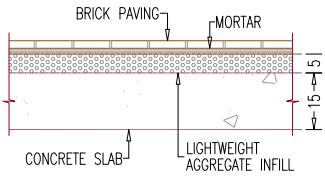

ROOFING SYSTEM

MATERIAL	THICKNESS (cm)	WEIGHT (kg/m^3)	WEIGHT (kg/m^2)
BRICK PAVING	2.0	1500	30
MORTAR	1.50	2100	31.5
AGGREGATE	5.0	1200	60
CONRETE SLAB	15.0	2400	360
DEAD LOAD*	DUE TO CONCRETE		20
	DUE TO MORTAR		20

D_L = 521.5 kg/m^2

Figure 4.46 *Dead loads - Roofing system.*

[2], as an aid to predict them. Such code regulation in its chapter V article `199.V.g` marks:

- An uniform live load equal to 100 kg/m^2 has to be used in the roof system of residential houses with an slope not higher than 5% (`section 199.V.g`)
- An uniform live load equal to 170 kg/m^2 has to be used in the storey system of residential houses (`section 199.V.b`).

Third Stage Loading Condition: Pushover

The third loading stage corresponds to a standard pushover applied in x direction. Hence, a displacement has been imposed to a set of nodes located along an edge of the slab of the sixth storey, the reason of conducting the pushover analysis in this way is to avoid a high concentration of forces to only few FE. The region where displacements in X direction have been applied is shown in figure 4.47. The purpose of imposing such displacement is to predict the force-displacement response of the structure. Obtained results for model `B-SSC` are presented in section 4.2.6.

4.2.6 Obtained Results for Model B-SSC

The obtained results for model `B-SSC` applying the pushover analysis (previously described) are summarized and discussed in this section with the aid of the figures described down below.

- Figure 4.50, which corresponds to the displacement-force response of model `B-SSC`.
- Figure 4.51 corresponding to the damage evolution of walls `W-01` and `W-02`, located along constructive axis **1** (rear façade), and whose isometric view is depicted in figure 4.47 on the left.
- Figure 4.52 corresponding to the damage evolution of walls `W-05`, `W-06` and `W-07`, located along constructive axis **3**, and whose isometric view is depicted in figure 4.47 on the right.
- Figure 4.53 corresponding to the damage evolution of walls `W-08`, `W-09`, `W10` and `W-07`, located along constructive axis **4**, whose isometric view is depicted in figure 4.48 on the left.

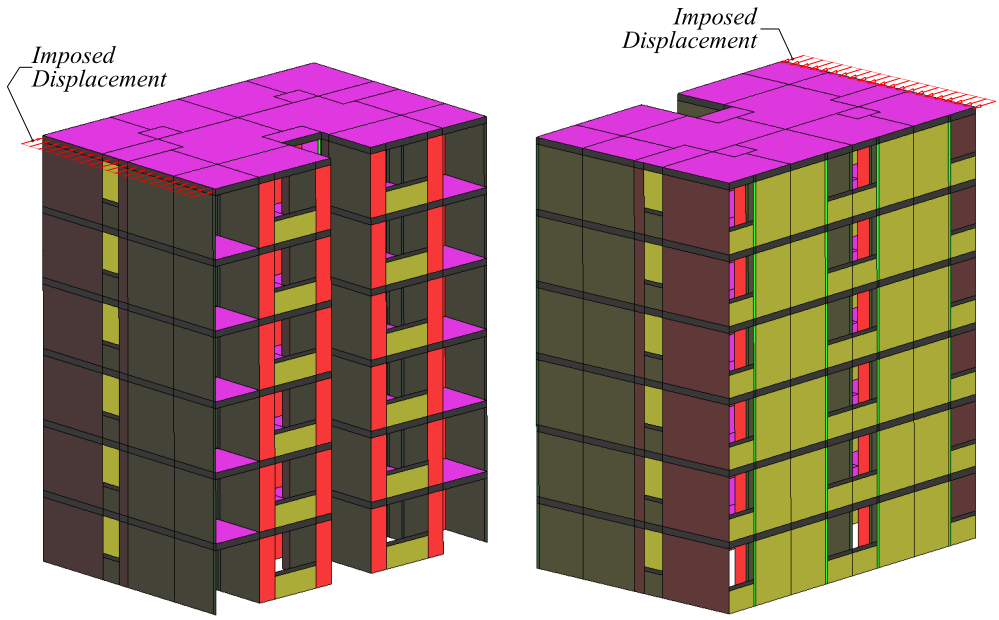

Figure 4.47 *Isometric view of GiD model for the* `B-SSC` *building.*

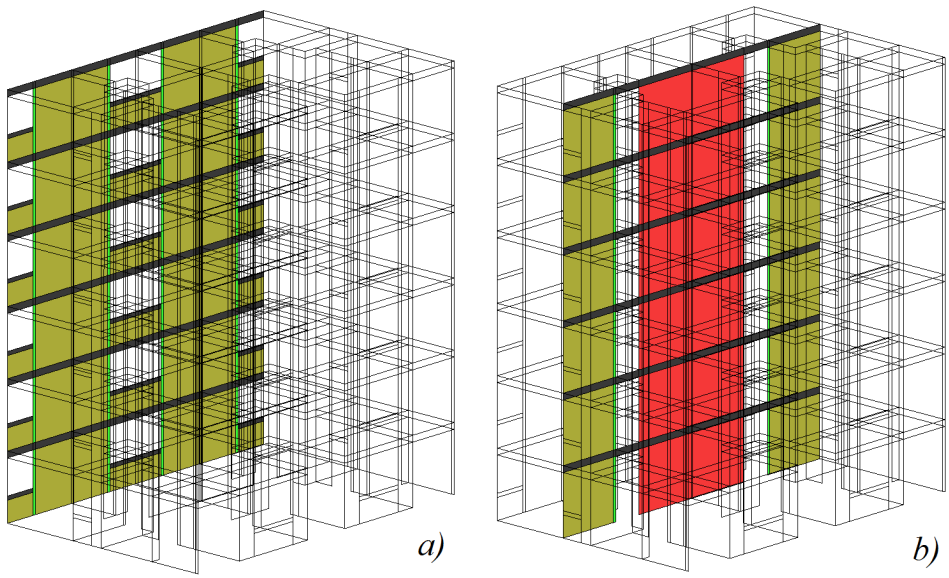

Figure 4.48 *View of constructive axis* ***1*** *and* ***3*** *of GiD model for the* `B-SSC` *building.*

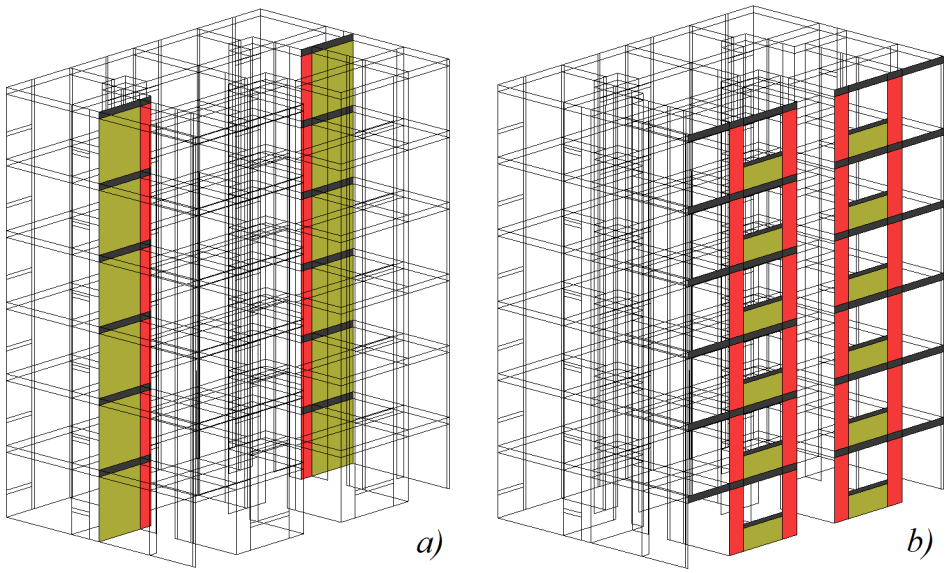

Figure 4.49 *View of constructive axis* **4** *and* **7** *of GiD model for the* `B-SSC` *building.*

- Figure 4.54 corresponding to the damage evolution of walls `W-15`, `W-16`, `W-17` and `W-18`, located along constructive axis **7** (front façade), and whose isometric view is depicted in figure 4.48 on the right.

Model `B-SSC` has been designed using a commercial code for design of masonry structures, named ANEMgcW [37] (based on reference [6]), and the corresponding procedure for its structural design has been briefly described in appendix E. It is important this clarification, since there is only one point of comparison among results obtained with the proposed methodology for model `B-SSC` and the results obtained (and shown in appendix E) using a design code, which is, the initial stiffness obtained for both cases.

$$\begin{aligned} {}^{1}\mathbf{K}_X &= 3'027,012.84\, kN/m & {}^{4}\mathbf{K}_X &= 3'111,957.63\, kN/m \\ {}^{2}\mathbf{K}_X &= 3'227,568.48\, kN/m & {}^{5}\mathbf{K}_X &= 3'310,423.74\, kN/m \\ {}^{3}\mathbf{K}_X &= 3'359,669.94\, kN/m & {}^{6}\mathbf{K}_X &= 3'373,992.94\, kN/m \end{aligned} \tag{4.8}$$

Equation 4.8 summarizes the stiffness obtained using ANEMgcW for each of the storeys of model `B-SSC`, such vales have been assembled into a so-called global stiffness matrix of the mass-concentrated model (figure G.2 appendix G), then a displacement at the top δ_{top} (storey 6th) has been imposed and the corresponding reaction at the bottom $V_{\delta_{top}}$ has been evaluated solving the corresponding linear system. The value corresponding to the stiffness $\mathbf{K}_{ds}$ is presented in equation 4.9.

$$\mathbf{K}_{dc} = \frac{V_{\delta_{top}}}{\delta_{top}} = 538,316.78\, kN/m \tag{4.9}$$

On the other hand, stiffness obtained with the methodology proposed in this work can be easily evaluated for the elastic range using equation 4.10.

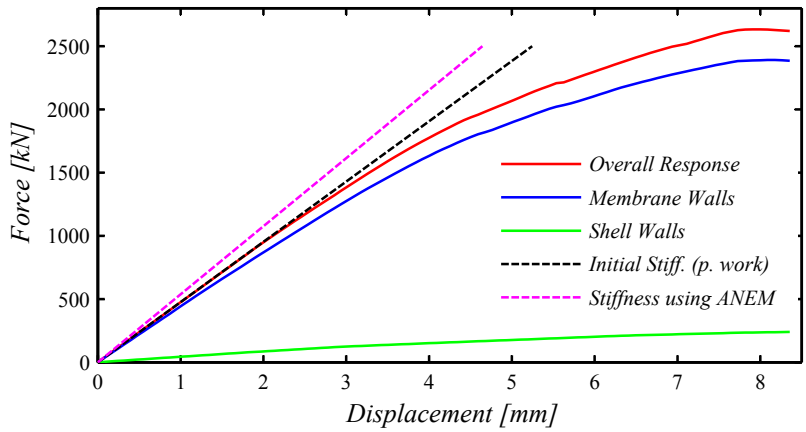

Figure 4.50 *Displacement-force response of the structure* `B-SSC` *in X direction.*

$$\mathbf{K}_{pw} = \frac{\Delta V_j}{\Delta \delta_j} = 476,580.49\ kN/m \tag{4.10}$$

where $\mathbf{K}_{pw}$ stands for the total stiffness of model `B-SSC` evaluated using the proposed methodology, $\Delta\delta_j$ and ΔV_j are respectively an increment of displacement and an increment of shear force within the elastic range.

A schematic representation of both stiffness are presented in figure 4.50, where can be seen that there is 12.95% of error among them.

Similarly as model `B-OSC`, the model `B-SSC` confirms reference [6] regarding the low stiffness presented by the bending-acting walls (green line), while their stiffness is compared with the membrane-acting walls (blue line), and that their stiffness perfectly could be neglected for analysis and design purposes. The red line of figure 4.50 represents the overall response of the structure.

Finally, let us consider figures 4.51 to 4.54, they correspond to a set of deformation stages (amplified 250 times) within the analysis process, where the damage variables of the element is also shown. In all three cases, images on the left represent the confining elements, whereas images on the right represent the masonry elements. The selected stages for the displacement have been *a)* $\delta = 2.00mm$, *b)* $\delta = 6.00mm$ and *c)* $\delta = 8.20mm$.

4.2.7 Damage Assessment for Model B-SSC

In this section, it is pretended to characterize the damage scenarios the structure `B-SSC` could undergo in a zone with high seismic activity, therefore, two main assumptions have to be done before starting:

1. The capacity spectrum and the bilinear capacity spectrum used to characterize the damage scenarios depicted in figure 4.55, correspond to the displacement-force response obtained from the pushover analysis, previously described, and whose results are shown in figure 4.50. Process to obtain the capacity spectrum and, consequently, the bilinear capacity spectrum are described later in this section.

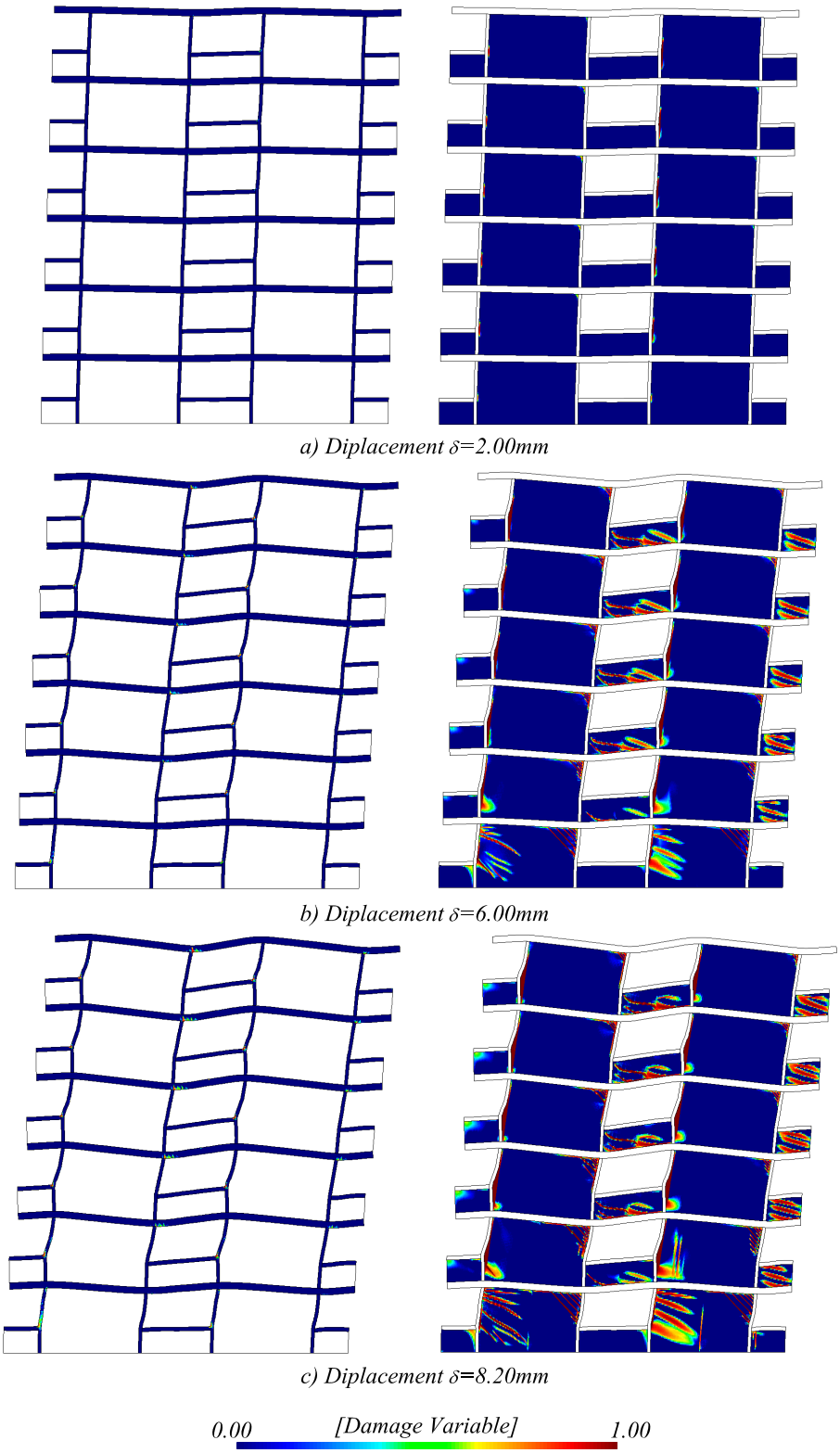

Figure 4.51 *Damage evolution on structural components on constructive axis* ***1****.*

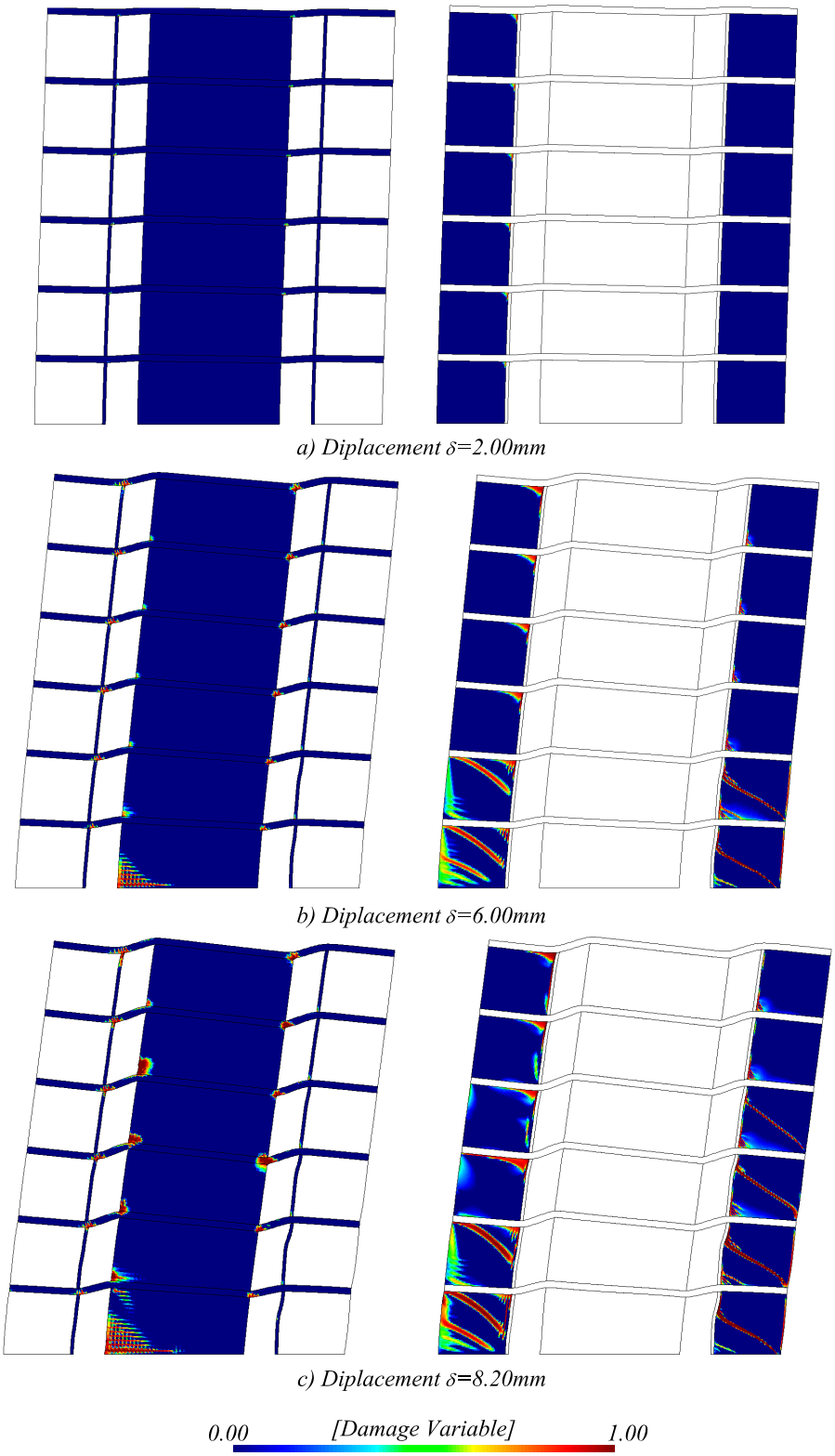

Figure 4.52 *Damage evolution on structural components on constructive axis **3**.*

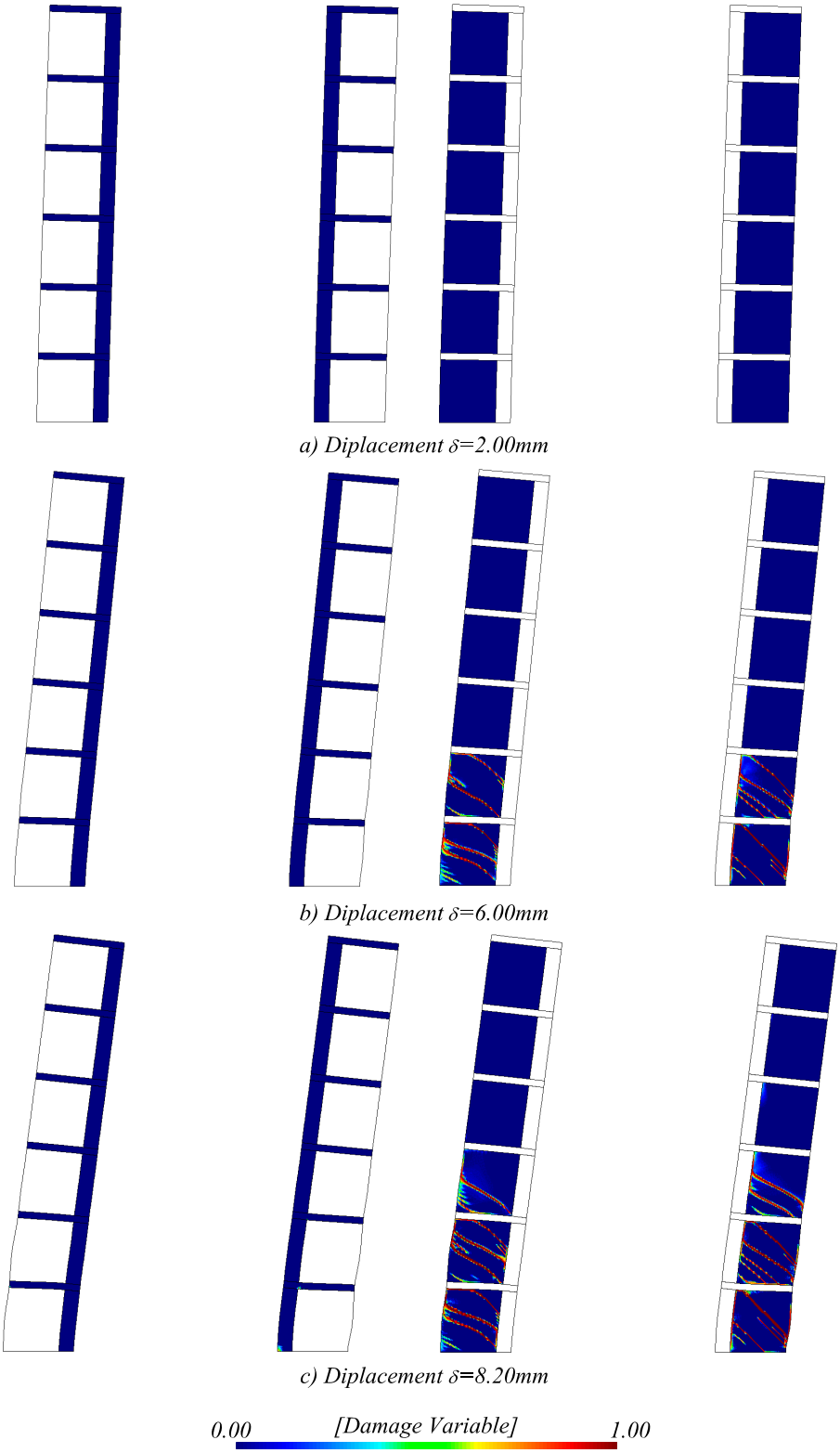

Figure 4.53 *Damage evolution on structural components on constructive axis 4.*

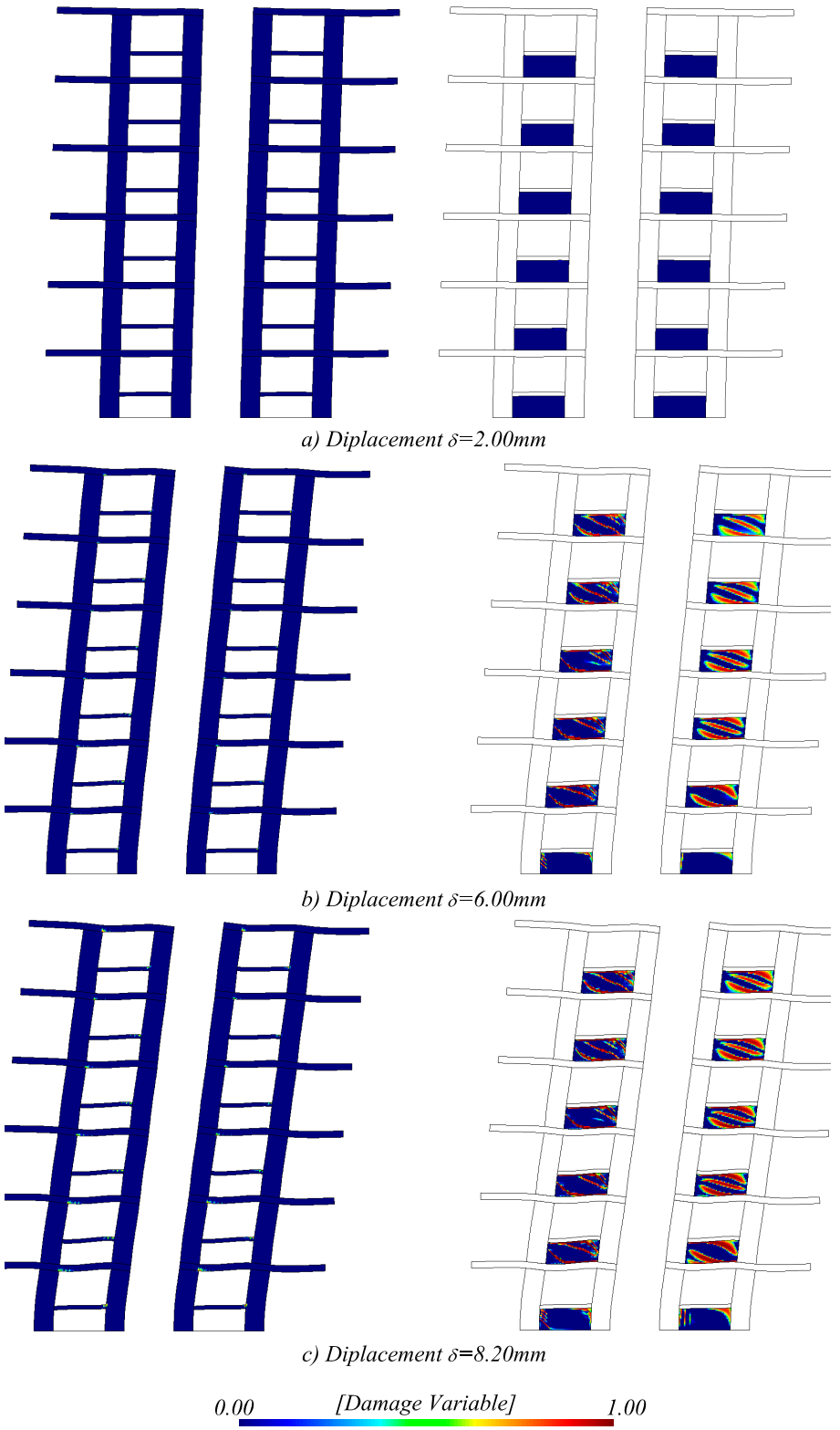

Figure 4.54 *Damage evolution on structural components on constructive axis* **7***.*

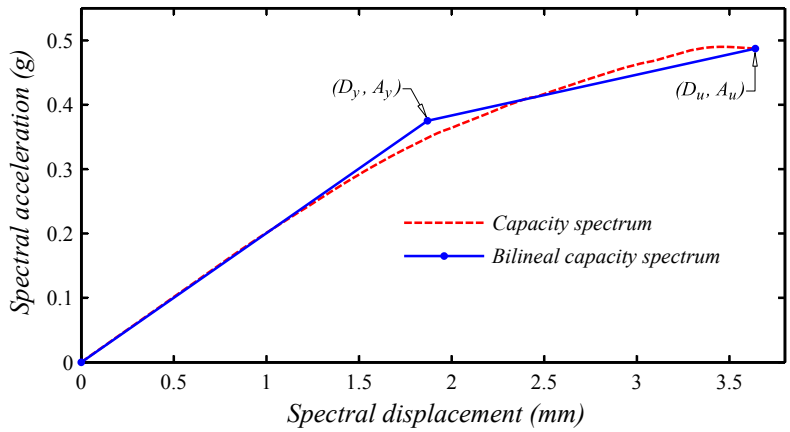

Figure 4.55 *Bilinear representation of the capacity curve displayed in figure 4.50 transformed to spectral displacement.*

2. For comparative purposes, two *locations* have been selected for the model `B-SSC`. The first location (location `L1` from now on) is somewhere in Mexico City within the seismic zone `ZIIIa` according to micro zone described in reference [3]. The second location (location `L2` from now on) is somewhere within the European Union where the soil is **D**, type **1** and has a peak ground acceleration equal to 0.20_g according to classification of Eurocode 8 [40]. The corresponding design spectra transformed to a $sd - sa$ according to methodology described in appendix G are shown in figure 4.58. The vertical hidden blue line in figure 4.58 represents a threshold equal to $4mm$ of spectral displacement sa, it has been used for representative purposes, and to take into account the magnitude of the spectral displacements used in the representation of the obtained results.

Before the capacity spectrum in figure 4.55 had been plot, two main simplifications to model `B-SSC` had to be performed. The first one consisted in converting it into a model with equivalent stiffness and *one-degree-of-freedom* per storey, where the mass of the corresponding storey is concentrated. The equivalent stiffness of each storey corresponding to the mass-concentrated model are shown in equation 4.11,

$$\begin{aligned} {}^1\mathbf{K}_X &= 2'987,042.83\, kN/m & {}^4\mathbf{K}_X &= 2'854,411.56\, kN/m \\ {}^2\mathbf{K}_X &= 2'974,362.83\, kN/m & {}^5\mathbf{K}_X &= 2'755,059.66\, kN/m \\ {}^3\mathbf{K}_X &= 2'930,764.48\, kN/m & {}^6\mathbf{K}_X &= 2'679,856.84\, kN/m \end{aligned} \tag{4.11}$$

whereas, the weight concentrated in each storey is presented in equation 4.12.

$$\begin{aligned} w_1 &= 1,019.95\, kN & w_4 &= 1,019.95\, kN \\ w_2 &= 1,019.95\, kN & w_5 &= 1,019.95\, kN \\ w_3 &= 1,019.95\, kN & w_6 &= 932.44\, kN \end{aligned} \tag{4.12}$$

The second simplification was to convert the mass-concentrated model into a *one-degree-of-freedom* model, this was achieved through a modal decomposition, using the

vibrational mode 1, whose corresponding values of the eigenvector for modal vibrational 1 are presented in equation 4.13

$$\begin{aligned} \phi_{1,1} &= 0.1299 \qquad \phi_{4,1} = 0.4544 \\ \phi_{2,1} &= 0.2529 \qquad \phi_{5,1} = 0.5210 \\ \phi_{3,1} &= 0.3630 \qquad \phi_{6,1} = 0.5563 \end{aligned} \tag{4.13}$$

and which substituted in equation G.2 and G.3 (appendix G) led to the values shown in equation 4.14.

$$PF_1 = 2.2959 \qquad ; \qquad \alpha_1 = 0.8633 \tag{4.14}$$

Using values of PF_1 and α_1 from equation 4.14, and equation 4.15, it was possible to plot the spectral capacity curve depicted in figure 4.55 (red hidden line), where subindex j represents the applied loading increments the structure is subjected to under a non-linear pushover analysis.

$$sd_j = \frac{\delta_j}{PF_1} \qquad ; \qquad sa_j = \frac{V_j}{\alpha_1 \, W} \tag{4.15}$$

Once the spectral capacity curve has been defined, it was possible to plot the bilinear capacity spectrum, which is essential to estimate the probabilistic damage, since all damage scenarios are based upon values of points (D_y, A_u) and (D_u, A_u), as described in equation 4.17. The construction of the bilinear capacity spectrum is bases on the three hypothesis described next,

1. The area under the spectral capacity curve must be equal to the equivalent bilinear capacity curve.
2. Coordinates of the point with maximum displacement (D_u, A_u) match in both curves.
3. The initial slope in both graphs must be the same.

which led to the corresponding values for points (D_y, A_u) and (D_u, A_u) shown in equation 4.16.

$$\begin{aligned} D_y &= 1.870mm \quad D_u = 3.640mm \\ A_y &= 0.375_g \qquad A_u = 0.487_g \end{aligned} \tag{4.16}$$

Fragility curves represent the probability in which a damage scenario ds on a structure could be reached or exceeded, as a function of the parameter that represent the intensity of the seismic action. Risk-EU [132] distinguishes four possible damage scenarios on a structure, namely, *slight* (ds_1), *moderated* (ds_2), *extensive* (ds_3) and *complete* (ds_4), whose definitions depends on points (D_y, A_y) and (D_u, A_u) of the bilinear capacity spectrum according to equation 4.17.

$$\begin{aligned} ds_1 &= 0.7 \, D_y \\ ds_2 &= D_y \\ ds_3 &= D_y + 0.25(D_u - D_y) \\ ds_4 &= D_u \end{aligned} \tag{4.17}$$

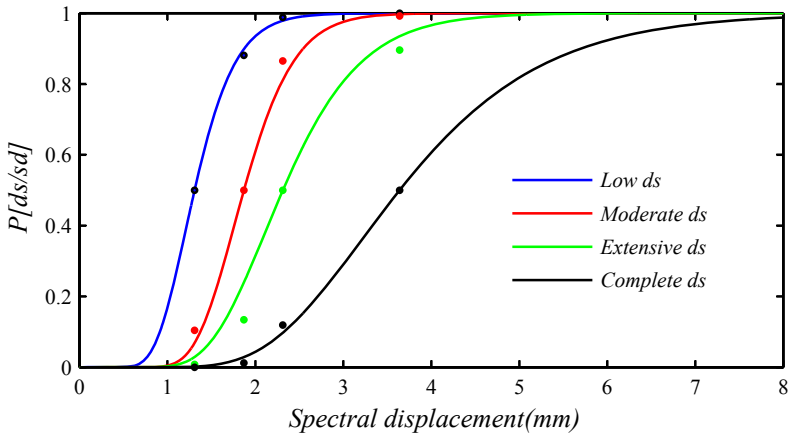

Figure 4.56 *Fragility curves for model B-SSC*

Since appendix G describes how to manage to plot fragility curves and the damage index for a given structure, in this section only will be reproduced the values (equation 4.18) that lead to figure 4.56 and 4.57.

$$\begin{aligned} ds_1 &= 1.309mm \quad ; \quad \beta_{ds_1} = 0.280 \\ ds_2 &= 1.870mm \quad ; \quad \beta_{ds_2} = 0.240 \\ ds_3 &= 2.313mm \quad ; \quad \beta_{ds_3} = 0.300 \\ ds_4 &= 3.640mm \quad ; \quad \beta_{ds_4} = 0.350 \end{aligned} \tag{4.18}$$

The seismic demand the structure undergoes, is obtained through its point of performance, in this section, to obtain it, will be used a linear equivalent approach. To do so, let us consider figure 4.58, corresponding to the design spectra for location `L1` and location `L2`, as can be seen, both spectra have been plot in a $sd - sa$ representation in order to link them together with the bilinear capacity spectrum shown in figure 4.55.

Figure 4.59 represent the superposition of both the design spectra and the bilinear capacity spectrum. The point of performance corresponding to the location `L1` is defined by point **A** ($sd_{L1} = 0.89mm$), which is the crossing of the bilinear capacity spectrum and the design spectrum for `L1`, as will be seen later, point **A** corresponds to a null damage state, since the seismic demand is low.

On the other hand, the crossing point of the prolongation of the first segment of the bilinear capacity spectrum, and the design spectrum for location `L2` correspond to the point of performance for location `L2` ($sd_{L2} = 2.78mm$).

Finally, using the fragility curves depicted in figure 4.56, and the point of performance shown in figure 4.59 for both locations, it is possible to probabilistically assess the damage scenarios model `B-SSC` could undergo, the results are summarized in table 4.9.

From table 4.9 can be seen the very low probability of occurrence of a *low* damage scenario, which is equal to $P_{(ds_1)} = 8.65\%$, whereas the remaining scenarios have no possibility of occurrence, this is obvious, since the model `B-SSC` has been designed to withstand the seismic conditions of location `L1` in the first place, as detailed in appendix E, so that, the expected damage can be represented using the damage index $DI = 0.021$.

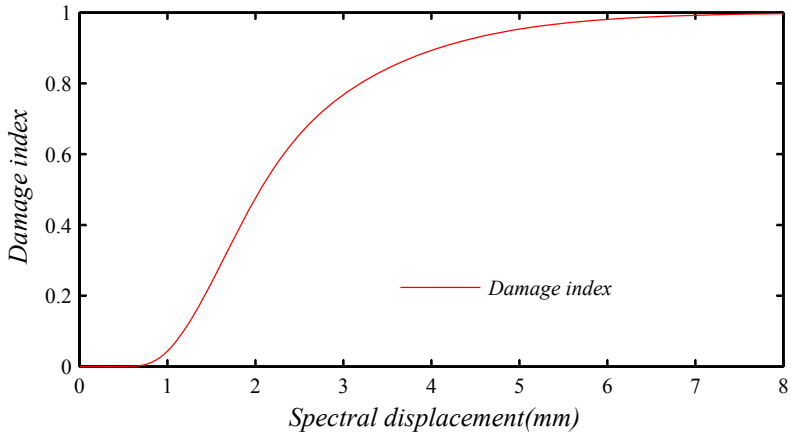

Figure 4.57 *Damage index for model B-SSC*

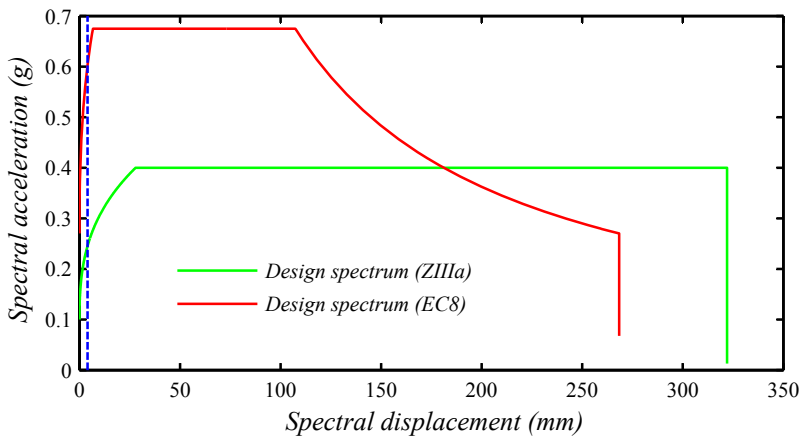

Figure 4.58 *Design spectra in sd − sa representation corresponding to* `ZIIIa` *and soil* ***D*** *type* ***1*** *with* $a_g = 0.2_g$.

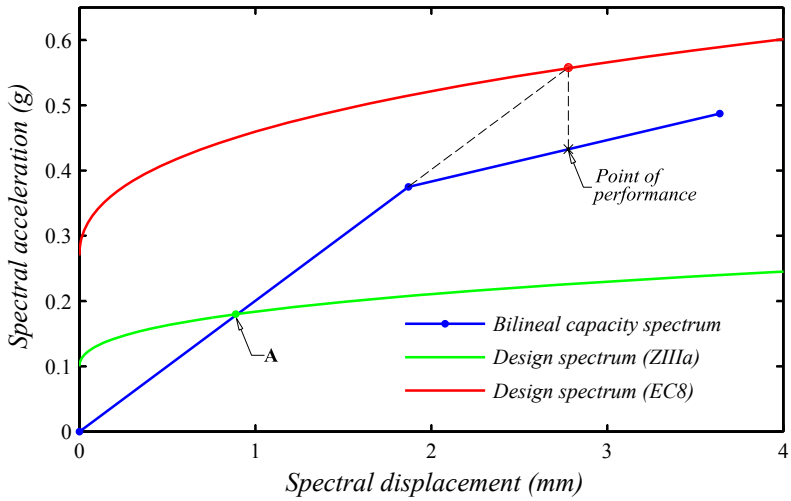

Figure 4.59 *Point of performance using a design spectra for seismic zone ZIIIa and seismic zone Type **1** Soil **D** according to EC8 [40].*

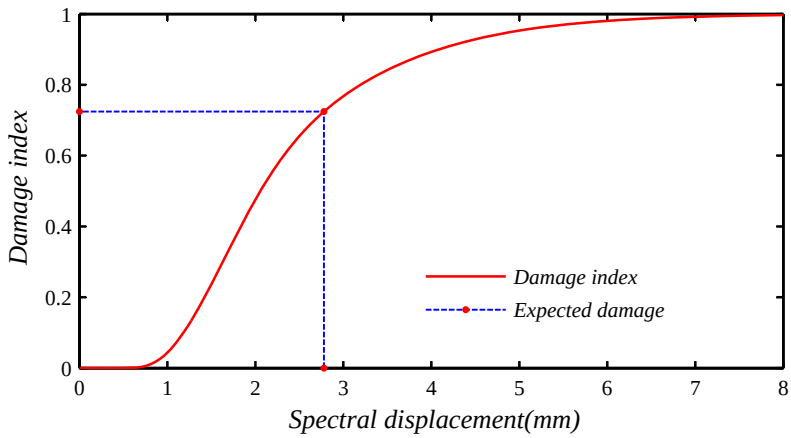

Figure 4.60 *Expected damage for model B-SSC and seismic zone Type **1** Soil **D** [40].*

ds	Location L1	Location L2
$P_{(ds_1)}$	8.65%	99.65%
$P_{(ds_2)}$	0.00%	95.02%
$P_{(ds_3)}$	0.00%	73.04%
$P_{(ds_4)}$	0.00%	22.12%

Table 4.9 *Probability of damage occurrence.*

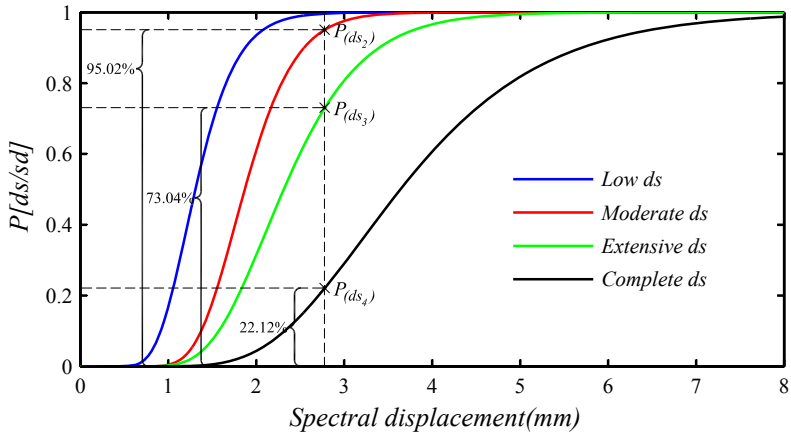

Figure 4.61 *Probability of damage for model B-SSC and seismic zone Type **1** Soil **D** [40].*

For location L2, however, since the seismic demand increases, so the probabilistic damage does, which was the reason of using such fictitious location. Results of model B-SSC at location L2 reports a damage index $DI = 0.7246$, being $DI = 1.0$ the index corresponding to the complete damage scenario.

Figure 4.61 is a graphical representation of the meaning of fragility curves, in such figure, it is represented (with a vertical hidden black line) the spectral displacement $ds_e = 2.78mm$ which correspond to the point of performance of structure SSC at location L2, the crossing line of the vertical black hidden line with the corresponding curve represents the probability of occurrence of the given damage scenario, which already have been summarized in table 4.9.

4.3 Computational Requirements

Model described on section 4.1 have to be just considered as an example, intended to show the capabilities and scopes of the process followed to perform the structural analysis of a masonry constructions. The model of section 4.1 is small while compared with a *real-life* masonry structure and needs a much less amount of computational resources.

In this section are described the improvements performed in PLCD, in order to

Model	**F.E.**	Initial Memory Req.	S.M. Info	Solver
B-OSC	30,868	572.70Mb	262.22Mb	243.62Mb
B-SSC	1'105,804	28.599Gb	9.82Gb	14.599Gb

Table 4.10 *Memory comparison between models B-OSC and B-SSC.*

make it possible to analyze large structures in a reasonably short amount of time, and consequently, be able to analyze structures such as model B-SSC.

Although here have studied alternatives to address the resolution of structures that require handling large amount of information, this section is not conclusive, since other comparison is required to be studied in depth, this is while using either a direct or an iterative solver for the resolution of linear equations, thus, be able to evaluate the use of one or other depending on the computational resources available.

Memory-Consuming Based Optimization

Let us consider table 4.10, where is shown a comparison among the RAM memory required for different process in the analysis of models B-OSC and B-SSC. From left to right, column 2 shows the amount of FE within the used mesh, column 3 shows the total amount RAM memory, column 4 depicts the required memory to store information of the simple materials such as internal variables, stresses and strains. Finally, column 5 shows the memory required for the PARDISO solver. Since model B-OSC (section 4.1) consists on a mesh with 30,868 FE, the amount of required memory (572.70Mb) seems reasonable, and the resources required can be easily fulfilled by a *conventional* desktop computer. However, when it comes to large structures, it becomes more difficult to fulfill the required memory.

Let us consider again model B-OSC shown in table 4.10. Expressed in term of percentages, the required memory to handle the information of simple materials is equal to 45.78%, whereas the solver uses 42.50% of the total. Analyzing such percentages makes clear to where should be directed the efforts on optimizing the consumed memory.

Using the previous scheme all the information regarding the components of the FE was allocated at the beginning of the analysis process using vectors, so it was necessary to implement a different scheme using user-defined data types, where, at the beginning of the analysis process, the information is reserved and only allocated while needed (once the FE is in a non-linear range), leading to a less necessity of RAM memory resources. Starting from the assumption that not all elements reach a non-linear behavior, the proposed programming scheme (shown below) was implemented in PLCd.

- It was used a *template* to store internal variable for every non-damaged FE with the same composite information. At this point it is not necessary to store strain or stress information of composite neither components of the laminated material.
- Once a component within a FE has reach a non-linear behavior, then allocation of memory to store information of the FE was required (internal variables, stresses and strains).

Model	Initial Memory Req.	Final Memory Req.
B-OSC	572.70Mb	329.4Mb
B-SSC	28.599Gb	19.00Gb

Table 4.11 *Memory comparison between models B-OSC and B-SSC using the proposed scheme and the direct solver PARDISO.*

```
! Composite Material Information.....................................
  TYPE TYPE_Sm_Inf_K
    REAL(8) :: PARKc, HACHE, STRAN(3), STRAT(3), STRAP(3), STRES(3),&
               SGTOT(3), SGTOTP(3), CTANg(3,3)
  END TYPE TYPE_Sm_Inf_K
  TYPE TYPE_Lay_Inf_K
    REAL(8) :: Mstra0(3), Fstra0(3), LSTRA(3), LSTRE(3), LSTREP(3), &
               CTANg(3,3)
  END TYPE TYPE_Lay_Inf_K
  TYPE TYPE_Composite
    TYPE(TYPE_IVar_sm),   ALLOCATABLE :: iVI(:)
    TYPE(TYPE_Lay_Inf_K), ALLOCATABLE :: L(:)
    TYPE(TYPE_Sm_Inf_K),  ALLOCATABLE :: Sm(:)
  END TYPE TYPE_Composite
! Internal Variables Information.....................................
  TYPE TYPE_IVar_sm
    INTEGER :: EUNLD
    REAL(8) :: CAPAP,  ANGFI, ANGSI, PREYS, HARDS, DEGMA, DEGMAplus, &
               DEGMAminu,  TAUMA, TAUMAplus, TAUMAminu
  END TYPE TYPE_IVar_sm
! Simple Material Information.....................................
  TYPE TYPE_Sm_Info ! Flag ASMT, AEMX
    LOGICAL :: Fl_Ani_S, Fl_Ani_E
    INTEGER :: NCRIT, NTINT, NCRIP, NINDI, NINDIp, NINDIm, NICUR,   &
               KFLUG, HCURV, NHARD, NMATX
    REAL(8) :: ECERO, GSUBF, GSUBC, SIGAS, ENE, PARKc, HACHE,       &
               ALPRI, SIKMA, RETEN, CUR_T(6), CUR_C(6), DMANX(3,3), &
               DMATX(3,3), ASMT(3,3), AEMX(3,3), STRAN(3), STRAT(3),&
               STRAP(3), STRES(3), SGTOT(3), SGTOTP(3), fp_11,      &
               fp_22, fp_12, fm_11, fm_22, fm_12
  END TYPE TYPE_Sm_Info

  LOGICAL :: FlgAll
  TYPE(TYPE_Composite) :: kKomp
  TYPE(TYPE_Sm_Info), ALLOCATABLE :: iSM(:)
  TYPE(TYPE_IVar_sm), ALLOCATABLE :: iVI(:)
```

Listing 4.1 *User-defined data types to call the constitutive equations.*

- Allocating at every loading step or iteration may be time consuming, however, it will be justified for large structures where a considerable amount of RAM would be required.
- For output and visualization purposes (writing information in GiD format) the information of non-damaged finite elements is evaluated using their local displacements, which will be a major drawback.

```
! Basic data type for internal variables
  TYPE TYPE_IVar_sm
    INTEGER :: EUNLD
    REAL(8) :: CAPAP, ANGFI, ANGSI, PREYS, HARDS, DEGMA, DEGMAplus, &
               DEGMAminu, TAUMA, TAUMAplus, TAUMAminu
  END TYPE TYPE_IVar_sm
! Composed data type, stresses/strains and type TYPE_IVar_sm
  TYPE TYPE_Sm
    TYPE(TYPE_IVar_sm) :: IVc, IVn ! Converged and Non-Converged
    REAL(8) :: STRSGc(3), STRATc(3), STRAPc(3), &
               STRSGn(3), STRATn(3), STRAPn(3)
  END TYPE TYPE_Sm
! Composed data type por finite elements, where a flag has been added
! if Dflg == .FALSE. --> Elastic Range
! if Dflg == .TRUE.  --> Non-lienar Range
  TYPE TYPE_SmElInfo
    LOGICAL :: Dflg
    TYPE(TYPE_Sm), ALLOCATABLE :: Sm(:)
  END TYPE TYPE_SmElInfo
! Finite element data type
  TYPE(TYPE_SmElInfo), ALLOCATABLE :: VBASms(:)
```

Listing 4.2 *User-defined data types to store internal variables stresses/strains for each FE.*

Basically, the process followed is this: if any of the components within any layer of the laminated material reach an non-linear range, such FE is considered as damaged, thus, information of the components has to be stored. Otherwise, strain and stresses are evaluated using the local displacements of the finite element. As can be notice this is a major disadvantage in terms of analysis time, since while writing the output information to GiD [35] the required information to be written of a simple material has to be evaluated first.

The used-defined data type implemented to store information of finite elements once it is in the non-linear range is presented in listing 4.2. As can be seen, memory for data type `Sm(:)` is only reserved at the beginning of the analysis, whereas the flag `Dflg` is always used.

The results obtained once the previously described scheme has been implemented in PLCD are shown in table 4.11, as can be appreciated, there is a considerable reduction on the amount of consumed memory, however, the 19.00Gb required by model `B-SSC` seems excessive to use a *conventional* desktop computer, and maybe to perform the analysis of such models would be required the node of a cluster. In any case, the other strategy comes to mind, this is the use of an iterative solver. To do so, has been implemented in PLCD the FEMT library developed by Vargas and Botello-Rionda [169], which contains routines running in parallel, to handle and solve the typical linear systems of equations resulting from finite element or finite volume discretizations for a large number of unknowns.

FEMT library consists of a sets of function embedded in the files **`libFEMSolver`** and **`libMETIS`**, hence for a proper linkage, the first thing to keep in mind is whether such library has been compiled for unix or windows platform, and for architecture of 32 or 64 bits.

In this section, it has been carried out a comparison only in terms of consumed memory, however, further comparisons in terms of running time while using an iterative solver are required, to fit the best alternative. Obtained results using the proposed

Model	Initial Memory Req.	Final Memory Req.
B-OSC	572.70Mb	132.51Mb
B-SSC	28.599Gb	4.75Gb

Table 4.12 *Memory comparison between models* `B-OSC` *and* `B-SSC` *using an iterative solver of library FEMT [169].*

scheme of only allocating the memory required for internal variables, strains and stresses of simple materials combined with the use of an iterative solver is depicted in table 4.12, as can be seen, there is a significant improvement in terms of memory management.

Parallelization of PLCD Using OMP directives

PLCD [34] is a state of the art implicit finite element written in Fortran, and originally developed by Prof. Oller at CIMNE. It has been developed to treat a large variety of composite materials through the use of Rules of Mixtures. This section covers the paralellization of the module used to solve mechanical problems with shell elements, which has been performed using OpenMP [13] directives in three different sections of the code. Such sections are shown below.

1. Loop over elements while evaluating the generalized strains $\hat{\boldsymbol{\varepsilon}}$ and the generalized stresses $\hat{\boldsymbol{\sigma}}$.
2. Loop over elements while integrating the constitutive equations (plasticity, damage, etc.).
3. Loop over elements while writing/reading information to perform a restart operation.

For convenience only sections 1 and 2 of list previously shown will be described here, since section 3 is only about writing or reading text files. In both of the cases described here, the key aspect for a quick parallelization process has been that data of called functions within parallel regions has been encapsulated.

Parallelization while evaluating generalized stresses and strains

The first part selected to be parallelized has been the loop over the elements where the generalized strains $\hat{\boldsymbol{\varepsilon}}$ and generalized stresses $\hat{\boldsymbol{\sigma}}$ are evaluated. Since the loop in this case is only over the elements is less time-consuming than the portion of code parallelized shown in next section.

This part has been parallelized using a `PARALLEL DO` directive (listing 4.3). Once variables defined as `PRIVATE` has been recognized, the process has been easily carried out.

The variables declared as locals to each tread (`PRIVATE` variables) are `II, XYcoord, RMTEL, THtot, Enod, fpars, DMATm, DMATb, DMATmb, DisplLoc, ElGenStra, ElGenStre, Bfact`. As can be noticed from listing 4.3, the only OpenMP directives required are the ones on lines 2, 3 and 23 of such listing.

```
! Starts Main Loop Over Elements.....................................
!$OMP PARALLEL DO PRIVATE(II,XYcoord,RMTEL,THtot,Enod,fpars,DMATm)&
!$OMP PRIVATE(DMATb, DMATmb, DisplLoc, ElGenStra, ElGenStre, Bfact)
  DO II=1,NELEM
    CALL DKTOPTelementInfo (II,'Small_Deform',XYcoord,RMTEL,THtot,  &
                            Enod,DMATm,DMATb,DMATmb,fpars)
    IF (TanStiffMat(II)%DamageFlag .EQ. 1) THEN
      DMATb(:,:) = TanStiffMat(II)%DBENX(:,:)
    ENDIF
    CALL DKTOPTelementDispl(II,RMTEL,DisplLoc)
    CALL DKTOPTelementStrainStress( DisplLoc,XYcoord, THtot,        &
                                    DMATm,DMATb,DMATmb,fpars,       &
                                    ElGenStra, ElGenStre,Bfact)
    VBAS5sh(II)%Bfact(:,:) = Bfact(:,:)
  ! Stores non-converged generalized stresses/strains...
    VBAS1e(II)%STRATn(1:6) = ElGenStra(:)
    VBAS1e(II)%STRSGn(1:6) = ElGenStre(:)
  ! Deactivate Element if I_Fase > VBAS5sh(IELEM)%EFASE...
    IF (VBAS5sh(II)%EFASE .GT. I_Fase) THEN
      VBAS1e(II)%STRSGn(1:8) = 0.0D0
    ENDIF
  ENDDO
!$OMP END PARALLEL DO
```

Listing 4.3 *Loop over elements running in parallel.*

Parallelization while evaluating the constitutive equations

A process less straightforward had to be follow to parallelize this section of the code.

```
!$OMP THREADPRIVATE (kKomp,iSM,iVI)
```

Listing 4.4 *Defining thread private variables.*

Variables **kKomp, iSM, iVI** are user-defined data types used to pass information to function **DKTOPT2DConstitutiveBlock**, which is where all the process regarding the integration of the constitutive equations is performed. Hence, such variables have been defined as **THREADPRIVATE** (listing 4.4) since, along the process running in parallel, each thread will need to store its own value.

```
! To allocate treadprivate variables...
  IF (FlgAll) THEN
!$OMP PARALLEL
    CALL DKTOPT_2DInt_Set_Cons_Info(kKomp, iSM, iVI)
!$OMP END PARALLEL
    FlgAll = .FALSE.
  ENDIF
```

Listing 4.5 *Allocating thread private variables.*

Once **THREADPRIVATE** variables have been declared, next step is to allocate each variable in each used tread. This operation is performed with the lines of code shown in listing 4.5, since the variables have been previously defined as **THREADPRIVATE**, it is only required to *open* a parallel region, where the same operation within such region will be performed by each thread. The use of a flag of allocation (**FlgAll**) is necessary so that this process is not repeated.

```
1 ! Starts Main Loop Over Elements.....................................
  ! Already defined as THREADPRIVATE
3 !   + kKomp, iSM, + iVI
  !$OMP PARALLEL DO PRIVATE(Ielem,LPROP,DmgFlg,KLAY,LSTRSG,DaGeStr)&
5 !$OMP SHARED(kInfo,VBAS5sh,J_LHS)
    DO Ielem=1,NELEM
7     LPROP = VBAS5sh(Ielem)%IMATC
      KLAY  = kInfo(LPROP)%NLays
9     CALL DKTOPT_2DInt_Get_Elem_Info(Ielem, kInfo(LPROP),kKomp, iVI)
      CALL DKTOPT_2DConstitutiveBlock(kKomp, kInfo(LPROP), iSM)
11    CALL DKTOPTCheckDamagedElement(Ielem,LPROP,kKomp,kInfo(LPROP),iVI,DmgFlg)
      CALL DKTOPT_2DInt_Write_Elem_Info(Ielem,kKomp,kInfo(LPROP))
13    CALL DKTOPTDamagedStresses(LPROP, KLAY, VBAS5sh(Ielem)%Yps, &
                                 Ielem,DmgFlg,LSTRSG(:,1:KLAY), DaGeStr)
15    CALL DKTOPTEvalElasticLoads(Ielem,DaGeStr)
    ENDDO
17 !$OMP END PARALLEL DO
```

Listing 4.6 *Loop over elements running in parallel.*

Listing 4.6 shows the aspect of the part where the constitutive equations for each simple material are integrated. As can be seen, only lines 4, 5 and 17 are OpenMP directives. The selected OpenMP directive for the loop of listing 4.6 is a **PARALLEL DO**, finally in line 4 of listing 4.6 **PRIVATE** variables are defines, whereas in line 5 is where **SHARED** variables have been defined. The purpose of each function within listing 4.6 has been briefly described below.

- Function **DKTOPT_2DInt_Get_Elem_Info()** gets the required information for the given finite element.
- Function **DKTOPT_2DConstitutiveBlock()** is where all the process regarding the integration of the constitutive equations is performed.
- Function **DKTOPTCheckDamagedElement()** checks if there is any simple material within the given finite element in a non-linear range.
- Function **DKTOPT_2DInt_Write_Elem_Info()**, allocates finite element memory if necessary.
- Function **DKTOPTDamagedStresses()** evaluates the generalized stresses, then, such information is stored in the **DaGeStr** variable.
- Finally, function **DKTOPTEvalElasticLoads()** evaluates the elastic loads.

The final operation of the portion of code depicted in listing 4.6 is to evaluate internal forces of each finite element, so internal forces can be assembled into a global vector usually referred to as **LHS**. Hence, it is necessary to restrict the access to the **LHS** vector to only one thread at the time. This can be done using the directive-pair **CRITCAL|END CRITICAL**. The portion of code depicted in listing 4.7 belongs to function **DKTOPTEvalElasticLoads()** (which evaluates and assembles the internal force vector), where can be noticed the use of the **CRITICAL** OpenMP directive-pair.

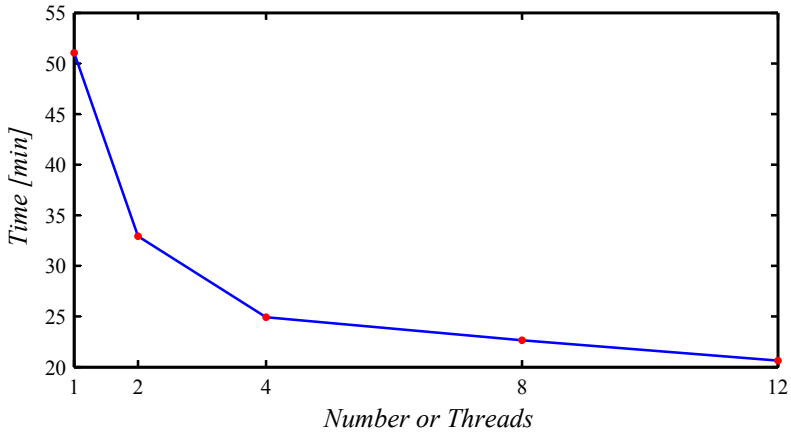

Figure 4.62 *Computational time improvement obtained for model B-SSC using different number of threads running in parallel for a total of 30 steps.*

```
! Assembles LHS vector [J_LHS].....................................
  DO II=1,3
    Ps = (Enod(II)-1) 6
    Pt = (II-1) 6
!$OMP CRITICAL (J_LHS_ASSEMBLE)
    J_LHS(Ps+1:Ps+6) = J_LHS(Ps+1:Ps+6) + ELOAD(Pt+1:Pt+6)
!$OMP END CRITICAL (J_LHS_ASSEMBLE)
  ENDDO
```

Listing 4.7 *Use of the critical OpenMP directive.*

Results of the implementation of the previously described concepts can be summarized with the use of graph on figure 4.62, that reports the time needed to perform 10 steps for each of the 3 different loading phases, for a total of 30 steps.

Have to be taken into consideration that the process of reading the input information, and allocation of the main variables has not been parallelized, hence, it was also necessary the use of graph on figure 4.63, where the time spent along one simple iteration is reported, omitting the time it takes to write output information, write information to perform restart operations, allocate the variables at the beginning of the analysis process, and so on.

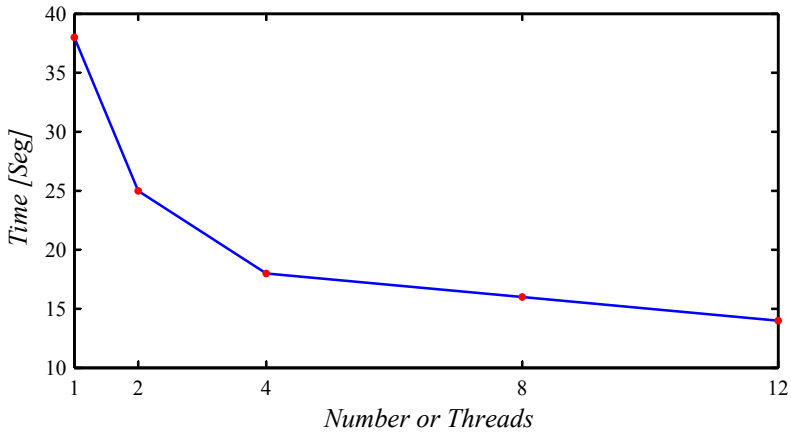

Figure 4.63 *Computational time improvement obtained for model* `B-SSC` *using different number of threads running in parallel on one single iteration.*

Chapter 5

Conclusions and Final Remarks

Main findings are presented in a brief summary, where it has been pointed out the starting point, the contributions and the conclusions belonging to the present study. Finally, future lines of study and developments has been suggested based on the work presented and on the main difficulties found while developing the current research.

5.1 Summary

The starting point of this work has been the use of a 3-node and 2-dimensional triangular shell element with one Gauss point combined with the state-of-the-art rule of mixtures theories for composite materials. Thus, make it possible to use composite materials whose components can be modeled with non-linear constitutive equations. Although the proposed methodology has only been applied to masonry structures in the present study, it can easily be extended to frame structures with or without masonry in-fills.

The first step to succeed in the present work has been, to propose, develop and implement in PLCD [34] a laminated shell element, able to reproduce the damage due to bending stresses (out-of-plane), besides of the typical damage due to membrane stresses (in-plane), this without being necessary to introduce additional degrees of freedom into its kinematics. Such idea comes with necessity of keeping the complexity of the resulting formulation for the element to a minimum, and consequently, also the required computational resources, thus, make the masonry structures described in this work computationally affordable.

The proposed element to reproduce the behavior of laminated materials, according to the classification of the existing theories, can be classified as a modification of the DB-ESL (*Displacement Based-Equivalent Single Layer*) theory, where it is taken into account the evolution of the eccentricity formed by the geometric and the mechanical planes of a bi-dimensional element during the damage process, this can be achieved since integration scheme is intended to be used with a secant constitutive tensors $\mathbf{D}_{ij}^{sec}$ instead of the elastic tensor $\mathbf{D}_{ij}$ according to [108]. As a result, generalized stresses and strains have to be referred to the mechanical plane, not to the geometrical plane as occurs in the classical DB-ESL formulation.

The use of bi-dimensional shell elements capable to reproduce not only the damage

due membrane stress, but also the damage due bending stresses, was mandatory to model three-dimensional structures, and demonstrate one of the main hypothesis the simplified design of confined masonry structures is based upon, which is the neglect of the bending-acting masonry walls. Also, it has been possible to notice the stiffness enhancement of masonry walls adjacent to short walls formed in the windows openings, the overall behavior of such structures, and damage evolution of the constituent structural elements while subjected to lateral forces.

Using the proposed scheme, not only it has been possible to obtain the force-displacement response for a confined masonry structure of one storey high, but also, for a medium-rise confined masonry building. In both cases, results have been compared with the active code regulation for construction in masonry and concrete of Mexico City finding good agreement among them. With the results obtained, has been possible to characterize the damage scenarios such structures could undergo in a zone with high seismic activity, to do so, it has been used the methodology proposed by Alzate [8] to assess a reliable seismic demand, and consequently, to state a probabilistic damage a structure would undergo given such seismic demand.

It is important to point out that the use of a macro-modeling technique combined with *plain* finite elements has proven been effective for most of the cases analyzed in chapter 3, which have been compare with some experimental results available in the literature. Using this scheme also has been possible to obtain good concordance among the results of models analyzed in chapter 4 and the results obtained using the construction code regulation for Mexico City described in references [2, 3, 4, 5, 6]. On the other hand, the possibility of using a large strain formulation approach for the studied structures seems rather inefficient, due to the small amount of deformation they undergo when cracking occurs.

In order to be able to reproduce the steel reinforcement pattern of *real-life* constructions, a computational tool was developed having in mind the 3 principal requisites shown next:

1. Reproduce a more realistic reinforcement pattern.

2. Mechanize process where volumetric part of components within a composite material is generated.

3. Capable of handling information of large meshes.

Such tool arose as the need of mechanizing and generates the composite material information given a large mesh of triangular finite elements, and a *real-life* steel reinforcement pattern of every layer within the composite. To achieve this, it is necessary to read pre-defined text files, where the information regarding the steel reinforcement patterns has been stored.

On the other hand, due to the size of the models considered in this work, it was also necessary to adopt a programming strategy that allow to reduce the execution time of analysis, and also to reduce the computational resources required in terms of memory RAM, such strategy is briefly described in next paragraphs.

- The first step in the running-time based optimization of the PLCD code, was to detect the most time-consuming processes (also called *hotspots* in computing programming terms) with the tool named VTune Amplifier Software [138]. One of the conclusions of using VTune was that intrinsic functions to perform matrix

operations had to be avoided, instead, the use of implied matrices operation functions had to be implemented. Also, the use of VTune pointed out the processes that would be necessary to parallelize.

- In order to take advantage of new technologies in current shared memory multiprocessing techniques to reduce analysis time, using OMP directives, the module of shells within the PLCD [34] code has been programmed to run in parallel. Hence, was paralellized the loop over the elements where the generalized strains ($\hat{\boldsymbol{\varepsilon}}$) and the corresponding generalized stresses ($\hat{\boldsymbol{\sigma}}$) are evaluated, also, the loop over the elements where the constitutive equations for each of their components is integrated was paralellized.

- In order to reduce the amount of memory stored along the execution process, it has been implemented a scheme where user-defined data structures have been used to store information for the finite elements, where only the information of components (internal variables, stresses and strains) are stored for elements within a *non-linear* range.

- Another alternative to the memory-consuming drawback has been explored, this is the use of iterative solvers for the solution of the linear system of equations. Although iterative solvers are more time-consuming than direct solvers, in cases of large structures their use is justified on the ground that they need less amount of memory to store the required matrices to solve the resulting linear system of equations.

5.2 Conclusions

This thesis deals with the analysis of large masonry structures, whose pursued objectives, introduced in section **1.2**, have been fulfilled satisfactorily. This is, a methodology to analyze masonry structures has been developed, implemented in the context of the finite element method, and finally, compared in some cases, with experimental results, and in other cases with building regulations obtaining good results. Other conclusions regarding the development of this thesis are listed below.

- The integration scheme over the thickness proposed in this work, combined with a bi-dimensional triangular element has proved that is capable to reproduce the damage due bending stresses while compared with three-dimensional finite elements, being not necessary the use of additional degrees of freedom.

- A significant advantage of the modification proposed to the DB-ESL theory, is being able to use laminated materials combined with the state-of-the-art rule of mixtures theories for composite, which in the case of the present work has been applied to model the behavior of the reinforced concrete confining elements. Also, the use of non-linear constitutive equations to model the behavior of its components is possible. This make possible to model and assess the damage of three-dimensional structures with a reasonable low requirement of computational resources.

- To extend the proposed scheme to a composite material is only required to obtain the secant constitutive tensor $\mathbf{D}_{ij}^{sec}$ of such composite.

- The proposed integration scheme over the thickness, due to its nature, in any case is able to reproduce debonding effects.
- For the tested models, it has been proved the significant difference among the stiffness of masonry walls when their planes are perpendicular (*bending-acting* walls) or parallel (*membrane-acting* walls) to the direction of the acting force. Such effect has been taken into account for most of the construction code regulations, assuming the higher damage will occur on the *membrane-acting* walls, and despising for designing purposes, the *bending-acting* walls, which coincides with obtained results of this work.
- In the studied cases of this work, has been observed the stiffener effect produced by the *short* masonry walls formed at the windows openings that entirely change the stiffness, and consequently, the structural behavior of the adjacent masonry walls.
- The analysis scheme for masonry buildings proposed in this work, stand on the basis that it is possible to obtain the parameters that define the mechanical and non-linear response of masonry elements, this, in order to be able to plot an anisotropic yield function. In this work a guidance using a construction code regulation has been proposed, as an attempt to settle the mechanical properties and non-linear response of masonry elements for practical purposes.
- The cases where it has been possible to perform a comparison of experimental results with the results obtained in this work, it has been achieved a well agreement in terms of cracking patterns and overall shear response. In some other cases, it only has been possible to compare obtained results with a construction code regulation, in terms of initial stiffness and overall shear strength, in such cases, also a reasonable well agreement has been achieved.
- It has been possible to model a typical confined masonry building of 6 stories height. Results obtained for such models have been compared with a construction code regulation in terms of their initial stiffness where a reasonable well agreement has been achieved. Also an analysis of probabilistic assessment of the global damage of the structure has been carried out using the scheme proposed by Alzate [8] and the design response spectrum for Mexico City.

5.3 Future Work

- The use of a macro-modeling technique applied for masonry structures has proved not being effective while attempting to reproduce the cracking propagation patterns throughout mortar joints. Such effect is typically present in two cases: a) in masonry walls where the strength of the mortar is considerably low compared with the strength of the masonry units, or b) in masonry walls with a poor bonding strength among masonry units and mortar joints. Although for a *real life* construction, a cracking propagation pattern throughout the masonry unit is not desired or expected, in this work, such effect was only possible to be reproduced using a simplified micro-modeling technique, which due to its nature, is costly from a computational point of view. To overcome this situation, it seems convenient to explore a solution like the one proposed by Pelà [130] where the use of macro-modeling techniques are combined with a crack tracking algorithm.

- The performed analysis have exhibit difficulties to reach a valid solution once a plastic process has started within a given element. Such situation is typical of linear triangular elements, it is fully documented in [32], and appears due the lack of satisfaction of the Babŭska–Brezzi condition [53]. Hence, a mixed formulation involving pressure and displacement fields [32] needs to be considered to enhance the current capabilities of the element.

- The evaluation of the dynamic response of masonry structures is almost mandatory to fully understand the failure mechanisms and reliably assess the structural safety, hence to fulfill this aspect, it is necessary the implementation of a time step integration scheme.

- Extend the formulation into one-dimensional elements with six degrees of freedom in such a way the can be coupled with the proposed shell elements. Achieving this would allow to reproduce the behavior of flat slabs structures, and to focus on the punching shear.

- In order to achieve a fully optimized formulation, improve the efficiency of the analysis process, and speed up both solution and convergence, a tangent stiffness matrix for the element have to be formulated or evaluated using perturbations techniques.

This page is intentionally left blank.

References

[1] *Manual de Diseño de Obras Civiles de la Comisión Federal de Electricidad, Diseño por Sismo.* Mexico, D.F., 1993.

[2] *Reglamento de Construcciones del Distrito Federal.* Mexico, D.F., 1993.

[3] *Normas Técnicas Complementarias para Diseño por Sismo.* Mexico, D.F., 2004.

[4] *Normas Técnicas Complementarias para Diseño y Construcciones de Estructuras de Concreto.* Mexico, D.F., 2004.

[5] *Normas Técnicas Complementarias sobre Criterios y Acciones para el Diseño Estructural de las Edificaciones.* Mexico, D.F., 2004.

[6] *Normas Técnicas Complementarias para Diseño y Construcciones de Estructuras de Mampostería.* México, D.F., 2004.

[7] Allman, D. A compatible triangular element including vertex rotations for plane elasticity analyses. *Computer & Structures 19*, 1-2 (1984), 1–8.

[8] Alzate, Y. V. *Análisis estructural estático y dinámico probabilista de edificios de hormigón armado. Aspectos metodológicos y aplicaciones a la evaluación del daño.* PhD thesis, Escola Tècnica Superior D'Enginyers de Camins, Canals I Ports. Universitat Politècnica de Catalunya, Barcelona, España, 2013.

[9] Ameny, P., Loov, R. E., and Shrive, N. G. *Prediction of elastic behaviour of masonry.* Centre for Research and Development in Masonry, 1983.

[10] Argyris, J. An excursion into large rotations. *Computer Methods in Applied Mechanics and Engineering 32* (1982), 85–155.

[11] Atkinson, R., Noland, J., Abrams, D., and McNary, S. A deformation failure theory for stack-bond brick masonry prisms in compression. In *Proceedings 7th International Brick Masonry Conference* (1985), pp. 577–592.

[12] Badillo, H. *Numerical modelling based on the multiscale homogenization theory. Application in composite materials and stuctures.* PhD thesis, Escola Tècnica Superior D'Enginyers de Camins, Canals I Ports. Universitat Politècnica de Catalunya, Barcelona, España, 2012.

[13] Barney, B., et al. Introduction to parallel computing. *Lawrence Livermore National Laboratory 6*, 13 (2010), 10. https://computing.llnl.gov/tutorials/openMP/#Introduction.

[14] Bathe, K.-J., and Dvorkin, E. A four node plate bending element based on reissner-mindlin plate theory and mixed interpolation. *International Journal for Numerical Methods in Engineering 21* (1985), 367–383.

[15] Batoz, J.-L., Bathe, K.-J., and Ho, L.-W. A study of three-node triangular plate bending elements. *International Journal for Numerical Methods in Engineering 15* (1980), 1771–1812.

[16] Battini, J., and Pacoste, C. Co-rotational beam element with warping effects in instability problems. *Computer Methods in Applied Mechanics and Engineering 191*, 17 (2002), 1755–1789.

[17] Bazant, Z. P., and Pijaudier-Cabot, G. Measurement of characteristic length of nonlocal continuum. *Journal of Engineering Mechanics 115*, 4 (1989), 755–767.

[18] Bazeley, G., Cheung, Y., Irons, M., and Zienkiewicz, O. Triangular elements in plate bending-conforming and nonconforming solutions. *Proceeding First Conference on Matrix in Structural Mechanics, Air Force Institute of Technology* (1966), 60–80.

[19] Beall, C. *Masonry design and detailing.* McGraw-Hill, 1997.

[20] Belytschko, T., and Hsieh, B. Non-linear transient finite element analysis with convected co-ordinates. *International Journal for Numerical Methods in Engineering 7* (1973), 255–271.

[21] Bergan, P., and Felippa, C. A triangular membrane element with rotational degree of freedom. *Computer Methods in Applied Mechanics and Engineering 50* (1985), 25–69.

[22] Bergan, P., and Horrigmoe, G. Incremental variational principles and finite element models for non-linear problems. *Computer Methods in Applied Mechanics and Engineering 7* (1976), 201–217.

[23] Betten, J. Creep theory of anisotropic solids. *Journal of Rheology 25* (1981), 565.

[24] Brzev, S. *Earthquake-resistant confined masonry construction.* NICEE, National Information Center of Earthquake Engineering, Indian Institute of Technology Kanpur, 2007.

[25] Car, E., Oller, S., and Oñate, E. An anisotropic elastoplastic constitutive model for large strain analysis of fiber reinforced composite materials. *Computer Methods in Applied Mechanics and Engineering 185*, 2 (2000), 245–277.

[26] Car, E., Oller, S., and Oñate, E. A large strain plasticity model for anisotropic materials—composite material application. *International Journal of Plasticity 17*, 11 (2001), 1437–1463.

[27] Carol, I., Rizzi, E., and Willam, K. An extended volumetric/deviatoric formulation of anisotropic damage based on a pseudo-log rate. *European Journal of Mechanics-A/Solids 21*, 5 (2002), 747–772.

[28] Carrera, E. Theories and finite elements for multilayered, anisotropic, composite plates and shells. *Archives of Computational Methods in Engineering 9*, 2 (2002), 87–140.

[29] Cervera, M., and Chiumenti, M. Mesh objective tensile cracking via a local continuum damage model and a crack tracking technique. *Computer methods in applied mechanics and engineering 196*, 1 (2006), 304–320.

[30] Chaboche, J. Continuum damage mechanics: Part i-general concepts. *Journal of Applied Mechanics 55*, 1 (1988), 59–64.

[31] Chaboche, J. Continuum damage mechanics: Part ii—damage growth, crack initiation, and crack growth. *Journal of Applied Mechanics 55*, 1 (1988), 65–72.

[32] Chiumenti, M., Valverde, Q., Agelet de Saracibar, C., and Cervera, M. A stabilized formulation for incompressible plasticity using linear triangles and tetrahedra. *International Journal of Plasticity 20*, 8 (2004), 1487–1504.

[33] Cicekli, U., Voyiadjis, G. Z., and Abu Al-Rub, R. K. A plasticity and anisotropic damage model for plain concrete. *International Journal of Plasticity 23*, 10 (2007), 1874–1900.

[34] CIMNE. *PLCd - Non-linear thermomechanic finite element code*. International Center of Numerical Methods in Engineering, Barcelona, España, 1991-2014. Finite element code oriented to PhD student education.

[35] CIMNE. *GiD - Adaptive and user-friendly pre and postprocessor for numerical simulations in science and engineering*. International Center of Numerical Methods in Engineering, Barcelona, España, 2014. http://www.gidhome.com/.

[36] Consejería de Medio Ambiente y Ordenación del Territorio. Norma Básica de la Edificación NBE FL-90. Muros resistentes de fábrica de ladrillo, 2004.

[37] Corona, G. *ANEMgcW Análisis y revisión de edificios de mampostería (http://www.gcingenieria.com/anem.htm)*. G. C. Ingeniería y Diseño, S. C.'.

[38] Crisafulli, F. J. *Seismic behaviour of reinforced concrete structures with masonry infills*. PhD thesis, University of Canterbury. Civil Engineering, Christchurch, New Zealand, 1997.

[39] Crisfield, M. A consistent co-rotational formulation for non-linear three-dimensional beam elements. *Computer Methods in Applied Mechanics and Engineering 81* (1990), 131–150.

[40] de Normalisation, C. E. Eurocode 8–design of structures for earthquake resistance–part 1: General rules, seismic actions and rules for buildings. *European Standard NF EN 1* (2004).

[41] Designers' Guide, M. ACI 530.1-92/ASCE/6-92. with ASTM references, 1992.

[42] Dhanasekar, M., Page, A., and Kleeman, P. The failure of brick masonry under biaxial stresses. *ICE Proceedings 79*, 2 (1985), 295–313.

[43] Dialer, C. Some remarks on the strength and deformation behaviour of shear stressed masonry panels under static monotonic loading. *Brick and Block Masonry 1* (1991), 276–283.

[44] Donea, J., and Lamain, L. A modified representation of transverse shear in c_0 quadrilateral plate elements. *Computer Methods in Applied Mechanics and Engineering 63* (1987), 39–48.

[45] Drysdale, R., Hamid, A., and Baker, L. *Masonry structures: Behavior and design.* Englewood Cliffs, NJ, 1994.

[46] Dvorkin, E., and Bathe, K.-J. A continuum mechanics based four node shell element for general non-linear analysis. *Engineering Computations 1* (1984), 77–88.

[47] Eijo, A. *Finite element modelling of delamination in advanced composite beams and plates using one- and two-dimensional finite elements based on the refined zigzag theory.* PhD dissertation, Escola Tècnica Superior D'Enginyers de Camins, Canals I Ports. Universitat Politècnica de Catalunya, Barcelona, España, 2014.

[48] Esteva, L. Behaviour under alternating loads of masonry diaphragms framed by reinforced concrete members. *Proceedings of the International Symposium on the Effects of Repeated Loadings of Materials and Structures V*, 1–36.

[49] Esteva, L. Comportamiento de muros de mampostería sujetos a carga vertical. *Instituto de Ingenieria, Universidad Nacional Autonoma de Mexico* (1961).

[50] Esteva, L. Estimaciones de daños probables producidos por temblores en edificios. *Instituto de Ingenieria, Universidad Nacional Autonoma de Mexico* (1963).

[51] Faria, R., Oliver, J., and Cervera, M. A strain-based plastic viscous-damage model for massive concrete structures. *International Journal of Solids and Structures 35*, 14 (1998), 1533–1558.

[52] Felippa, C. A study of optimal membrane triangles with drilling freedom. *Computer Methods in Applied Mechanics and Engineering 192*, 16 (2003), 2125–2168.

[53] Fortin, M., and Brezzi, F. *Mixed and hybrid finite element methods.* Springer, 1991.

[54] Fraeijs de Veubeke, B. *Stresses in shells.* Springer-Verlag, 1962.

[55] Fundación, I. *Edificaciones de mampostería para vivienda.* Fundación ICA, 1999.

[56] Ganju, T. Nonlinear finite element analysis of clay brick masonry. *Proceedings 6th Australasian Conference on Mechanics of Structures and Materials* (1977), 59–65.

[57] g.c. ingeniería y diseño, s. c. ANEMgcW 3.07 - Análisis de Edificios de Mampostería., 2007.

[58] Hamid, A., and Drysdale, R. Effect of strain gradient on tensile strength of concrete blocks. In *Masonry: Materials, Properties, and Performance: a Symposium* (1982), no. 778, ASTM International, p. 57.

[59] Hendry, A. W., Sinha, B. P., and Davies, S. *Design of masonry structures.* Taylor & Francis, 2004.

[60] Hernández, O. Recomendaciones para el diseño y construcción de estructuras de mampostería. *Instituto de Ingenieria, Universidad Nacional Autonoma de Mexico* (1975).

[61] Hernández, O., and Meli, R. Relación entre hundimientos y agrietamiento en muros de mampostería. *Instituto de Ingenieria, Universidad Nacional Autonoma de Mexico*, 350 (1975).

[62] Hillerborg, A., Modéer, M., and Petersson, P.-E. Analysis of crack formation and crack growth in concrete by means of fracture mechanics and finite elements. *Cement and concrete research 6*, 6 (1976), 773–781.

[63] Hooley, R., and Hibbert, P. Bounding plane stress solution by finite elements. *Journal of the Structural Division, ASCE 92* (1966), 39–48.

[64] Hughes, T., and Brezzi, F. On drilling degrees of freedom. *Computer Methods in Applied Mechanics and Engineering 72* (1989), 105–121.

[65] Instituto de Ingeniería, UNAM. *Diseño y Construcción de Edificios de Mampostería, No. 403.* Mexico, D.F.

[66] Jason, L., Huerta, A., Pijaudier-Cabot, G., and Ghavamian, S. An elastic plastic damage formulation for concrete: Application to elementary tests and comparison with an isotropic damage model. *Computer methods in applied mechanics and engineering 195*, 52 (2006), 7077–7092.

[67] Ju, J. On energy-based coupled elastoplastic damage theories: constitutive modeling and computational aspects. *International Journal of Solids and Structures 25*, 7 (1989), 803–833.

[68] Kachanov, L. Time of the rupture process under creep conditions. *Isv. Akad. Nauk. SSR. Otd Tekh. Nauk 8* (1958), 26–31.

[69] Kachanov, L. *Introduction to continuum damage mechanics.* Martinus Nijhoff Dortrecht, The Netherland, 1986.

[70] Khosravi, P., Ganesan, R., and Sedaghati, R. Corotational non-linear analysis of thin plates and shells using a new shell element. *International Journal for Numerical Methods in Engineering 69* (2007), 859–885.

[71] Knight, N. Raasch challenge for shell elements. *The American Institute of Aeronautics and Astronautics Journal 35* (1997), 375–371.

[72] Kojić, M., and Bathe, K.-J. *Inelastic analysis of solids and structures.* Springer, 2005.

[73] Kraus, H. *Thin elastic shells.* John Wiley & Sons, New York, 1967.

[74] Kupfer, H., Hilsdorf, H. K., and Rusch, H. Behavior of concrete under biaxial stresses. In *ACI Journal Proceedings* (1969), vol. 66, ACI.

[75] Lemaitre, J. Coupled elasto-plasticity and damage constitutive equations. *Computer Methods in Applied Mechanics and Engineering 51*, 1 (1985), 31–49.

[76] Lemaitre, J., and Chaboche, J. Aspect phénomènologique de la rupture par endommagement. *Journal de Mécanique Appliquée 2*, 3 (1978), 317–365.

[77] Levy, M. Extrait du mémoire sur les équations générales des mouvements intérieurs des corps solides ductiles au delà des limites où l'élasticité pourrait les ramener à leur premier état; présenté le 20 juin 1870. *Journal de Mathématiques Pures et Appliquées* (1871), 369–372.

[78] Lourenco, P. B., Milani, G., Tralli, A., and Zucchini, A. Analysis of masonry structures: review of and recent trends in homogenization techniques. *Canadian Journal of Civil Engineering 34*, 11 (2007), 1443–1457.

[79] Lourenço, P. *Computational strategies for masonry structures.* PhD dissertation, Delft University, Delft, Netherlands, 1996.

[80] Lubliner, J., Oliver, J., Oller, S., and Oñate, E. A plastic-damage model for concrete. *International Journal of Solids and Structures 25*, 3 (1989), 299–326.

[81] MacNeal, R., and RL, H. A proposed standard set of problems to test finite element accuracy. *Finite Elements in Analysis and Design 1* (1985), 1–20.

[82] Madinaveitia, M. Ensayes de muros de mampostería con cargas excéntricas. *Instituto de Ingenieria, Universidad Nacional Autonoma de Mexico* (1971).

[83] Madinaveitia, M., and Rodríguez, G. Resistencia a carga vertical de muros fabricados con materiales usuales en el distrito federal. *Instituto de Ingenieria, Universidad Nacional Autonoma de Mexico* (1970).

[84] Mahaney, J. A., Paret, T. F., Kehoe, B. E., Freeman, S. A., Consortium, U. C. U. S. E., et al. The capacity spectrum method for evaluating structural response during the loma prieta earthquake. 501–10.

[85] Maire, J., and Chaboche, J. A new formulation of continuum damage mechanics (cdm) for composite materials. *Aerospace Science and Technology 1*, 4 (1997), 247–257.

[86] Marguerre, K. Zur thorie der gekrummten platte grosser formanderung. *Proceedings 5th International Congress of Applied Mechanics* (1938), 98–101.

[87] Martínez, X. *Micro-mechanical simulation of composite materials using the serial/parallel mixing theory.* PhD thesis, Escola Tècnica Superior D'Enginyers de Camins, Canals I Ports. Universitat Politècnica de Catalunya, Barcelona, España, 2008.

[88] Martinez, X., Oller, S., Rastellini, F., and Barbat, A. A numerical procedure simulating rc structures reinforced with frp using the serial/parallel mixing theory. *Computers & Structures 86* (2008), 1604–1618.

[89] Mazars, J., and Pijaudier-Cabot, G. Continuum damage theory-application to concrete. *Journal of Engineering Mechanics 115*, 2 (1989), 345–365.

[90] McNary, W. S., and Abrams, D. P. Mechanics of masonry in compression. *Journal of Structural Engineering 111*, 4 (1985), 857–870.

[91] Meli, R. *Comportamiento sísmico de muros de mampostería*, second ed. Instituto de Ingenieria, Universidad Nacional Autonoma de Mexico, Mexico, D.F., May 1979.

[92] Meli, R. Diseño sísmico de edificios de muros de mampostería. la práctica actual y el comportamiento observado. *Sociedad Mexicana de Ingeniería Sísmica 40* (1990), 7–28.

[93] Meli, R., and Alcocer, S. M. Implementation of structural earthquake-disaster mitigation programs in developing countries. *Natural Hazards Review 5*, 1 (2004), 29–39.

[94] Meli, R., and Hernández, O. Propiedades de piezas para mampostería producidas en el distrito federal. *Instituto de Ingenieria, Universidad Nacional Autonoma de Mexico* (1971).

[95] Meli, R., and Hernández, O. Efectos de hundimientos diferenciales en construcciones a base de muros de mampostería. *Instituto de Ingenieria, Universidad Nacional Autonoma de Mexico* (1975).

[96] Meli, R., and Reyes, A. Propiedades mecánicas de la mampostería. *Instituto de Ingenieria, Universidad Nacional Autonoma de Mexico* (1971).

[97] Meli, R., and Salgado, G. Comportamiento de muros de mampostería sujetos a carga lateral. *Instituto de Ingenieria, Universidad Nacional Autonoma de Mexico* (1969).

[98] Meli, R., Zeevart, W., and Esteva, L. Comportamiento de muros de mampostería hueca ante carga lateral alternada. *Instituto de Ingenieria, Universidad Nacional Autonoma de Mexico* (1968).

[99] Milani, G., Lourenço, P., and Tralli, A. 3d homogenized limit analysis of masonry buildings under horizontal loads. *Engineering Structures 29*, 11 (2007), 3134–3148.

[100] Militello, C., and Felippa, C. The first ANDES elements: 9-DOF plate bending triangles. *Computer Methods in Applied Mechanics and Engineering 93* (1991), 217–246.

[101] Mindlin, R. Influence of rotatory inertia and shear in flexural motions of isotropic elastic plates. *Journal of Applied Mechanics 18* (1951), 31–38.

[102] Mises, R. v. Mechanik der festen körper im plastisch-deformablen zustand. *Nachrichten von der Gesellschaft der Wissenschaften zu Göttingen, Mathematisch-Physikalische Klasse*, 582–592 (1913).

[103] Molina Herrera, M., Oller Martínez, S. H., Barbat Barbat, H. A., and Martínez, X. Estudio de estructuras de hormigón reforzadas con frp mediante la teoría de mezclas serie/paralelo. *Revista internacional de Ingenieria de estructuras 13*, 1 (2009), 29–54.

[104] Moroni, M., Astroza, M., and Acevedo, C. Performance and seismic vulnerability of masonry housing types used in chile. *Journal of performance of constructed facilities 18*, 3 (2004), 173–179.

[105] Nour-Omid, B., and Rankin, C. Finite rotation analysis and consistent linearization using projectors. *Computer Methods in Applied Mechanics and Engineering 93* (1991), 353–384.

[106] Novozhilov, V. *Theory of thin plates*. P. Noordhoff, 1959.

[107] Oñate, E. *Cálculo de Estructuras por el Método de Elementos Finitos. Analisis Elástico Lineal*. Centro Internacional de Métodos Numericos en Ingeniería, Barcelona, España, 1995.

[108] Ochoa, O., and Reddy, J. *Finite Element Analysis of Composite Laminates*. Klawer Academic Publishers, 1992.

[109] Oh, B., and BAZANT, Z. Crack band theory for fracture of concrete. *Materials and Structures, January-February* (1983), 155–177.

[110] Oliver, J. A consistent characteristic length for smeared cracking models. *International Journal for Numerical Methods in Engineering 28*, 2 (1989), 461–474.

[111] Oliver, J., Cervera, M., Oller, S., and Lubliner, J. Isotropic damage models and smeared crack analysis of concrete. In *Second international conference on computer aided analysis and design of concrete structures* (1990), vol. 2, pp. 945–958.

[112] Oliver, J., Huespe, A., Pulido, M., and Chaves, E. From continuum mechanics to fracture mechanics: the strong discontinuity approach. *Engineering Fracture Mechanics 69*, 2 (2002), 113–136.

[113] Oller, S. *Un Modelo de Daño Continuo Para Materiales Friccionales*. PhD thesis, Escola Tècnica Superior D'Enginyers de Camins, Canals I Ports. Universitat Politècnica de Catalunya, Barcelona, España, 1998.

[114] Oller, S. *Fractura Mecánica, un Enfoque Global*. Centro Internacional de Métodos Numericos en Ingeniería, Barcelona, España, 2001.

[115] Oller, S., Botello, S., Miquel, J., and Oñate, E. An anisotropic elastoplastic model based on an isotropic formulation. *Engineering Computations 12*, 3 (1995), 245–262.

[116] Oller, S., Car, E., and Lubliner, J. Definition of a general implicit orthotropic yield criterion. *Computer methods in applied mechanics and engineering 192*, 7 (2003), 895–912.

[117] Oller, S., Miquel Canet, J., and Zalamea, F. Composite material behavior using a homogenization double scale method. *Journal of engineering mechanics 131*, 1 (2005), 65–79.

[118] Oller, S., Oñate, E., and Miquel, J. Mixing anisotropic formulation for analysis of composites. *Communications in numerical methods in engineering 12*, 8 (1996), 471–482.

[119] Oller, S., Oñate, E., Miquel Canet, J., and Botello, S. A finite element model for analysis of multiphase composite materials. In *ICCM/9.* (1993), vol. 3, pp. 94–103.

[120] Oñate, E., Oller, S., Botello, S., and Canet, J. M. *Métodos avanzados de cálculo de estructuras de materiales compuestos.* Centro Internacional de Métodos Numéricos en Ingeniería (CIMNE), 1991.

[121] Organizmo Nacional de Normalización y Certificación de la Construcción y Edificación S.C. Building industry - blocks, bricks, brincks or partition masonry units and paving block - Compresive Strengh - Method of test, 2004.

[122] Ortiz, M., and Popov, E. P. Plain concrete as a composite material. *Mechanics of Materials 1*, 2 (1982), 139–150.

[123] Pacoste, C. Co-rotational flat facet triangular element for shell instability analysis. *Computer Methods in Applied Mechanics and Engineering 156*, 1 (1998), 75–110.

[124] Page, A. W. Finite element model for masonry. *Journal of Structural Division 104*, 8 (1973), 1267–1285.

[125] Page, A. W. The biaxial compressive strength of brick masonry. In *ICE Proceedings* (1981), vol. 71, Thomas Telford, pp. 893–906.

[126] Page, A. W. The strength of brick masonry under biaxial compression-tension. *International Journal of Masonry Construction 3*, 1 (1983), 23–31.

[127] Paredes, J. A. *Modelización numerica del comportamiento constitutivo del daño local y global y su correlacion con la evolucion de las recuencias naturales en estructuras de hormigón reforzado.* PhD dissertation, Escola Tècnica Superior D'Enginyers de Camins, Canals I Ports. Universitat Politècnica de Catalunya, Barcelona, España, 2013.

[128] Paredes, J. A., Barbat, A. H., and Oller, S. A compression–tension concrete damage model, applied to a wind turbine reinforced concrete tower. *Engineering Structures 33*, 12, 3559–3569.

[129] Paulay, T., and Priestley, M. *Seismic design of reinforced concrete and masonry structures.* J. Wiley & Sons, USA, 1992.

[130] Pelà, L. *Continuum damage model for nonlinear analysis of masonry structures.* PhD thesis, Università degli studi di Ferrara, Ferrara, Italy, 2009.

[131] Peng, X., and Crisfield, M. A consistent co-rotational formulation for shells using the constant stress/constant moment triangle. *International Journal for Numerical Methods in Engineering 35*, 9 (1990), 1829–1847.

[132] Pierre Mouroux and Etienne Bertrand and Myriam Bour and Benoit Le Brun and Simon Depinois and Philippe Masure and the RISK-EU team. *The European Rusk-EU project: An advanced approach to earthquake risk scenarios, with applications to different European towns.* The European Commission, 2004.

[133] Rankin, C., and Brogan, F. An element independent corotational procedure for the treatment of large rotations. *Journal of Pressure Vessel Technology 108* (1986), 165–174.

[134] Rankin, C., and Nour-Omid, B. The use of projectors to improve finite element performance. *Computers & Structures 30* (1988), 257–267.

[135] Rastellini, F., Oller, S., Salomón, O., and Oñate, E. Composite materials non-linear modelling for long fibre-reinforced. *Computers & Structures 86* (2008), 879–896.

[136] Rastellini, F. G. *Modelación numérica de la no-linealidad constitutiva de laminados compuestos*. PhD thesis, Escola Tècnica Superior D'Enginyers de Camins, Canals I Ports. Universitat Politècnica de Catalunya, Barcelona, España, 2006.

[137] Rathbun, J. Wind forces on a tall building. *Proceedings of the American Society of Civil Engineers 64* (1938), 1355–1375.

[138] Reinders, J. Vtune performance analyzer essentials: Measurement and tuning techniques for software developers. engineer to engineer series. *Intel Press 1*, 2 (2005), 6.

[139] Reuss, A. Berücksichtigung der elastischen formänderung in der plastizitätstheorie. *ZAMM-Journal of Applied Mathematics and Mechanics/Zeitschrift für Angewandte Mathematik und Mechanik 10*, 3 (1930), 266–274.

[140] Roca, P., Cervera, M., Gariup, G., et al. Structural analysis of masonry historical constructions. classical and advanced approaches. *Archives of Computational Methods in Engineering 17*, 3 (2010), 299–325.

[141] Roca, P., Massanas, M., Cervera, M., and Arun, G. Structural analysis of küçük ayasofya mosque in ístanbul. *Structural analysis of historical constructions IV. Balkema, Amsterdam* (2004), 679–686.

[142] Rosenhaupt, S., and Sokal, L. Masonry walls on continuous beams. *Journal of the Structural Division 91*, 1 (1965), 155–172.

[143] Rots, J. G. *Structural masonry: An experimental/numerical basis for practical design rules*. AA Balkema, 1997.

[144] Rots, J. G., and De Borst, R. Analysis of mixed-mode fracture in concrete. *Journal of engineering mechanics 113*, 11 (1987), 1739–1758.

[145] Samarasinghe, W., Page, A., and Hendry, A. A finite element model for the in-plane behavior of brickwork. *Proceedings Institute of Civil Engineers 73* (1982), 171–178.

[146] San Bartolomé, A. Colección del Ingeniero Civil, Libro No. 4, 1990.

[147] Sanchez-Palencia, E., and Zaoui, A. Homogenization techniques for composite media. In *Homogenization Techniques for Composite Media* (1987), vol. 272.

[148] Saw, C. Linear elastic finite element analysis of masonry walls on beams. *Building Science 9* (1974), 299–307.

[149] Schenk, O., Gärtner, K., Karypis, G., Röllin, S., and Hagemann, M. Pardiso solver project. *URL: http://www.pardiso-project.org* (2010).

[150] Schlegel, R., Will, J., and Rautenstrauch, K. Materialmodelle für nichtlineare berechnungen komplexer mauerwerkstrukturen mit ansys.

[151] Simo, J., Fox, D., and MS, R. On a stress resultant geometrically exact shell model, part III: Computational aspects of the non-linear theory. *Computer Methods in Applied Mechanics and Engineering 79* (1990), 21–70.

[152] Simo, J., and Hughes, T. *Computational inelasticity*, vol. 7 of *Interdisciplinary applied mathematics*. Springer, 1998.

[153] Simo, J., and Ju, J. Strain-and stress-based continuum damage models ii. computational aspects. *International journal of solids and structures 23*, 7 (1987), 841–869.

[154] Simo, J., and Ju, J. Strain-and stress-based continuum damage models i. formulation. *Mathematical and Computer Modelling 12*, 3 (1989), 378.

[155] St Venant, B. d. Mémoire sur l'etablissement des equations différentielles des mouvements intérieurs opérés dans les corps solids ductiles au delà des limites où l'elasticité pourrait les ramener à leur premier etat. *Comptes Rendus70 473* (1870).

[156] Standards Association of New Zealand. Nzs 3120:1983 concrete Masonry Units, 1983.

[157] Szwabowicz, M. Variational formulation in the geometrically non-linear elastic shell theory. *International Journal of Engineering Science 22* (1986), 1161–1175.

[158] Tao, X., and Phillips, D. V. A simplified isotropic damage model for concrete under bi-axial stress states. *Cement and Concrete Composites 27*, 6 (2005), 716–726.

[159] Timoshenko, S., and Goodie, J. *Teoría de la Elasticidad*. Ediciones Urmo S. A, Bilbao, España, 1968.

[160] Timoshenko, S., and Woinowsky-Kringer, S. *Teoría de Placas y Láminas*. Ediciones Urmo S. A., Bilbao, España, 1970.

[161] Tollmien, W., Schlichting, H., and Görtler, H. Spannungsverteilung in plastischen körpern. In *Ludwig Prandtl Gesammelte Abhandlungen*. Springer, 1961, pp. 133–148.

[162] Tresca, H.-É. *Sur l'écoulement des corps solides soumis à une forte pression*. Gauthier-Villars, 1867.

[163] Truesdell, C., and Toupin, R. *The classical field theories*. Springer, 1960.

[164] Turkstra, C. Resistencia de muros de mampostería ante cargas verticales excéntricas. *Instituto de Ingenieria, Universidad Nacional Autonoma de Mexico* (1970).

[165] Turner, M., Clough, R., Martin, H., and Topp, L. Stiffness and deflection analysis of complex structures. *Journal of the Aeronautical Sciences (Institute of the Aeronautical Sciences) 23* (1956), 805–824.

[166] Tzamtzis, A., and Asteris, P. Finite element analysis of masonry structures: Part I - review of previous work. *Ninth North American Masonry Conference* (2003).

[167] Van der Pluijm, R. Material properties of masonry and its components under tension and shear. In *Proceedings of the 6 th Canadian Masonry Symposium. University of Saskatchevan* (Saskatoon, Saskatchevan, 1992).

[168] Van der Pluijm, R. Shear behaviour of bed joints. In *Proceedings of the 6th North American Masonry Conference. Drexel University* (Philadelphia, Pennsylvania, USA, 1993).

[169] Vargas-Félix, M., and Botello-Rionda, S. FEMT, an open source library and tools for solving large systems of equations in parallel.

[170] Vermeltfoort, A. T., and Raijmakers, T. Deformation controlled tests in masonry shear walls Part 2 (in Deutch). *Delft: Report B-92-1156, TNO-Bouw, Eindhoven University of Technology* (1992).

[171] Wempner, G. Finite elements, finite rotations and small strains of flexible shells. *International Journal of Solids and Structures 5* (1969), 117–153.

[172] Zienkiewicz, O. *El método de los elementos finitos*, 3 ed. Editorial Reverté, Barcelona, España, 1979.

Appendices

Appendix A

Damage Constitutive Model

In this appendix, a brief description of formulation regarding to this branch of *Continuum Mechanics* is reproduced, emphasising to models in which damage is described by one or two scalars.

A.1 Effective Stress Concept

Continuum damage mechanics is based upon the definition of the effective stress $\bar{\boldsymbol{\sigma}}$ (measured in the *non-damaged* space) firstly introduced by Kachanov [69], and later on such concept was used in accordance with *equivalence deformation* by Lemaitre-Chaboche [76], $\bar{\boldsymbol{\sigma}}$ can be computed as

$$\bar{\boldsymbol{\sigma}} = \mathbf{C}_0 : \boldsymbol{\varepsilon} \tag{A.1}$$

being $\mathbf{C}$ an isotropic linear-elastic four order tensor. In the case of an isotropic damage model, damage occurs equal in all directions and only depends on a scalar damage variable d, hence equation (A.1) takes the form [111]

$$\bar{\boldsymbol{\sigma}} = \frac{\boldsymbol{\sigma}}{1-d} \tag{A.2}$$

damage stress $\boldsymbol{\sigma}$ under an effective stress $\bar{\boldsymbol{\sigma}}$ can be also represented as

$$\boldsymbol{\sigma} = (1-d)\bar{\boldsymbol{\sigma}} = (1-d)\mathbf{C}_0 : \boldsymbol{\varepsilon} \tag{A.3}$$

Under such assumptions damage internal variable d becomes a measure of loss of stiffness, whose limits are $0 \leq d \leq 1$. A fully damage state is represented by $d = 1$ whereas $d = 0$ represents a non-damaged state.

A.2 Thermodynamic Framework and Constitutive Relationship

Constitutive relationship is obtained by writing the dissipation of the thermo-mechanical process. Helmholtz free energy potential will be needed as a measurement of the total potential energy. Hence, for an isotropic damage model under constant temperature,

using $\boldsymbol{\varepsilon}$ and d as free and internal variables respectively, Helmholtz free energy potential can be defined as

$$\boldsymbol{\Psi} = \boldsymbol{\Psi}(\boldsymbol{\varepsilon}, d) = (1-d)\boldsymbol{\Psi}^0 \tag{A.4}$$

being $\boldsymbol{\Psi}^0$ Helmholtz initial free energy for an undamaged state, for the case of small strains is given by

$$\boldsymbol{\Psi}^0(\boldsymbol{\varepsilon}) = \frac{1}{2}\boldsymbol{\varepsilon} : \mathbf{C}_0 : \boldsymbol{\varepsilon} \quad ; \quad \boldsymbol{\Psi}^0(\boldsymbol{\varepsilon}) = \frac{1}{2}\varepsilon_{ij}\, C_{ijkl}\, \varepsilon_{kl} \tag{A.5}$$

where $\mathbf{C}_0$ is the undamaged constitutive tensor. Finally dissipative potential energy subjected to a thermally stable process is set using the Clausius-Planck inequality.

$$\Xi = \left(\boldsymbol{\sigma} - \frac{\partial \boldsymbol{\Psi}}{\partial \boldsymbol{\varepsilon}}\right) : \dot{\boldsymbol{\varepsilon}} - \frac{\partial \boldsymbol{\Psi}}{\partial \dot{d}} \geq 0 \tag{A.6}$$

Finally, constitutive hyper-elastic equation for damage model with one damage scalar variable is defined as:

$$\boldsymbol{\sigma} = \frac{\partial \boldsymbol{\Psi}}{\partial \boldsymbol{\varepsilon}} = (1-d)\frac{\partial \boldsymbol{\Psi}_0}{\partial \boldsymbol{\varepsilon}} = (1-d)\mathbf{C}_0 : \boldsymbol{\varepsilon} \tag{A.7}$$

A.3 Damage Criterion

Damage criterion depends on mechanical properties of a given material, and in its general form is given by following expression [111]

$$\mathbb{F}(\boldsymbol{\sigma}_0; \boldsymbol{q}) = f(\boldsymbol{\sigma}_0) - c(d) \leq 0 \tag{A.8}$$

where $\boldsymbol{q} \equiv \{d\}$, $f(\boldsymbol{\sigma}_0)$ is a function of stress tensor $\boldsymbol{\sigma}_0 = \mathbf{C}_0 : \boldsymbol{\varepsilon}$, and $c(d)$ is an stress-like variable, representing the current damage threshold, as its variable controls the size of the (monotonically) expanding damage surface. The initial value of the damage threshold is $c_0 = \boldsymbol{\sigma}_0$, where $\boldsymbol{\sigma}_0$ is the initial uniaxial damage stress.

A.4 Evolution Law of Internal Variables

The expansion of the damage bounding surface for loading, unloading and reloading conditions is controlled by the Kuhn-Tucker relations and the damage consistency conditions, which are:

$$\dot{r} \geq 0 \quad ; \quad \mathbb{F}(\boldsymbol{\sigma}_0; \boldsymbol{q}) \leq 0 \quad ; \quad \dot{c}\mathbb{F}(\boldsymbol{\sigma}_0; \boldsymbol{q}) = 0 \tag{A.9}$$

Which leads to the loading condition:

$$\dot{f} = \dot{c} \tag{A.10}$$

Leading to the explicit definition of the current values of the initial variable $c(d)$ in the form

$$c(d) = max\left\{c_0, max(\mathbb{F})\right\} \tag{A.11}$$

Equation (A.11) allows to compute the current values for $c(d)$ in terms of the current value of $\mathbb{F}(\boldsymbol{\sigma}_0; \boldsymbol{q})$, which depends explicitly on the current total strains.

Finally, damage index $d = d(r)$ is explicitly defined in terms of the corresponding current value of damage threshold, so that it is a monotonically increasing function such that $0 \leq d \leq 1$.

Within the present work, following functions to represent damage evolution are used: where H_S is the softening modulus.

- Linear Softening

$$d(r) = \begin{cases} (1 + H_S)(1 - \dfrac{c_0}{c}) & c_0 \leq c \leq c_u = c_0 \left(1 - \dfrac{1}{H_S}\right) \\ 1 & c \leq c_u \end{cases} \tag{A.12}$$

- Exponential Softening

$$d(r) = 1 - \frac{c_0}{c} exp \left\{ -2H_S \left(\frac{c - c_0}{c_0} \right) \right\} \quad ; \quad c_0 \leq c \tag{A.13}$$

A.5 Tangent Operator

The tangent constitutive tensor $\mathbf{C}^{tan}$ can be obtained explicitly. The stress increment is given by:

$$\begin{aligned} \dot{\boldsymbol{\sigma}} &= \mathbf{C}^{tan} : \dot{\boldsymbol{\varepsilon}} \\ &= (1 - d)\mathbf{C} : \dot{\boldsymbol{\varepsilon}} - \dot{d}\mathbf{C} : \boldsymbol{\varepsilon} \\ &= (1 - d)\mathbf{C} : \dot{\boldsymbol{\varepsilon}} - \dot{d}\boldsymbol{\sigma} \end{aligned} \tag{A.14}$$

In the elastic regime, the stress rate is expressed as:

$$\dot{\boldsymbol{\sigma}} = (1 - d)\mathbf{C} : \dot{\boldsymbol{\varepsilon}} \quad ; \quad \dot{d} = 0 \tag{A.15}$$

Recalling that the rate of the damage index has been expressed as $\dot{d} = d'\dot{r}$ and that the loading direction $\dot{r} = \dot{\tau}$, then the stress increment can be expressed as:

$$\dot{\boldsymbol{\sigma}} = (1 - d)\mathbf{C} : \dot{\boldsymbol{\varepsilon}} - \frac{d'}{\tau}\boldsymbol{\sigma} \otimes \boldsymbol{\sigma} : \dot{\boldsymbol{\varepsilon}} \tag{A.16}$$

$$\dot{\boldsymbol{\sigma}} = \left[(1 - d)\mathbf{C} - \frac{d'}{\tau}\boldsymbol{\sigma} \otimes \boldsymbol{\sigma} \right] \dot{\boldsymbol{\varepsilon}} \tag{A.17}$$

And the tangent constitutive tensor stays as:

$$\mathbf{C}^{tan} = (1 - d)\mathbf{C} - \frac{d'}{\tau}\boldsymbol{\sigma} \otimes \boldsymbol{\sigma} \tag{A.18}$$

This page is intentionally left blank.

Appendix B

Plasticity

This Appendix reproduces the governing equations of classical rate-independent plasticity model following formulation presented in [152], where a comprehensive exposition on stress-space formulation within the context of the three dimensional infinitesimal theory has been driven.

B.1 General Formulation

1. *Additive decomposition of the strain tensor.* Assumption that strain tensor $\boldsymbol{\varepsilon}$ can be decomposed into an elastic $\boldsymbol{\varepsilon}^e$ and plastic part $\boldsymbol{\varepsilon}^p$ is made, hence

$$\boldsymbol{\varepsilon} = \boldsymbol{\varepsilon}^e + \boldsymbol{\varepsilon}^p \tag{B.1}$$

Since $\boldsymbol{\varepsilon}$ is regarded as an independent variable and evolution of $\boldsymbol{\varepsilon}^p$ will be defined as a flow rule, equation (B.1) should be viewed as a definition of elastic strain tensor as $\boldsymbol{\varepsilon}^e = \boldsymbol{\varepsilon} - \boldsymbol{\varepsilon}^p$.

2. *(Elastic) stress response.* Stress tensor $\boldsymbol{\sigma}$ is related to elastic strain $\boldsymbol{\varepsilon}$ by means of a stored-energy function $W : \mathcal{B} \times \mathbb{S} \to \mathbb{R}$ according to the (hyperelastic) relationship

$$\boldsymbol{\sigma}(\boldsymbol{x}, t) = \frac{\partial W\left[\boldsymbol{x}, \boldsymbol{\varepsilon}^e(\boldsymbol{x}, t)\right]}{\partial \boldsymbol{\varepsilon}^p} \tag{B.2}$$

For linearized elasticity, W is a quadratic form in the elastic strain, i.e., $W = \frac{1}{2}\boldsymbol{\varepsilon}^e : \mathbf{C} : \boldsymbol{\varepsilon}^e$, where $\mathbf{C}$ is the tensor of *elastic moduli* which is assumed constant. Then equations (B.1) and (B.2) imply

$$\boldsymbol{\sigma} = \mathbf{C} : [\boldsymbol{\varepsilon} - \boldsymbol{\varepsilon}^p] \tag{B.3}$$

It is observed that equations (B.2) -(B.3) and the decomposition (B.1) are *local*. Therefore, although the total strain is the (symmetric) gradient of the displacement field, the elastic strain *is not* in general the gradient of an elastic displacement field. Shall be noticed that $\boldsymbol{\varepsilon}^p$ and, consequently, $\boldsymbol{\varepsilon}^e$ are *assumed to be symmetric at the outset*, i.e., $\boldsymbol{\varepsilon}^p \in \mathbb{S}$. Thus the notion of a plastic spin plays no role in classical plasticity.

3. *Elastic domain and yield condition. Yield Criterion* function $f : \mathbb{S} \times \mathbb{R}^m \to \mathbb{R}$ which constrains the admissible states $\{\boldsymbol{\sigma}, \boldsymbol{q}\} \in \mathbb{S} \times \mathbb{R}^m$ has been define to lie in the set $\mathbb{E}_\sigma$ as

$$\mathbb{E}_\sigma := \{(\boldsymbol{\sigma}, \boldsymbol{q}) \in \mathbb{S} \times \mathbb{R}^m \mid f(\boldsymbol{\sigma}, \boldsymbol{q}) \leq 0\} \tag{B.4}$$

Interior of $\mathbb{E}_\sigma$ is referred to as $\text{int}(\mathbb{E}_\sigma)$ and given by

$$int(\mathbb{E}_\sigma) := \{(\boldsymbol{\sigma}, \boldsymbol{q}) \in \mathbb{E} \times \mathbb{R}^m \mid f(\boldsymbol{\sigma}, \boldsymbol{q}) < 0\} \tag{B.5}$$

as the *elastic domain*; whereas the boundary of $\mathbb{E}_\sigma$, denoted by $\partial\mathbb{E}_\sigma$ and defined as

$$\partial\mathbb{E}_\sigma := \{(\boldsymbol{\sigma}, \boldsymbol{q}) \in \mathbb{E} \times \mathbb{R}^m \mid f(\boldsymbol{\sigma}, \boldsymbol{q}) = 0\} \tag{B.6}$$

is called the *yield surface in stress space*. Can be noticed that $\{(\boldsymbol{\sigma}, \boldsymbol{q})\}$ outside $\mathbb{E}_\sigma$ are *nonadmissible* and are ruled out in classical plasticity.

4. *Flow rule and hardening law.* Irreversibility of plastic flow is introduced by the following equations of evolution for $\{\boldsymbol{\varepsilon}^p, \boldsymbol{q}\}$, called *flow rule* and *hardening law*, respectively;

$$\begin{aligned} \dot{\boldsymbol{\varepsilon}}^p &= \gamma \boldsymbol{r}(\boldsymbol{\sigma}, \boldsymbol{q}), \\ \dot{\boldsymbol{q}} &= -\gamma \boldsymbol{h}(\boldsymbol{\sigma}, \boldsymbol{q}). \end{aligned} \tag{B.7}$$

Where $\boldsymbol{r} : \mathbb{S} \times \mathbb{R}^m \to \mathbb{S}$ and $\boldsymbol{h} : \mathbb{S} \times \mathbb{R}^m \to \mathbb{R}^m$ are *prescribed* function which define direction of plastic flow and type of hardening. Parameter $\gamma \geq 0$ is a non-negative function, called *the consistency parameter*, assumed to obey following *Kuhn-Tucker complementary conditions*:

$$\gamma \geq 0, \qquad f(\boldsymbol{\sigma}, \boldsymbol{q}) \leq 0, \qquad \gamma f(\boldsymbol{\sigma}, \boldsymbol{q}) = 0. \tag{B.8}$$

In addition to condition B.8, $\gamma \geq 0$ satisfies the *consistency requirement*

$$\gamma \dot{f}(\boldsymbol{\sigma}, \boldsymbol{q}) = 0 \tag{B.9}$$

In the classical literature, conditions B.8 and B.9 are known as *loading/unloading* and *consistency conditions*, respectively.

5. To exploit condition (B.9), derivative of f have to be evaluated at $(\boldsymbol{\sigma}, \boldsymbol{q}) \in \mathbb{E}_\sigma$. Using chain rule, along with the rate forms of the stress-strain relationship (B.4), the flow rule, and the hardening law (B.7), is found that

$$\begin{aligned} \dot{f} &= \partial_\sigma f : \dot{\boldsymbol{\sigma}} + \partial_q f \cdot \dot{\boldsymbol{q}} \\ &= \partial_\sigma f : \mathbf{C} : [\dot{\boldsymbol{\varepsilon}} - \dot{\boldsymbol{\varepsilon}}^p] + \partial_q f \cdot \dot{\boldsymbol{q}} \\ &= \partial_\sigma f : \mathbf{C} : \dot{\boldsymbol{\varepsilon}} - \gamma \left[\partial_\sigma f : \mathbf{C} : \boldsymbol{r} + \partial_q f \cdot \boldsymbol{h}\right] \leq 0 \end{aligned} \tag{B.10}$$

Assuming that flow rule, hardening law, and yield conditions in stress space are such that following inquiry hold

$$[\partial_\sigma f : \mathbf{C} : \boldsymbol{r} + \partial_q f \cdot \boldsymbol{h}] > 0 \tag{B.11}$$

for all admissible states $[\boldsymbol{\sigma}, \boldsymbol{q}] \in \partial_\sigma$. Such assumption only holds for perfect plasticity, yielding (B.9) to

$$\dot{f} = 0 \iff \gamma = \frac{\langle \partial_\sigma f : \mathbf{C} : \dot{\boldsymbol{\varepsilon}} \rangle}{\partial_\sigma f : \mathbf{C} : \boldsymbol{r} + \partial_q f \cdot \boldsymbol{h}} \tag{B.12}$$

Finally, according to (B.2) and (B.7):

$$\dot{\boldsymbol{\sigma}} = \mathbf{C} : [\dot{\boldsymbol{\varepsilon}} - \dot{\boldsymbol{\varepsilon}}^p] = \mathbf{C} : [\dot{\boldsymbol{\varepsilon}} - \gamma \boldsymbol{r}] \tag{B.13}$$

Then, substituting (B.12) in (B.13) then yields the rate of change of $\boldsymbol{\sigma}$ in terms of the total strain rate $\dot{\boldsymbol{\varepsilon}}$ as follows

$$\dot{\boldsymbol{\sigma}} = \mathbf{C}^{tan} : \dot{\boldsymbol{\varepsilon}} \tag{B.14}$$

being $\mathbf{C}^{tan}$ the so-called tensor of tangent elastoplastic moduli given by the expression:

$$\mathbf{C}^{ep} = \begin{cases} \mathbf{C} & if \;\; \gamma = 0 \\ \mathbf{C} = \mathbf{C} - \dfrac{\mathbf{C} : \boldsymbol{r} \otimes \mathbf{C} : \partial_\sigma f}{\partial_\sigma f : \mathbf{C} : \boldsymbol{r} + \partial_q f \cdot \boldsymbol{h}} & if \;\; \gamma > 0 \end{cases} \tag{B.15}$$

Can be noticed that $\mathbf{C}^{tan}$ is generally *non-symmetric* for arbitrary $\boldsymbol{r}(\boldsymbol{\sigma}, \boldsymbol{q})$, except in the case where

$$\boldsymbol{r}(\boldsymbol{\sigma}, \boldsymbol{q}) = \partial_\sigma f(\boldsymbol{\sigma}, \boldsymbol{q}) \tag{B.16}$$

which has special significance and is called *associative flow rule*.

B.2 J_2 Flow Theory with Isotropic/Kinematic Hardening

A choice of internal plastic variables which is typically of metal plasticity is $\boldsymbol{q} := \{\alpha, \overline{\beta}\}$. Where, α is the equivalent plastic strain that defines the *isotropic hardening* of the von Mises yield surface, and $\overline{\beta}$ defines the center of the von Mises yield surface in stress deviator space. The resulting J_2-plasticity model has the following yield condition flow rule and hardening law:

$$
\begin{aligned}
\boldsymbol{\eta} &:= \operatorname{dev}[\boldsymbol{\sigma}] - \overline{\beta} \\
\operatorname{tr}\left[\overline{\beta}\right] &= 0 \\
f(\boldsymbol{\sigma}, \boldsymbol{q}) &= \|\boldsymbol{\eta}\| - \sqrt{\frac{1}{2}} K'(\alpha) \\
\dot{\boldsymbol{\varepsilon}}^p &= \gamma \frac{\boldsymbol{\eta}}{\|\boldsymbol{\eta}\|} \\
\dot{\overline{\boldsymbol{\beta}}} &= \gamma \frac{2}{3} H'(\alpha) \frac{\boldsymbol{\eta}}{\|\boldsymbol{\eta}\|} \\
\dot{\alpha} &= \gamma \sqrt{\frac{2}{3}}
\end{aligned}
\tag{B.17}
$$

Functions $K'(\alpha)$ and $H'(\alpha)$ are called the isoparametric and hardening modulus, respectively. Since $\|\dot{\boldsymbol{\varepsilon}}\| = \gamma$, relationship $(\text{B.17})_6$ implies that

$$
\alpha(t) := \int_0^t \sqrt{\frac{2}{3}} \ \|\dot{\boldsymbol{\varepsilon}}^p(\tau)\| \ d\tau \tag{B.18}
$$

which agrees with the usual definition of equivalent plastic strain.

Now, the plastic consistency parameter given by B.12 in the general case takes the explicit form:

$$
\gamma = \frac{\langle \boldsymbol{n} : \dot{\boldsymbol{\varepsilon}} \rangle}{1 + \dfrac{H' + K'}{3\mu}} \tag{B.19}
$$

where

$$
\boldsymbol{n} := \frac{\boldsymbol{\eta}}{\|\boldsymbol{\eta}\|} \tag{B.20}
$$

Since $\operatorname{tr}[\boldsymbol{n}] = 0$, $\boldsymbol{n} : \dot{\boldsymbol{\varepsilon}} \equiv \boldsymbol{n} : \operatorname{dev}[\dot{\boldsymbol{\varepsilon}}]$. Finally for $\langle \gamma \rangle = \gamma \geq 0$, i.e., for plastic loading, the elastoplastic tangent moduli are obtained from (B.15) as

$$
\mathbf{C}^{ep} = \kappa \mathbf{1} \otimes \mathbf{1} + 2\mu \left[\mathbf{I} - \frac{1}{3} \mathbf{1} \otimes \mathbf{1} - \frac{\boldsymbol{n} \otimes \boldsymbol{n}}{1 + \frac{H' + K'}{3\mu}} \right] \qquad \text{for} \gamma > 0 \tag{B.21}
$$

B.3 J_2 Flow Theory - Projection onto Plane-Stress Subspace

Equations resulting from the plane-stress constraint $\sigma_{3i} \equiv 0$ for $i = 1,2,3$ plays a crucial role in the algorithmic treatment of the plane-stress problem. *Symmetry* of second order tensor vector space $\mathbb{S}$ implies that $\dim[\mathbb{S}] = 6$. The *plane-stress* subspace ($\mathbb{S}_P \subset \mathbb{S}$) is obtained from $\mathbb{S}$ by appending *three* additional constrains as follows

$$
\mathbb{S}_P := \{ \boldsymbol{\sigma} \in \mathbb{S} \mid \sigma_{13} = \sigma_{23} = \sigma_{33} \equiv 0 \} \tag{B.22}
$$

Similarly, subspace of *deviatoric* symmetric second-order tensors, denoted by $\mathbb{S}_D \subset \mathbb{S}$ is defined by three additional constrains on $\mathbb{S}$:

$$\mathbb{S}_D := \{\boldsymbol{S} \in \mathbb{S} \mid S_{13} \equiv S_{23} = 0, \;\; \mathrm{tr}[\mathbf{S}] := S_{kk} \equiv 0\} \tag{B.23}$$

Hence, $\dim[\mathbb{S}_P] = \dim[\mathbb{S}_D] = 3$. Since both $\mathbb{S}_D \subset \mathbb{S}$ and $\mathbb{S}_P \subset \mathbb{S}$ are isomorphic to $\mathbb{R}^3$, using vector notation and express $\boldsymbol{\sigma} \in \mathbb{S}_P$ and $\boldsymbol{S} \in \mathbb{S}_D$ as

$$\boldsymbol{\sigma} := [\sigma_{11} \;\; \sigma_{22} \;\; \sigma_{12}]^{\mathrm{T}} \quad \boldsymbol{S} := [S_{11} \;\; S_{22} \;\; S_{12}]^{\mathrm{T}} \tag{B.24}$$

The mapping $\bar{\mathbf{P}} : \mathbb{S}_P \to \mathbb{S}_D$ connecting the *constrained* stress tensor $\boldsymbol{\sigma} \in \mathbb{S}_P$ and its deviatoric $\boldsymbol{S} := \mathrm{dev}[\boldsymbol{\sigma}] \in \mathbb{S}_D$ and using matrix notation

$$\boldsymbol{S} := \mathrm{dev}[\boldsymbol{\sigma}] = \bar{\mathbf{P}}\boldsymbol{\sigma} \tag{B.25}$$

where

$$\bar{P} := \frac{1}{3}\begin{bmatrix} 2 & -1 & 0 \\ -1 & 2 & 0 \\ 0 & 0 & 3 \end{bmatrix} \tag{B.26}$$

Although the component S_{33} is *non-zero*, it *need not be explicitly included in* (B.24). Also can be noticed that $\bar{\mathbf{P}}$ *is not* a projection, i.e., $\bar{\mathbf{P}}\bar{\mathbf{P}} \neq \bar{\mathbf{P}}$.

This page is intentionally left blank.

Appendix C

Architectural Drawings for Model B-SSC

In this appendix, are outlined the architectural drawings used as the starting point for the model presented in section 4.2 (model B-SSC from now on), structural design presented in appendix E and structural information presented in appendix F are based upon the architectural information presented in this appendix.

In order to be certain that the architectural project presented in this section can be considered as a typical masonry building as the ones designed and constructed at Mexico City, Architect Jorge Espinosa de los Montero (Head of the Departmental Unit for Projects at the National Housing Institute in Mexico City, or *Jefe de la Unidad Departamental de proyectos de Obra del Instituto Nacional de la Vivienda* in Spanish) has been consulted, highlighting the following observations:

- In order for a governmental institution such as INVI (National Housing Institute, in Spanish) to be allowed to fund a dwelling unit, the area of such dwelling unit have to be equal or less than 54 m^2. Ergo, for the case presented in this section in a *real* situation, the owner of a dwelling will be required for an off-front payment equivalent to the $3m^2$ of the surplus area, since the area of the proposed dwelling is $57m^2$.

- A common rule for masonry buildings constructed in Mexico City is that four apartments have to be *connected* with only one stair hallways (as can be seen in figure C.1). Buildings as the one of figure C.1 are named H buildings in a non-formal sense. The *regulation* of using one stair hallways to connect four apartments is based on the economy of the construction, and to reduce to a minimum the non-constructed area of the property given the lack-of-space situation undergone in Mexico City.

Although both of the previously cited characteristics are not comply, regarding the remaining architectural characteristic of the construction, such as, space distribution in plan view, building height, dimension of window openings, and so on, can be considered as typical, hence, for the pursued purposes of this work, the drawings presented in this section can be considered as a typical masonry building designed and constructed in the present days at Mexico City.

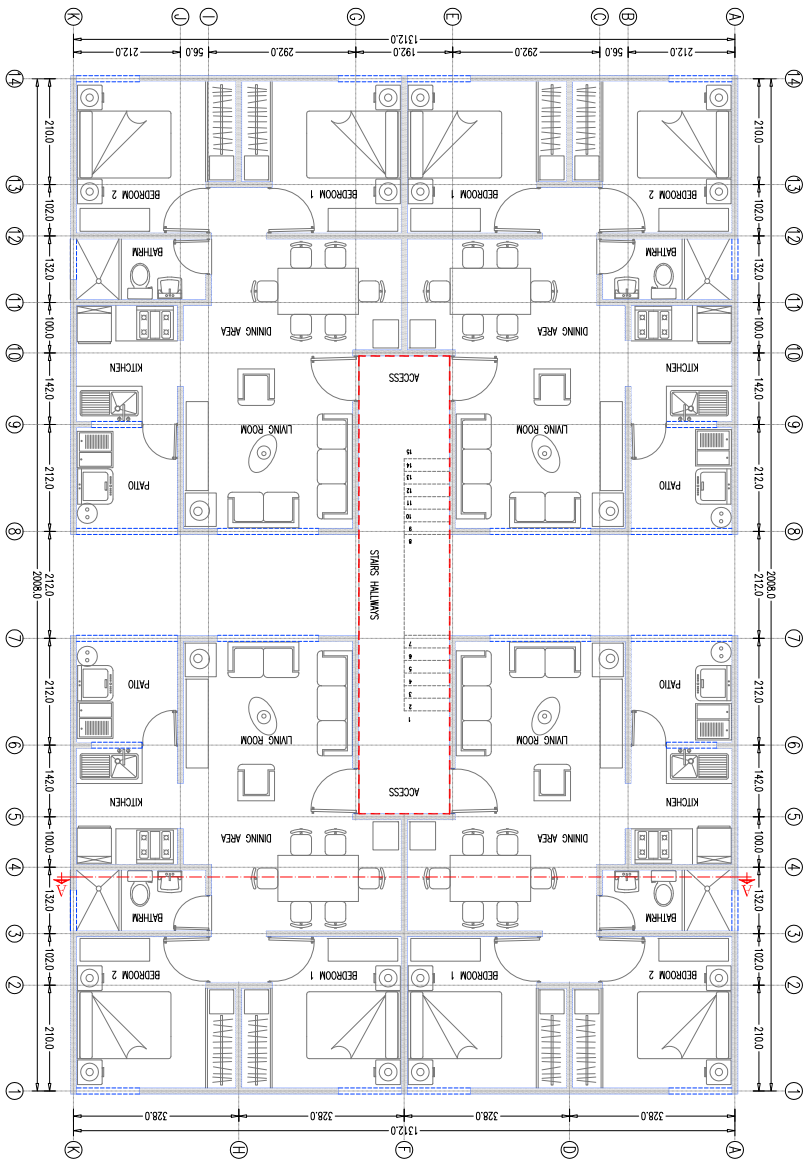

Figure C.1 *Architectural Drawing - Typical floor Plan. Four-Unit Storey with one stairs block.*

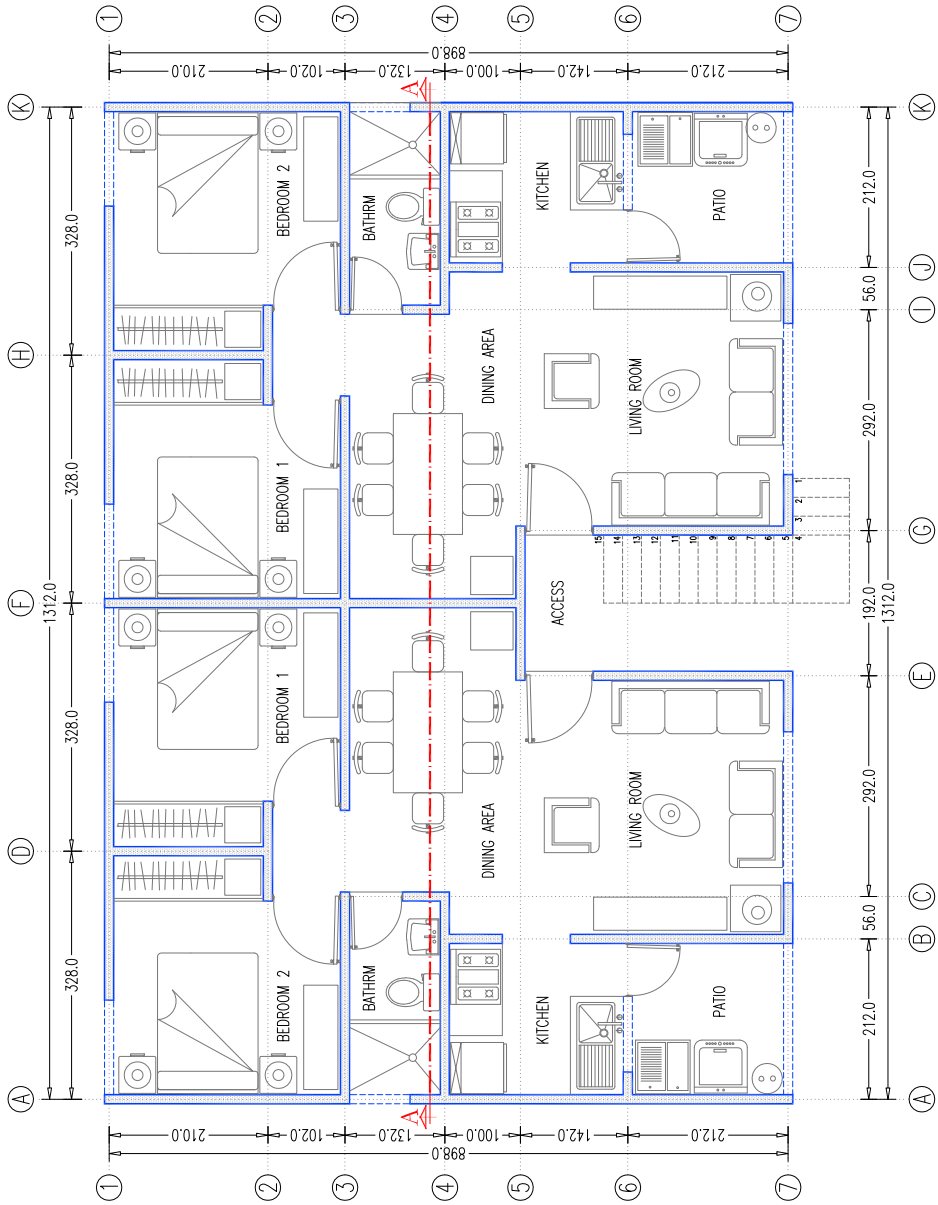

Figure C.2 *Architectural Drawing - Floor Plan. Two-Unit Storey (L+0.00m).*

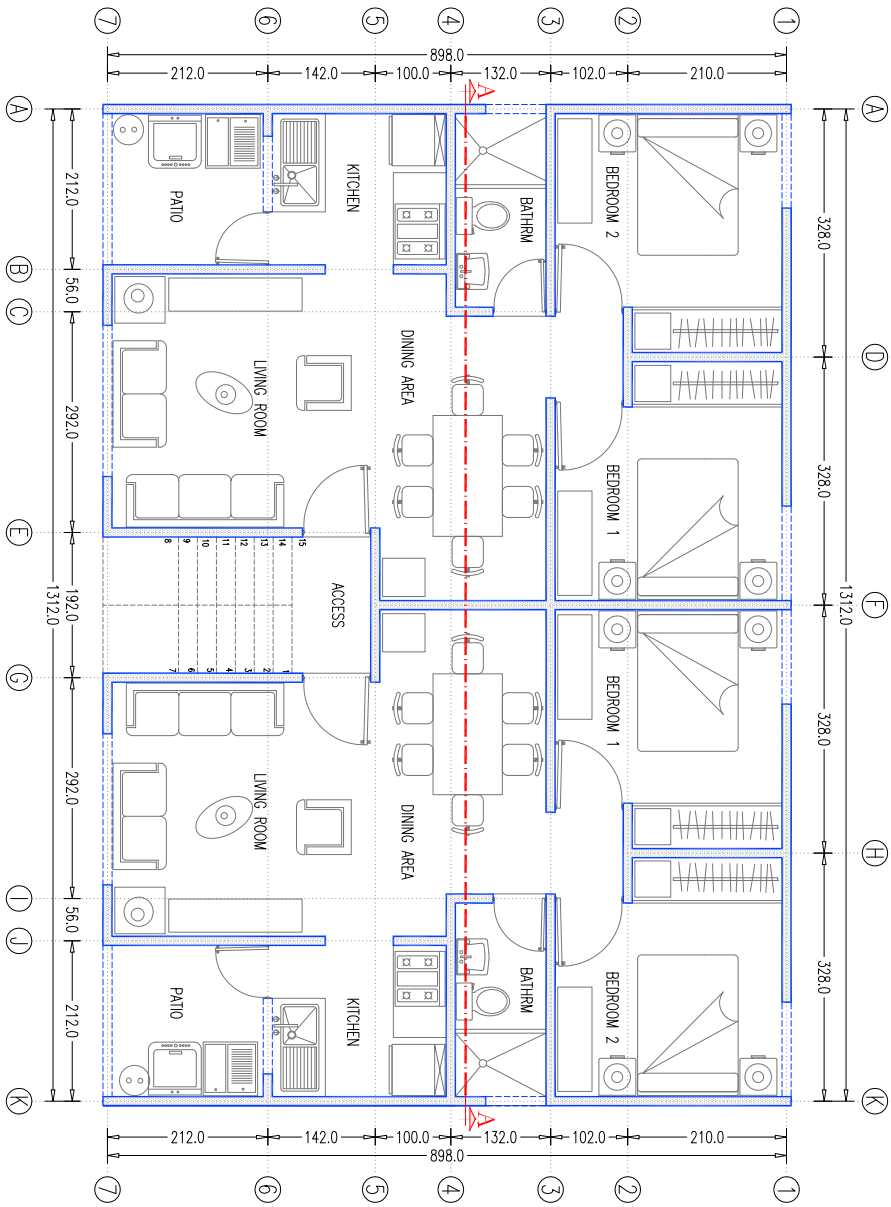

Figure C.3 *Architectural Drawing - Typical Plan. Two-Unit Storey (L+2.63m, +5.26m, +7.89m, +10.52m, +13.15m).*

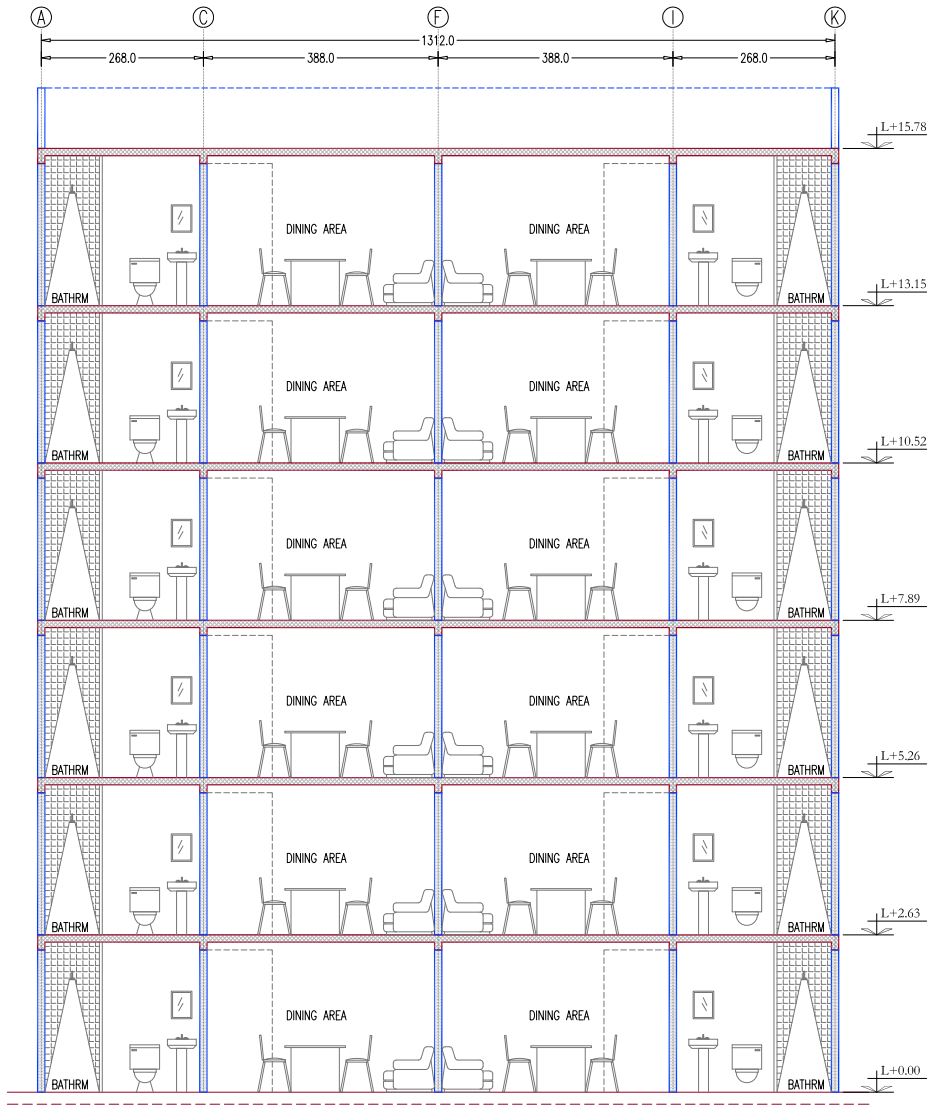

Figure C.4 *Architectural Drawing - Section A-A'.*

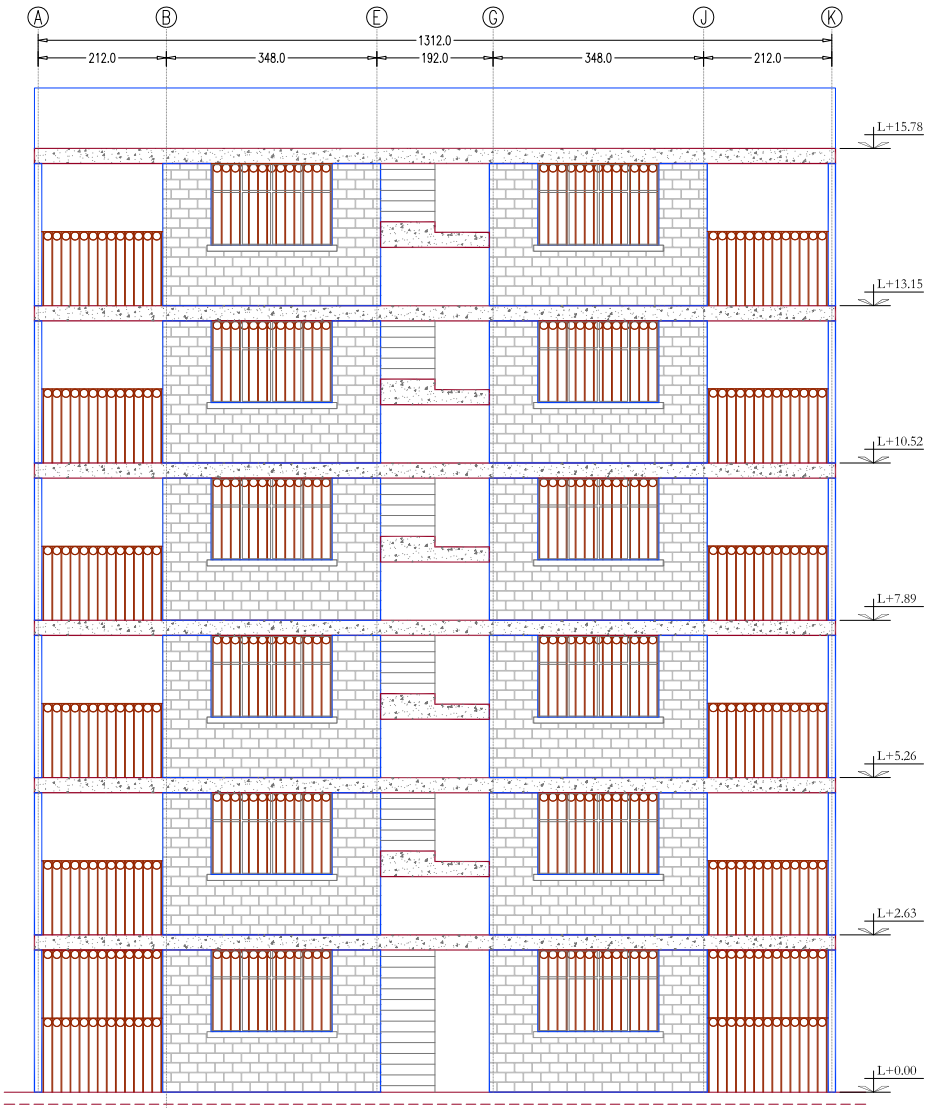

Figure C.5 *Architectural Drawing - Principal Facade.*

Appendix D

Design of a Masonry Building Using a Mexican Design Code

Present appendix is intended to reproduce, in a brief manner, the methodology an engineer should follow to design one structure composed by confined bearing walls in accordance with the buildings code shown below

- `Normas Técnicas Complementarias para el Diseño por Sismo 2004` [3].
- `Normas Técnicas Complementarias para Diseño y Construcciones de Estructuras de Mampostería, 2004 [6]`.
- `Normas Técnicas Complementarias para Diseño y Construcciones de Estructuras de Concreto, 2004 [4]`.
- `Normas Técnicas Complementarias sobre Criterios y Acciones para el Diseño Estructural de las Edificaciones, 2004` [5].
- `Reglamento de Construccion del Distrito Federal 1993` [2].
- `Manual de Diseño de Obras Civiles de la Comisión Federal de Electricidad - Diseño por Sismo, 1997` [1].

Also, reader may consult reference [65] to abound on the subject.

Designing a building with confined masonry, as most of the designing process has to be an *iterative* process, and some factor has to be settled before starting it. In the first place, have to be properly executed the architectural project, and with it, three major issues:

- *Unit*. Due the diversity of units in the market to form masonry, selected unit has to be clearly specified, since both mechanical properties and dynamical response are tightly linked to it.
- *Construction Location*. It is straightforward realize that location will be needed to evaluate accidental forces, such as wind or seismic forces.
- *Bearing wall locations*. It is also clear that sometimes partition walls not intended to have any *structural* response are commonly used, and such kind of walls have to be clearly specified in the architectural drawings, along with lengths and heights.

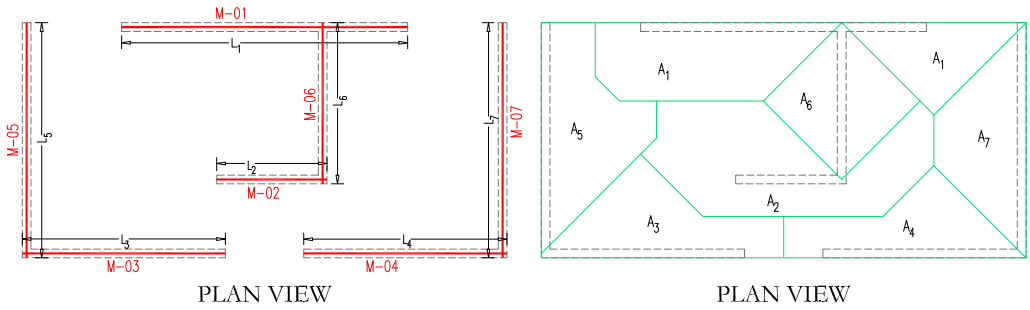

Figure D.1 *Location of masonry bearing walls and its tributary areas.*

As a typical structural designing scheme, in such kind of buildings, reinforced concrete walls are used combined with confined masonry walls as stiffeners. Economical and architectural factor has direct impact on engineer's choices while selecting which wall have to be made of reinforced concrete.

Major advantage of using concrete bearing walls is noticed while designing the structure under lateral forces, due their stiffness, dynamical response of the structure is changed, lowering the elastic fundamental period of vibration of the structure.

Let us assume drawings of figure (D.1) depict the view in plan of a 6-storey confined masonry building (arrangement of walls will be the same in the 6 storeys). Basic information regarding walls will be required, such as

- *Geometry.* Figure (D.1) on the left, shows a way the distinction of walls shall be made, assigning them a number, and consequently; its length, thickness and height. Such information will be needed in the first place to evaluate its weight, and in the other hand, to evaluate its stiffness, as will be seen later in this section, on equation D.4.

- *Shape.* Shape of a wall has to be understood as the shape in plan distinguished among 4 possibilities: **I**, **L**, **T** or **O**. Part II, `Section 4.4.4` of reference [65] explains how could be incremented the inertia modulus I of the wall due presence flanges.

- *Type of unit and mortar.* `Tables 2.7`, `2.8` and `2.9` of reference [6] relates both the type of unit and mortar being f_m^* and v_m^* the resistance under compression and the shear resistance of masonry respectively.

D.1 Vertical In-plane Loads

1. As a general rule of thumb, the first step is to review the loading resistance of walls under vertical forces, this is doing by fulfilling that $P_U \leq P_R$, from next equations

$$P_U = \phi(W_D + W_L) \tag{D.1}$$

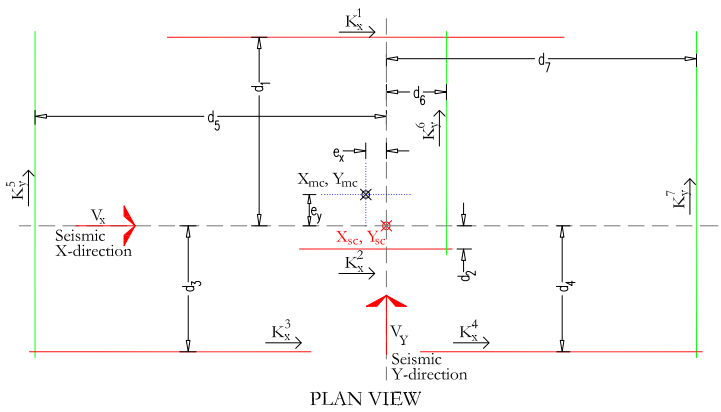

Figure D.2 *Location of stiffness direction and centroids.*

$$P_R = F_R F_E (f_m^* A_T + \sum A_S F_Y) \tag{D.2}$$

where

P_U	=	Nominal vertical load.
P_R	=	Design vertical load.
W_D	=	Dead load.
W_L	=	Live load.
ϕ	=	Loading factor (`Section 3.4` Reference [5]).
F_R	=	Resistance factor (`Section 3.1.4` from [6]).
F_E	=	Eccentricity factor (`Section 3.2.2.3` from [6])
f_m^*	=	Resistance under compression of masonry.
A_T	=	Total area of the wall.
A_S	=	Area of reinforcement steel.
F_Y	=	Yield strength of reinforcement steel.

Equations D.1 and D.2 only apply while designing a masonry wall.

D.2 Lateral In-plane Loads

A general procedure to estimate the lateral seismic forces following the so-called seismic *detailed* analysis is presented next.

2. Total stiffness ${}^k\mathbf{K}_{x,y}$ have to be evaluated in the form

$${}^k\mathbf{K}_x = \sum_{i=1,n} {}^k K_x^i \quad ; \quad {}^k\mathbf{K}_y = \sum_{i=1,n} {}^k K_y^i \quad ; \tag{D.3}$$

where subindex k stands for storey, $K_{x,y}$ is the stiffness of the wall and it depends on its orientations, as can be seen from figure (D.2), for walls *M-01*, *M-02*, *M-03*

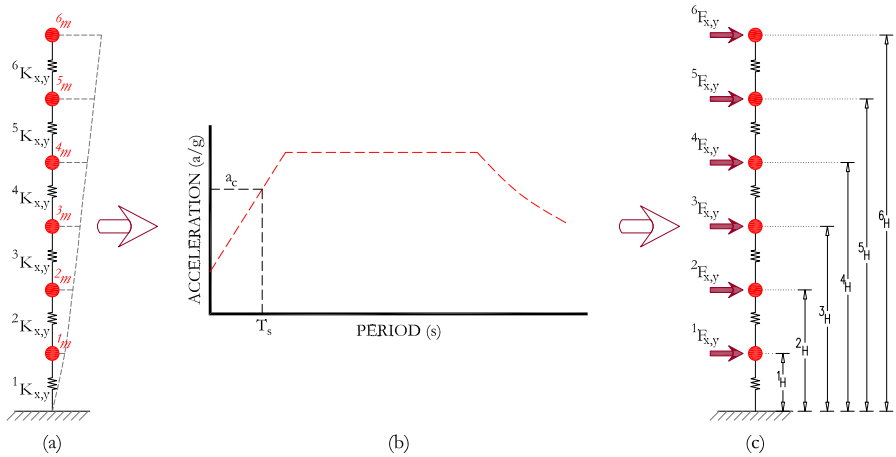

Figure D.3 *Representation of modal-spectral scheme.*

and *M-04* $K_y^1 = K_y^2 = K_y^3 = K_y^4 = 0$, being straightforward that walls only have stiffness along its longitudinal direction. Stiffness K shall be evaluated as follows.

$$K_m^i = \frac{1}{h^i\left[\frac{(h^i)^2}{3E^iI^i} + \frac{1}{A_T^iG^i}\right]} \quad ; \quad K_c^i = \frac{1}{h^i\left[\frac{(h^i)^2}{3E^iI^i} + \frac{6}{5A_T^iG^i}\right]} \tag{D.4}$$

where

E = Young modulus of masonry from `section 2.8.5.` reference [6].
I = Inertia modulus obtained according to part II, `section 4.4.4` from [65].
A_T = Cross section's area, without flanges.
G = Shear modulus according to `Section 2.8.6` reference [65].
h = Non-restricted height.

K_m^i and K_c^i are stiffness for a confined masonry and concrete wall respectively. Finally, center of stiffness for each storey ${}^kX_{CS}, {}^kY_{CS}$ has to be evaluated.

3. Evaluate total mass ${}^km$ and center of mass ${}^kX_{SM}, {}^kY_{SM}$ of each storey. Mass shall be evaluated according to Title Sixth, Chapter IV and V of reference [2].

4. Elastic fundamental period of vibration T_s in x and y direction have to be evaluated solving and dynamic model with a single degree of freedom figure (D.3a).

5. Peak modal response is used with an elastic response spectrum to represent the dynamic effects due ground motion a_c (D.3b).

6. Lateral forces over the entire storey in each direction (fig.D.3c) are evaluated using equation D.5.

$${}^kF_{x,y} = \frac{(a_c)_{x,y}}{Q_{x,y}} \times \frac{W_T}{\sum_{k=1,n}{}^kW^kH} \times {}^kW^kH \tag{D.5}$$

where

^{k}F = Entire lateral force of storey k.
a_c = Ground acceleration.
Q = Structural behavior factor, defined in `section 5` of reference [3].
W_T = Entire weight of the structure.
^{k}W = Weight of storey k.
^{k}H = Height of storey k (fig.D.3).

7. First step to insure resistance of a given wall under lateral forced is to fulfil condition among shear strengths $V_U \leq V_R$, equations (D.6) and (D.7) detail the way they are determined.

$$V_U = \phi \left(V_D + V_T \right) \tag{D.6}$$

$$V_R = F_R \left(0.50 v_m^* A_T^i + 0.3 P^i \right) \quad \leq \quad 1.5 F_R v_m^* A_T^i \tag{D.7}$$

From equation (D.6) V_D of wall i on storey k has to be understood as a *direct* distribution of shear $F_{x,y}$, determined as shown below,

$$^{k}V_D^i = \frac{^{k}K^i}{^{k}\mathbf{K}} \; ^{k}F_{x,y} \tag{D.8}$$

on the other hand, V_T is a distribution of shear due horizontal torsional moment $(M_T)_{x,y}$ (fig.D.2), in the form:

$$^{k}(M_T)_x = {}^{k}(F_x e_y) \quad ; \quad {}^{k}(M_T)_y = {}^{k}(F_y e_x) \tag{D.9}$$

$$^{k}V_T^i = \left(^{k}M_T \right)_{x,y} \frac{^{k}\left(K^i d^i \right)}{\sum_{i=1,n} {}^{k}\left[K^i \left(d^i \right)^2 \right]} \tag{D.10}$$

Have to be noticed that $V_D = V_T = 0$ for seismic forces acting on perpendicular direction of the wall, since V_U is only evaluated when direction of lateral forces lie parallel to longitudinal direction of the given wall.

where

V_U = Nominal shear strength.
V_R = Design shear strength.
ϕ = Loading factor (`section 3.4` reference [5]).
F_R = Resistance factor (`section 3.1.4` reference [6]).
$^{k}(M_T)_{x,y}$ = Horizontal torsional moment of storey k.
$^{k}e_{x,y}$ = Eccentricity at storey k.
$^{k}d^i$ = Distance from center of stiffness to a given wall i (fig. D.2).
v_m^* = Shear resistance of masonry.
P = Gravity load, equal to $P = W_D + W_L$ (eq. D.1).

8. Finally in-plane flexural moment condition of resistance $M_U \leq M_R$ have to be fulfilled.

$$^{k}M_U^i = \frac{\sum (^{k}h)^2}{\sum {}^{k}h} \; ^{k}V_D^i \tag{D.11}$$

$$M_R = \begin{cases} F_R M_o + 0.30 P_U d & if \;\; 0 \leq P_U \leq \dfrac{P_R}{3} \\ (1.5 F_R M_o + 0.15 P_R d)\left(1 - \dfrac{P_U}{P_R}\right) & if \;\; P_U > \dfrac{P_R}{3} \end{cases} \tag{D.12}$$

where

M_U = Nominal in-plane flexural moment strength.
M_R = Design in-plane flexural moment.
P_U = Nominal vertical load (Eq. D.1).
P_R = Design vertical load (Eq. D.2).
F_R = Resistance factor (section 3.1.4 reference [6]).
M_o = $A_S f_y d'$. flexural strength of wall.
d = Distance from steel centroid of confined column under tensile stress to farthest fiber under compression stress (fig D.4).
d' = Distance between centroid of steel (fig. D.4).

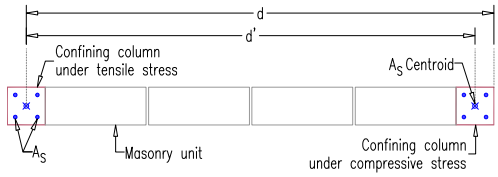

Figure D.4 *Typical view in plan of a confined masonry wall.*

Appendix E

Structural Analysis Using a Commercial Software

The results presented in this section have been obtained using a commercial software for analysis and design of masonry structures named ANEMgcW [37], which is based on reference [6] to perform the analysis and design of masonry walls, in reference [4] to review the concrete walls and confining elements, and also in reference [3] to predict the seismic response of the analysed structures.

The procedure followed to obtain the results shown in this section are listed below:

1. With the architectural information presented in appendix C, the bearing walls have been distinguished, measured and enumerated, the result is displayed in figure E.1. An output of such information obtained using ANEMgcW is also displayed in figure E.3.

2. An analysis of the tributary areas of the walls enumerated in step **1** has been carried out, results are displayed in figure E.2.

3. Information such as: weights of walls and floor systems, and mechanical properties have to be given to ANEMgcW as an input.

Have to be pointed out that the model `B-SSC` has been designed to withstand the ground acceleration due to a seismic event as if it was located in seismic zone ZIIIa [3], the corresponding design spectrum for such zone is depicted in figure E.4, where it is also shown the response period $T_X = 0.146s$ reported as an output by ANEMgcW.

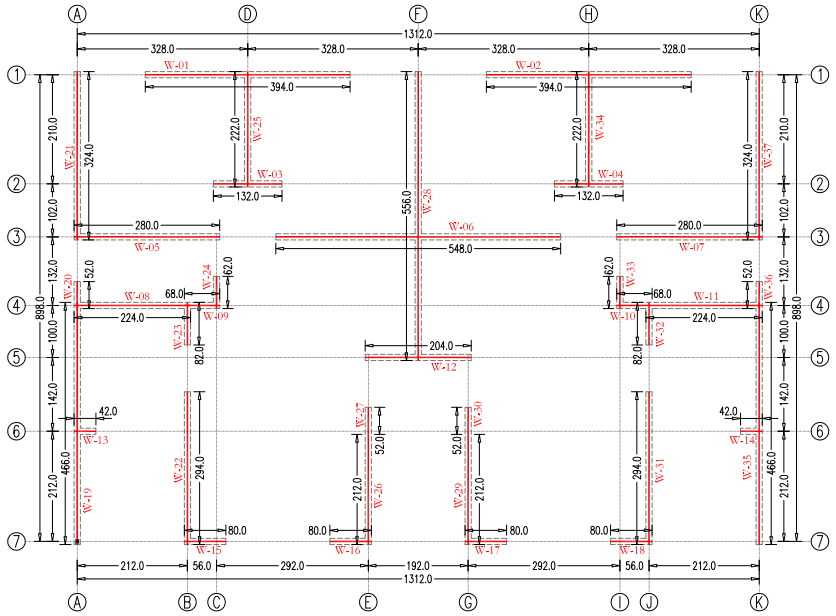

Figure E.1 *Location of masonry bearing walls.*

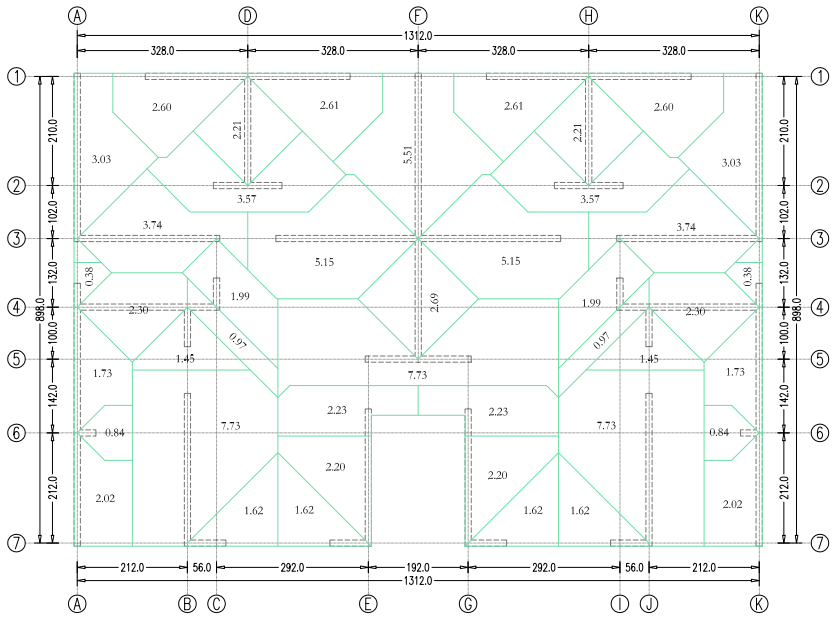

Figure E.2 *Localization of tributary areas over bearing walls*

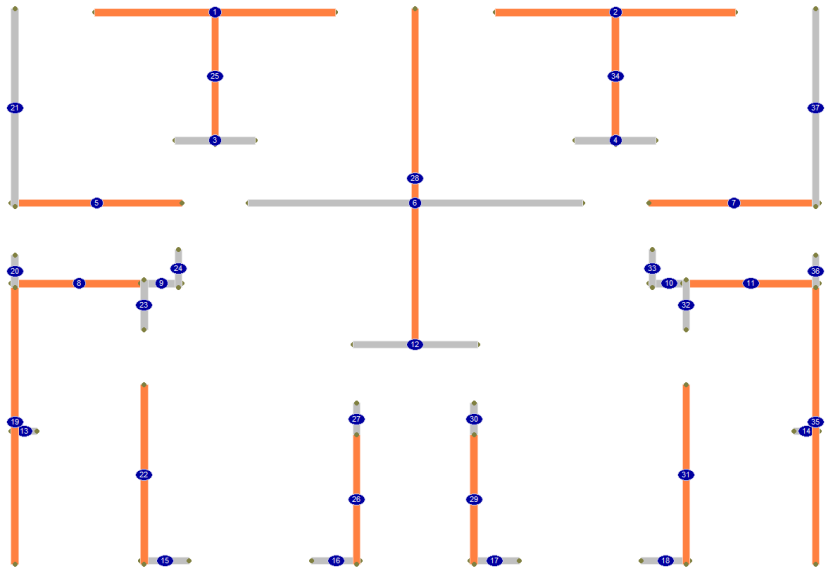

Figure E.3 *Localization of bearing walls (ANEM output).*

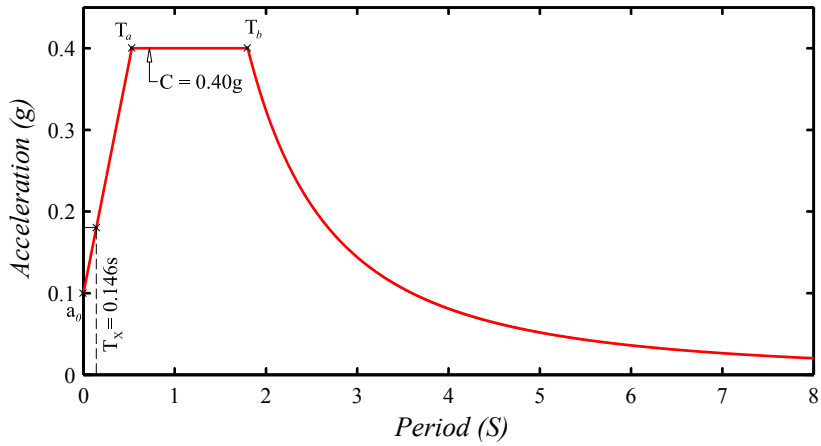

Figure E.4 *Seismic design spectrum for Zone IIIa at Mexico City.*

ANÁLISIS SÍSMICO DINÁMICO [RDF2004]

PESO TOTAL EN SISMO 634.68 T

CORTANTES BASALES

estático total	X:	169.25 T
	Y:	169.25 T
estático reducido	X:	101.90 T
	Y:	100.65 T
mínimo	X:	81.52 T [factor: 0.8]
	Y:	80.52 T

Nivel	W (T)	Centro de masa x (m)	y (m)
6	95.05	6.560	4.635
5	107.93	6.560	4.701
4	107.93	6.560	4.701
3	107.93	6.560	4.701
2	107.93	6.560	4.701
1	107.93	6.560	4.701
Suma	634.68		

Modo	Periodo (seg) x	y	Aceleración espectral x	y	Coef.Participación x	y	Q'x	Q'y
1	0.146	0.141	0.183	0.180	-7.483	-7.467	1.138	1.133
2	0.050	0.049	0.129	0.128	2.431	2.456	1.048	1.046
3	0.032	0.031	0.118	0.117	1.336	1.355	1.030	1.029
4	0.024	0.024	0.114	0.113	0.818	0.832	1.023	1.022
5	0.020	0.020	0.112	0.111	-0.497	-0.518	1.019	1.019
6	0.019	0.018	0.111	0.110	0.292	0.340	1.018	1.017

Modo	Peso modal efectivo x (T)	y (T)	% de peso total x	y
1	549.38	546.94	86.56	86.18
2	57.95	59.19	9.13	9.33
3	17.52	18.00	2.76	2.84
4	6.57	6.78	1.04	1.07
5	2.42	2.63	0.38	0.41
6	0.83	1.13	0.13	0.18
Suma	634.68	634.68	100.00	100.00

Modo	Cortantes basales Vx (T)	Vy (T)	Alturas efectivas Hx (m)	Hy (m)	Momentos de volteo Mx (T*m)	My (T*m)
1	88.20	86.74	10.788	10.820	951.49	938.50
2	7.11	7.23	-3.428	-3.179	-24.38	-22.99
3	2.01	2.05	2.203	2.034	4.42	4.18
4	0.73	0.75	-1.802	-1.691	-1.32	-1.27
5	0.26	0.29	1.499	1.295	0.40	0.37
6	0.09	0.12	-0.839	-0.529	-0.08	-0.06
Comb	88.51	87.07			951.82	938.79

Ent.	Momento de volteo x (T*m)	y (T*m)	Rigidez total x (T/m)	y (T/m)	Cortante x (T)	y (T)	Distorsión*Q' en C.Masa Q'x:1.138	Q'y:1.133	Desplaz. en C.Masa x (cm)	y (cm)
6	52.855	52.593	308564	312432	20.097	19.997	0.00003	0.00003	0.11	0.10
5	160.014	158.828	317223	326507	40.833	40.491	0.00006	0.00005	0.10	0.09
4	313.528	310.518	329008	347810	58.620	57.943	0.00008	0.00007	0.09	0.08
3	504.031	498.291	337454	363283	72.887	71.868	0.00009	0.00009	0.07	0.06
2	720.818	711.630	342474	372986	83.066	81.770	0.00010	0.00009	0.05	0.05
1	951.817	938.795	343934	375865	88.515	87.068	0.00011	0.00010	0.03	0.02

Nivel	Cortante x (T)	y (T)	Pos.Cortante x (m)	y (m)	Centro de torsión x (m)	y (m)	Excent.Calculada (m) SismoX	SismoY	Dimensiones planta x (m)	y (m)
6	20.10	20.00	6.560	4.635	6.560	5.998	-1.363	0.000	13.240	9.100
5	40.83	40.49	6.560	4.669	6.560	5.945	-1.277	0.000	13.240	9.100
4	58.62	57.94	6.560	4.679	6.560	5.867	-1.188	0.000	13.240	9.100
3	72.89	71.87	6.560	4.683	6.560	5.815	-1.132	0.000	13.240	9.100
2	83.07	81.77	6.560	4.685	6.560	5.784	-1.099	0.000	13.240	9.100
1	88.51	87.07	6.560	4.686	6.560	5.775	-1.089	0.000	13.240	9.100

Nivel	Excent. de diseño (m) SismoX	SismoY	Excentricidades [1.5e+0.1b ; e-0.1b] sismo dirección X e1 (m)	e2 (m)	sismo dirección Y e1 (m)	e2 (m)	Momentos Torsionantes [V*e] sismo dirección X m1 (T*m)	m2 (T*m)	sismo dirección Y m1 (T*m)	m2 (T*m)
6	-1.363	0.000	-2.955	-0.453	1.324	-1.324	-59.38	-9.11	26.48	-26.48
5	-1.277	0.000	-2.825	-0.367	1.324	-1.324	-115.36	-14.97	53.61	-53.61
4	-1.188	0.000	-2.692	-0.278	1.324	-1.324	-157.82	-16.31	76.72	-76.72
3	-1.132	0.000	-2.608	-0.222	1.324	-1.324	-190.11	-16.19	95.15	-95.15
2	-1.099	0.000	-2.558	-0.189	1.324	-1.324	-212.49	-15.68	108.26	-108.26
1	-1.089	0.000	-2.543	-0.179	1.324	-1.324	-225.09	-15.82	115.28	-115.28

Fuerzas sísmicas equivalentes

	Fuerzas sísmicas		Posición de fuerzas sísmicas sismo direc.X		sismo direc.Y	
Nivel	x (T)	y (T)	Y1 (m)	Y2 (m)	X1 (m)	X2 (m)
6	20.097	19.997	3.044	5.545	7.884	5.236
5	20.736	20.494	3.246	5.662	7.884	5.236
4	17.788	17.451	3.479	5.792	7.884	5.236
3	14.267	13.925	3.552	5.823	7.884	5.236
2	10.178	9.903	3.585	5.835	7.884	5.236
1	5.449	5.297	3.462	5.749	7.884	5.236
Suma	88.515	87.068				

REVISION POR CARGA LATERAL

MURO	ENT	Fr	P (T)	K (T/m)	Vd (T)	Vt (T)	Vt' (T)	Vu (T)	distor*Q'	Vr (T)
1	1	0.700	31.63	25,302	6.51	-0.10	0.75	7.30	0.00012	12.43
	2	0.700	26.46	25,302	6.14	-0.10	0.71	6.87	0.00012	11.35
	3	0.700	21.29	25,302	5.47	-0.11	0.64	6.10	0.00010	10.26
	4	0.700	16.12	25,302	4.51	-0.11	0.53	5.01	0.00009	9.18
	5	0.700	10.95	25,302	3.26	-0.11	0.38	3.59	0.00006	8.09
	6	0.700	5.78	25,302	1.65	-0.07	0.19	1.80	0.00003	7.01
2	1	0.700	31.63	25,302	6.51	-0.10	0.75	7.30	0.00012	12.43
	2	0.700	26.46	25,302	6.14	-0.10	0.71	6.87	0.00012	11.35
	3	0.700	21.29	25,302	5.47	-0.11	0.64	6.10	0.00010	10.26
	4	0.700	16.12	25,302	4.51	-0.11	0.53	5.01	0.00009	9.18
	5	0.700	10.95	25,302	3.26	-0.11	0.38	3.59	0.00006	8.09
	6	0.700	5.78	25,302	1.65	-0.07	0.19	1.80	0.00003	7.01
3	1		16.59	8,130	2.09	-0.01	0.08	2.32	0.00012	
	2		13.90	8,130	1.97	-0.01	0.08	2.18	0.00012	
	3		11.20	8,130	1.76	-0.01	0.07	1.94	0.00010	
	4		8.50	8,130	1.45	-0.01	0.06	1.60	0.00009	
	5		5.81	8,130	1.05	-0.01	0.04	1.15	0.00006	
	6		3.11	8,130	0.53	-0.01	0.02	0.58	0.00003	
4	1		16.59	8,130	2.09	-0.01	0.08	2.32	0.00012	
	2		13.90	8,130	1.97	-0.01	0.08	2.18	0.00012	
	3		11.20	8,130	1.76	-0.01	0.07	1.94	0.00010	
	4		8.50	8,130	1.45	-0.01	0.06	1.60	0.00009	
	5		5.81	8,130	1.05	-0.01	0.04	1.15	0.00006	
	6		3.11	8,130	0.53	-0.01	0.02	0.58	0.00003	
5	1	0.700	22.59	16,112	4.15	0.00	0.01	4.56	0.00012	8.86
	2	0.700	18.89	15,917	3.86	0.00	0.01	4.25	0.00012	8.08
	3	0.700	15.20	15,331	3.31	0.00	0.01	3.64	0.00010	7.31
	4	0.700	11.51	14,608	2.60	0.00	0.00	2.86	0.00008	6.53
	5	0.700	7.82	13,694	1.76	0.01	0.01	1.95	0.00006	5.76
	6	0.700	4.13	13,404	0.87	0.01	0.00	0.97	0.00003	4.98
6	1		55.46	162,496	41.82	-0.02	0.13	46.02	0.00012	
	2		46.42	162,496	39.41	-0.02	0.11	43.37	0.00012	
	3		37.38	162,496	35.10	-0.01	0.06	38.62	0.00010	
	4		28.33	162,496	28.95	0.02	0.01	31.87	0.00008	
	5		19.29	162,496	20.92	0.15	0.07	23.19	0.00006	
	6		10.25	162,496	10.58	0.13	0.06	11.80	0.00003	
7	1	0.700	22.59	16,112	4.15	0.00	0.01	4.56	0.00012	8.86
	2	0.700	18.89	15,917	3.86	0.00	0.01	4.25	0.00012	8.08
	3	0.700	15.20	15,331	3.31	0.00	0.01	3.64	0.00010	7.31
	4	0.700	11.51	14,608	2.60	0.00	0.00	2.86	0.00008	6.53
	5	0.700	7.82	13,694	1.76	0.01	0.01	1.95	0.00006	5.76
	6	0.700	4.13	13,404	0.87	0.01	0.00	0.97	0.00003	4.98
8	1	0.700	16.02	15,807	4.07	0.35	0.18	4.92	0.00013	6.66
	2	0.700	13.39	15,807	3.83	0.34	0.17	4.65	0.00013	6.10
	3	0.700	10.77	15,466	3.34	0.31	0.16	4.07	0.00011	5.55
	4	0.700	8.14	13,909	2.48	0.25	0.12	3.05	0.00009	5.00
	5	0.700	5.52	11,394	1.47	0.17	0.08	1.83	0.00007	4.45
	6	0.700	2.89	8,317	0.54	0.07	0.03	0.68	0.00004	3.90
9	1		5.97	4,979	1.28	0.11	0.06	1.55	0.00013	
	2		4.99	4,644	1.13	0.10	0.05	1.37	0.00013	
	3		4.02	3,710	0.80	0.08	0.04	0.98	0.00011	
	4		3.04	2,691	0.48	0.05	0.02	0.59	0.00009	
	5		2.07	1,577	0.20	0.02	0.01	0.25	0.00007	
	6		1.09	1,258	0.08	0.01	0.00	0.10	0.00004	
10	1		5.97	4,979	1.28	0.11	0.06	1.55	0.00013	
	2		4.99	4,644	1.13	0.10	0.05	1.37	0.00013	
	3		4.02	3,710	0.80	0.08	0.04	0.98	0.00011	
	4		3.04	2,691	0.48	0.05	0.02	0.59	0.00009	
	5		2.07	1,577	0.20	0.02	0.01	0.25	0.00007	
	6		1.09	1,258	0.08	0.01	0.00	0.10	0.00004	
11	1	0.700	16.02	15,807	4.07	0.35	0.18	4.92	0.00013	6.66
	2	0.700	13.39	15,807	3.83	0.34	0.17	4.65	0.00013	6.10
	3	0.700	10.77	15,466	3.34	0.31	0.16	4.07	0.00011	5.55
	4	0.700	8.14	13,909	2.48	0.25	0.12	3.05	0.00009	5.00
	5	0.700	5.52	11,394	1.47	0.17	0.08	1.83	0.00007	4.45
	6	0.700	2.89	8,317	0.54	0.07	0.03	0.68	0.00004	3.90

REVISION POR CARGA LATERAL

MURO	ENT	Fr	P (T)	K (T/m)	Vd (T)	Vt (T)	Vt' (T)	Vu (T)	distor*Q'	Vr (T)
12	1		32.21	24,585	6.33	1.00	0.51	8.23	0.00014	
	2		26.99	24,585	5.96	0.95	0.49	7.77	0.00014	
	3		21.77	24,585	5.31	0.89	0.45	6.97	0.00012	
	4		16.56	24,585	4.38	0.79	0.38	5.81	0.00010	
	5		11.34	24,585	3.16	0.63	0.29	4.27	0.00008	
	6		6.12	24,585	1.60	0.34	0.15	2.19	0.00004	
13	1		4.40	720	0.19	0.05	0.02	0.26	0.00016	
	2		3.68	720	0.17	0.05	0.02	0.25	0.00015	
	3		2.97	704	0.15	0.04	0.02	0.22	0.00014	
	4		2.25	638	0.11	0.03	0.02	0.17	0.00011	
	5		1.53	519	0.07	0.02	0.01	0.10	0.00008	
	6		0.82	306	0.02	0.01	0.00	0.03	0.00004	
14	1		4.40	720	0.19	0.05	0.02	0.26	0.00016	
	2		3.68	720	0.17	0.05	0.02	0.25	0.00015	
	3		2.97	704	0.15	0.04	0.02	0.22	0.00014	
	4		2.25	638	0.11	0.03	0.02	0.17	0.00011	
	5		1.53	519	0.07	0.02	0.01	0.10	0.00008	
	6		0.82	306	0.02	0.01	0.00	0.03	0.00004	
15	1		8.44	3,689	0.95	0.39	0.20	1.54	0.00018	
	2		7.07	3,589	0.87	0.36	0.18	1.41	0.00017	
	3		5.69	3,272	0.71	0.30	0.15	1.16	0.00015	
	4		4.32	2,843	0.51	0.23	0.11	0.85	0.00013	
	5		2.94	2,227	0.29	0.14	0.07	0.49	0.00010	
	6		1.56	2,012	0.13	0.07	0.03	0.23	0.00005	
16	1		8.44	3,689	0.95	0.39	0.20	1.54	0.00018	
	2		7.07	3,589	0.87	0.36	0.18	1.41	0.00017	
	3		5.69	3,272	0.71	0.30	0.15	1.16	0.00015	
	4		4.32	2,843	0.51	0.23	0.11	0.85	0.00013	
	5		2.94	2,227	0.29	0.14	0.07	0.49	0.00010	
	6		1.56	2,012	0.13	0.07	0.03	0.23	0.00005	
17	1		8.44	3,689	0.95	0.39	0.20	1.54	0.00018	
	2		7.07	3,589	0.87	0.36	0.18	1.41	0.00017	
	3		5.69	3,272	0.71	0.30	0.15	1.16	0.00015	
	4		4.32	2,843	0.51	0.23	0.11	0.85	0.00013	
	5		2.94	2,227	0.29	0.14	0.07	0.49	0.00010	
	6		1.56	2,012	0.13	0.07	0.03	0.23	0.00005	
18	1		8.44	3,689	0.95	0.39	0.20	1.54	0.00018	
	2		7.07	3,589	0.87	0.36	0.18	1.41	0.00017	
	3		5.69	3,272	0.71	0.30	0.15	1.16	0.00015	
	4		4.32	2,843	0.51	0.23	0.11	0.85	0.00013	
	5		2.94	2,227	0.29	0.14	0.07	0.49	0.00010	
	6		1.56	2,012	0.13	0.07	0.03	0.23	0.00005	
19	1	0.700	30.25	35,644	8.26	2.17	4.25	12.88	0.00016	13.20
	2	0.700	25.28	35,458	7.77	2.05	4.02	12.13	0.00015	12.16
	3	0.700	20.31	34,910	6.91	1.83	3.65	10.81	0.00013	11.12
	4	0.700	15.34	34,258	5.71	1.51	3.10	8.96	0.00011	10.07
	5	0.700	10.38	33,469	4.15	1.09	2.34	6.54	0.00008	9.03
	6	0.700	5.41	33,227	2.13	0.55	1.23	3.35	0.00004	7.99
20	1		3.49	1,123	0.26	0.07	0.13	0.41	0.00016	
	2		2.92	1,094	0.24	0.06	0.12	0.37	0.00015	
	3		2.34	1,000	0.20	0.05	0.10	0.31	0.00013	
	4		1.77	865	0.14	0.04	0.08	0.23	0.00011	
	5		1.19	654	0.08	0.02	0.05	0.13	0.00008	
	6		0.62	574	0.04	0.01	0.02	0.06	0.00004	
21	1		23.71	77,890	18.04	4.75	9.28	28.14	0.00016	
	2		19.82	77,076	16.90	4.46	8.75	26.38	0.00015	
	3		15.93	74,643	14.77	3.91	7.80	23.11	0.00013	
	4		12.03	71,683	11.94	3.15	6.48	18.74	0.00011	
	5		8.14	68,002	8.43	2.21	4.76	13.28	0.00008	
	6		4.25	66,849	4.28	1.11	2.48	6.74	0.00004	
22	1	0.700	35.00	17,517	4.06	0.72	1.41	5.73	0.00014	11.67
	2	0.700	29.32	17,320	3.80	0.68	1.33	5.36	0.00013	10.48
	3	0.700	23.63	16,725	3.31	0.59	1.18	4.68	0.00012	9.28
	4	0.700	17.95	15,994	2.66	0.48	0.98	3.78	0.00010	8.09
	5	0.700	12.27	15,072	1.87	0.33	0.71	2.66	0.00008	6.90
	6	0.700	6.59	14,781	0.95	0.17	0.37	1.35	0.00004	5.71
23	1		8.03	4,704	1.09	0.19	0.38	1.54	0.00014	
	2		6.72	4,704	1.03	0.18	0.36	1.46	0.00013	
	3		5.41	4,611	0.91	0.16	0.33	1.29	0.00012	
	4		4.10	4,166	0.69	0.12	0.25	0.98	0.00010	
	5		2.79	3,357	0.42	0.07	0.16	0.59	0.00008	
	6		1.48	2,160	0.14	0.02	0.05	0.20	0.00004	
24	1		8.72	1,845	0.43	0.07	0.13	0.59	0.00014	
	2		7.31	1,796	0.39	0.06	0.12	0.54	0.00013	
	3		5.89	1,639	0.32	0.05	0.10	0.45	0.00012	
	4		4.48	1,418	0.24	0.04	0.08	0.33	0.00010	
	5		3.06	1,084	0.13	0.02	0.04	0.19	0.00007	
	6		1.65	962	0.06	0.01	0.02	0.09	0.00004	

REVISION POR CARGA LATERAL

MURO	ENT	Fr	P (T)	K (T/m)	Vd (T)	Vt (T)	Vt' (T)	Vu (T)	distor*Q'	Vr (T)
25	1	0.700	15.67	15,612	3.62	0.48	0.93	4.81	0.00013	6.55
	2	0.700	13.10	15,612	3.42	0.45	0.89	4.55	0.00013	6.01
	3	0.700	10.53	15,272	3.02	0.40	0.80	4.03	0.00011	5.47
	4	0.700	7.96	13,720	2.29	0.30	0.62	3.05	0.00010	4.94
	5	0.700	5.39	11,214	1.39	0.18	0.39	1.86	0.00007	4.40
	6	0.700	2.83	8,151	0.52	0.07	0.15	0.70	0.00004	3.86
26	1	0.700	15.23	9,666	2.24	0.09	0.17	2.61	0.00012	6.31
	2	0.700	12.73	9,503	2.08	0.08	0.16	2.43	0.00011	5.79
	3	0.700	10.24	9,010	1.78	0.07	0.14	2.08	0.00010	5.27
	4	0.700	7.74	8,392	1.40	0.05	0.11	1.63	0.00008	4.74
	5	0.700	5.25	7,595	0.94	0.04	0.08	1.10	0.00006	4.22
	6	0.700	2.75	7,339	0.47	0.02	0.04	0.55	0.00003	3.69
27	1		8.98	574	0.13	0.01	0.01	0.16	0.00012	
	2		7.53	574	0.13	0.00	0.01	0.15	0.00011	
	3		6.07	574	0.11	0.00	0.01	0.13	0.00010	
	4		4.62	574	0.10	0.00	0.01	0.11	0.00008	
	5		3.17	574	0.07	0.00	0.01	0.08	0.00006	
	6		1.71	574	0.04	0.00	0.00	0.04	0.00003	
28	1	0.700	47.14	46,711	10.82	0.00	0.00	11.90	0.00011	18.07
	2	0.700	39.45	46,711	10.24	0.00	0.00	11.26	0.00010	16.46
	3	0.700	31.75	46,515	9.20	0.00	0.00	10.12	0.00009	14.84
	4	0.700	24.05	45,673	7.61	0.00	0.00	8.37	0.00008	13.22
	5	0.700	16.35	44,465	5.51	0.00	0.00	6.07	0.00006	11.61
	6	0.700	8.66	43,198	2.76	0.00	0.00	3.04	0.00003	9.99
29	1	0.700	15.23	9,666	2.24	0.09	0.17	2.61	0.00012	6.31
	2	0.700	12.73	9,503	2.08	0.08	0.16	2.43	0.00011	5.79
	3	0.700	10.24	9,010	1.78	0.07	0.14	2.08	0.00010	5.27
	4	0.700	7.74	8,392	1.40	0.05	0.11	1.63	0.00008	4.74
	5	0.700	5.25	7,595	0.94	0.04	0.08	1.10	0.00006	4.22
	6	0.700	2.75	7,339	0.47	0.02	0.04	0.55	0.00003	3.69
30	1		8.98	574	0.13	0.01	0.01	0.16	0.00012	
	2		7.53	574	0.13	0.00	0.01	0.15	0.00011	
	3		6.07	574	0.11	0.00	0.01	0.13	0.00010	
	4		4.62	574	0.10	0.00	0.01	0.11	0.00008	
	5		3.17	574	0.07	0.00	0.01	0.08	0.00006	
	6		1.71	574	0.04	0.00	0.00	0.04	0.00003	
31	1	0.700	35.00	17,517	4.06	0.72	1.41	5.73	0.00014	11.67
	2	0.700	29.32	17,320	3.80	0.68	1.33	5.36	0.00013	10.48
	3	0.700	23.63	16,725	3.31	0.59	1.18	4.68	0.00012	9.28
	4	0.700	17.95	15,994	2.66	0.48	0.98	3.78	0.00010	8.09
	5	0.700	12.27	15,072	1.87	0.33	0.71	2.66	0.00008	6.90
	6	0.700	6.59	14,781	0.95	0.17	0.37	1.35	0.00004	5.71
32	1		8.03	4,704	1.09	0.19	0.38	1.54	0.00014	
	2		6.72	4,704	1.03	0.18	0.36	1.46	0.00013	
	3		5.41	4,611	0.91	0.16	0.33	1.29	0.00012	
	4		4.10	4,166	0.69	0.12	0.25	0.98	0.00010	
	5		2.79	3,357	0.42	0.07	0.16	0.59	0.00008	
	6		1.48	2,160	0.14	0.02	0.05	0.20	0.00004	
33	1		8.72	1,845	0.43	0.07	0.13	0.59	0.00014	
	2		7.31	1,796	0.39	0.06	0.12	0.54	0.00013	
	3		5.89	1,639	0.32	0.05	0.10	0.45	0.00012	
	4		4.48	1,418	0.24	0.04	0.08	0.33	0.00010	
	5		3.06	1,084	0.13	0.02	0.04	0.19	0.00007	
	6		1.65	962	0.06	0.01	0.02	0.09	0.00004	
34	1	0.700	15.67	15,612	3.62	0.48	0.93	4.81	0.00013	6.55
	2	0.700	13.10	15,612	3.42	0.45	0.89	4.55	0.00013	6.01
	3	0.700	10.53	15,272	3.02	0.40	0.80	4.03	0.00011	5.47
	4	0.700	7.96	13,720	2.29	0.30	0.62	3.05	0.00010	4.94
	5	0.700	5.39	11,214	1.39	0.18	0.39	1.86	0.00007	4.40
	6	0.700	2.83	8,151	0.52	0.07	0.15	0.70	0.00004	3.86
35	1	0.700	30.25	35,644	8.26	2.17	4.25	12.88	0.00016	13.20
	2	0.700	25.28	35,458	7.77	2.05	4.02	12.13	0.00015	12.16
	3	0.700	20.31	34,910	6.91	1.83	3.65	10.81	0.00013	11.12
	4	0.700	15.34	34,258	5.71	1.51	3.10	8.96	0.00011	10.07
	5	0.700	10.38	33,469	4.15	1.09	2.34	6.54	0.00008	9.03
	6	0.700	5.41	33,227	2.13	0.55	1.23	3.35	0.00004	7.99
36	1		3.49	1,123	0.26	0.07	0.13	0.41	0.00016	
	2		2.92	1,094	0.24	0.06	0.12	0.37	0.00015	
	3		2.34	1,000	0.20	0.05	0.10	0.31	0.00013	
	4		1.77	865	0.14	0.04	0.08	0.23	0.00011	
	5		1.19	654	0.08	0.02	0.05	0.13	0.00008	
	6		0.62	574	0.04	0.01	0.02	0.06	0.00004	
37	1		23.71	77,890	18.04	4.75	9.28	28.14	0.00016	
	2		19.82	77,076	16.90	4.46	8.75	26.38	0.00015	
	3		15.93	74,643	14.77	3.91	7.80	23.11	0.00013	
	4		12.03	71,683	11.94	3.15	6.48	18.74	0.00011	
	5		8.14	68,002	8.43	2.21	4.76	13.28	0.00008	
	6		4.25	66,849	4.28	1.11	2.48	6.74	0.00004	

This page is intentionally left blank.

Appendix F

Structural Drawings and Composite Materials

This section depicts the structural drawings generated with the information obtained in appendix E, the set of figures shown in this appendix correspond to:

- Figure F.1 depicts the typical steel reinforcement pattern for all concrete slabs of building `B-SSC`.
- Figures F.2 and F.3 are the structural plan view of each level belonging to building `B-SSC`.
- Figures F.4 to F.6 are structural elevation of some construction axis.
- Figure F.7 display the set of structural elements used to confine the masonry walls, whereas F.8 display the cross sections of the used concrete walls.
- On the other hand, Figures F.9 to F.16 represent the `SCM` as described in section 3.7 to model building `B-SSC` using the proposed scheme of this work.

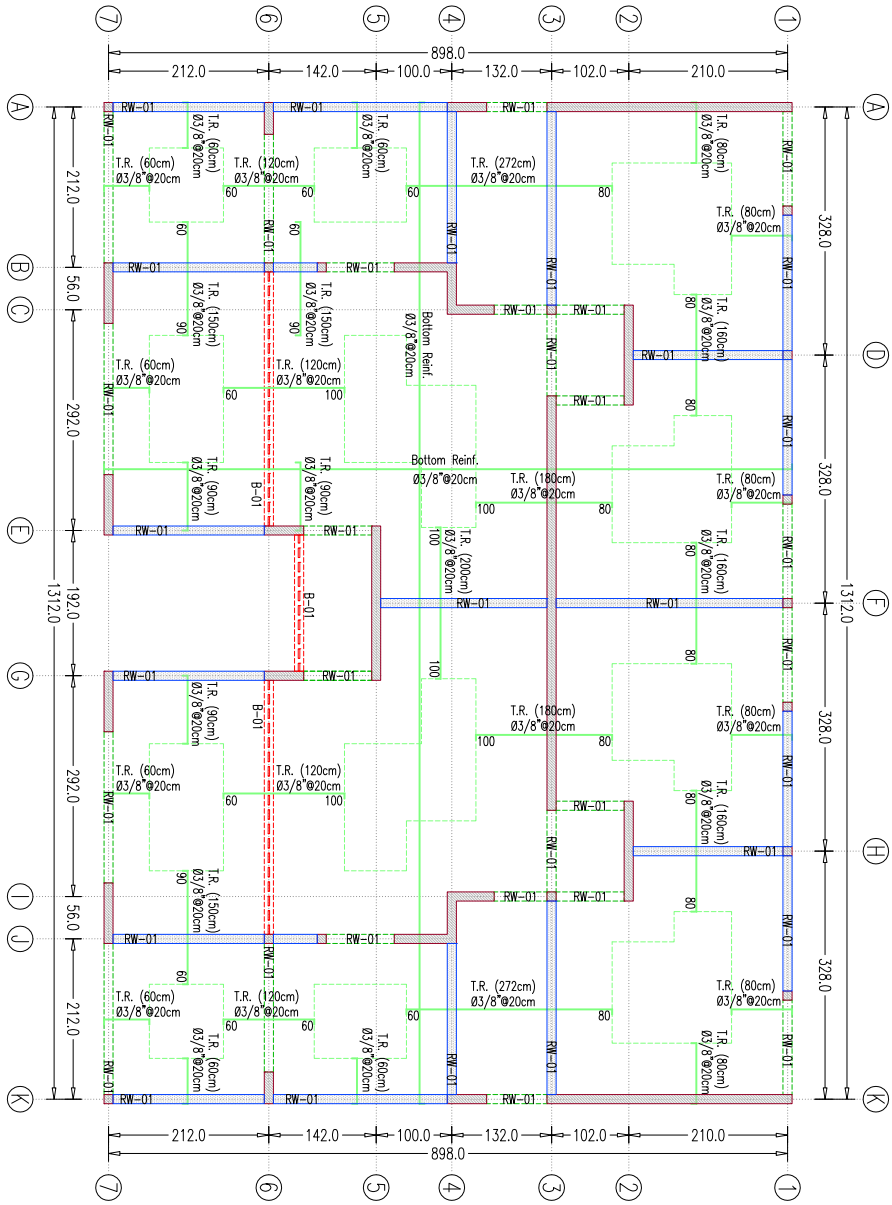

Figure F.1 *Structural Plan - Slab (Steel Reinforcement).*

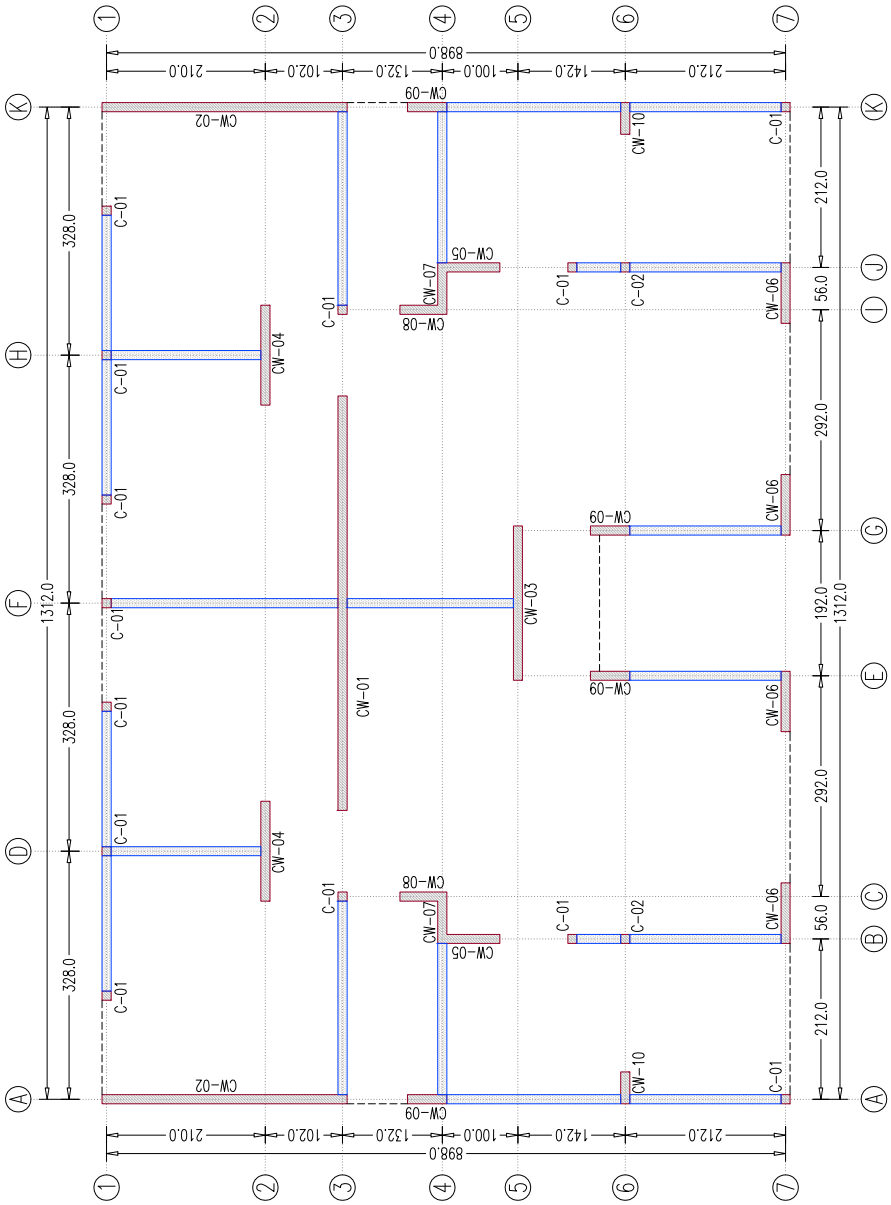

Figure F.2 *Structural Plan - Walls and Columns (L+0.00m, L+2.85m).*

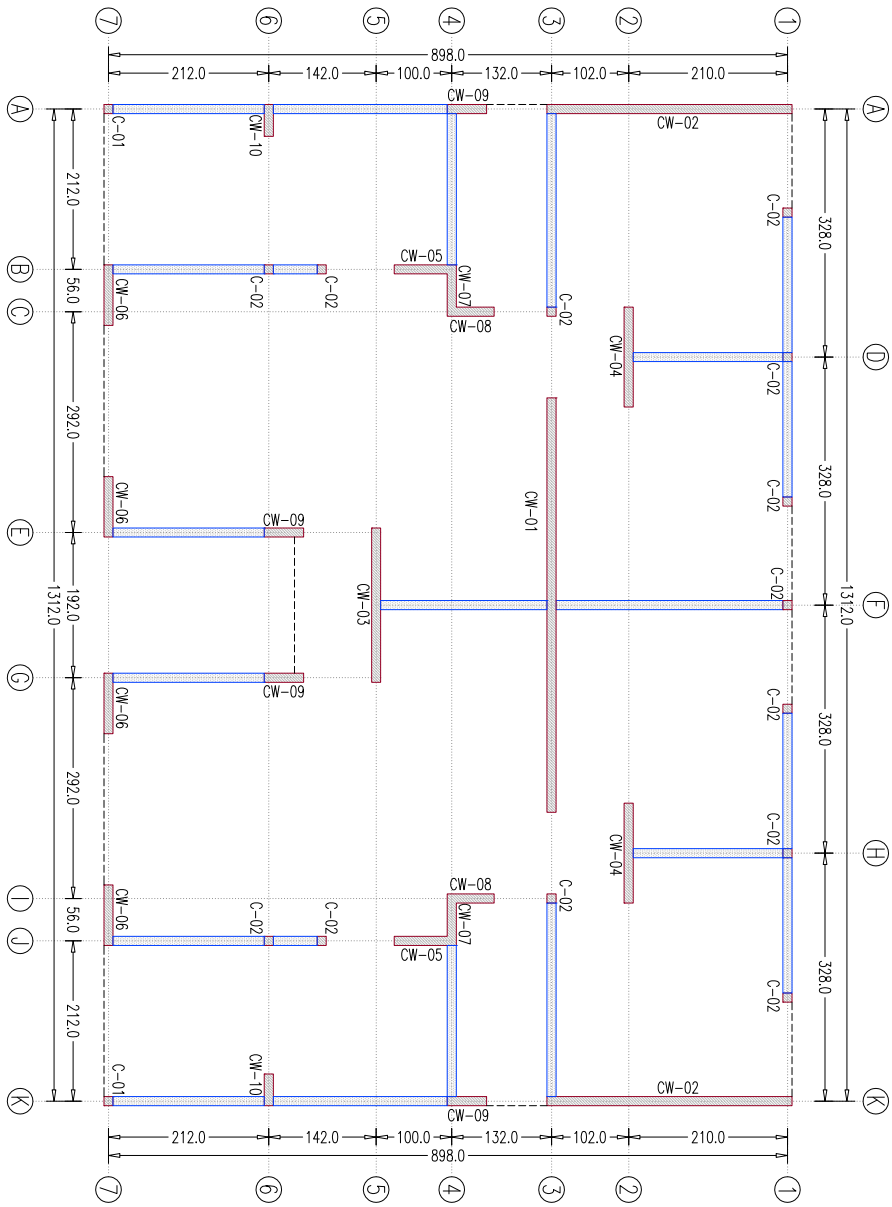

Figure F.3 *Structural Plan - Walls and Columns (L+5.45m, L+8.05m, L+10.65m).*

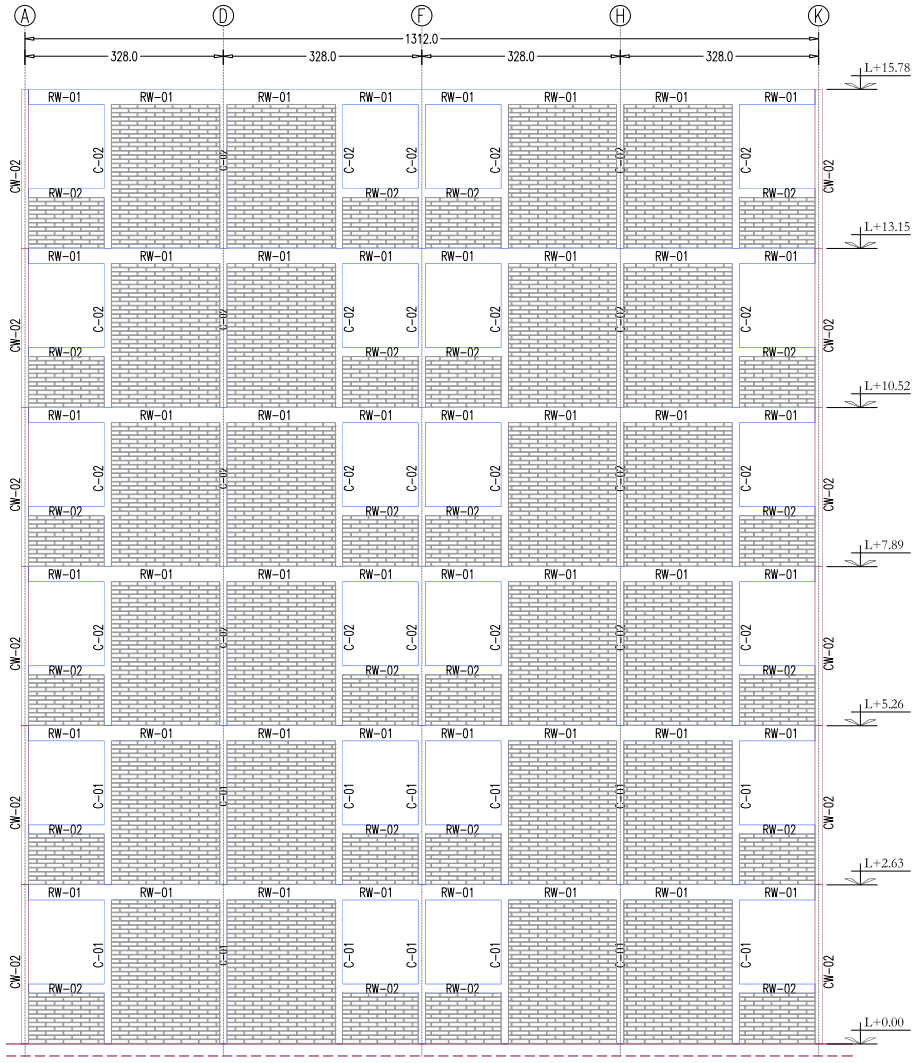

Figure F.4 *Structural Elevation - Axis **1**.*

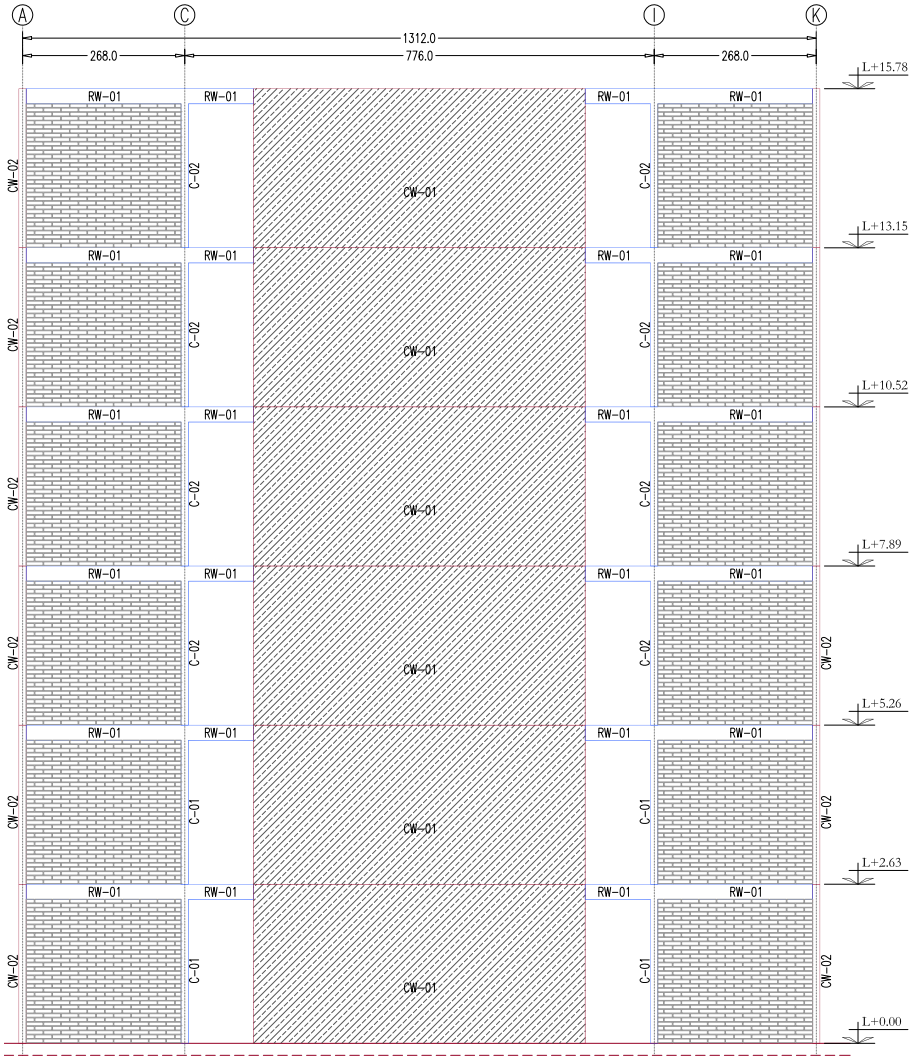

Figure F.5 *Structural Elevation - Axis 3.*

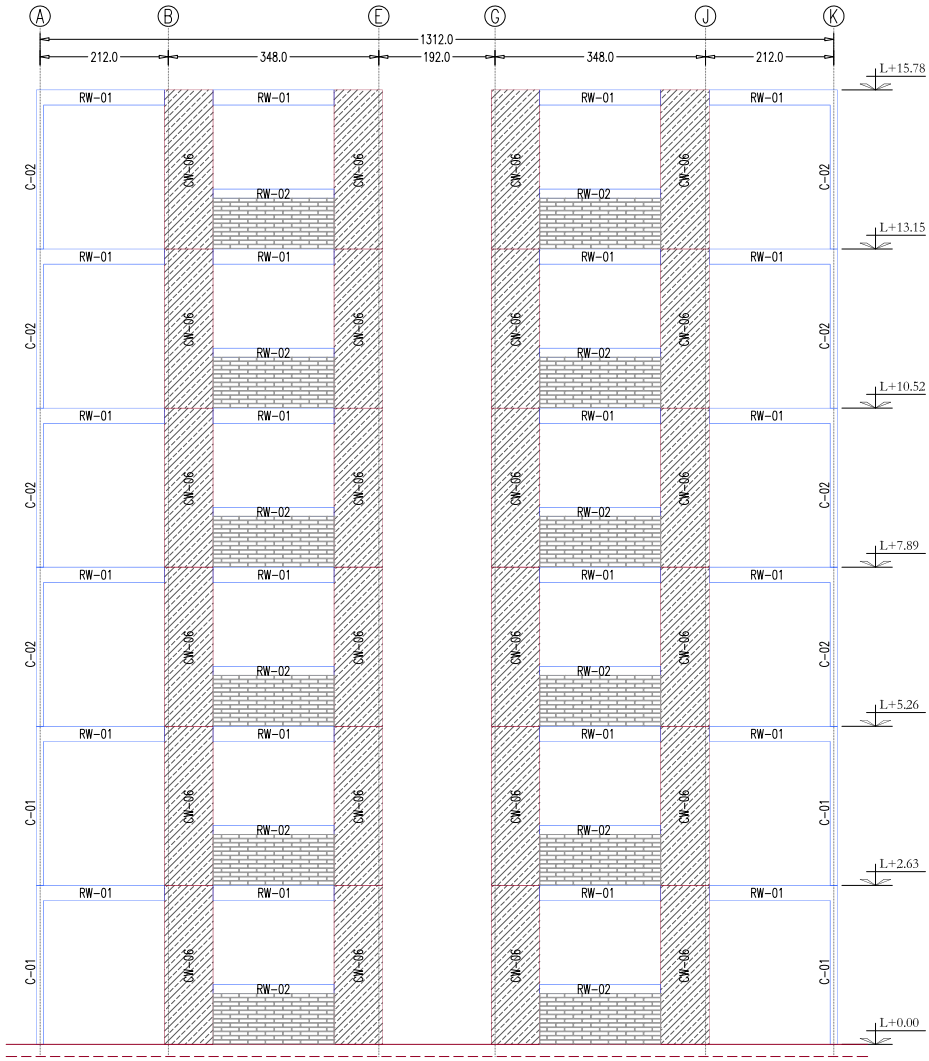

Figure F.6 *Structural Elevation - Axis 7.*

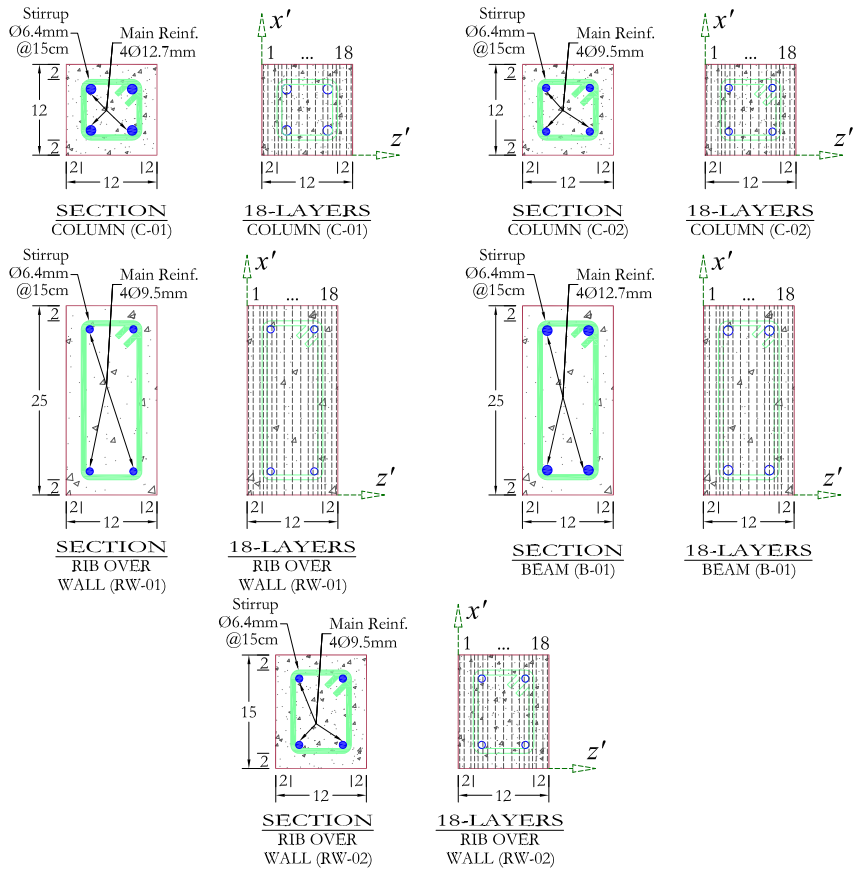

Figure F.7 *Structural Cross Sections - RC Elements.*

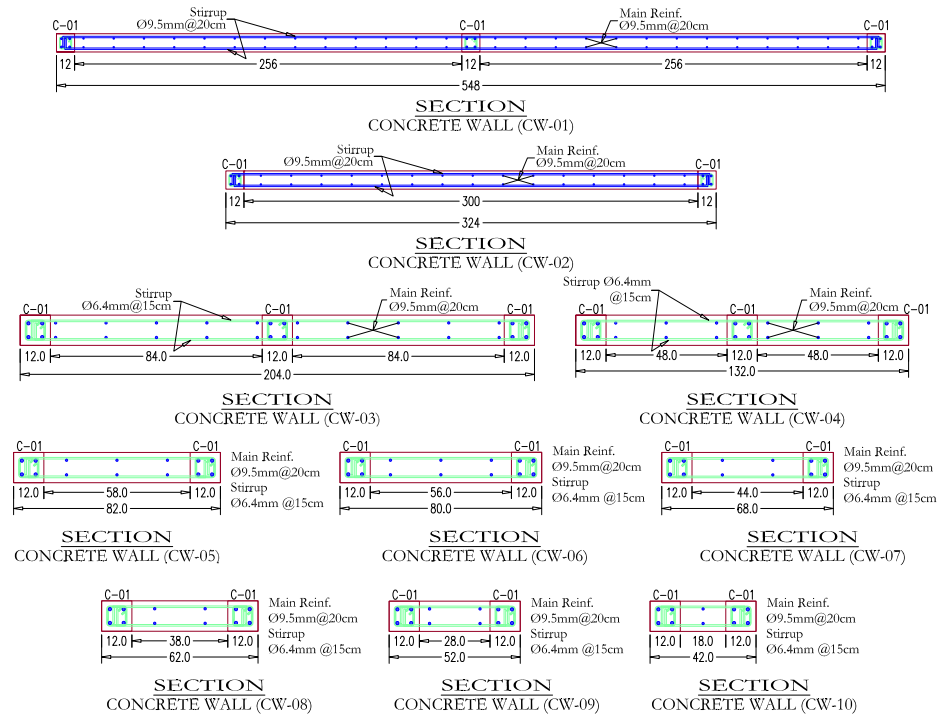

Figure F.8 *Structural Cross Sections - RC Walls.*

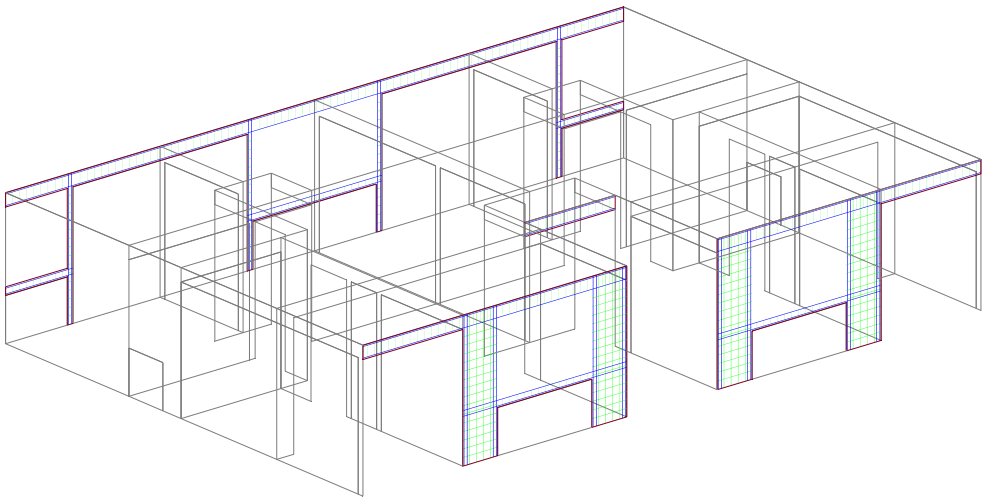

Figure F.9 *Steel fibers of Axis **1**, **5a** and **7**.*

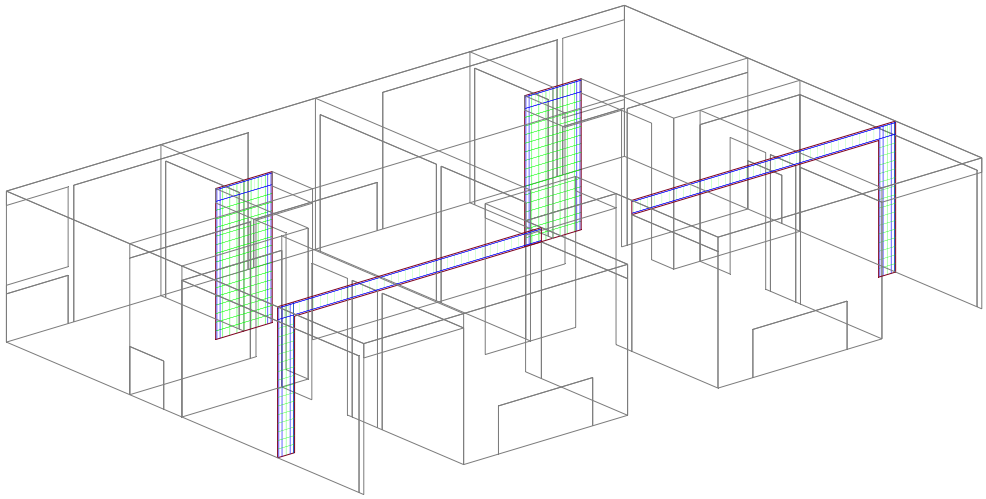

Figure F.10 *Steel fibers of Axis **2** and **6**.*

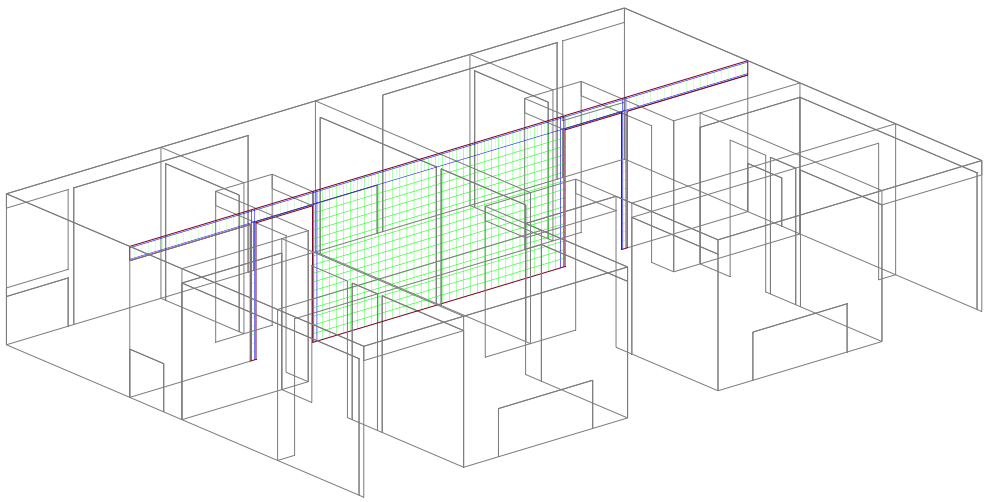

Figure F.11 *Steel fibers of Axis **3**.*

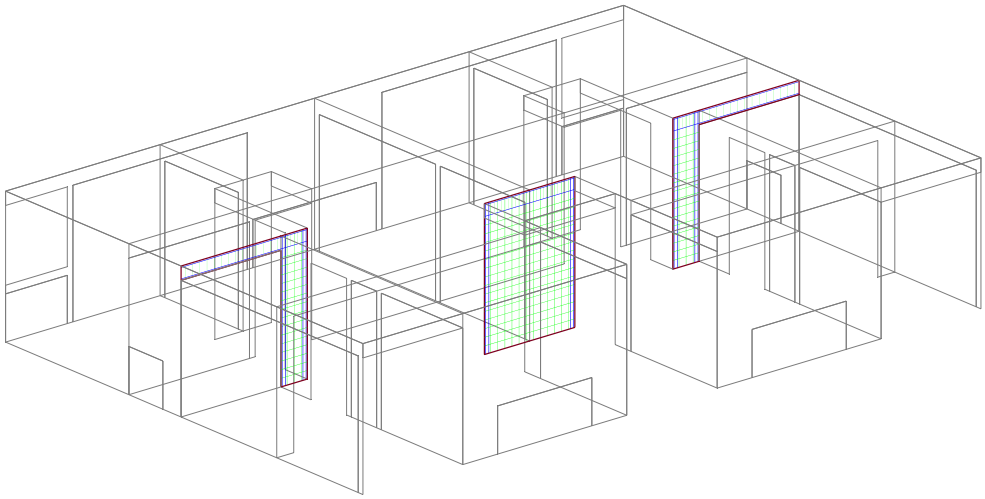

Figure F.12 *Steel fibers of Axis* ***4*** *and* ***5****.*

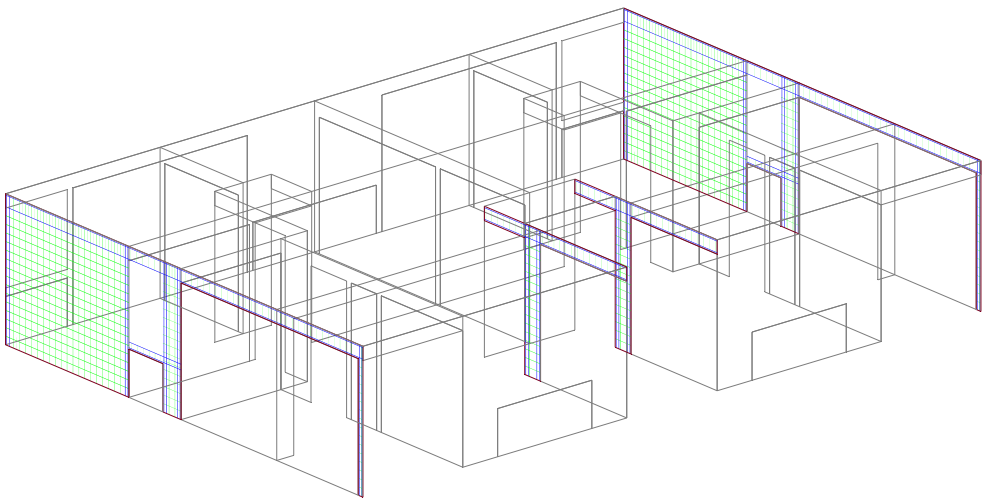

Figure F.13 *Steel fibers of Axis* ***A****,* ***E****,* ***G*** *and* ***K****.*

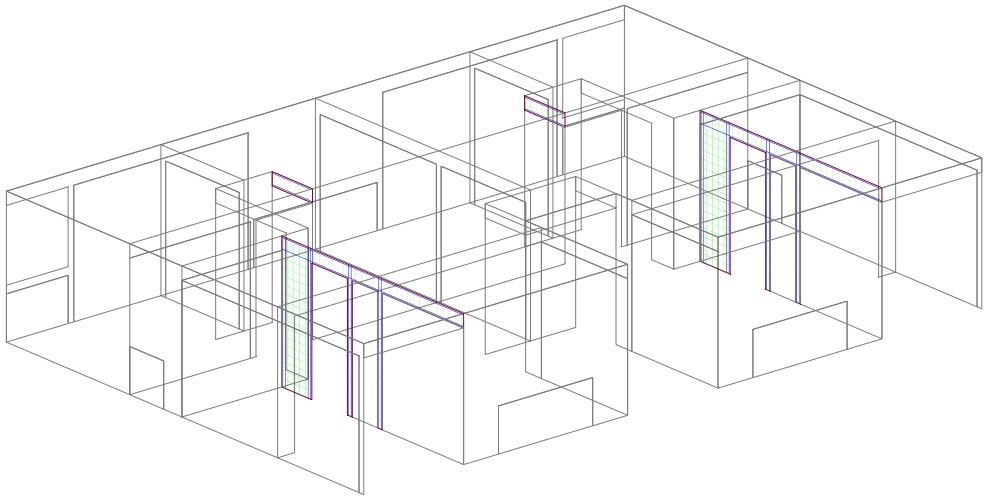

Figure F.14 *Steel fibers of Axis* ***B****,* ***D1****,* ***G1*** *and* ***J****.*

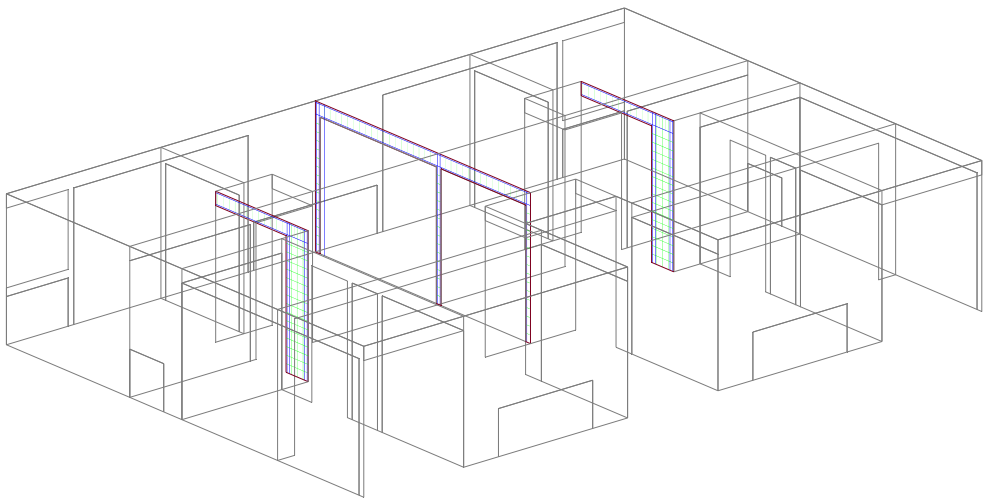

Figure F.15 *Steel fibers of Axis* ***C****,* ***F*** *and* ***I****.*

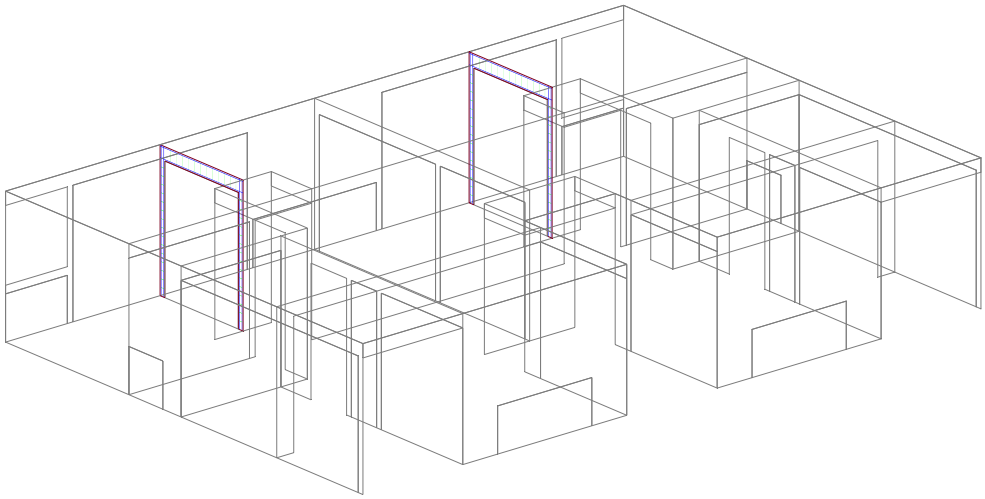

Figure F.16 *Steel fibers of Axis* ***D*** *and* ***H****.*

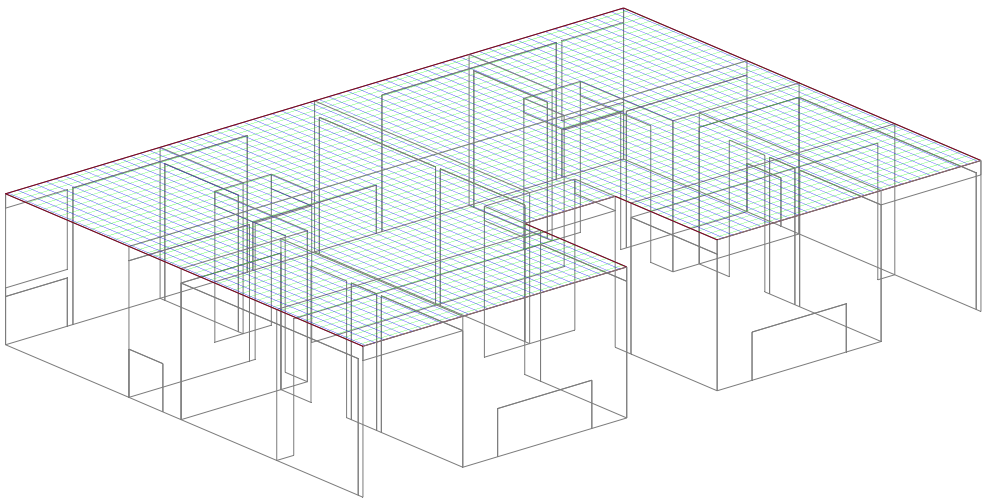

Figure F.17 *Steel fibers of concrete slab.*

This page is intentionally left blank.

Appendix G

Seismic Demand and Probabilistic Damage Assessment

The present appendix briefly describes the methodology proposed by Alzate [8] to assess a reliable seismic demand, and consequently, to state a probabilistic damage a structure would undergo given such seismic demand. The methodology proposed by Alzate [8] is based upon the capacity spectrum, the followed steps are summarized in next paragraph, and finally, they are described from section G.1 to section G.4.

1. The starting point is the capacity curve of a given structure obtained from a standard pushover analysis, the capacity curve need to be transform into a *spectral* capacity curve, and later, in a *bilinear* capacity curve using the method described in section G.1.

2. It is necessary to obtain a *performance point* (which represents the seismic demand), to do so, it is necessary to overlaying an elastic response spectrum in a $sa - sd$ representation (section G.2) and the obtained bilinear capacity spectrum (section G.1) using the linear equivalent approach described in section G.3.

3. Finally, using the points (D_y, A_y) and (D_u, A_u) which define the bilinear capacity spectrum, can be plot a set of fragility curves, and consequently, be able to obtain an expected damage index (section G.4).

Using the information obtained from step **3**, it is possible to link together the capacity of a given structure, with the expected seismic demand (using an elastic response spectrum) such structure would undergo, thus concluding, the probability of taking place each of the damage states defined by Risk-EU [132].

G.1 Standard Capacity Curve and Bilinear Capacity Spectrum

The standard capacity curve, or simply capacity curve shown in figure G.1 correspond to the work done by Alzate [8] and reports the displacement-force response of a building

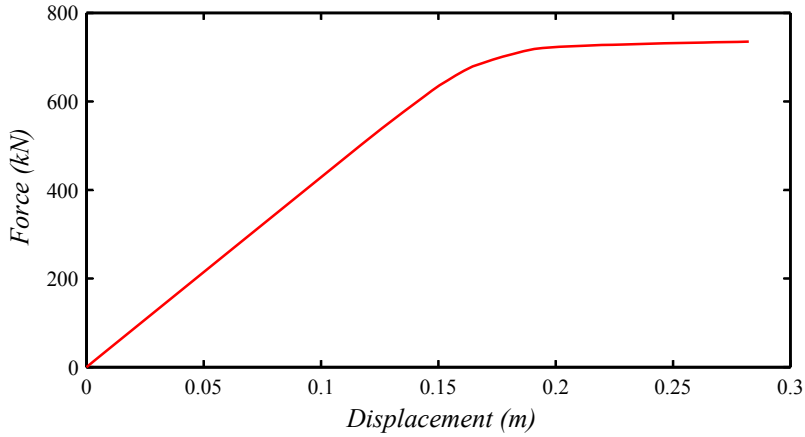

Figure G.1 *Standard capacity curve for Omega Building (UPC Campus Nord, Barcelona, Spain).*

located in Barcelona, Spain.

Graph on figure G.1 has been obtained with a pushover analysis with monotonic adaptive load pattern, and have to be seen as the starting point to obtain the probabilistic damage assessment of a building using the method described in this appendix.

Since elastic response spectra are calculated for a one-degree-of-freedom structure, it is convenient to represent the capacity curve of the studied structure using the same convention. A proposal for this has been carried out by Alzate [8], is based upon fundamentals of structural dynamics, and consists on the two main simplifications described next.

1. The starting point for the first simplification is a structure as the one depicted in figure G.2 on the left, namely, a structure with several storeys and several degrees of freedom on each storey. An equivalent stiffness per storey can be obtained using equation G.1,

$$ {}^{k}\mathbf{K}_x = \sum_{i=1,n} {}^{k}K_x^i \quad ; \quad {}^{k}\mathbf{K}_y = \sum_{i=1,n} {}^{k}K_y^i \tag{G.1} $$

where subindex k stands for storey, $K_{x,y}$ is the stiffness of a given structural element, and $\mathbf{K}$ is the total stiffness of the k storey, also, the mass of the whole storey have to be concentrated in a single degree of freedom. The result is an equivalent model as the one shown in figure G.2 on the right, referred from now on, as the *mass-concentrated* model.

2. The second simplification comes from converting the mass-concentrated model into an equivalent one-degree-of-freedom model using the modal participation factor shown in equation G.2.

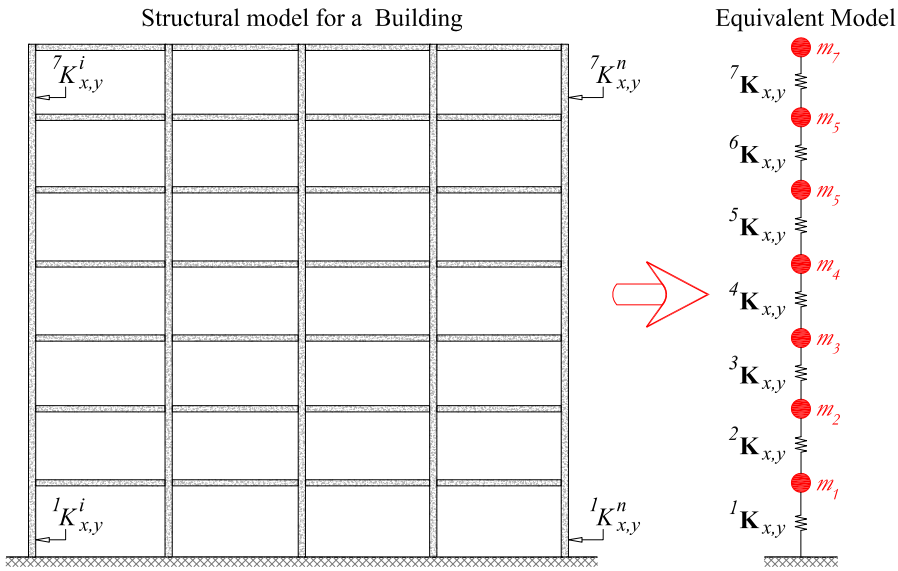

Figure G.2 *Structural model and its equivalent mass-concentrated model*

$$PF_m = \frac{\sum_{i=1}^{n} \frac{w_i \, \phi_{im}}{g}}{\sum_{i=1}^{n} \frac{w_i \, \phi_{im}^2}{g}} \tag{G.2}$$

where ϕ_{im} is the component i of the vibrational mode m, w_i is the weight of the storey i, and g the gravitational constant. On the other hand, the effective mass coefficient α_m on equation G.3 represents the total amount of mass used by each vibrational mode.

$$\alpha_m = \frac{\left[\sum_{i=1}^{n} \left(\frac{w_i \, \phi_{im}}{g}\right)\right]^2}{\sum_{i=1}^{n} \left(\frac{w_i}{g}\right) \sum_{i=1}^{n} \left(\frac{w_i \, \phi_{im}^2}{g}\right)} \tag{G.3}$$

In plain words, using equations G.2 and G.3 it is possible to represent each vibrational mode of a multi-degree-of-freedom model as an equivalent one-degree-of-freedom model with a normalized mass m^* and a normalized stiffness $\mathbf{K}^*$.

The idea behind such concepts can be better illustrated using figure G.3, where $f_i = m_i \, a_i$, being a_i the acceleration a mass m_i undergoes, which in turn produces a seismic force f_i, V is the entire shear force at the basement of the structure, $^{i}\mathbf{K}$ is the condensed stiffness for storey i, δ_{roof} is the resulting displacement at the top of the structure once a force f_i has been applied. On the other hand, *sa* and *sd* are respectively, the spectral acceleration and the spectral displacements.

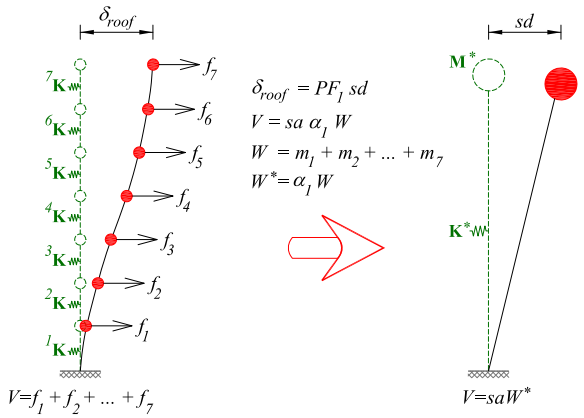

Figure G.3 *Mass-concentrated model and its equivalent one d.o.f. model.*

Finally, the use of equations G.4 makes possible the transformation of a capacity curve into a spectral capacity curve

$$sd_j = \frac{\delta_j}{PF_1} \qquad ; \qquad sa_j = \frac{V_j}{\alpha_1\, W} \tag{G.4}$$

where subindex j represents the applied loading increments the structure is subjected to under a non-linear pushover analysis.

The concept that is pretended to be synthesized with the use of figure G.3 is: the displacement at the top of a given structure produced by a given load pattern is equivalent to the spectral displacement of the vibrational system of a structure with one-degree-of-freedom. Thus, it is possible to transform the standard curve capacity (fig. G.1) into the spectral capacity curve of an equivalent structure with only one-degree-of-freedom shown in figure G.4.

Finally, once defined the spectral capacity curve with the use of the previously defined concepts, it is possible to plot a spectral capacity curve in a *bilinear* format (also displayed in figure G.4), which is useful to define the damage states undergone by a given structure, the main hypothesis to construct it are:

1. The area under the spectral capacity curve must be equal to the equivalent bilinear capacity curve.
2. Coordinates of the point with maximum displacement (D_u, A_u) match in both curves.
3. The initial slope in both graphs must be the same.

G.2 Seismic Design Spectrum and sa-sd Representation

Most of the countries, where an intense seismic activity is present, usually possess mandatory code regulations for the structural design of construction, where seismicity

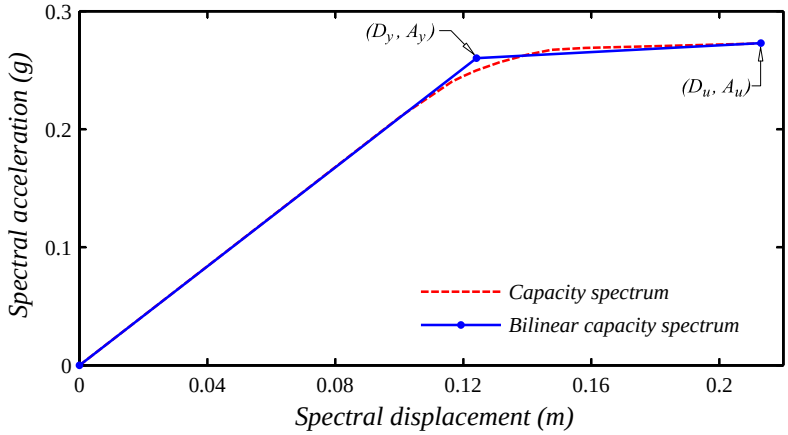

Figure G.4 *Bilinear capacity curve for Omega Building (UPC Campus Nord, Barcelona, Spain).*

condition are taken into account with the use of design spectra plotted for one-degree-of-freedom structures, usually, with damping equal to 5%. In general, design spectra are divided in sections where the acceleration, velocity and displacement are constant, and can be plot with the use of simplistic function.

In the countries of the European union, for instance, it is recommended the use of EUROCODE 8 [40] to prove compliance with the requirements for mechanical strength, stability and safety in case of seismic activity. The proposed spectra in [40] are based on studies of different research groups that use a selected set of European strong motion data, their shapes are considered for varying seismicity conditions and subsoil classification, and can be plot using the set of equations G.5 to G.8.

$$0 \leq T \leq T_B : sa(T) = a_g\, S \left[1 + \frac{T}{T_B}(2.5\eta - 1)\right] \tag{G.5}$$

$$T_B \leq T \leq T_C : sa(T) = 2.5\, a_g\, S\, \eta \tag{G.6}$$

$$T_C \leq T \leq T_D : sa(T) = 2.5\, a_g\, S\, \eta \left[\frac{T_C}{T}\right] \tag{G.7}$$

$$T_D \leq T \leq 4s : sa(T) = 2.5\, a_g\, S\, \eta \left[\frac{T_C\, T_D}{T^2}\right] \tag{G.8}$$

where

Soil Type	S	$T_B(S)$	$T_C(S)$	$T_D(S)$
A	1.00	0.15	0.4	2
B	1.20	0.15	0.5	2
C	1.15	0.20	0.6	2
D	1.35	0.20	0.8	2
F	1.40	0.15	0.5	2

Table G.1 *Parameters for seismic design spectra, Eurocode 8, Type 1.*

Soil Type	S	$T_B(S)$	$T_C(S)$	$T_D(S)$
A	1.00	0.05	0.25	1.2
B	1.35	0.05	0.25	1.2
C	1.50	0.10	0.25	1.2
D	1.80	0.10	0.30	1.2
F	1.60	0.05	0.25	1.2

Table G.2 *Parameters for seismic design spectra, Eurocode 8, Type 2.*

$sa(T)$ = Design spectrum as a function of the vibrational period.
T = Vibrational period of a linear system with one-degree-of-freedom.
a_g = Design ground acceleration.
T_B = Vibrational period defining the lower limit of the constant acceleration segment.
T_C = Vibrational period defining the upper limit of the constant acceleration segment, and the beginning of the constant velocity segment.
T_D = Vibrational period defining the end of the constant velocity segment, and the beginning of the constant displacement segment.
S = Soil factor.
η = Damping correction factor.

The elastic design spectra for different seismicity conditions and subsoil classes can be created using equations G.5 to G.8 and parameters of tables G.1 and G.2. EC8 [40] defines two different spectra according to the surface wave magnitude M_s, namely, for $M_s < 5.5$ parameters for soil type 1 have to be used (table G.1), on the other hand, for $M_s > 5.5$ parameters for soil type 2 have to be selected (table G.2).

The design spectra, for a given damping, created using equations G.5 to G.8 and tables G.1 and G.2 link together the spectral acceleration *sa* with the vibrational period T of an one-degree-of-freedom structure, however, Mahaney *et al* in [84] proposes the use of a representation in a $sa - sd$ format, exploiting the fact that the response spec-

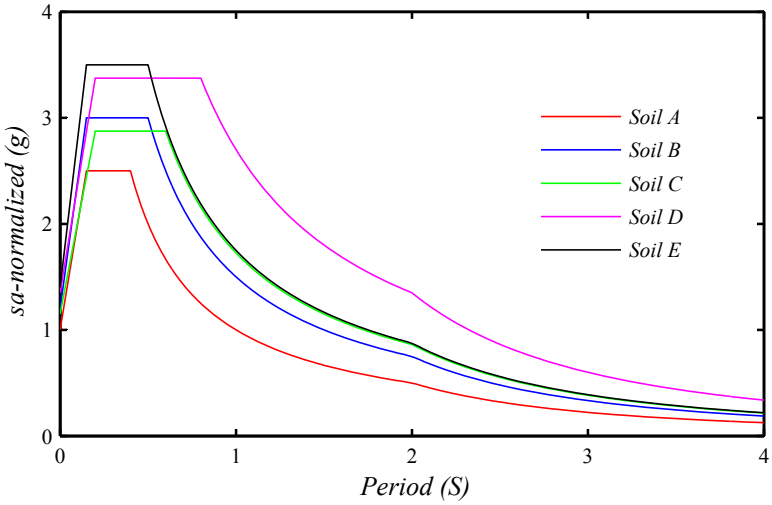

Figure G.5 *Design spectra for soil type 1, Eurocode 8 [40].*

tra corresponding to small damping are approximated with the use of pseudo-spectra. Also, because the damping ratio of building usually are among 5% and 20% of the critical damping, spectra or pseudo-spectra can be used indistinctly, validating the use of equation G.9 which is only valid for pseudo-spectra.

$$sd(\omega) = \frac{1}{\omega} sv(\omega) = \frac{1}{\omega^2} sa(\omega) \tag{G.9}$$

From equation G.9 ω is the angular frequency, sa, sv y sd are respectively, the response spectra of acceleration, velocity and displacement.

$$\omega = \frac{2\,\pi}{T} \tag{G.10}$$

Keeping in mind equation G.9 and the existing relationship among the angular frequency (or pulsation) ω with the vibrational period T described by equation G.10, the spectral displacement is now obtained using equation G.11.

$$sd_i = \frac{T_i^2\, sa_i}{4\,\pi^2} \tag{G.11}$$

The use of equation G.11 is useful to plot a design spectrum in a $sa - sd$ representation, for instance, figure G.6 is a $sa - sd$ representation of design spectra shown in figure G.5.

G.3 Capacity on Demand and Performance Point

In section G.2 has been presented a brief description of elastic design spectra, and how to manage to represent them in such a way they link the spectral acceleration sa with the spectral displacement sd. Also, in section G.1 has been reproduced a description of how to represent the standard capacity curve of a given construction in

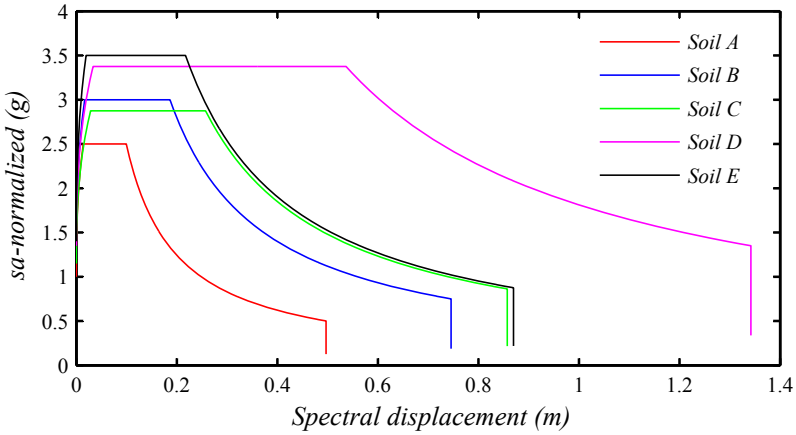

Figure G.6 *Design spectra for soil type 1, Eurocode 8 [40], $sa - sd$ representation.*

	$P(ds_1)$	$P(ds_2)$	$P(ds_3)$	$P(ds_4)$
$P(ds_1 = 0.50)$	0.500	0.119	0.012	0.000
$P(ds_2 = 0.50)$	0.896	0.500	0.135	0.008
$P(ds_3 = 0.50)$	0.992	0.866	0.500	0.104
$P(ds_4 = 0.50)$	1.000	0.988	0.881	0.500

Table G.3 *Distribucion de probabilidad para ds_i.*

a bilinear capacity (fig. G.4). This section describes the process to link together such information, and therefore, obtain the expected spectral displacement sd_e (also referred as the *performance point*) used to assess the seismic demand of the studied structure.

Although in reference [8] Alzate describes two possible schemes to assess the performance point, in the present appendix, it is only described one of them: the linear equivalent approach, and although its main drawback is that it does not take into account the ductility of the structure, for the descriptive purposes intended in this appendix is sufficient, reader may abound in the topic using reference [8].

The linear equivalent approach consists in assuming the structure remains in the liner elastic range the whole process, therefore, it is only necessary to prolong the initial segment of the bilinear capacity spectrum and cross it, with the design spectra in $sa-sd$ format. The projection of the resulting intersection point to the bilinear capacity curve represents the performance point.

To illustrate this concept, Alzate [8] uses a design spectrum type 1 (according to EC8) for a soil type D, and proposes a peak ground acceleration $PGA = 0.20g$ (figure G.6), which combined with the bilinear capacity curve for the Omega Building (fig. G.4) leads to a spectral displacement $sd_e = 0.19m$, as can be seen in figure G.7.

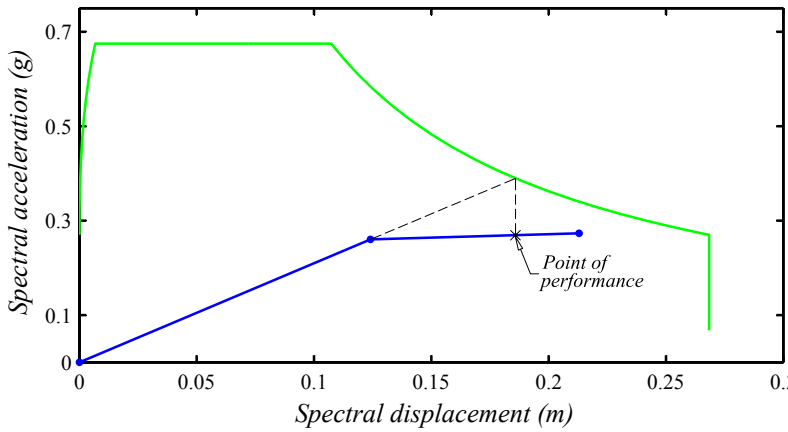

Figure G.7 *Graphic representation of a linear equivalent approximation.*

G.4 Fragility Curves and Damage Index

Fragility curves represent the probability in which a given damage scenario ds on a structure could be reached or exceeded, as a function of the parameter that represent the intensity of the seismic action. Risk-EU [132] distinguishes four possible damage scenarios on a structure, namely, *slight*, *moderated*, *extensive* and *complete*. Risk-EU [132] also proposes to define such damage scenarios ds in a simplified form, which is based on the points (D_y, A_y) and (D_u, A_u) of the bilinear capacity spectrum (figure G.4), leading to the equation G.12, where ds_1 correspond to a slight damage scenario, ds_2 to a moderate damage scenario, ds_3 to an extensive damage scenario, and finally ds_4 to a complete damage scenario.

$$\begin{aligned} ds_1 &= 0.7\, D_y \\ ds_2 &= D_y \\ ds_3 &= D_y + 0.25(D_u - D_y) \\ ds_4 &= D_u \end{aligned} \tag{G.12}$$

Using equations G.12 Alzate [8] reports values $ds_1 = 0.0869m$, $ds_2 = 0.1241m$, $ds_3 = 0.1464m$, and $ds_4 = 0.2133m$ for the Omega Building.

Once displacements corresponding to all considered damage scenarios have been assessed, in order to plot the corresponding fragility curves it is necessary to take in consideration next hypothesis:

1. The existing probability that a damage scenario, in terms of its corresponding spectral displacement threshold ds_i can be reached or exceeded is equal to 50%.

2. The fragility curves hold a cumulative distribution function $\mathbf{\Phi}$ described in equation G.13.

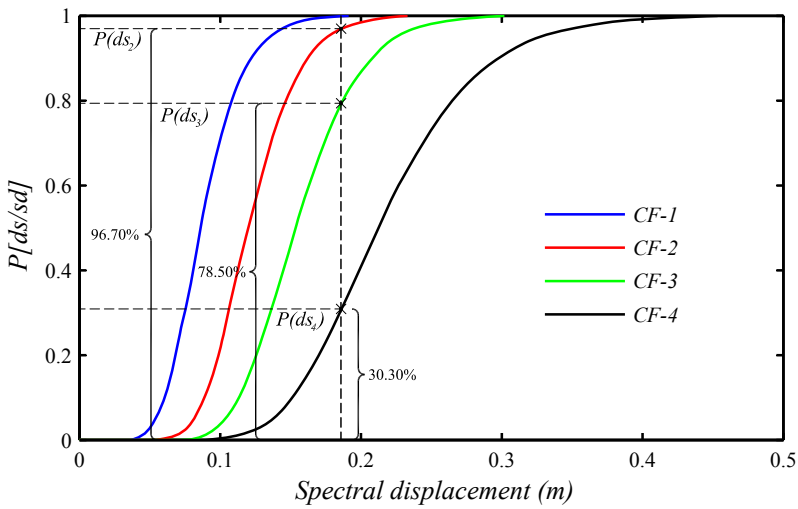

Figure G.8 *Fragility curves for Omega Building (UPC Campus Nord, Barcelona, Spain).*

$$P[ds_i/sd] = \mathbf{\Phi}\left[\frac{1}{\beta_{ds_i}} ln\left(\frac{sd}{ds_i}\right)\right] \tag{G.13}$$

where ds is the spectral displacement, β_{ds_i} is the standard deviation of the natural logarithm of variable ds_i.

3. The expected damage on the studied structure holds a binomial probability distribution.

Applying hypothesis **1** and **3** has made possible to obtain the probability distribution listed in table G.3 for the considered damage scenarios ds_i. On the other hand, equation G.13 described in hypothesis **2** allows approximating the damage factors β_{ds_i} using a least squares technique.

Although the Risk-EU project [132] proposes the assessment of the damage factors β_{ds_i} as a function of the ductility of the studied structure μ_u, defined as

$$\mu_u = \frac{D_u}{D_y} \tag{G.14}$$

using equation G.15, in the present work, such damage factors β_{ds_i} have been obtained using a least squares approximation.

$$\begin{aligned} \beta_{ds_1} &= 0.25 + 0.07\nu_u \\ \beta_{ds_2} &= 0.20 + 0.18\nu_u \\ \beta_{ds_3} &= 0.10 + 0.40\nu_u \\ \beta_{ds_4} &= 0.15 + 0.50\nu_u \end{aligned} \tag{G.15}$$

Using equations G.12 and the hypothesis previously described, Alzate [8] reports values shown in equation G.16,

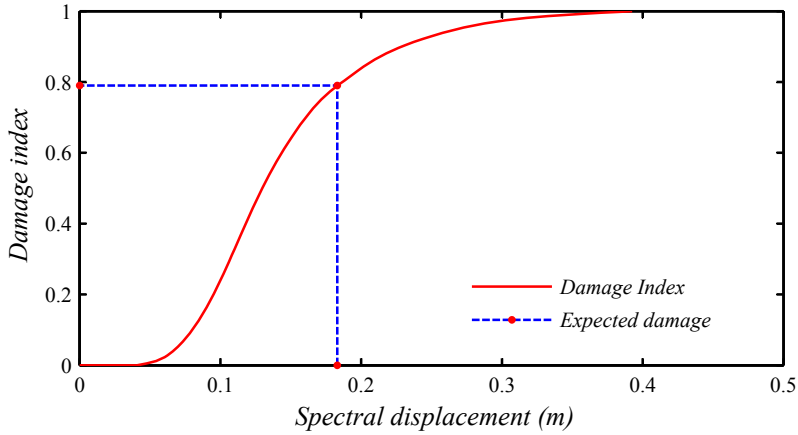

Figure G.9 *Damage index curve for Omega Building (UPC Campus Nord, Barcelona, Spain).*

$$\begin{aligned} ds_1 &= 0.0869 \quad ; \quad \beta_{ds_1} = 0.268 \\ ds_2 &= 0.1204 \quad ; \quad \beta_{ds_2} = 0.220 \\ ds_3 &= 0.1512 \quad ; \quad \beta_{ds_3} = 0.232 \\ ds_4 &= 0.2133 \quad ; \quad \beta_{ds_4} = 0.282 \end{aligned} \tag{G.16}$$

and using function $\mathbf{\Phi}$ described in equation G.13 plots the fragility curves shown in figure G.8, corresponding to the Omega Building, used as the reference example, also Alzate reports the probability of occurrence of the considered damage scenarios for the spectral displacement of the performance point $sd_e = 0.19m$.

Finally, using the fragility curves shown in figure G.8, it is possible to assess the probability of occurrence of the considered damage scenarios $P(ds_i)$ applying the equation G.17.

$$P(ds_i) = \begin{cases} 1 - CF_{i+1} & i = 0 \\ CF_{i+1} - CF_i & 0 < i < 4 \\ CF_i & i = 4 \end{cases} \qquad i \in \{0, 1, ..., 4\} \tag{G.17}$$

where CF_i is the value of the fragility curve associated to the damage i. On the other hand, it is convenient to use a parameter that represent the global damage of the structure, therefore, using the previously calculated probabilities with equation G.17, it is possible to obtain an expected damage index ID with equation G.18. This damage index represent a normalized damage scenario for the studied structure, the resulting graph is depicted in figure G.9.

$$ID = \frac{1}{n} \sum_{i=0}^{n} P(ds_i) \tag{G.18}$$